Characterizing the Particle-Particle and Particle-Polymer Interactions that Control Cellulose Nanocrystal Dispersion

Characterizing the Particle-Particle and Particle-Polymer Interactions that Control Cellulose Nanocrystal Dispersion

By MICHAEL S. REID, B.Sc., M.Sc.

A Thesis Submitted to the School of Graduate Studies in Partial Fulfillment of the Requirements
for the Degree Doctor of Philosophy

McMaster University

DOCTOR OF PHILOSOPHY (2017) McMaster University
(Chemical Engineering) Hamilton, Ontario

TITLE: CHARACTERIZING THE PATICLE-PARTICLE AND PARTICLE-POLYMER INTERACTIONS THAT CONTROL CELLULOSE NANOCRYSTAL DISPERSIBILITY

AUTHOR: Michael S. Reid
B.Sc. Honours (University of Guelph)
M.Sc. Chemistry (University of Alberta)

SUPERVISORS: Professor Emily D. Cranston

NUMBER OF PAGES: xi, 169

Abstract

Cellulose nanocrystals (CNCs) are rigid rod-shaped nanoparticles derived from bio-based resources and are considered an emerging nanomaterial based on their commercial availability and favourable properties. CNCs have great potential as reinforcing agents in hybrid materials and composite applications if they are well-dispersed. Whereas colloidal stability is effectively described by established theories, dispersing nanoparticles from an aggregated state, and their interaction with polymers can be difficult to predict and control. Herein, the particle-particle and particle-polymer interactions that govern CNC dispersibility in aqueous and non-aqueous environments are examined. The surface chemistry, morphology and colloidal/thermal stability of CNCs from North American industrial producers were extensively characterized such that particle interactions could be reproducibly measured from a known starting material. Industrially produced CNCs compared well to those produced at the bench-scale, implying that laboratory results should be translatable to the development of new CNC-based products. To examine particle-particle interactions within dry CNC aggregates, a surface plasmon resonance-based platform was developed to monitor CNC film swelling in a range of solvents and salt solutions. Water was observed to interrupt particle-particle hydrogen bonding most effectively, however film stability, and ultimately particle aggregation, was maintained by strong van der Waals interactions. Moreover, particle spacing and overall film thickness was found to be independent of the CNC surface chemistries and surface charge densities examined, yet the rate of film swelling scaled with the ionic strength of the surrounding media. Polyethylene glycol (PEG) was used as a model, non-ionic, water-soluble polymer to investigate polymer adsorption to CNC surfaces in water. PEG did not adsorb to CNCs despite the abundance of hydroxyl groups, which is in direct contrast to silica particles that are well known to hydrogen bond with PEG. Combining the knowledge of both particle-particle and particle-polymer interactions, PEG nanocomposites reinforced with CNCs and silica were compared and particle dispersibility was related to composite performance. Although PEG does not adsorb to CNCs in aqueous environments, polymer adsorption *does* occur in dry polymer nanocomposites leading to good dispersibility and improved mechanical properties. Overall, the work presented here yields new insight into the forces that govern CNC dispersion and provides a foundation from which a variety of new CNC-based products can be developed.

Lay Abstract

Using particles derived from renewable resources to reinforce plastics and other materials has the potential to make products lighter, stronger and more environmentally friendly. However, to make these products we need to understand how to control and distribute particles uniformly throughout hybrid/composite materials. This work uses particles extracted from trees and cotton, known as cellulose nanocrystals, to reveal which factors govern particle dispersion in reinforced composite materials. To do so, first the properties and performance of commercially available cellulose nanocrystals were extensively analyzed and compared to form the basis from which interactions can be understood. Next, particle films were measured in water, organic solvents and salt solutions to better understand how aggregated cellulose nanocrystals can be separated within composite materials. The interactions between water-soluble polymers and cellulose nanocrystals were then investigated to reveal how polymer adsorption impacts particle dispersibility. Finally reinforced polymer composites were prepared with uniformly distributed cellulose nanocrystals and the crystallization and mechanical properties were investigated. By developing a deeper understanding of the factors that control cellulose nanocrystal dispersion we can learn how to make a variety of new and improved environmentally conscious products.

Acknowledgements

I would like to extend a great deal of thanks and appreciation to all of those I had the pleasure of working with throughout my time at McMaster University. I would like to sincerely thank my research supervisor Dr. Emily D. Cranston for her guidance and friendship throughout my studies. Emily, while your unparalleled work ethic, dedication and passion are things I admire, it is your care, thoughtfulness and compassion that I aspire too. A lifetime of gratitude is not enough to express how fortunate I feel to have had you as my supervisor.

My appreciation goes to Dr. Marco Villalobos, and all those I worked with at Cabot. The support and insight you have provided throughout my studies have been indispensible and I am truly grateful.

To my family, I can’t thank you enough for all your love and support. Without it I could never have been where I am today. While it seems that my next step will take me an ocean away, I cherish knowing that I have your love and a place to call home.

Above all else I would like to express my deepest and most heartfelt love and appreciation to my wife Laura. Over the last decade I somehow convinced you to move across the country, move back, buy a house (and not live in it), work and live in cities miles apart, and now move across the ocean. Throughout it all you never hesitated or faltered, doubted or complained. You have always met new challenges head on with enthusiasm and strength, and these meager acknowledgements cannot even begin to describe how in awe I am of you. While I don’t know where our future will take us, I can tell that whether it is over mountains, across oceans or through deserts, I can’t wait to do it together.

Acknowledgement of Funding and Research Support

The entirety of this work was financially supported by Cabot Corporation in the form of a collaborative research contract with McMaster University and an NSERC Industrial Postgraduate Scholarship (2013 – 2016) to myself, Michael Reid. Research direction and technical support from Dr. Marco Villalobos, Dr. Toivo Kodas, and Dr. Ani Nikova are greatly acknowledged. Additionally, all management and staff are thanked for their support during my two internships at Cabot's Research and Development Facility in Billerica, MA, USA. We recognize Cabot's continuous commitment to responsible innovation, thank them for their dedication to our nanocellulose research program, and are honoured to have had the opportunity to work with them throughout these projects.

Table of Contents

Chapter 1

Chapter 2

Chapter 3

Chapter 4

Chapter 5

Chapter 6

Chapter 7

Chapter 8

Abbreviations

AFM	atomic force microscopy
AGU	anhydro-D-glucopyranose units
BC	bacterial cellulose
CNC	cellulose nanocrystal
CNF	cellulose nanofibril
CNM	cellulose nanomaterial
CNT	carbon nanotubes
DLS	dynamic light scattering
DSC	differential scanning calorimetry
MFC	microfibrillated cellulose
PE	polyethylene
PEG	polyethylene glycol
PEO	polyethylene oxide
PMMA	poly(methyl methacrylate)
POM	polarized optical microscopy
PP	polypropylene
PS	polystyrene
QCM-D	quartz crystal microbalance with dissipation
SPR	surface plasmon resonance
TC	terminal enzyme complexes
TEMPO	2,2,6,6-tetramethylpiperidine-N-oxyl
TGA	thermal gravimetric analysis
T_g	glass transition temperature
XRD	X-ray diffraction
XPS	X-ray photoelectron spectroscopy

Mathematical Constants and Symbols

I	ionic strength
k	Boltzmann's constant
N_A	Avogadro's number
r	particle separation
R	gas constant
R_δ	effective radius of dispersion
T	temperature
V_T	total interaction potential
V_{vdW}	van der Waals interaction potential

V_E	electrostatic double-layer interaction potential
V_H	heat of vaporization
W_a	work of adhesion
W_c	work of cohesion
γ	surface energy (or tension)
ΔG_{mix}	Gibbs free energy of mixing
ΔH_{mix}	enthalpy of mixing
ΔS_{mix}	entropy of mixing
δ_D	Hansen solubility parameter dispersive component
δ_H	Hansen solubility parameter hydrogen bonding component
δ_P	Hansen solubility parameter polar component
δ_t	Hildebrand solubility parameter
ε_r	dielectric constant
ε_o	permittivity of free space
ν_o	solute molar volume
ρ	number of interacting molecules per unit volume
ϕ	solute volume fraction
χ	Flory-Huggins interaction parameter

Contributions

Fatona, A.; Chen, Y.; Reid, M. S.; Brook, M. A.; Moran-Mirabal, J. M., (2015) "One-step in-mould modification of PDMS surfaces and its application in the fabrication of self-driven microfluidic channels", *Lab on a Chip*, 15, 4322-4330. (Impact factor: 6.0)

Reid, M. S.; Villalobos, M.; Cranston, E. D., (2016) "Cellulose nanocrystal interactions probed by thin film swelling to predict dispersibility", *Nanoscale*, 8, 12247-12257. (Impact factor: 7.4)

Reid, M. S.; Villalobos, M.; Cranston, E. D., (2017) "Benchmarking cellulose nanocrystals: From the laboratory to industry", *Langmuir*, 33, 1583–1598 (Impact factor: 3.8)

Reid, M. S.; Villalobos, M.; Cranston, E. D., (2017) "The role of hydrogen bonding in non-ionic polymer adsorption to cellulose nanocrystals and silica colloids", *Current Opinion in Colloid and Interface Science*, 29, 76-82. (Impact factor: 6.1)

Reid, M. S.; Kedzior, S. A.; Villalobos, M.; Cranston, E. D., (2017) "Effect of ionic strength and surface charge density on the kinetics of cellulose nanocrystal thin film swelling", *Langmuir,* 33, 7403-7411. (Impact factor: 3.8)

Reid, M. S.; Marway, H. S.; Moran-Hidalgo, C.; Villalobos, M.; Cranston, E. D., (2017) "Comparison of polyethylene glycol adsorption to nanocellulose versus fumed silica in water", *Cellulose,* DOI: 10.1007/s10570-017-1482-8. (Impact factor: 3.4)

Reid, M. S.; Stimpson, T. C.; Niinivaara, E.; Villalobos, M.; Cranston, E. D. (2017) "Comparing soft semicrystalline polymer nanocomposites reinforced with cellulose nanocrystals and fumed silica" submitted to *Industrial & Engineering Chemistry Research*. (Impact factor: 2.8)

Agarwal, U.; Bortner, M.; Bras J.; Camarero, S.; Chan, K.; Clift, M.; Cranston, E. D.; Eichhorn, S.; Foster, E. J.; Fox, D.; Hamad, W.; Heux, L.; Jean, B.; Moon, R.; Nieh, W.; Reid, M. S.; Rennekar, S.; Shatkin, J.; Simonsen, J.; Wanasekara, N.; Youngblood J., (2017) "Characterization of cellulose nanomaterials" *Chemical Society Reviews*, manuscript in preparation. (Impact factor: 38.6)

Vanderfleet, O. M.; Reid M. S.; Cranston, E. D. (2017) "Controlling the colloidal and thermal stability of cellulose nanocrystals through mixed acid hydrolysis" manuscript in preparation.

Chapter 1

Introduction and Objectives

1.1 Introduction

Prompted by the desire for green, sustainable and affordable technologies, nanocellulose research has rapidly expanded over the last two decades.[1] Not only limited to academic interest, the number of patents citing cellulose nanocrystals (CNCs), cellulose micro/nanofibrils and bacterial cellulose has similarly increased.[2] Although current commercial use of nanocellulose is limited, potential applications range from foods and cosmetics to polymer nanocomposites and cements. Regardless of the application, maintaining well-dispersed, individualized particles (or fibrils) is critical, as aggregation significantly reduces surface area, increases the percolation threshold and often negates any nanoscale advantage. As a result, the development of nanocellulose-based products necessitates a thorough understanding of the surface forces that govern nanoparticle dispersibility.

CNCs were first reported in 1947 by Nickerson and Habrle,[3] however they have only been a material of interest since the 1990s, with the majority of work occurring in the last decade.[1] Traditionally, rod-shaped CNCs have been extracted from natural cellulose sources through acid hydrolysis at the bench scale using well established protocols.[4] However, with the growing interest in sustainable materials, a number of industrial CNC producers have now entered the marketplace.[5] Currently, CNCs are produced at various scales across North America using slightly different hydrolysis conditions and a variety of cellulose sources: *CelluForce* is the world's largest producer, operating at a 1 ton/day capacity, using traditional sulfuric acid hydrolysis of bleached Kraft wood pulp. *Alberta Innovates Technology Futures* (recently renamed *InnoTech Alberta*) operates a pilot scale facility that produces CNCs at a kg/day capacity using a variety of wood and cotton based sources. The *USDA Forest Products Lab*, currently produces CNCs from strip-cut dissolving pulp with an extended acid hydrolysis time and a capacity of tens of kilograms per day. When considering the variety of CNCs available it is important to recognize that the cellulose source, hydrolysis temperature and hydrolysis time can have a significant impact on CNC morphology (e.g., length, width, crystal structure, etc.) and surface chemistry (e.g., surface charge density, bound oligosaccharides, etc.).[6–10] It is therefore critical to have a thorough understanding of these aspects as variations can significantly impact interactions between CNC particles and other product constituents (e.g., polymers, surfactants, salts, etc.).

Because nanocellulose has a high density of surface hydroxyl groups and generally forms stable colloidal suspensions in water, aqueous based applications such as emulsions, gels and liquid formulations have been a key research area of interest. However, the high aspect ratio and impressive mechanical properties of CNCs (elastic modulus reported to be upwards of 150 GPa[11]) make them ideal reinforcing agents for polymer nanocomposites. Indeed, early examples of CNC reinforced polymer nanocomposites by Cavaillé and coworkers report mechanical property improvements of nearly three orders of magnitude.[12–15] To date, numerous groups have prepared CNC reinforced nanocomposites, yet poor compatibility with hydrophobic polymers remains a problem and often leads to highly aggregated material and only marginal improvement of mechanical properties.[11] Several surface modification routes for CNCs have been proposed to improve compatibility[16] but deeper understanding of the particle-particle and particle-polymer interactions is required to progress the field further.

While polymer nanocomposites have been used for more than a century, with early examples being clay-reinforced Bakelite and carbon black-toughened tires, current interest is often attributed to Toyota's introduction of nanoclay-polyamide composites as engine components in 1989.[17] Additionally, the development of advanced characterization techniques such as electron and surface probe microscopies, has allowed for deeper understanding of both particle-particle and particle-polymer interactions. Subsequently, the study of nanoparticles for use in advanced materials including aerogels, hydrogels, cements, emulsions, foams, membranes and polymer nanocomposites has surged with the availability of many organic and inorganic nanomaterials.[18]

Despite the interest, and the countless publications in the academic literature, nanocomposites, apart from elastomeric materials, have yet to make a significant impact within the commodity market. Indeed, to date only a handful of nanocomposite products are commercially available.[19] While the cost of some nanomaterials, such as carbon nanotubes and graphenes, make their use economically prohibitive, the more demanding challenge within the field is predicting and controlling nanoparticle dispersibility and behaviour.

Although it is generally accepted that the balance between particle-particle interactions ("cohesion") and particle-polymer interactions ("adhesion") governs dispersibility, predicting and measuring these interactions is a non-trivial task. Conventional approaches such as contact angle measurements and fibre pulling techniques are largely not applicable to nanomaterials due to the nanoscale dimensions. Additionally, while solubility parameters including the Hildebrand solubility parameter and the Hansen solubility parameters, have been used as a framework for understanding particle-polymer interactions, they cannot be strictly applied to suspensions and dispersions as entropic effects, such as solvent structuring around particles or specific chemical interactions, are not effectively incorporated into standard solution theory.[20] As a result, measuring particle-particle and particle-polymer interactions in novel ways, such as with new, sophisticated surface sensitive techniques, is required.

1.2 Thesis Objectives

As an emerging green nanomaterial, CNCs have potential use in a variety of aqueous and non-aqueous applications. However, to further develop these applications, a deeper understanding of the interactions between particles and polymers is required. Moreover, for CNCs to move beyond just an academic interest, industrially produced material will play an essential role. It is therefore critical to have a thorough understanding of the materials produced at both the bench and industrial scale and the potential impact on particle behaviour. The overall objective of this thesis is to investigate particle-particle and particle-polymer interactions in CNC systems and elucidate how these interactions govern dispersibility and composite properties. The specific goals of this work are as follows:

1. **Thoroughly characterize and benchmark CNCs** currently produced at the industrial scale in North America. This will provide a strong basis from which researchers can understand particle-particle and particle-polymer interactions and work with a "known starting material" which is crucial for reproducible research and product development.

2. **Develop new methods to probe and measure particle-particle interactions** within CNC aggregates in both aqueous and non-aqueous environments. Commercially available CNC materials are generally sold as spray dried or freeze dried powders and are highly aggregated - it is therefore essential to measure and understand the primary forces holding CNCs together so that they can be overcome to properly disperse CNCs.

3. **Explore particle-polymer interactions** between CNCs and non-ionic, water-soluble polymers and compare them directly to a well-understood system of silica particles. Furthermore, this work aims to explore the role of hydrogen bonding in CNC systems and how intermolecular forces change based on the surrounding media.

4. **Demonstrate good dispersion of CNCs in a polymer nanocomposite** based on the understanding developed in the objectives outlined above. Polymer nanocomposites reinforced with CNCs and fumed silica are prepared and particle dispersibility is linked to composite performance.

1.3 Thesis Outline

This thesis is composed of five peer-reviewed publications, and one manuscript to be submitted for publication, constituting five research chapters.

Chapter 1 *– Introduction and Objectives.* This chapter briefly introduces and discusses the motivation and research goals to provide a framework for this thesis. The specific thesis objectives and outline are presented.

Chapter 2 *– Background and Literature Review.* This chapter provides a thorough examination of the concepts and literature relevant to the field of cellulose nanocrystals and polymer nanocomposites. Current challenges related to CNC nanocomposite development and strategies to overcome these limitations are highlighted. In addition to a list of conventional characterization methods used in this thesis, two less common surface sensitive techniques, namely surface plasmon resonance spectroscopy (SPR) and quartz crystal microbalance with dissipation (QCM-D), are described.

Chapter 3 *– Benchmarking Cellulose Nanocrystals: From the Laboratory to Industrial Production.* This chapter extensively characterizes and evaluates CNCs extracted by sulfuric acid hydrolysis from the current North American industrial producers. Morphology, colloidal stability, thermal stability, and surface chemistry are examined with reference to traditional laboratory extracted CNCs. Moreover, particle properties are examined following additional purification steps. This work has been published in *Langmuir.*[5]

Chapter 4 *– Cellulose Nanocrystal Interactions Probed by Thin Film Swelling to Predict Dispersibility.* This work presents a new SPR-based platform to examine the forces that govern particle-particle interactions in the aggregated state. Film swelling is measured in a range of organic solvents. While the focus is specifically given to CNCs, this method is applicable to any nanoparticle that can be deposited as a thin film. For CNCs, it was observed that electrostatic double-layer forces do not play a significant role during the dispersion of CNCs and that van der Waals forces largely control aggregation. This work has been published in *Nanoscale*.[21]

Chapter 5 *– Effect of Ionic Strength and Surface Charge Density on the Kinetics of Cellulose Nanocrystal Thin Film Swelling.* Work within this chapter uses the SPR platform developed in Chapter 4 to investigate the kinetics of CNC thin film swelling. CNC surface charge density and ionic strength of the media were specifically controlled to investigate how electrostatic double-layer forces impact particle dispersion. Total swollen film thickness was observed to be independent of ionic strength, however, the rate of swelling scaled with osmotic pressure. This work has been published in *Langmuir*.[22]

Chapter 6 *– Non-Ionic Polymer Adsorption to Cellulose Nanocrystals and Silica Colloids.* This chapter examines particle-polymer interactions by investigating non-ionic polymer adsorption to CNCs (using QCM-D and other techniques) in direct comparison to fumed silica. Polyethylene glycol is used as a model linear polymer to investigate the role of hydrogen bonding during polymer adsorption. Despite the abundance of hydroxyl groups, and recent reports to the contrary, polyethylene glycol was found not to adsorb to CNC surfaces in aqueous environments, which agrees with previous papermaking know-how. The work within this chapter is comprised of two publications: (1) a research article published in *Cellulose* and (2) a review article published in *Current Opinions in Colloid & Interface Science.*[23]

Chapter 7 *– Comparing Soft Semicrystalline Polymer Nanocomposites Reinforced with Cellulose Nanocrystals and Fumed Silica.* This chapter investigates and compares polyethylene oxide polymer nanocomposites reinforced with CNCs and fumed silica. Particle dispersion, polymer crystallization, and polymer adsorption are examined as they relate to the mechanical properties of the composite. Void of water, polyethylene oxide is observed to adsorb to CNC surfaces resulting in good dispersibility and improved mechanical properties. Work within this chapter is currently being prepared for submission to *Industrial & Engineering Chemistry Research* as an invited publication.

Chapter 8 *– Concluding Remarks.* This chapter summarizes the major contributions of this thesis and presents future work towards developing a better understanding of CNC behaviour and potential CNC applications.

References

(1) Österberg, M.; Cranston, E. D. Special Issue on Nanocellulose- Editorial. *Nord. Pulp Pap. Res. J.* **2014**, *29* (1), 1–2.

(2) Charreau, H.; Foresti, M. L.; Vazquez, A. Nanocellulose Patents Trends: A Comprehensive Review on Patents on Cellulose Nanocrystals, Microfibrillated and Bacterial Cellulose. *Recent Pat. Nanotechnol.* **2013**, *7* (1), 56–80.

(3) Nickerson, R. F.; Habrle, J. A. Cellulose Intercrystalline Structure. *Ind. Eng. Chem.* **1947**, *39* (11), 1507–1512.

(4) Dong, X.; Revol, J.; Gray, D. G. Effect of Microcrystallite Preparation Conditions on the Formation of Colloid Crystals of Cellulose. *Cellulose* **1998**, *5* (1), 19–32.

(5) Reid, M. S.; Villalobos, M.; Cranston, E. D. Benchmarking Cellulose Nanocrystals: From the Laboratory to Industrial Production. *Langmuir* **2017**, *33* (7), 1583–1598.

(6) Bouchard, J.; Méthot, M.; Fraschini, C.; Beck, S. Effect of Oligosaccharide Deposition on the Surface of Cellulose Nanocrystals as a Function of Acid Hydrolysis Temperature. *Cellulose* **2016**.

(7) Beck-Candanedo, S.; Roman, M.; Gray, D. G. Effect of Reaction Conditions on the Properties and Behavior of Wood Cellulose Nanocrystal Suspensions. *Biomacromolecules* **2005**, *6* (2), 1048–1054.

(8) Chen, L.; Wang, Q.; Hirth, K.; Baez, C.; Agarwal, U. P.; Zhu, J. Y. Tailoring the Yield and Characteristics of Wood Cellulose Nanocrystals (CNC) Using Concentrated Acid Hydrolysis. *Cellulose* **2015**, *22* (3), 1753–1762.

(9) Wang, Q.; Zhao, X.; Zhu, J. Y. Kinetics of Strong Acid Hydrolysis of a Bleached Kraft Pulp for Producing Cellulose Nanocrystals (CNCs). *Ind. Eng. Chem. Res.* **2014**, *53* (27), 11007–11014.

(10) Dong, S.; Bortner, M. J.; Roman, M. Analysis of the Sulfuric Acid Hydrolysis of Wood Pulp for Cellulose Nanocrystal Production: A Central Composite Design Study. *Ind. Crops Prod.* **2016**, *93*, 76–87.

(11) Mariano, M.; El Kissi, N.; Dufresne, A. Cellulose Nanocrystals and Related Nanocomposites: Review of Some Properties and Challenges. *J. Polym. Sci. Part B Polym. Phys.* **2014**, *52*, 791–806.

(12) Helbert, W.; Cavaillé, J. Y.; Dufresne, A. Thermoplastic Nanocomposites Filled with Wheat Straw Cellulose Whiskers. Part I: Processing and Mechanical Behavior. *Polym. Compos.* **1996**, *17* (4), 604–611.

(13) Helbert, W.; Cavaille, J. Y.; Dufresne, A; Fourier, U. J. Straw Cellulose Whiskers . Part I : Processing and Mechanical Behavior. *Polym. Compos.* **1996**, *17* (4), 604–611.

(14) Favier, V.; Cavaille, J. Y.; Canova, G. R.; Shrivastava, S. C. Mechanical Percolation in Cellulose Whisker Nanocomposites. *Polym. Eng. Sci.* **1997**, *37* (10), 1732–1739.

(15) Favier, V.; Chanzy, H.; Cavaille, J. Y. Polymer Nanocomposites Reinforced by Cellulose Whiskers. *Macromolecules* **1995**, *28* (18), 6365–6367.

(16) Habibi, Y. Key Advances in the Chemical Modification of Nanocelluloses. *Chem. Soc. Rev.* **2014**, *43* (5), 1519–1542.

(17) Okada, A.; Usuki, A. Twenty Years of Polymer-Clay Nanocomposites. *Macromol. Mater. Eng.* **2006**, *291* (12), 1449–1476.

(18) Balazs, A. C.; Emrick, T.; Russell, T. P. Nanoparticle Polymer Composites: Where Two Small Worlds Meet. *Science* **2006**, *314* (5802), 1107–1110.

(19) Paul, D. R. R.; Robeson, L. M. M. Polymer Nanotechnology: Nanocomposites. *Polymer (Guildf).* **2008**, *49* (15), 3187–3204.

(20) Bergin, S. D.; Sun, Z.; Rickard, D.; Streich, P. V; Hamilton, J. P.; Coleman, J. N. Multicomponent Solubility Parameters for Single-Walled Carbon Nanotube-Solvent Mixtures. *ACS Nano* **2009**, *3* (8), 2340–2350.

(21) Reid, M. S.; Villalobos, M.; Cranston, E. D. Cellulose Nanocrystal Interactions Probed by Thin Film Swelling to Predict Dispersibility. *Nanoscale* **2016**, *8* (24), 12247–12257.

(22) Reid, M. S.; Kedzior, S. A.; Villalobos, M.; Cranston, E. D. Effect of Ionic Strength and Surface Charge Density on the Kinetics of Cellulose Nanocrystal Thin Film Swelling. *Langmuir* **2017**, acs.langmuir.7b01740.

(23) Reid, M. S.; Villalobos, M.; Cranston, E. D. The Role of Hydrogen Bonding in Non-Ionic Polymer Adsorption to Cellulose Nanocrystals and Silica Colloids. *Curr. Opin. Colloid Interface Sci.* **2017**, *29*, 76–82.

Chapter 2

Background and Literature Review

2.1 Cellulose

Cellulose is the world's most abundant organic polymer and can be considered as a nearly inexhaustible renewable resource. Contributing to nearly one-third of the total mass of plants the annual production of cellulose is estimated to be greater than 1.5×10^{12} tons.[1,2] While the vast majority of cellulose in the biosphere comes in the form of higher order plants such as trees, grasses, and cotton, cellulose is additionally produced by a variety of marine animals (e.g. tunicate), bacteria, fungi, and algae.[3] Regardless of the source or molecular weight, cellulose chains are composed of β-1,4-linked anhydro-ᴅ-glucopyranose units (AGU) in which each glucose residue is rotated 180° with respect to its neighbour, yielding an asymmetric dimer repeat unit termed cellobiose (Figure 2.1). In addition to the asymmetry of the repeating unit, cellulose chains possess directional asymmetry where terminal groups are chemically unique and are deemed as the reducing end, with a hemiacetal unit functionality, and the nonreducing end, having an additional hydroxyl group bound to the C4 carbon (Figure 2.1).

Unlike amylose, which is composed of α-1,4-linked AGU, the β-1,4-linked AGU of cellulose in the $^4C1$ chair conformation, maintain hydroxyl groups in the equatorial plain, which allow for intramolecular hydrogen bonding. Specifically, hydrogen bonds from the O(3′)-H hydroxyl to the O(5) ring oxygen across the glycosidic linkage and from the O(2)-H hydroxyl to the O(6′) hydroxyl of the next residue maintain an extended, and rigid chain conformation allowing cellulose chains to organize into hierarchical fibre-like structures. In addition, the axial position of the hydrogen atoms along the polymer backbone result in predominately hydrophobic regions and give rise to hydrophobic interactions and the amphiphilic nature of cellulose.[4] The high density of intramolecular hydrogen bonds, along with hydrophobic interactions make cellulose a (relatively) stiff polymer chain with low conformational entropy. These factors, along with both intramolecular and intermolecular van der Waals forces, make cellulose insoluble in water and most other conventional solvents.[5]

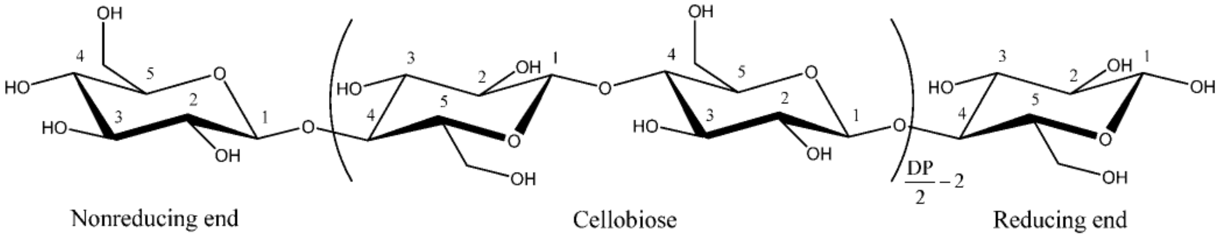

Figure 2.1. The chemical structure of cellulose highlighting the cellobiose repeat unit and directional asymmetry with the reducing and nonreducing terminal groups. For clarity, hydrogen atoms, which occupy axial positions, are not displayed. Figure reproduced from [3].

The biosynthesis of cellulose occurs within terminal enzyme complexes (TC) composed of individual globular complexes located across the plasma membrane of the cell. Currently the exact structure of the globular complexes is unclear however, each contain several catalytic sites that extrude individual cellulose chains.[1] The arrangement of the globular complexes in the plasma membrane varies between organisms but generally organizes to produce either linear or rosette-like TC, giving rise to the ribbon-like or cable-like cellulose microfibrils, respectively. For plants, it is generally accepted that 36 individual cellulose chains (six per globular complex) are polymerized in a rosette-like TC and rapidly assemble into highly ordered elementary fibrils via hydrogen bonding and van der Waals forces. Subsequent organization aggregates elementary fibrils into larger microfibrils with cross section dimensions ranging from 5 to 50 nm depending on the organism.[6] In turn, microfibrils form the basis for cellulose fibres, which act as the major structural component within higher order plants.

Cellulose chains have been reported to have a degree of polymerization from 500 to 15 000, depending on the source, and can extend to several microns in length.[1] Along the length of elementary fibrils, highly ordered, or crystalline regions, are interrupted by defects, or amorphous cellulose, due to chain dislocations resulting from internal strain from the twisting and tilted structure of the elementary fibril.[3] While the degree of crystallinity and measurement methodology is a hotly debated topic,[7] cellulose exists in numerous polymorphs (I, II, III, IV) which can be identified by unique intramolecular and intermolecular hydrogen bonds.[8] Cellulose I, often referred to, as “native” or “natural” cellulose, consists of parallel cellulose chains and is produced by plants, tunicate, algae, and bacteria. Considered to be metastable, cellulose I can be converted to the more thermodynamically favourable cellulose II by either regeneration (solubilization and recrystallization) or mercerization (aqueous sodium hydroxide treatments). Cellulose II, composed of antiparallel ordered chains, has numerous industrial applications and is used to make products such as cellophane and Rayon, amongst others. While cellulose II production is of great industrial and technical relevance, the cellulose I crystal structure has been reported to have the highest elastic modulus and is the focus of this work.[9]

To date, two distinct polymorphs of cellulose I have been discovered to coexist in various proportions depending on cellulose source: Iα with a triclinic structure is the dominant polymorph produced by algae and bacteria, and Iβ consisting of a monoclinic structure is the predominant polymorph produced by higher order plants and tunicates (Figure 2.2). Cellulose chains in both Iα and Iβ crystal structures hydrogen bond along the equatorial plane, referred to as the "hydrogen bonding plane", and organize into sheets which subsequently assemble, or laminate, via van der Waals forces and hydrophobic interactions to form elementary fibrils (Figure 2.2). Synchrotron x-ray diffraction experiments have revealed the unit cell parameters for both crystal structures, however the most noticeable difference between the two polymorphs is the relative displacement of the cellulose sheets between neighbouring hydrogen bonding planes.[6] For Iα, subsequent hydrogen bonding planes are displaced by c/4 along the c-axis of the unit cell (Figure 2.2c) whereas, within Iβ, displacement of hydrogen bonding planes alternates between c/4 and –c/4 (Figure 2.2d). Although intramolecular hydrogen bonding along the cellulose chain is well established, there is less concusses surrounding the positions of intermolecular hydrogen bonds between cellulose I polymorphs. It has been proposed that rotational position of the hydroxmethyl group alters intermolecular hydrogen bonding and gives rise to the differences observed between Iα and Iβ structures.[8] Nonetheless, the intermolecular hydrogen bonding, van der Waals forces and hydrophobic interactions collectively provide strong intermolecular interactions that stabilize cellulose elementary fibrils yielding a rigid material with good mechanical properties.

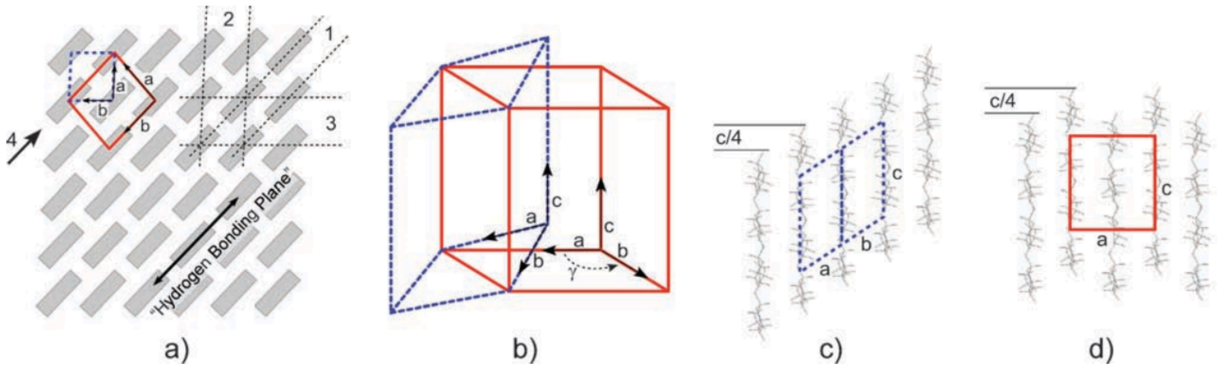

Figure 2.2. Schematic representation of the unit cells for cellulose Iα (triclinic, dashed line) and Iβ (monoclinic, solid line). (a) projection along the chain direction with the Iα and Iβ unit cells superimposed on the cellulose I crystal lattice, showing the parallelogram shape of both unit cells when looking down the c-axis. The corresponding lattice planes for 1, 2, and 3, are $(110)_t$, $(010)_t$, and $(100)_t$ for Iα and $(200)_m$, $(110)_m$, and $(1\bar{1}0)_m$ for Iβ. (b) relative configuration of Iα with respect to Iβ unit cell and the displacement of the hydrogen bonding sheets for (c) Iα of +c/4, and for (d) Iβ alternating +c/4 and -c/4. Figure reproduced from [6].

Cellulose in its native form of wood and plant fibres has been used for millennia, as an energy source, for clothing and as building materials. Today, the use of cellulose and cellulose derivatives has expanded to a countless number of applications including pharmaceuticals, cosmetics, foodstuffs, coatings, films and membranes, amongst others. Many of these applications make use of modified cellulose in the form of cellulose esters and ethers, via well-established carbohydrate chemistries that have been practiced for more than a century.[2] More recently, novel forms of cellulose particles and fibres, termed for example, crystallites, nanocrystals, whiskers, nanofibrils, and nanofibers, all collectively referred to as cellulose nanomaterials or nanocelluloses, have been investigated as emerging materials with many unique and attractive properties.

2.2 Cellulose Nanomaterials

Cellulose nanomaterials (CNM) refer to a family of cellulosic materials derived from nanostructures present within naturally occurring cellulose and possessing at least one nano scale dimension.[10] This includes both isolated nanoparticles or nanostructured materials. Much like macroscopic cellulose fibres, the renewability, biocompatibility, and mechanical properties of CNM make them an attractive material for numerous composite, biomedical, and rheological applications.[11] Similar to other nanomaterials (e.g., graphene, carbon nanotubes, nanoclays, and metal and inorganic nanoparticles), CNM have high surface-area-to-volume ratios and unique nano scale properties (e.g. self-assembly and alignment in external fields) that are not present in macroscopic materials.[3]

The production of CNM, while varying by cellulose source and application, can be classified as either top-down or bottom-up approaches. Top-down production of CNM includes extraction processes whereby mechanical, chemical or enzymatic methods (and often a combination thereof) are used to isolate CNM from macroscopic cellulose sources (e.g. woods, plants and grasses). In contrast, the bottom-up production of CNM, refers to the excretion and growth of nano scale cellulose from bacteria. Although each particle type is distinct, having a characteristic size, ratio, morphology, and degree of crystallinity, CNM can be classified broadly into distinct subcategories of microfibrillated cellulose (MFC), cellulose nanofibrils (CNF), bacterial cellulose (BC) and cellulose nanocrystals (CNCs). Notably, MFC and CNF are often classified together, however here the distinction is made between the nanostructured material of MFC and the completely isolated nanoparticles of CNF. Moreover, the nomenclature surrounding CNM has yet to be fully standardized (CSA Z5100-14 and ISO/WD TS 21400 propose naming and test methods for CNM characterization and further Standards are in progress through CSA, ISO Technical Committee 6 and 229 as well as TAPPI). Naming conventions have evolved over the past three decades making distinction between materials somewhat difficult. Common names for MFC, CNF, CNCs and BC along with electron microscopy images showing typical particle dimensions are presented in Table 2.1 and Figure 2.3, respectively.

Table 2.1. Classification of cellulose nanomaterials with common names, sources, dimensions and production methods. Table values adapted from [12] and [6].

Type of cellulose nanomaterial	Other names	Sources	Length (μm)	Width (nm)	Production method
Microfibrillated cellulose (MFC)	microfibrils, nanofibrillated cellulose (NFC)	wood, sugar beet, potato tuber, hemp, flax	0.5 – 10's	10 – 100	Mechanical refining of highly purified wood and plant fibres with or without chemical or enzymatic pretreatment
Cellulose nanofibrils (CNF)	nanofibrillated cellulose (NFC), cellulose nanofibers	wood, sugar beet, potato tuber, hemp, flax	0.5 – 2	4 – 20	High pressure homogenization and fractionation of purified wood and plant fibres with or without pretreatmet
Cellulose nanocrystals (CNC)	nanocrystalline cellulose, cellulose whiskers, cellulose nanowhiskers, cellulose nano rods	wood, cotton, hemp, flax, wheat straw, ramie, Avicel, tunicite, algae and bacteria	0.05–0.5	5 – 20	Acid hydrolysis of wood and plant fibres or refined cellulose including microcrystalline cellulose, MFC or BC
Bacterial cellulose (BC)	bacterial nanocellulose, microbialcellulose, biocellulose	Low molecular weight sugars and alcohols	>1	30 – 50	Bacterial growth

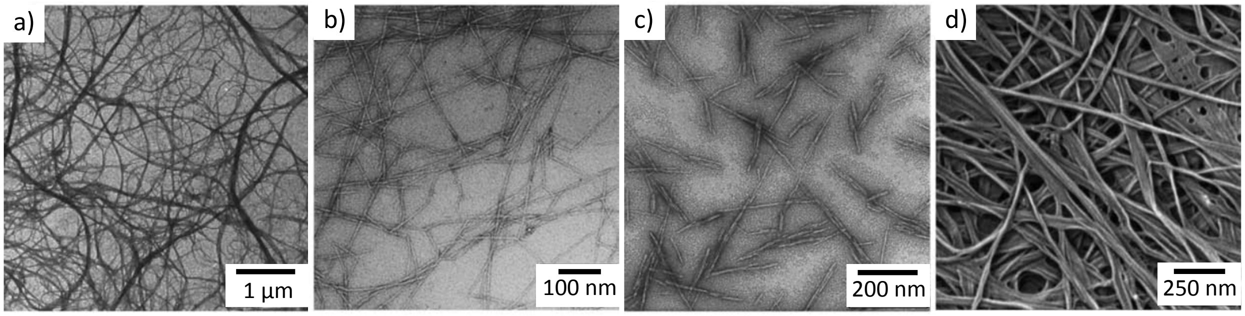

Figure 2.3. Transmission electron microscopy images of a) MFC, b) CNF and c) CNCs. d) Scanning electron microscopy image of BC fibres. Figure adapted from [6].

2.2.1 Microfibrillated Cellulose and Cellulose Nanofibrils

The production of MFC and CNF is typically comprised of multiple operations designed to produce specific grades and fibre dimensions, as well as to reduce energy consumption. Depending on the duration and ordering of each process, more than 50 types of MFC and CNF can be obtained from a single cellulose source.[13,14] Much like papermaking, prior to production, cellulose sources are purified via cooking and bleaching methods to remove unwanted hemicelluloses and lignin. Subsequent processes, while varying greatly within the literature, can be generally classified as:

1) *Mechanical pretreatment,* where blending, grinding and refining begin cellulose fibre delamination.

2) *Biological/chemical pretreatment,* implemented to promote fibrillation and reduce energy consumption.[15] These processes include enzymatic hydrolysis, which cleaves cellulose amorphous regions, or chemical treatments that introduce surface charge groups, promoting

fibrillation via electrostatic repulsion. Of particular note is the carboxylation of cellulose fibres via 2,2,6,6-tetramethylpiperidine-N-oxyl (TEMPO) mediated oxidation, which selectively oxidizes the primary alcohol of cellulose to a carboxyl group.[16] Since its introduction in 1993 by David and Flitsch[17] TEMPO mediated oxidation has become one of the most well studied and common routes to introduce surface charge to MFC and CNF.

3) *Principle mechanical treatment*, conventionally conducted by grinding and homogenization, mechanically disintegrates cellulose fibres into MFC and CNF under high pressure. Historically, mechanical treatment has been a significant barrier to commercialization due to high energy consumption (>70 MW h/t), however, due to pretreatment methodologies, disintegration requires significantly less energy (~2 MW h/t).[14] Commonly, mechanical treatments are conducted using a homogenizer or microfluidizer, although other less conventional methods have been reported.[14]

4) *Post-treatment*, including further chemical modification to add functionality and improve compatibility with polymeric matrices, and fractionation to isolate material with specific dimensions. Although the dimensions and surface chemistry of MFC and CNF are greatly dependent on cellulose source and processing conditions, MFC consists of elementary fibrils bundles, with lengths of 0.5 – 10's µm and widths of 10 – 100 nm. Whereas, CNFs with lengths of 0.5 – 2 µm and widths of 4 – 20 nm, are considered to be isolated elementary fibrils.

The high aspect ratio of MFC and CNF make them promising candidates for applications in papermaking, packaging, coatings, cosmetics, pharmaceuticals as well as in the oil and gas industry.[12,18] The micron length particles greatly reduce the threshold to percolation making them ideal reinforcing agents[19] and also yielding many interesting viscoelastic and rheological properties such as gelation and shear thinning.[20] Moreover, particle flexibility, resulting from the presence of both amorphous and crystalline regions leads to significant molecular entanglement allowing for the creation of robust physically entangled hydrogels[21] and aerogels.[22,23]

2.2.2 Bacterial Cellulose

Secreted by bacteria during fermentation, BC is noted for its superior chemical purity, high crystallinity, biocompatibility, and ultrafine network architecture, in comparison to other cellulose sources. Whereas, plants produce cellulose as a support against osmotic pressure, it is believed that bacteria secrete cellulose at the air water interface as a pathway to access oxygen and for protection from UV radiation and harsh chemical environments.[24] BC is produced by bacteria belonging to the genera *Gluconacetobacter, Agrobacterium, Alcaligenes, Azotobacter, Rhizobium,* and *Escherichia,* amongst others. The BC nanofibrils are high aspect ratio materials (>1 µm in length) exhibiting ribbon-like cross sectional morphology (6–10 nm by 30–50 nm) whose specific dimensions depend on bacteria type and culturing conditions.[6] Unlike plant based CNM, the bottom-up approach of BC allows for cellulose growth into specific macroscopic architectures including fleeces, films, spheres, and tubes.[24] Due to its high purity and the well-established infrastructure within the biomedical industry, BC has been extensively investigated for wound healing, tissue scaffold and implant applications.[25] Notably, BC based topical wound dressings are currently commercially available under the trade names XCell, Bioprocess, and Biofill.

2.2.3 Cellulose Nanocrystals

CNM produced by acid hydrolysis are typically referred to as cellulose nanocrystals (CNC). Other methods, such as oxidation and enzymatic treatments have been demonstrated in literature, however acid hydrolysis is by far the most thoroughly investigated.[26] Unlike the MFC and CNF, which contain both amorphous and crystalline regions (leading to particle flexibility), CNCs are composed solely of highly ordered cellulose and exhibit rigid rod-like morphologies.[6] First reported, following the acid hydrolysis of cotton, in 1947 by Nickerson and Habrle[27] and later imaged in 1950 by Rånby and Ribi,[28] CNCs have since been extracted from a number of sources including grasses, woods, algae, agricultural waste, BC, and tunicate.[3] The dimensions of CNCs greatly depend on cellulose source and extraction methodology but typically CNCs extracted from cotton, wood and other higher order plants are 50 – 500 nm in length and 3 – 20 nm in cross section. In contrast, CNCs produced from BC and tunicate, referred to as b-CNC and t-CNC respectively, can be several microns in length with cross sectional dimensions ranging from 6 – 50 nm.[6]

Exposing purified cellulose to strong acids, favourably hydrolyzes the more accessible disordered regions of the elementary fibril, leaving highly ordered cellulose in the form of rod-shaped particles. Although CNCs have been extracted using a variety of mineral acids, including phosphoric and hydrochloric acid,[29,30] as well as organic acids such as maleic and oxalic acid,[31] CNCs obtained via sulfuric acid hydrolysis have been the primary focus of both academia and industry.[32] Pioneered by Dr. Gray's group at McGill University, CNCs are extracted at the bench scale by digesting cellulose in strong sulfuric acid (~64 wt %) at 45°C for 45 min.[33] This process efficiently removes disordered and defect cellulose regions and grafts anionic sulfate half ester groups (OSO_3^-) to the particle surface (200 – 350 mmol/kg)[32] that serve to electrostatically stabilize CNCs in aqueous environments (Figure 2.4).[33]

Critical to CNC commercialization, a significant amount of research has focused on optimizing the sulfuric acid hydrolysis extraction process. It has been found that changes to the hydrolysis temperature, reaction time and acid concentration greatly affect particle dimensions, surface charge density, and the overall yield making thorough characterization a critical aspect of CNC applications. Currently, CNCs are produced at various scales across North America using slightly different hydrolysis conditions and a variety of cellulose sources: *CelluForce*, is the world's largest producer, operating at a 1 ton/day capacity, using traditional 64 wt % sulfuric acid hydrolysis of bleached Kraft pulp. *Alberta Innovates Technology Futures* (recently renamed *InnoTech Alberta*) operates a pilot scale facility that produces CNCs at a kg/day capacity using a variety of wood and cotton based sources. The *USDA Forest Products Lab*, currently produces

CNCs from strip-cut dissolving pulp with an extended 60 min hydrolysis time with a capacity of tens of kg/day.

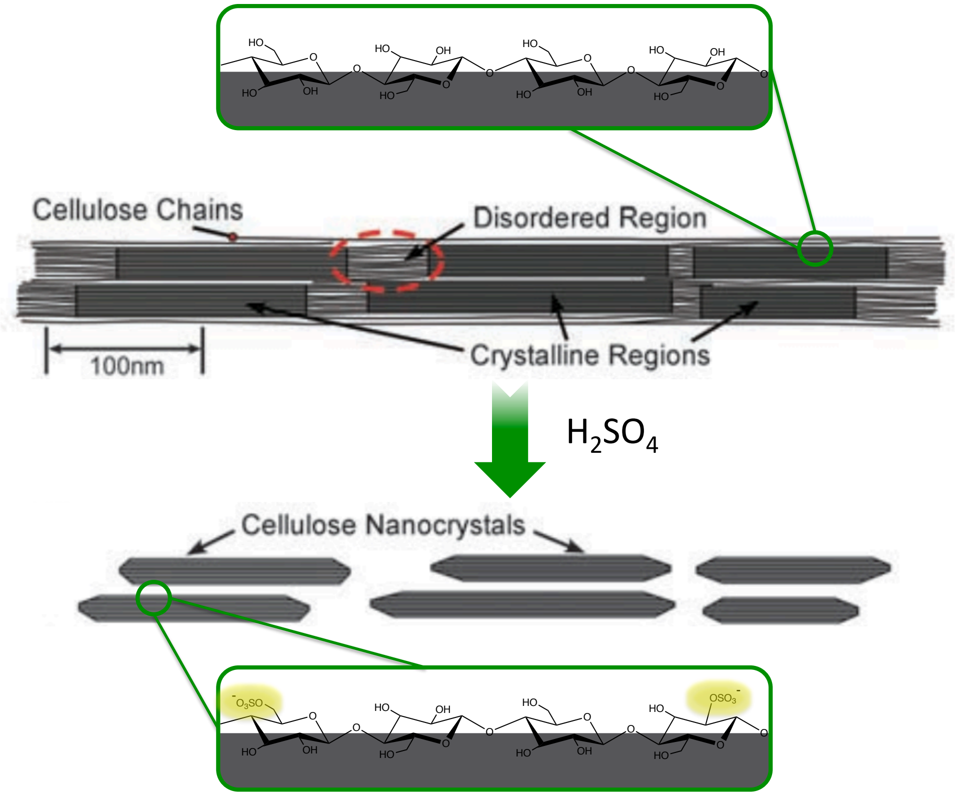

Figure 2.4. Schematic representation of sulfuric acid hydrolysis of cellulose fibres into CNCs with grafted surface sulfate half esters. Figure adapted from [6].

Much of the early literature surrounding CNCs investigated the fascinating liquid crystal behaviour of the material.[34–37] Similar to other colloidally stable high aspect ratio rod-shaped particles (e.g. tobacco mosaic viruses, DNA fragments, polymer whiskers, etc.) CNCs spontaneously self-assemble, above a critical concentration, to form nematic structures, whereby particles separate into isotropic and anisotropic phases to maximize translational entropy (Figure 2.5). In addition, CNCs exhibit chiral nematic ordering, or cholesteric liquid crystalline behaviour in which each pseudo layer in the liquid is rotated with respect to the adjacent layer (Figure 2.5).[38] This behaviour is proposed to be resultant from the inherent chirality of the asymmetric cellulose polymer, and in turn the twisted/screw-like morphology of CNCs.[38,39] The formation of anisotropic phases occurs as liquid crystalline droplets, referred to as 'tactoids', spontaneously nucleate from suspension and settle due to higher particle density in comparison to isotropic phases (Figure 1.5a). These structures can be preserved within polymerized matrices[40,41] or upon drying as thin films[42] and are similar to the structural colour observed in many insect shells, making CNCs excellent candidates for cosmetic, sensors and security applications.

In addition to self-assembly and optical properties, CNCs are being targeted for a number of other applications including, as emulsion stabilizers,[43–48] rheological modifiers,[49–51] membranes and, barriers[52] and tissue scaffolds,[53] to name a few. Of particular interest within academia and industry is the use of CNCs as reinforcing agents, due to their high aspect ratio, high specific modulus and low density.[6] Reinforcement applications include polymeric hydrogels,[54,55] adhesives,[56] coatings,[52] electrolytic supports,[57] cements[58] and as reinforced rigid polymer nanocomposites.[19,59]

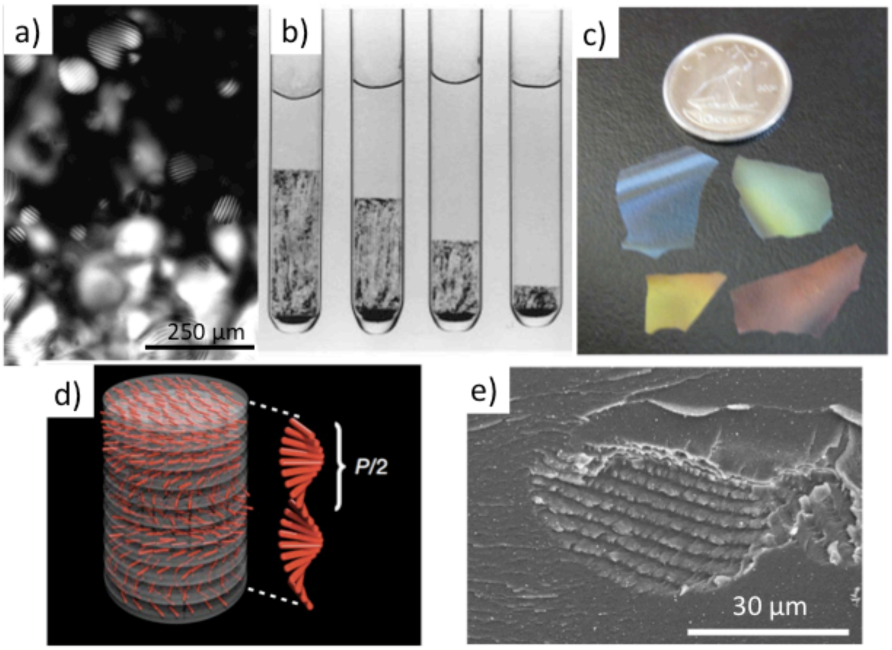

Figure 2.5. Aggregated illustration of the various self-assemblies of CNCs. a) Nucleation of anisotropic phases of CNCs in 7 wt % suspension showing the characteristic fingerprint texture by polarized optical microscopy. b) Phase separation of suspensions containing 8.78, 7.75, 6.85, and 5.78 wt % of CNCs viewed between crossed-polarizers, adapted from [34]. c) Free standing CNC templated silica films following pyrolysis, displaying controllable optical properties, adapted from [40]. d) Schematic representation of the chiral nematic liquid crystal formation of CNCs, adapted from [40]. e) Scanning electron microscopy image of a CNC tactoid embedded in polyacrylamide matrix, adapted from [60].

2.3 Nanocomposite Materials

In a broad sense, the term *nanocomposite* refers to any hybrid material containing a component with at least one dimension less than 100 nm. In this work we take “nanocomposites” to include multicomponent aerogels, hydrogels, cements, emulsions, foams, liquid formulations, and polymer nanocomposites. The term *polymer nanocomposite* however, is typically used when speaking of rigid or solid matrix materials (including thermoplastics, thermosets, elastomers and latexes) that have been reinforced or enhanced (e.g. improved electronic or thermal properties) by the inclusion of nanoscale or nanostructured materials. These have a number of applications including coatings, thin films, membranes and barriers, as well as bulk materials such as tires, consumer products (sporting equipment, tools, etc.), or automotive and aeronautical components, some of which are commercially available (Table 2.2).[61,62] While the work herein aims to understand CNC particle-particle and particle-polymer interactions in a variety of environments, the understanding and challenges encountered previously within the field of polymer nanocomposites can be generally applied to all nanocomposite systems.

2.3.1 Polymer Nanocomposites and the Structure-Property Relationship

For nearly a century, polymeric systems have been reinforced with organic and inorganic nanomaterials. Clay-reinforced Bakelite and carbon black-toughened tires are perhaps the most notable examples of successful early polymer nanocomposites. The current interest within the field is often attributed to the introduction of nanoclay-polyamide composites by Toyota in 1989, as well as the development of advanced characterization techniques with nanoscale resolution.[63,64] Subsequently, the study of polymer nanocomposites has surged with the availability of many organic and inorganic nanomaterials, with attractive optical, electronic, thermal and mechanical properties.[12,61,65–70] Despite the interest, reinforced polymeric nanocomposites, apart from elastomeric materials, have yet to make a significant impact within the commodity market due to high cost, poor control of particle dispersibility and poor mechanical properties.[71] Some commercial "success stories", which arose due to extensive industrial and academic research, are highlighted in Table 2.2. It can be expected that as demand for high performance materials increases and more efficient production methods are introduced, the cost of nanomaterials will decrease, making nanocomposites more economical. Addressing particle dispersibility and mechanical properties, or the so-called "structure-property relationship" is more challenging. Yet regardless of the material or matrix, understanding the balance between particle-particle and particle-polymer interactions, is critical to improving properties of the polymeric systems.[72]

Table 2.2. Examples of some currently commercially available polymer nanocomposites. Table reproduced from [61].

Polymer Matrix	Nanoparticle	Property improvement	Application	Company and/or product trade name
Polyamide 6	Exfoliated clay	Stiffness	Timing belt cover: automotive	Toyota/Ube
TPO (thermoplastic polyolefin)	Exfoliated clay	Stiffness/strength	Exterior step assist	General Motors
Epoxy	Carbon nanotubes	Strength/stiffness	Tennis racket	Babolat
Epoxy	Carbon nanotubes	Strength/stiffness	Hockey sticks	Montreal: Nitro Hybtonite®
Polyisobutylene	Exfoliated clay	Permeability barrier	Tennis balls, tires, soccer balls	InMat LLC
SBR, natural rubber, polybutadiene	Carbon black (20-100 nm: primary particles)	Strength, wear and abrasion	Tires	Various
Various	MWCNT	Electrical conductivity	Electrostatic dissipation	Hyperion
Unknown	Silver	Antimicrobial	Wound care/bandage	Curad®
Nylon MXD6, PP	Exfoliated clay	Barrier	Beverage containers, film	Imperm™: Nanocor
SBR rubber	Not disclosed	Improved tire performance in winter	Winter tires	Pirelli
Natural Rubber	Silver	Antimicrobial	Latex gloves	
Various	Silica	Viscosity control, thixotropic agent	Various	
Polyamides nylon6, 66, 12	Exfoliated clay	Barrier	Auto fuel systems	Ube

Despite a tremendous volume of work within the area, the field of polymer nanocomposites remains relatively young with the majority of work occurring in the last 15-25 years.[73] The complexity and variety of systems being studied, in addition to numerous compounding and processing methodologies, makes it difficult to establish trends or "design rules" from the literature. Moreover, working with nanoscale materials is inherently more challenging than traditional macroscopic reinforcing agents. For example, a typical strategy to improve interfacial adhesion is to chemically functionalize the filler. While this has a limited impact on macroscopic materials such as glass fibres, chemically modifying carbon nanotubes or graphenes introduces defects, altering mechanical (and electronic) properties and dispersion behaviour. As a result, it can be difficult to isolate the effect of functionalization making it challenging to predict and control the macroscopic properties of nanocomposites.

The impact of nanoscale dimensions is further revealed when considering the relative size of the nanomaterial fillers and the polymer chains that make up the matrix. For micron sized particles with diameters of ~10 μm, the dimension of individual polymer chains is insignificant and the interfacial area of the bound polymer is relatively small in comparison to the bulk of the particle.[73] For many cases, polymer adsorption to microparticles can be approximated as adsorption to an infinitely flat surface. In contrast, nanoparticles have dimensions that are similar to, or smaller than the radius of gyration of individual polymer chains. As a result, the interfacial area of the bound polymer (i.e., the interphase) cannot be ignored, as it occupies nearly the same volume as the particle itself. Moreover, the geometry of nanoparticles can potentially introduce entropic barriers, as polymer chains must conform to the particle surface.[61,74]

While a distinction between bound and bulk polymer is made in rigid polymer composites, the relative sizes of, and conformation of, polymer chains and nanomaterials in liquid formations and emulsions is similarly important. Polymer conformation at the particle surface can have a significant impact on colloidal, rheological, and interfacial behaviour.[75,76] For example, grafted polymers in a "brush-like" conformation can serve to sterically stabilize particles in both aqueous and non-aqueous environments.[77,78] In contrast, tightly bound polymers with low surface coverage can limit colloidal stability and in fact induce flocculation.[79] As a result, it is essential to have a clear understanding of polymer behaviour at particle surfaces regardless of the application.

Understanding the physical origin of composite properties, be it as a hydrogel, aerogel, polymer composite or liquid formulation requires detailed knowledge that encompasses length and time scales spanning several orders of magnitude. The nanoscale interactions between polymer chains and the particle surface are ultimately dependent on the surface chemistry of the particle. These interactions, although occurring at the nanoscale and over a period of pico or nano seconds determine the long-term macroscopic (i.e. millimetres, centimetres or metres) properties that occur on timescales of seconds, weeks or years.[73] Bridging the gap between nanoscale interactions and macroscopic properties is not a trivial task. Moreover, formulation and compounding methods have a tremendous impact on the structure-property relationship as they introduce a variety of non-thermodynamically-controlled factors (i.e., shear) that are difficult to predict.

Investigating molecular structure, particle-polymer interactions, particle dispersion, self-assembly and compounding processes are areas of keen interest, however combining these ideas to form a cohesive understanding remains a major challenge within the community. Nonetheless, nanomaterials present clear advantages whereby structural and functional enhancements are often observed at volume fractions below 5 % which is significantly lower than conventional fillers (e.g. glass fibres, talc, and calcium carbonate), which require loadings of 20 – 40%.[64] The field of polymer nanocomposites and other nano enhanced systems has progressed significantly, with many notable works, leading to impressive thermal, electronic, mechanical and rheological enhancements, yet the field remains still in its infancy.[73]

2.3.2 Analytical Models for Reinforced Polymer Nanocomposites

Since the introduction of nanoclay-polyamide composites by Toyota, mechanically reinforcing polymer matrices with rigid nanomaterials has been a primary focus within the literature.[64] The potential to impart (relatively) soft polymers with improved mechanical properties at low filler loadings is an attractive route to create strong, lightweight materials. Indeed, early examples of CNC-reinforced thermoplastics exhibit storage and elastic modulus improvements of more than an order of magnitude at loadings of less than 5% by volume.[80–82] While a full review of all polymer composites produced to date with CNCs and CNFs is outside the scope of this literature review and is not a primary topic in this thesis, the subject is addressed further in *Chapter 7* and the models generally used to predict nanocellulose-polymer composite mechanical properties are discussed below.

Various analytical models have been proposed to describe the reinforcing effect of high aspect ratio cellulose nanomaterials. While the field of analytical modeling is expansive, it is relevant to discuss two of the common strategies. Generally, the analytical models employed can be classified as either mean field or percolation based approaches (Figure 2.6).[6] To date the majority of mean field models are based on the empirical Halpin-Tsai equations, in which composite properties can be effectively modeled as a series of laminated plains as described by the Halpin-Kardos model.[82,83] Using this approach, it is assumed that filler particles are non-interacting, linearly elastic and that bonding between matrix and filler is perfect (i.e. no particle slippage). Following a mean field approach there is no critical volume fraction where significant improvement is predicted.

In contrast, percolation based approaches such as the Ouali model[84] propose that the composite is composed of three phases: the matrix, percolating filler network, and non-percolating filler phase. Below a critical volume fraction, the Ouali model predicts limited or no improvement within the composite. Above a critical filler volume fraction, well-dispersed filler forms a percolating network (when no particle alignment is observed), yielding significant improvement in composite properties. Early work within the field of CNM polymer composites proposed that percolation models could describe composite behaviour.[80–82] However, re-evaluation of these early works suggest that mean field approximations are more effective at describing the mechanical properties of the composite.[6] In fact to date there has yet to be any convincing work to suggest that percolation based approaches can be applied to CNM reinforced composites.[6]

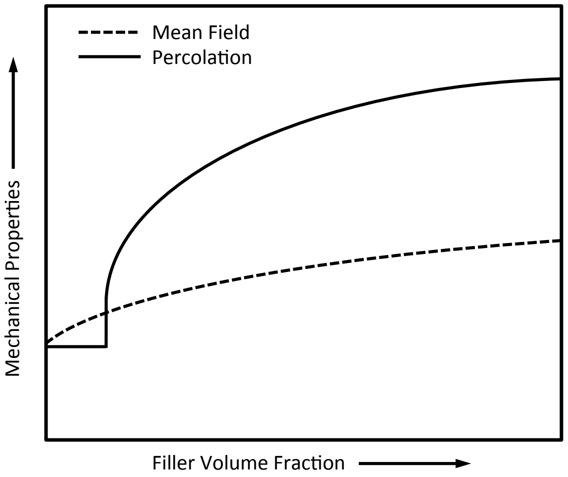

Figure 2.6. Schematic representation of the mechanical properties predicted by mean field and percolation based analytical models.

2.4 Particle Dispersion

For nearly all solid and liquid-based hybrid material/nanocomposite applications, maintaining well-dispersed, individualized nanoparticles is critical. Aggregation significantly reduces surface area, makes the particle size, shape and size-distribution unpredictable and often negates any nanoscale advantage that existed. For polymer composites specifically, aggregation increases the percolation threshold and/or invalidates the analytical models. The performance of materials containing nanoparticles cannot be fully projected or tailored unless dispersion is controlled. Dispersing particles, and maintaining dispersion, requires that attractive particle-particle interactions such as van der Waals forces, hydrogen bonding and polymer bridging be interrupted, and that particle spacing be preserved.

2.4.1 Colloidal Stability

In liquid media, particles constantly undergo Brownian motion, and thus particle collisions are frequent. To maintain colloidal stability (i.e. keep the nanoparticles fully dispersed and suspended) during collisions, repulsive forces between particles (electrostatic double layer and steric) must be sufficient to maintain particle spacing, and thus limit attractive van der Waals interactions. Colloidal stability can be described by the Derjaguin-Landau-Verwey-Overbeek (DLVO) theory whereby the total interaction potential (V_T) between particles (or molecules) is the summation of the van der Waals potential (V_{vdW}) and the electrostatic double-layer potential (V_E):

$$V_T(r) = V_{vdW}(r) + V_E(r) \tag{2. 1}$$

where r is the distance between particles. Van der Waals forces describe three distinct interactions: permanent dipole-permanent dipole (Keesom forces), permanent dipole-induced dipole (Debye force) and induced dipole-induced dipole (London or dispersion forces). Whereas, both Keesom and Debye forces act over (relatively) short distances, and in many cases are not present, dispersion forces are long-range interactions (greater than 10 nm) but weak, and are present between all materials due to the polarizability of electron clouds.[85] As a result, dispersion forces are the dominant force within van der Waals interactions and are often solely considered in colloidal suspensions.

Van der Waals forces are considered to be nonretarded and additive.[85] The van der Waals potential between two atoms can be described as a pair-wise interaction by:

$$V_{vdW}(r) = -C/r^6 \tag{2. 2}$$

where C is an energy constant. For a two-body problem (i.e. two particles, or a particle at a surface, etc.), the summation of all pair-wise interactions yields the total van der Waals interaction potential. While complex geometries make integration of all pair-wise interactions difficult, interaction potentials of relatively simple geometries, such as spheres, cylinders and planar surfaces have been solved and are given in terms of the Hamaker constant (A):

$$A = \pi^2 C \rho_1 \rho_2 \tag{2. 3}$$

where $\rho_1$and ρ_2 are the number of interacting molecules per unit volume. The Hamaker constant ranges from 10^{-19} to 10^{-21} J (in vacuum).[85] Although, in unique environments the Hamaker constant can be negative, giving rise to repulsive van der Waals forces and in some cases superlubricity,[86,87] in conventional systems (as discussed in this work), van der Waals forces are always attractive and the most significant driver of aggregation.

Opposing attractive van der Waals forces are repulsive electrostatic double-layer interactions; present due to the ion distribution surrounding colloidal particles. In suspension charged species are neutralized by an equal but oppositely charged region of solvated counterions, which remain near the particle surface to form what is termed the *diffuse electric double-layer*. The distribution of ions extending from the particle surface, and the resulting electrostatic potential, can be described by the Poisson-Boltzmann equation. The Poisson-Boltzmann equation is a nonlinear second-order differential equation of which the solutions can be difficult to evaluate and are beyond the scope of this work. Nonetheless as particles approach each other the concentration of ions within the gap increases (in comparison to bulk) resulting in an osmotic pressure that creates a repulsive force between the particles. The double layer thickness or the Debye length (κ^{-1}) where repulsive interactions are effective in the presence of monovalent ions is defined as:

$$\kappa^{-1} = \sqrt{\frac{\varepsilon_r \varepsilon_o kT}{2\, N_A e^2 I}} \qquad (2.\,4)$$

where ε_r is the dielectric constant of the medium, ε_o is the permittivity of free space, k is Boltzmann's constant, T is the temperature, N_A is Avagdro's number, e is the elementary charge and I is the ionic strength of the solution. While the Debye length is proportional to the ionic strength of the media, and can be calculated to extend several microns into the bulk for low ionic strength systems, from a practical standpoint, electrostatic double-layer repulsion is only effective to approximately 1 μm from the particle surface.

In addition to electrostatic double-layer forces, steric stabilization is commonly used to maintain colloidally stability.[88] Largely achived by grafting brush-like layers to the particle surface, steric stabilization is advantageous in that particles remain stable in high ionic strengths, high solid contents and in non-aqueous media where solvated ions are not present.[77] Stabilization has been proposed to arise by either enthalpic or entropic pathways (or both),[88] however it is generally accepted that changes in entropy are primarily responsible for stabilization, particularly in non-aqueous environments. During particle collision, compression of the grafted polymer layer causes an entropically unfavourable conformational change. As a result, for interacting particles under isothermal conditions, the Gibbs free energy becomes positive, leading to net repulsion between the particles.[88]

2.4.2 Dispersion in Polymer Nanocomposite Applications

A significant hurdle for polymer nanocomposites is achieving both good distribution and good dispersion (Figure 2.7). Distribution of particles within a matrix is highly dependent on the processing method and the application of sheer.[19] While processing methods constitute a significant portion of the literature in the field of polymer nanocomposites, investigation of these methods is beyond the scope of this work. Dispersion, however, can be controlled by adjusting interfacial interactions (i.e. particle-particle and particle-polymer interactions) and is of primary focus herein.

Whereas it is well understood that in liquid media electrostatic repulsion and/or steric stabilization maintain dispersion and colloidal stability, in environments such as polymer composites these repulsive interactions are largely not present. Moreover, unlike aqueous environments (and other polar solvents) where wetting can replace interparticle hydrogen bonds,[89] polymer wetting is often much less favourable, resulting in highly aggregated nanoparticles. As a result, achieving good particle dispersion in composite applications requires a thorough understanding of both particle-particle and particle-polymer interactions. Understanding, measuring, controlling and predicting these interactions is a non-trivial task and is a major focus within the literature and the work presented in the following sections.

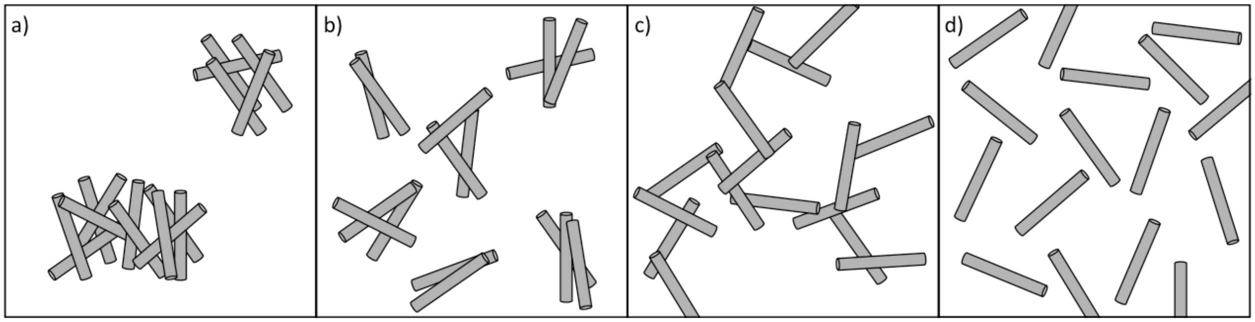

Figure 2.7. Schematic representation of various particle distributions and dispersions in composites. a) poor distribution, poor dispersion, b) good distribution, poor dispersion, c) poor distribution, good dispersion, d) good distribution, good dispersion.

2.5 Measuring and Predicting Particle Dispersibility

Limiting phase separation in multicomponent materials/systems is a ubiquitous challenge when preparing composite materials. Creaming, and oil leakage of emulsions, sedimentation of liquid formulations and aggregation of reinforcing agents are commonly observed in nanocomposite materials. In some cases, however controlled phase separation can been advantageous. For example, co-continuous immiscible polymer blends have been used to create double percolated networks, whereby carbon black or carbon nanotubes are “jammed” between the polymer phases to produce conductive composites with ultra low particle loadings.[90,91] To achieve this selective particle dispersion, particle-particle and particle-polymer interactions must be thoroughly understood and finely controlled. The challenge within double percolated networks, much like other polymer nanocomposites, is effectively measuring particle-polymer and particle-particle interactions such that particle dispersion can be predicted and controlled, as described further below.

2.5.1 Wettability and Surface Energy

For polymer nanocomposites, predicting good adhesion (or strong particle-polymer interactions) between the constituents is often achieved by evaluating the wetting of the reinforcing agent (or other functional material) by the polymer matrix. As such the contact angle, and subsequently the surface energy, via the Young equation, (Equation 2.5) between the phases is an important measure when predicting particle dispersion (Figure 2.8). While the surface energy of a liquid is simply taken as the surface tension, measuring the surface energy of a solid (as in the case of nanomaterials) is significantly more challenging as the surface energy cannot be measured directly, but only approximated from a series of liquid-solid contact angle measurements.[92] Nonetheless wetting of the solid surface (contact angle < 90˚) is indicative of favourable interactions between the liquid and solid phases, suggesting good adhesion within the composite material.

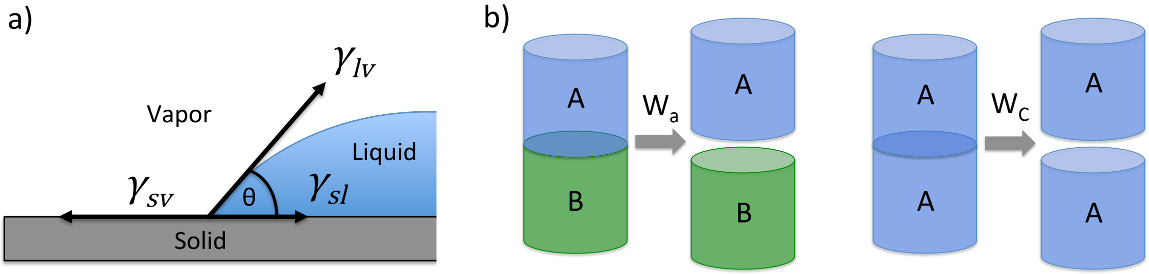

Figure 2.8. Schematic diagrams presenting a) the formulation of the Young's equation by measuring the contact angle and b) representations of the work of adhesion and the work of cohesion (where in the case of polymer nanocomposites, A represents the nanofiller and B the polymer matrix).

The Young equation describes the balance of interfacial forces at equilibrium between solid (s), liquid (l) and vapour (v) phases, while assuming the surface is homogenous and smooth (Figure 2.8a)[93]:

$$\gamma_{sv} = \gamma_{sl} + \gamma_{lv}\cos\theta \qquad (2.5)$$

where γ is the surface energy (or tension) of each interface and θ is the contact angle. The surface energy is a measure of the work required to increase the area of the surface (or interface). Applied to nanocomposites, the surface energy is more effectively used to describe the work of adhesion (W_a) (Figure 2.8b), defined as the work required to separate two dissimilar surfaces. For example a solid/liquid interface:

$$W_{sl} = \gamma_{lv} + \gamma_{sv} - \gamma_{sl} \tag{2. 6}$$

where W_{sl} is the work of adhesion between solid and liquid phases (i.e., $W_a = W_{sl}$). Similarly, the work of cohesion (W_C) (Figure 2.8b), or the work required to create a new surface between similar phases is defined as:

$$W_C = \gamma_A + \gamma_A - 0 = 2\gamma_A \tag{2. 7}$$

where γ_A is the surface energy of a single phase (liquid or solid phases). Combining Equations (2.5) and (2.6) yields the Young-Dupré equation which can be experimentally applied to calculate the work of adhesion between liquid and solid phases:[93]

$$W_{sl} = \gamma_{lv} + (1 + \cos\theta) \tag{2. 8}$$

Aggregating these concepts, we expect good nanocomposites to exhibit a low work of cohesion and a high work of adhesion.[94] In other words, good dispersion requires minimal attractive particle-particle interactions (low W_C) such that particles can be easily separated, and strong particle-polymer interactions (high W_a), creating a strong particle-polymer interface. While the Young-Dupré equation contains only two unknowns, it is deceptively simple. Specifically, from an experimental standpoint, measuring contact angle of nanomaterials is challenging.[95]

Traditional contact angle measurements require uniform, flat surfaces from which probe liquids are deposited (e.g. water, methylene iodide, molten polymer, etc.).[96] While macroscopic surfaces (e.g. polymers, glasses, metals, etc.) can be readily prepared, creating surfaces composed of nanomaterials can be challenging, resulting in only qualitative values. Often surfaces (or films) of nanomaterials, are porous, rough, and non-uniform, all of which impact the validity of Young's equation.[97] As such, more sophisticated techniques have been employed to investigate wettability of nanomaterials.[98–101] For example Nuriel *et al.* prepared both PP and PEG nanocomposites reinforced with CNT via solvent casting. Where the CNT protruded from the composite surface SEM imaging was used to measure the contact angle (Figure 2.9).[98] Using the Owens and Wendt equation[102] the polar and dispersive components of the surface energy of multiwall CNT were determined to be 26.9 mJ/m^2 and 18.4 mJ/m^2 respectively (γ = 45.3 mJ/m^2). Comparative values (γ = 27.8 mJ/m^2) were measured by Barber *et al.* via AFM, whereby a single carbon nanotube grown on the tip of a AFM cantilever was pressed into polymer melts and probe liquids (Figure 2.9).[99] Using a modified Wilhelmy model, wetting of the CNT by the polymer melt, applies a downward force to the cantilever from which the contact angle and surface energy was calculated. Experiments by both Nuriel *et al.* and Barber *et al.* compare reasonably well to surface energies measured for untreated graphite fibres (γ = 40.3 mJ/m^2) suggesting that in many cases model systems can be applied to evaluate surface energies of nanomaterials.[95]

Although wettability measurements provide insight into particle-polymer interactions, contact angle can only be considered as a qualitative/relative evaluation method as sample preparation and measurement technique can significantly impact results. For example contact angles between PEG and CNT have been reported to range from 25–73° leading to a large discrepancy in the calculated surface energy and work of adhesion.[95] Moreover, whereas contact angle is useful for predicting behaviour and dispersibility of rigid polymer nanocomposites, these measurements do not provide insight into phenomena such as adsorption of dissolved polymers, which is critical for emulsion and liquid formulation development.

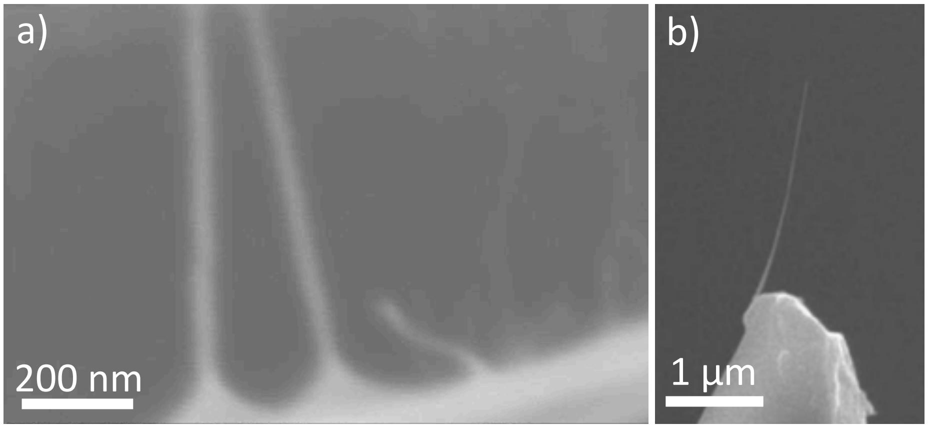

Figure 2.9. a) SEM image of CNT protruding from a PEG nanocomposite where the contact angle is measured. Image reproduced from[98] b) SEM image of a single carbon nanotube grown from at the tip of an AFM cantilever. Image reproduced from [99]

2.5.2 Predicting Dispersion via Solubility Parameters

Solubility parameters have long been used to better predict the miscibility of small molecules such as pigments and polymers.[103] First described by Hildebrand and Scott more than 50 years ago, the Hildebrand solubility parameter (δ_t), is defined as the square root of the cohesive energy density:

$$\delta_t = \left(\frac{\Delta H_V - RT}{V_H}\right)^{\frac{1}{2}} \tag{2. 9}$$

where ΔH_V is the heat of vaporization, V_H is the molar volume, R is the gas constant and T is the temperature.[104] Much like surface tension, the heat of vaporization of solvents is readily measured, yet the solubility of polymers and other small molecules must be qualitatively determined by a series of dissolution experiments, where miscible solvents and polymers have similar Hildebrand solubility parameters (i.e., minimization of the Flory-Huggins interaction parameter).[105] The Hildebrand solubility parameter is useful as a qualitative measure of polymer solubility, however it only provides insight into the total interaction between constituents. Distinguishing between dispersive, polar and hydrogen bonding components of the cohesive energy density builds a more detailed understanding of interactions. As a result, the Hansen solubility parameters have become a more effective measure of solubility.[103]

Whereas both the Hildebrand and Hansen solubility parameters were originally formulated to describe the solubility of small molecules and polymers, numerous works have adapted solubility parameters to predict the dispersibility of particles in a variety of aqueous and non-aqueous environments.[106–110] To understand dispersibility of nanoparticles we first consider small molecule dissolution. A solute is soluble when the free energy of mixing ($\mathit{\Delta} G_{mix}$) is negative.

$$\mathit{\Delta} G_{mix} = \mathit{\Delta} H_{mix} - T\mathit{\Delta} S_{mix} \tag{2. 10}$$

Where $\mathit{\Delta} H_{mix}$ and $\mathit{\Delta} S_{mix}$ are the enthalpy and entropy of mixing respectively. As result, a miscible solution is defined as having $\mathit{\Delta} H_{mix} < T\mathit{\Delta} S_{mix}$.[106] In general, $\mathit{\Delta} S_{mix}$ is a measure of the disorder associated with mixing and is always positive. For small molecules, including polymers, the entropy of mixing is large, allowing for a comparatively large enthalpy of mixing. However, for (relatively) large rigid structures, such as nanoparticles, the entropy of mixing is typically small.[106] As a result, in order to approach spontaneous dispersion of nanoparticles the enthalpy of mixing must be small (i.e., to minimize $\mathit{\Delta} G_{mix}$). The result is that enthalpic particle-solvent interactions become critically important to the dispersion of nanoparticles and that distinguishing between dispersive, polar and hydrogen bonding components is particularly useful. The impact of cohesive energy density, or more practically the Hildebrand solubility parameter, is described by the Flory-Huggins (Equation 2.11) and the Hildebrand-Scatchard (Equation 2.12) expressions for enthalpy.[106]

$$\mathit{\Delta} H_{mix} = \frac{\chi}{\nu_o}\phi(1-\phi)kT \tag{2. 11}$$

$$\mathit{\Delta} H_{mix} = \left(\delta_{t,A} - \delta_{t,B}\right)^2 \phi(1-\phi) \tag{2. 12}$$

where χ is the Flory-Huggins interaction parameter, ϕ is the solute volume fraction, ν_o is the solvent molecular volume and $\delta_{t,A}$ and $\delta_{t,B}$ are the Hildebrand solubility parameters for the solute and solvent respectively.[105] From Equation 8 it is clear that, to reduce the enthalpy of mixing, and thus improve particle dispersibility, the difference between the solute and solvent Hildebrand parameters must be minimized. Combining Equations 2.11 and 2.13 yields a concentration independent relation between the χ and the Hildebrand solubility parameters.

$$\chi = \frac{v_o}{kT}(\delta_{t,A} - \delta_{t,B})^2 \tag{2. 13}$$

Much like conventional polymer solubility, a Flory-Huggins parameter that approaches zero is indicative of good miscibility/dispersibility between the components, yet will always remain positive.[105] Applying this to nanocomposites, good dispersion is predicted when the particle and polymer matrix have similar solubility parameters. From this, Hildebrand solubility parameter can be readily expanded to include the dispersive (δ_D), polar (δ_P) and hydrogen bonding (δ_H) components of the Hansen solubility parameters.

$$\chi = \frac{v_o}{kT}\left((\delta_{D,A} - \delta_{D,B})^2 + (\delta_{P,A} - \delta_{P,B})^2 + (\delta_{H,A} - \delta_{H,B})^2\right) \tag{2. 14}$$

Working within the three-parameter space of the Hansen solubility parameters allows for a geometric approach from which good solvation/dispersion is predicted for polymers/particles as a distance away from the solute or as an effective radius of dispersion (R_δ). This is represented graphically in (Figure 2.10).

$$R_\delta = \sqrt{(\delta_{D,A} - \delta_{D,B})^2 + (\delta_{P,A} - \delta_{P,B})^2 + (\delta_{H,A} - \delta_{H,B})^2} \tag{2. 15}$$

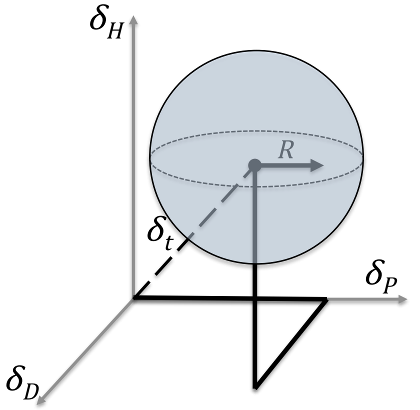

Figure 2.10. Schematic representation of the geometric approach describing the solubility/dispersibility space of the Hansen solubility parameters. At the centre of the sphere is the solubility parameters of the solute and miscible solvents are contained within the effective radius of dispersion.

Similar to polymers, the Hansen solubility parameters of nanoparticles are approximated, by a series of dispersibility experiments, whereby solution/dispersion quality is assessed by turbidity and sedimentation.[106] The Hansen solubility parameters have been approximated for several nanoparticles, including clays,[111] CNT,[106,109,110,112,113] and CNCs.[106,108] To date, the most extensive investigation has been reported by Bergin *et al.* who analysed the dispersibility of CNT in more than 60 solvents.[106] Of the solvents investigated, 14 were identified as good solvents, yielding Hansen solubility parameters of CNT to be $\delta_D \approx$ 18.0 MPa$^{1/2}$ $\delta_P \approx$ 7.8 MPa$^{1/2}$ $\delta_H \approx$ 6.8 MPa$^{1/2}$ in agreement with previous studies by Detriche et al.[109,110]

Similarly Gårdebjer *et al.* used a series of aqueous and non-aqueous solvents to asses the dispersibility of CNCs following surface modification.[107] Overall, dispersibility in δ_D dominated solvents (i.e., $\delta_D > \delta_P + \delta_H$) such as heptane and toluene was improved by grafting of long chain aliphatic carbon chains. The resulting solubility parameters for native and surface modified CNCs were approximated to be $\delta_t \approx$ 29.6 MPa$^{1/2}$ and $\delta_t \approx$ 23.2 MPa$^{1/2}$ respectively.

It is critical to recognize that nanoparticles are not small molecules, and that although Hansen solubility parameters can be assigned, and can serve as an entry point from which dispersibility can be investigated, notable limitations of the methodology exist. For example, when investigating CNT, Bergin *et al.* observed that several solvents within the effective radius of dispersion (Figure 1.8) were incompatible with CNT.[106] According to standard solution theory this should not be the case as solubility of small molecules (for a given entropy of mixing) should solely be determined by its relation to the Flory-Huggins parameter. Discrepancy from standard solution theory points to potential entropic effects, such as solvent structuring or caging around the particle, or specific interactions that are not effectively characterized by dispersive, polar or hydrogen bonding components.[106]

2.5.3 Modeling and Simulations to Predict Nanoparticle Compatibility/Dispersibility

Modeling and simulations are becoming increasingly practical methods to probe both particle-particle[114] and particle-polymers interactions.[115–119] With the continuous development of parallel computing and the rise of graphical processing units, simulations which were previously considered computationally too demanding have become routine.[120] Although simulations have significantly improved over the last two decades, multi-scale analysis, whereby nanoscale interactions can be used to predict bulk mechanical and rheological properties still remains technically difficult.[121] Moreover, selecting the appropriate force fields and initial conditions such that simulations accurately represent "real-life" conditions must be considered.[6] Nonetheless modeling can provide insight into nanoscale interactions and behaviours that are difficult to probe experimentally, such as polymer adsorption.[117–119] Additionally, simulations can be useful where conflicting results exist in literature and perhaps most importantly help guide experimentalists to new areas of interest.[121]

Although multi-scale analysis remains a significant challenge, and has only become practically achievable in the last decade, several works have employed a variety of methods to investigate nanocomposites[122–126] In a recent work, Alian *et al.* simulated bulk mechanical properties of epoxy composites reinforced with CNT.[122] Particle aggregation was investigated by simulating individual CNT and bundles containing three and seven tubes. Unsurprisingly, composites containing individual CNT exhibited the largest effective Young's modulus however, a 20% and 36% reduction was observed when bundles of three and seven CNT were simulated, respectively. This not only highlights the dramatic effect of particle aggregation, but also provides insight into behaviours that are experimentally challenging to investigate (i.e., it is not possible to control aggregation between three and seven particles).

Whereas experimentally it requires months or years to effectively alter and characterize the surface chemistry of particles, modeling can (relatively) rapidly interchange and investigate a variety of particle surfaces, including polymer grafting densities, chain lengths and functionalities.[120] Recently, Qin *et al.* simulated poly(methyl methacrylate) (PMMA) composites reinforced with native and TEMPO-modified CNCs using multi-scale analysis that combined atomistic molecular dynamics surface energy calculations with coarse-grained simulations to predict the composite glass transition temperature ($\mathrm{T_g}$).[115] Their work predicts that with greater modification (i.e., higher charge density) the T_g will increase due to better interfacial adhesion between the particle and the polymer matrix. Furthermore, reducing particle separation (presumably resultant from increased particle loading) increases the volume of bound polymer and similarly increases the T_g.[115]

While modeling and simulations can serve as a guide or confirmation for experimental results, and will become increasingly applicable in the future, it is critical to recognize that simulations often do not reflect experimental initial conditions. Notably, simulated models for cellulose typically do not incorporate, charged surface groups or bound oligosaccharides that are present following sulfuric acid hydrolysis and thus may not accurately represent interfacial behaviour of CNCs.[127] Additionally, as more advanced analytical systems are being developed it is important to note that the interfacial area within polymer nanocomposites significantly exceeds conventional composites systems and it is not clear whether current methods can accurately predict mechanical properties. Moreover, the large particle-polymer interface can ultimately change the properties of the bulk matrix leading to unaccounted enhancement. For modeling to be an effective tool a deeper understanding of particle-particle and particle-polymer interactions must be established.[6]

2.6 Surface Modification to Control Interactions and Nanocomposite Properties

To date, although it remains difficult to directly measure particle-particle and particle-polymer interactions, at the most general level it can be assumed that like dissolves/disperses like. For example hydrophilic particles, functionalized (physically or chemically) with hydrophobic groups exhibit improved dispersibility in hydrophobic solvents and matrices. The challenge then is to functionalize the particle surface while maintaining desirable properties (mechanical, electrical, optical, etc.). As a result, in an effort to control both particle-particle and particle-polymer interactions (and dispersion as a whole) a significant portion of the polymer nanocomposite literature is devoted to surface modification.[128–132]

Perhaps the most elegant example of controlled dispersion was reported by Kumar and coworkers, where silica particle assembly in a polystyrene (PS) matrix was shifted from spherical aggregates, to sheets, to strings, and finally individualized nanoparticles (Figure 2.11).[72,133,134] Within their pivotal work, silica dispersion was controlled by grafting PS chains to the particle surface.[72] By altering both the grafting density (from 6 to 74 chains per particle) and the graft chain length (17 to 158 kDa), particle-particle and particle-polymer interactions could be finely controlled. For example, increasing the chain length of grafted PS increased particle-polymer interactions improving dispersion. However, at low grafting density, attractive particle-particle interactions were sufficient to maintain a degree of aggregation thus yielding string-like morphologies. Increasing the grafting density drastically reduced particle-particle interactions resulting in individualized particles throughout the matrix. From the perspective of mechanical properties, it was also demonstrated that perfect dispersion was not always required but that favourable and tailorable mechanical properties could be obtained through the controlled aggregation of the nanofiller. The fine balance of grafting density and chain length within this work allows for a variety of morphologies to be obtained and highlights the importance of understanding both particle-particle and particle-polymer interactions.[72]

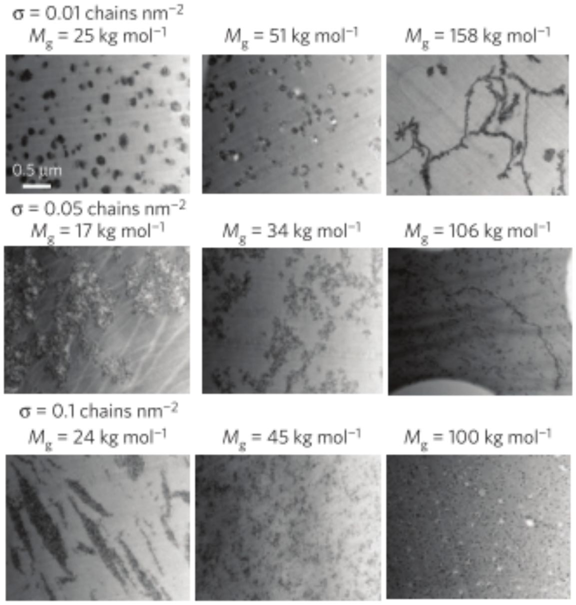

Figure 2.11. TEM images of PS grafted silica particles in a PS matrix showing spherical aggregates, sheets, strings and individualized particles. M_g is molecular weight of the grafted PS and σ is the grafting density. Image reprinted from [72].

Of the variety of nanoparticles described in the literature, surface modification of silica particles is perhaps the most widely investigated and well understood. Early patents for silica particles were filed in the 1940s and over the last 30 years production has reached ton per hour quantities making silica particles widely available for a number of applications including paints, coatings, drug delivery, catalyst supports or as reinforcing agents in composite materials and concrete/cement.[135,136] Shortly following the pioneering work by Stöber in the early 1950s, surface modified silica particles have been commercially available, greatly expanding the control of particle-particle and particle-polymer interactions.[137–139] Both physical and chemical pathways are used to modify silica, however, covalent modification via organochlorosilanes, organoalkoxysilanes or organosilazanes are primarily used.[135] Similar to silica, nanoclays and CNT are well established nanoparticles, yet do not have as ubiquitous surface modification pathways. As a result, intensive research has focused on improving dispersibility of these high aspect ratio particles.

2.6.1 Nanoclay Surface Modification

Regardless of the application, nanoclay composites centre around the ability to maximize interfacial area via intercalation and exfoliation of the silicate layers (Figure 2.12). Numerous works have investigated nanoclay processing and extruder screw configuration,[61,140–142] in an effort to achieve better exfoliation, however, regardless of the processing technique, complete exfoliation can only occur if there is good thermodynamic affinity between the polymer and the particle.

Intercalation of polymer chains into the confined space between clay silicate layers leads to a large entropic penalty for the polymer. It is therefore assumed that intercalation must be largely driven by energetic attraction between the polymer and the nanoclay.[61] As such the hydrophilic nature of the clay makes intercalation and exfoliation into hydrophobic/non-polar solvents/matrices challenging and clays typically remain as immiscible nanostructures. As a result, a significant amount of research has focused on the development and use of organic/hydrophobic treatments to improve affinity between polymer and nanoclays.[61,143]

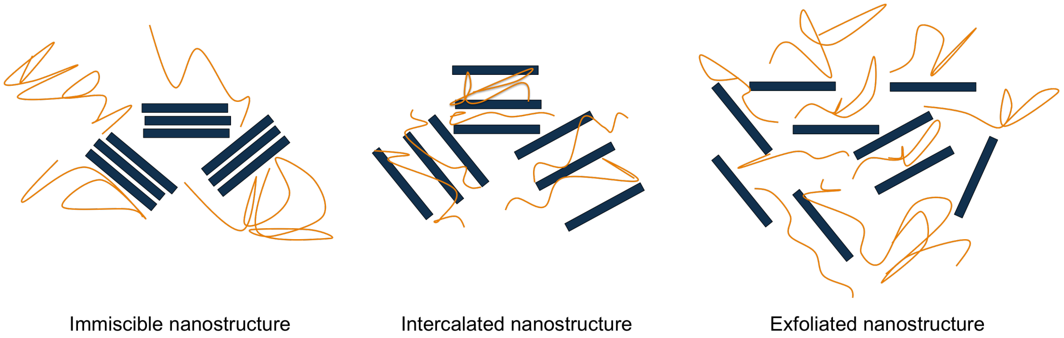

Figure 2.12. Schematic representation of immiscible, intercalated and fully exfoliated nanoclay structures. Figure reproduced from [143].

Several organic modifications for nanoclays have been proposed in literature including cation exchange, silane grafting and polymer adsorption.[144] Cation exchange is perhaps the most ubiquitous modification pathway and proceeds as metallic cations, located in the galleries between silicate layers, are exchanged with organic salts; making intercalation more efficient or to act as reactive sites during polymerization.[65,145] Ion exchange can occur using primary, secondary, tertiary, and quaternary alkylammonium or alkylphosphonium cations (surfactants) however, the effectiveness of the organic modification is dependent on molecular weight, packing density and functionality of the cation and typically must be tailored to a single polymer matrix.[65,145]. For example intercalation and mechanical performance of linear low density polyethylene was improved using clays modified with a two tailed alkylammonium salt.[146] Using the same surface modification in nylon 6 composites, yielded less intercalation and minimal mechanical improvement.[147] Upon replacing two tailed surfactant with a single tailed alkylammonium salt, nanoclays were completely exfoliated and mechanical properties were significantly improved when compared to the homopolymer. While, the two tailed alkylamonium salt increased gallery spacing, the presence of more hydrophobic tails limits access of the polar nylon component to the silicate surface. As a result, the energetic interaction is not sufficient to overcome the entropic penalty of intercalation. In contrast, single chained alkylamonium salts increase gallery spacing enough to promote intercalation, but also allows for polymer chains to reach the hydrophilic silicate surface, resulting in exfoliated layers.[147]

2.6.2 Carbon Nanotube Surface Modification

Much like other nanomaterials, CNT have the propensity to aggregate due to attractive van der Waals forces, making dispersion in solvents and polymers challenging. Specifically, CNTs do not possess either charged surface groups or extended “hairy” morphologies required for electrostatic or steric stabilization, respectively. As a result, the high aspect ratio particles tend to form bundles that require exfoliation prior to or during formulation. Numerous methodologies have been proposed to improve dispersibility, but the most common route is surface modification that imparts electrostatic or steric stabilization and better interfacial adhesion. These approaches can be classified as either non-covalent (e.g. polymer or surfactant adsorption, π-stacking, peptide coupling)[148,149] or covalent (e.g. Prato reaction, aryl diazonium) (Figure 2.13),[132,150,151] each with its own benefits and drawbacks. Notably, covalent modification while yielding robust and specific chemical handles creates defects in the nanotube structure, disrupting the extended π-conjugated network and potentially reducing both the electronic and mechanical properties.[129,152,153] Nonetheless, covalent modification has been effectively used to improve both the dispersibility of and interfacial adhesion of CNT within polymer matrices.[154] For example, Zhu *et al.* demonstrated that where native CNT reduced the mechanical properties of epoxy composites, covalently fluorinated CNT showed a 30% improvement over neat epoxy resins.[155] Similarly, Liu *et al.* showed a nearly 80% improvement in the tensile modulus of polylactic acid by including less than 1 wt % of hydroxyl modified CNTs.[156]

In contrast, non-covalent treatments preserve the chemical structure of CNT. Commonly surfactants are used to improve dispersibility in solvents, however, they can desorb from the particle surface, increase interfacial resistance and induce polymer crystallization.[150,157,158] Polymer adsorption however, is a nearly irreversible process that has been demonstrated to improve dispersibility and compatibility with the polymer matrix.[159,160] Besides polymers and surfactants, π-stacking via pyrene "paddles" and peptide coupling have been used to improve dispersibility and create supramolecular structures at the nanotube surface.[148,149]

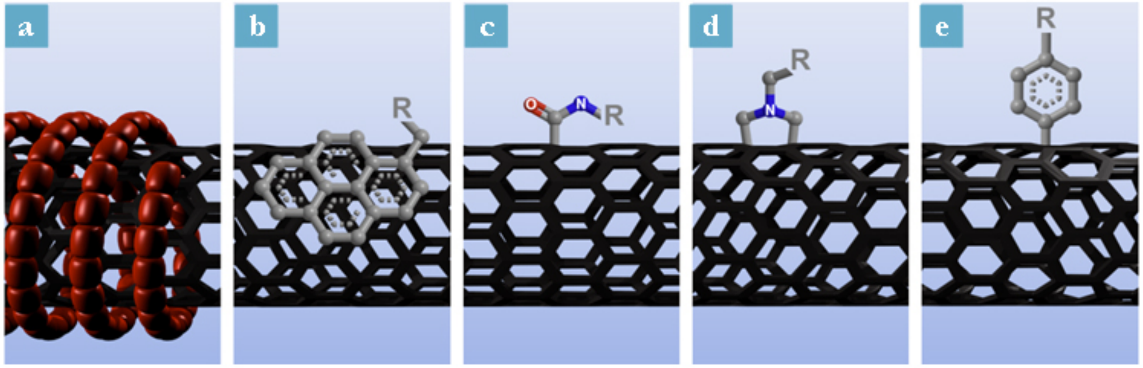

Figure 2.13. Schematic representation of surface modification of CNTs: a) polymer adsorption, b) π-stacking, c) peptide coupling, d) Prato reaction, e) aryl diazonium. Figure reproduced from [151].

2.6.3 Cellulose Nanocrystal Surface Modification

Currently a major hurdle limiting the application of CNCs is the hydrophilic nature of the particles. In aqueous environments, particle-particle interactions are interrupted by enthalpic wetting (replacing CNC/CNC with CNC/H_2O hydrogen bonds), and electrostatic repulsion, of which the later is responsible for colloidal stability.[89] While external energy is required to completely disperse particles (i.e., "unhinge" loosely tethered bundles during production and to overcome van der Waals forces) native CNCs have been used in numerous aqueous applications including cements, drilling fluids, and emulsions.[43,44,48,58,161] In hydrophobic environments, van der Waals forces and hydrogen bonding between CNCs create strong particle-particle interactions leading to aggregation. As a result, a major focus within the community is the surface modification of CNCs to improve dispersibility and increase functionality.[130,162]

Non-covalent surface modification of CNCs was first demonstrated by Heux *et al.* who used PEG based phosphoric ester surfactants to disperse CNCs in non-polar solvents.[163] Concentrated suspensions in toluene and cyclohexane both exhibited chiral nematic self-assembly, indicating that good particle dispersion was maintained for several days. Since this initial report, numerous works have used surfactants to control the behaviour of CNCs in both aqueous and non-aqueous environments.[48,164–166] Similarly, polymer adsorption has become an attractive method to modify the surface of CNCs.[49,167,168] Cationic polyelectrolytes readily adsorb to anionic cellulose surfaces, allowing for layer-by-layer assembly of multilayer films for numerous coatings, capacitor and battery applications.[168–170] Additionally, many non-ionic polymers such as polysaccharides have been thoroughly investigated as environmentally conscious methods to control the dispersion and gelation of CNC.[49,171–173]

Generally, covalent modification of CNCs (and other nanocelluloses) are more robust and tailorable than physical adsorption of surfactants or polymers. As a result, numerous chemical modifications of CNCs have been demonstrated, many of which have been extensively reviewed.[130,162] Modification via oxidation, esterification, amidation, carbamation and etherification, amongst others, are common approaches to control particle behaviour. Recently, Peng *et al.* demonstrated that acetyl, hexanoyl, dodecanoyl, oleoyl, and methacryloyl functionalization via esterification improved the dispersibility of CNC in a variety of non-aqueous solvents.[108] Similarly hexanoyl, lauroyl, and stearoyl modified CNCs exhibited better dispersibility and thermal properties in melt processed low density polyethylene composites.[174]

Polymer grafting either by "grafting-to" or "grafting-from" is becoming an increasingly popular method to improve dispersibility of CNCs in hydrophobic solvents and polymer matrices.[130] Whereas, miscibility and steric effects can limit graft density during grafting-to modifications, high density and aqueous based reactions can be achieved via grafting-from approaches. For example, to reach a grafting density sufficient to allow polycaprolactone crystallization at the CNC surface, a grafting-to modification was conducted for more than seven days with continuous catalyst and polymer addition.[175] In contrast, grafting-from reactions are more rapid (less than 24 hours) with a variety of pathways including ring opening polymerization, free radical polymerization and various controlled polymerization routes (e.g. atom-transfer radical-polymerization (ATRP), reversible addition-fragmentation chain-transfer polymerization (RAFT), nitroxide-mediated), amongst others.[176–180] Although numerous modification pathways have been demonstrated in the literature, unlike for silica, modification of CNCs is not firmly established and has yet to be demonstrated at an industrial scale.

2.7 Characterization Methods

A significant portion of the work presented in this thesis aims to characterize (and benchmark) CNCs and elucidate the main surface forces that govern both particle-particle and particle-polymer interactions in CNC systems. While conventional methods are employed to probe particle morphology, chemistry and physical properties, (including: atomic force microscopy (AFM), conductometric titration, differential scanning calorimetry (DSC), dynamic light scattering (DLS), isothermal titration calorimetry (ITC), polarized optical microscopy (POM), thermal gravimetric analysis (TGA), transmission electron microscopy (TEM), X-ray diffraction

(XRD), X-ray photoelectron spectroscopy (XPS), and zeta potential), less commonly used surface sensitive techniques are additionally used. Specifically, surface plasmon resonance spectroscopy (SPR) and quartz crystal microbalance with dissipation (QCM-D) are employed to understand particle-particle and particle-polymer interactions to improve our ability to design better composites. These techniques are highly sophisticated and precise, which is required for detailed nano-characterization; in some parts of this thesis, SPR and QCM-D are used/extended (or data is treated/presented) in novel ways that have not been described previously in the literature. These techniques constitute a major part of this work and as a result, in addition to the relevant experimental details provided in each research chapter, SPR and QCM-D are discussed further below.

2.7.1 Surface Plasmon Resonance Spectroscopy

SPR is a label free, optical technique that measures binding events or changes in film thickness and refractive index at a sensor-media interface by monitoring laser reflection intensity as a function of angular position. Figure 2.14a shows the experimental setup of SPR spectroscopy following the Kretchmann configuration in which, *p*-polarized laser light is reflected through a prism, off of a plasmonic material (gold or silver) to a photodetector. As the angle of incidence (θ) increases, the laser passes through the angle of total internal reflection (TIR) after which, at a critical angle, the photon momentum matches that of the electrons within the sensor material's conduction band. The electrons absorb the resonant laser energy, creating what is termed as a surface plasmon, sharply reducing the reflected laser intensity at the photodetector. The angular position of the intensity minimum is referred to as the peak angle and is highly sensitive to the plasmon environment such as bulk refractive index, film thickness and film density. For example, the swelling of a film bound to a sensor, or the adsorption/desorption of molecules/polymers would result in a change in the peak angle.

Layer parameters (thickness and refractive index) of the sensor and bound film (Figure 2.14b) are modeled by fitting the entire SPR angular data (reflectivity vs. θ) using the Fresnel equations. Moreover, employing multiple laser wavelengths allows for independent determination of layer thickness and refractive index.[181] SPR is capable of operating in both liquid and vapour and is traditionally used in biological research fields to investigate specific and non-specific binding and on/off kinetics for biomolecules where only the peak intensity is collected and a binary yes/no result is obtained without fitting the entire SPR angular curve. In this work, we extend the use of SPR to materials science and take advantage of all of the optical data present in the SPR curves. Previously, regenerated cellulose and nanocellulose films have been explored using SPR to study, for example, enzymatic degradation,[182] swelling[183] and polymer adsorption.[49,184] A detailed description of the SPR data analysis used to interpret particle-particle interactions is provided in *Chapter 4* and *Chapter 5*.

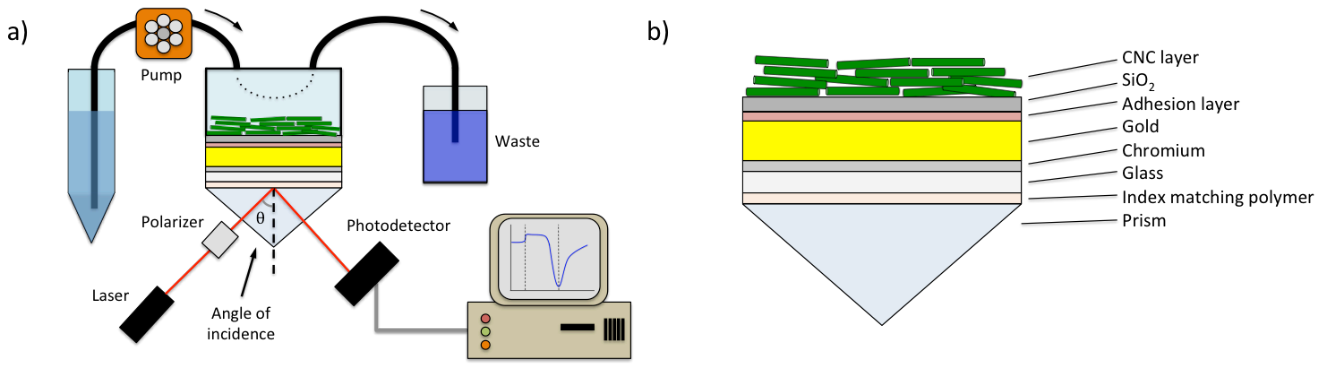

Figure 2.14. Schematic representation of a) SPR spectroscopy experimental layout following the Kretchmann configuration with fluid flow cell and computer output displaying typical intensity vs. angle curve, b) sensor layer diagram.

2.7.2 Quartz Crystal Microbalance with Dissipation

QCM-D is a label free, surface sensitive technique that measures the change in bound mass per unit area by monitoring the shift in frequency of a resonating quartz crystal sensor. During operation, an alternating electric field induces a standing shear wave in the quartz sensor that resonates between 5 and 20 MHz.[185] In addition, sensors are driven at odd integer overtones of resonance, yielding measurements that are more sensitive to regions at and above the sensor surface. Adsorbing material (Figure 2.15a) is characterized by a reduction in the resonance frequency or an increase in oscillation period (Figure 2.5b). The magnitude of the frequency shift can be used to calculate the mass of adsorbed (or desorbed) material by using the Sauerbrey or Voigt viscoelastic models.[186] Under the Sauerbrey assumption, adsorbed mass behaves elastically and the QCM-D instrument is capable of measuring changes on the order of ng/cm^2 by:

$$\frac{\Delta f}{n} = \frac{-2\Gamma_s f^2}{A\sqrt{(\mu\rho_q)}} = -C\Gamma_s \tag{2. 16}$$

where Δf is the shift in resonant frequency, n is the overtone number, f is the fundamental frequency of the crystal, Γ_s is the change in mass, A is the electrode area, ρ_q is the density of the quartz and, μ is the shear modulus. Constants f, A, ρ_q and μ are instrument specific and are typically reduced to the constant C.[185] In addition to measuring the change in frequency, some QCM-D instruments also monitor the dissipation (D) or energy lost per oscillation cycle (Figure 2.15 c). Removing the driving electric field, the oscillatory decay of the sensor is monitored and the dissipation is given by:

$$D = \frac{E_L}{2\pi E_S} \tag{2. 17}$$

where E_L is the energy lost over one oscillation cycle and E_S is the total energy stored in the sensor. The time scale of decay provides insight into the rigidity or viscoelasticity of the adsorbed layer. Similarly to SPR, QCM-D has been used previously to monitor polymer adsorption,[49,172,186,187] swelling[188–190] and enzymatic degradation[191,192] of cellulose and nanocellulose thin films.

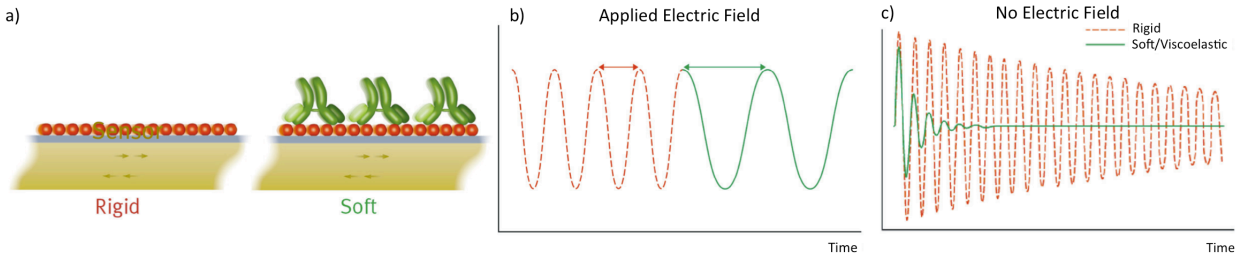

Figure 2.15. Schematic representation of the changes to the QCM-D sensor resonance frequency during adsorption experiments. a) Shows adsorption of rigid and soft species. b) Displays the shift in resonance frequency for each species adsorbed and c) shows a comparison of the dissipation of each species. Adapted from [193].

References

(1) Somerville, C. Cellulose Synthesis in Higher Plants. *Annu Rev Cell Dev Biol* **2006**, *22*, 53–78.

(2) Klemm, D.; Heublein, B.; Fink, H. P.; Bohn, A. Cellulose: Fascinating Biopolymer and Sustainable Raw Material. *Angew. Chemie - Int. Ed.* **2005**, *44* (22), 3358–3393.

(3) Habibi, Y.; Lucia, L. A.; Rojas, O. J. Cellulose Nanocrystals: Chemistry, Self-Assembly, and Applications. *Chem. Rev.* **2010**, *110* (6), 3479–3500.

(4) Medronho, B.; Romano, A.; Miguel, M. G.; Stigsson, L.; Lindman, B. Rationalizing Cellulose (In)solubility: Reviewing Basic Physicochemical Aspects and Role of Hydrophobic Interactions. *Cellulose* **2012**, *19*, 581–587.

(5) Lindman, B.; Karlström, G.; Stigsson, L. On the Mechanism of Dissolution of Cellulose. *J. Mol. Liq.* **2010**, *156* (1), 76–81.

(6) Moon, R. J.; Martini, A.; Nairn, J.; Simonsen, J.; Youngblood, J. Cellulose Nanomaterials Review: Structure, Properties and Nanocomposites. *Chem. Soc. Rev.* **2011**, *40* (7), 3941–3994.

(7) Ahvenainen, P.; Kontro, I.; Svedström, K. Comparison of Sample Crystallinity Determination Methods by X-Ray Diffraction for Challenging Cellulose I Materials. *Cellulose* **2016**, *23* (2), 1073–1086.

(8) O'Sullivan, A. C. Cellulose: The Structure Slowly Unravels. *Cellulose* **1997**, *4* (3), 173–207.

(9) Nishiyama, Y. Structure and Properties of the Cellulose Microfibril. *J. Wood Sci.* **2009**, *55* (4), 241–249.

(10) Canadian Standards Association. *Cellulosic Nanomaterials — Test Methods for Characterization (CSA Z5100-14)*; 2014.

(11) Eichhorn, S. J.; Dufresne, A.; Aranguren, M.; Marcovich, N. E.; Capadona, J. R.; Rowan, S. J.; Weder, C.; Thielemans, W.; Roman, M.; Renneckar, S.; et al. Review: Current International Research into Cellulose Nanofibres and Nanocomposites. *J. Mater. Sci.* **2010**, *45* (1), 1–33.

(12) Klemm, D.; Kramer, F.; Moritz, S.; Lindström, T.; Ankerfors, M.; Gray, D. G.; Dorris, A. Nanocelluloses: A New Family of Nature-Based Materials. *Angew. Chemie - Int. Ed.* **2011**, *50*, 5438–5466.

(13) Nechyporchuk, O.; Belgacem, M. N.; Pignon, F. Current Progress in Rheology of Cellulose Nanofibril Suspensions. *Biomacromolecules* **2016**, *17* (7), 2311–2320.

(14) Nechyporchuk, O.; Belgacem, M. N.; Bras, J. Production of Cellulose Nanofibrils: A Review of Recent Advances. *Industrial Crops and Products*. Elsevier B.V. December 2015, pp 2–25.

(15) Li, Q.; McGinnis, S.; Sydnor, C.; Wong, A.; Renneckar, S. Nanocellulose Life Cycle Assessment. *ACS Sustain. Chem. Eng.* **2013**, *1* (8), 919–928.

(16) Isogai, A.; Saito, T.; Fukuzumi, H. TEMPO-Oxidized Cellulose Nanofibers. *Nanoscale* **2011**, *3* (1), 71–85.

(17) Davis, N. J.; Flitscb, S. L. Selective Oxidation of Monosaccharide Uranic Acids Derivatives to. **1993**, *34* (7), 1181–1184.

(18) Birkett, G. C.; Sicoli, S.; Horvath, L.; Foster, J.; Kim, Y.; Renneckar, S.; Goodell, B. Investigation of Nanofibrillated Cellulose for Hydrophobic Packaging Material:

Examining Alternatives to Solvent Exchange and Lyophilization. *BioResources* **2017**, *12* (2), 4314–4326.
(19) Oksman, K.; Aitomäki, Y.; Mathew, A. P.; Siqueira, G.; Zhou, Q.; Butylina, S.; Tanpichai, S.; Zhou, X.; Hooshmand, S. Review of the Recent Developments in Cellulose Nanocomposite Processing. *Compos. Part A Appl. Sci. Manuf.* **2016**, *83*, 2–18.
(20) Lindström, T. Aspects on Nanofibrillated Cellulose (NFC) Processing, Rheology and NFC-Film Properties. *Curr. Opin. Colloid Interface Sci.* **2017**, *29*, 68–75.
(21) Saito, T.; Uematsu, T.; Kimura, S.; Enomae, T.; Isogai, A. Self-Aligned Integration of Native Cellulose Nanofibrils towards Producing Diverse Bulk Materials. *Soft Matter* **2011**, *7* (19), 8804.
(22) Pääkkö, M.; Vapaavuori, J.; Silvennoinen, R.; Kosonen, H.; Ankerfors, M.; Lindström, T.; Berglund, L. A.; Ikkala, O. Long and Entangled Native Cellulose I Nanofibers Allow Flexible Aerogels and Hierarchically Porous Templates for Functionalities. *Soft Matter* **2008**, *4* (12), 2492.
(23) Sehaqui, H.; Salajková, M.; Zhou, Q.; Berglund, L. A. Mechanical Performance Tailoring of Tough Ultra-High Porosity Foams Prepared from Cellulose I Nanofiber Suspensions. *Soft Matter* **2010**, *6* (8), 1824.
(24) Huang, Y.; Zhu, C.; Yang, J.; Nie, Y.; Chen, C.; Sun, D. Recent Advances in Bacterial Cellulose. *Cellulose* **2013**.
(25) Jorfi, M.; Foster, E. J. Recent Advances in Nanocellulose for Biomedical Applications. *J. Appl. Polym. Sci.* **2015**, *132* (14), 1–19.
(26) Sacui, I. a.; Nieuwendaal, R. C.; Burnett, D. J.; Stranick, S. J.; Jorfi, M.; Weder, C.; Foster, E. J.; Olsson, R. T.; Gilman, J. W. Comparison of the Properties of Cellulose Nanocrystals and Cellulose Nanofibrils Isolated from Bacteria, Tunicate, and Wood Processed Using Acid, Enzymatic, Mechanical, and Oxidative Methods. *ACS Appl. Mater. Interfaces* **2014**, *6* (9), 6127–6138.
(27) Nickerson, R. F.; Habrle, J. A. Cellulose Intercrystalline Structure. *Ind. Eng. Chem.* **1947**, *39* (11), 1507–1512.
(28) Rånby, B. .; Ribi, E. Uber Den Feinbau Zellulose. *Experientia* **1950**, *6*, 12–14.
(29) Camarero Espinosa, S.; Kuhnt, T.; Foster, E. J.; Weder, C. Isolation of Thermally Stable Cellulose Nanocrystals by Phosphoric Acid Hydrolysis. *Biomacromolecules* **2013**, *14* (4), 1223–1230.
(30) Kontturi, E.; Meriluoto, A.; Penttilä, P. A.; Baccile, N.; Malho, J.-M.; Potthast, A.; Rosenau, T.; Ruokolainen, J.; Serimaa, R.; Laine, J.; et al. Degradation and Crystallization of Cellulose in Hydrogen Chloride Vapor for High-Yield Isolation of Cellulose Nanocrystals. *Angew. Chemie Int. Ed.* **2016**, *55* (46), 14455–14458.
(31) Chen, L.; Zhu, J. Y.; Baez, C.; Kitin, P.; Elder, T. Highly Thermal-Stable and Functional Cellulose Nanocrystals and Nanofibrils Produced Using Fully Recyclable Organic Acids. *Green Chem.* **2016**, *18* (13), 3835–3843.
(32) Reid, M. S.; Villalobos, M.; Cranston, E. D. Benchmarking Cellulose Nanocrystals: From the Laboratory to Industrial Production. *Langmuir* **2017**, *33* (7), 1583–1598.
(33) Dong, X.; Revol, J.; Gray, D. G. Effect of Microcrystallite Preparation Conditions on the Formation of Colloid Crystals of Cellulose. *Cellulose* **1998**, *5* (1), 19–32.
(34) Dong, X. M.; Kimura, T.; Revol, J.-F.; Gray, D. G. Effects of Ionic Strength on the Isotropic−Chiral Nematic Phase Transition of Suspensions of Cellulose Crystallites. *Langmuir* **1996**, *12* (8), 2076–2082.

(35) Dong, X. M.; Gray, D. G. Effect of Counterions on Ordered Phase Formation in Suspensions of Charged Rodlike Cellulose Crystallites. *Langmuir* **1997**, *13* (8), 2404–2409.

(36) Revol, J. F.; Bradford, H.; Giasson, J.; Marchessault, R. H.; Gray, D. G. Helicoidal Self-Ordering of Cellulose Microfibrils in Aqueous Suspension. *Int. J. Biol. Macromol.* **1992**, *14* (3), 170–172.

(37) Revol, J.-F.; Godbout, L.; Dong, X.-M.; Gray, D. G.; Chanzy, H.; Maret, G. Chiral Nematic Suspensions of Cellulose Crystallites; Phase Separation and Magnetic Field Orientation. *Liq. Cryst.* **1994**, *16* (1), 127–134.

(38) Giese, M.; Blusch, L. K.; Khan, M. K.; MacLachlan, M. J. Functional Materials from Cellulose-Derived Liquid-Crystal Templates. *Angew. Chemie - Int. Ed.* **2015**, *54* (10), 2888–2910.

(39) Majoinen, J.; Hassinen, J.; Haataja, J. S.; Rekola, H. T.; Kontturi, E.; Kostiainen, M. A.; Ras, R. H. A.; Törmä, P.; Ikkala, O. Chiral Plasmonics Using Twisting along Cellulose Nanocrystals as a Template for Gold Nanoparticles. *Adv. Mater.* **2016**, 6–11.

(40) Shopsowitz, K. E.; Qi, H.; Hamad, W. Y.; Maclachlan, M. J. Free-Standing Mesoporous Silica Films with Tunable Chiral Nematic Structures. *Nature* **2010**, *468* (7322), 422–425.

(41) Kelly, J. A.; Manchee, C. P. K.; Cheng, S.; Ahn, J. M.; Shopsowitz, K. E.; Hamad, W. Y.; MacLachlan, M. J. Evaluation of Form Birefringence in Chiral Nematic Mesoporous Materials. *J. Mater. Chem. C* **2014**, *2* (26), 5093.

(42) Beck, S.; Bouchard, J.; Berry, R. Controlling the Reflection Wavelength of Iridescent Solid Films of Nanocrystalline Cellulose. *Biomacromolecules* **2011**, *12*, 167–172.

(43) Kalashnikova, I.; Bizot, H.; Cathala, B.; Capron, I. New Pickering Emulsions Stabilized by Bacterial Cellulose Nanocrystals. *Langmuir* **2011**, *27* (12), 7471–7479.

(44) Kalashnikova, I.; Bizot, H.; Cathala, B.; Capron, I. Modulation of Cellulose Nanocrystals Amphiphilic Properties to Stabilize Oil/water Interface. *Biomacromolecules* **2012**, *13* (1), 267–275.

(45) Tasset, S.; Cathala, B.; Bizot, H.; Capron, I. Versatile Cellular Foams Derived from CNC-Stabilized Pickering Emulsions. *RSC Adv.* **2014**, *4* (2), 893.

(46) Kalashnikova, I.; Bizot, H.; Bertoncini, P.; Cathala, B.; Capron, I. Cellulosic Nanorods of Various Aspect Ratios for Oil in Water Pickering Emulsions. *Soft Matter* **2013**, *9* (3), 952.

(47) Capron, I.; Cathala, B. Surfactant-Free High Internal Phase Emulsions Stabilized by Cellulose Nanocrystals. *Biomacromolecules* **2013**, *14* (2), 291–296.

(48) Hu, Z.; Ballinger, S.; Pelton, R.; Cranston, E. D. Surfactant-Enhanced Cellulose Nanocrystal Pickering Emulsions. *J. Colloid Interface Sci.* **2015**, *439*, 139–148.

(49) Hu, Z.; Cranston, E. D.; Ng, R.; Pelton, R. Tuning Cellulose Nanocrystal Gelation with Polysaccharides and Surfactants. *Langmuir* **2014**, *30* (10), 2684–2692.

(50) Shafiei-Sabet, S.; Hamad, W. Y.; Hatzikiriakos, S. G. Rheology of Nanocrystalline Cellulose Aqueous Suspensions. *Langmuir* **2012**, *28* (49), 17124–17133.

(51) Shafiei-Sabet, S.; Hamad, W. Y.; Hatzikiriakos, S. G. Ionic Strength Effects on the Microstructure and Shear Rheology of Cellulose Nanocrystal Suspensions. *Cellulose* **2014**, *21* (5), 3347–3359.

(52) Hubbe, M. A.; Ferrer, A.; Tyagi, P.; Yin, Y.; Salas, C.; Pal, L.; Rojas, O. J. Nanocellulose in Thin Films, Coatings, and Plies for Packaging Applications: A Review. *BioResources* **2017**, *12* (1), 2143–2233.

(53) Camarero-Espinosa, S.; Rothen-Rutishauser, B.; Weder, C.; Foster, E. J. Directed Cell

Growth in Multi-Zonal Scaffolds for Cartilage Tissue Engineering. *Biomaterials* **2015**, *74*, 42–52.

(54) De France, K. J.; Chan, K. J. W.; Cranston, E. D.; Hoare, T. Enhanced Mechanical Properties in Cellulose Nanocrystal–Poly(oligoethylene Glycol Methacrylate) Injectable Nanocomposite Hydrogels through Control of Physical and Chemical Cross-Linking. *Biomacromolecules* **2016**, *17* (2), 649–660.

(55) Yang, X.; Bakaic, E.; Hoare, T.; Cranston, E. D. Injectable Polysaccharide Hydrogels Reinforced with Cellulose Nanocrystals: Morphology, Rheology, Degradation, and Cytotoxicity. *Biomacromolecules* **2013**, *14* (12), 4447–4455.

(56) Charreau, H.; Foresti, M. L.; Vazquez, A. Nanocellulose Patents Trends: A Comprehensive Review on Patents on Cellulose Nanocrystals, Microfibrillated and Bacterial Cellulose. *Recent Pat. Nanotechnol.* **2013**, *7* (1), 56–80.

(57) Yang, X.; Shi, K.; Zhitomirsky, I.; Cranston, E. D. Cellulose Nanocrystal Aerogels as Universal 3D Lightweight Substrates for Supercapacitor Materials. *Adv. Mater.* **2015**, *27* (40), 6104–6109.

(58) Cao, Y.; Zavaterri, P.; Youngblood, J.; Moon, R.; Weiss, J. The Influence of Cellulose Nanocrystal Additions on the Performance of Cement Paste. *Cem. Concr. Compos.* **2015**, *56*, 73–83.

(59) Mariano, M.; El Kissi, N.; Dufresne, A. Cellulose Nanocrystals and Related Nanocomposites: Review of Some Properties and Challenges. *J. Polym. Sci. Part B Polym. Phys.* **2014**, *52*, 791–806.

(60) Wang, P.-X.; Hamad, W. Y.; MacLachlan, M. J. Structure and Transformation of Tactoids in Cellulose Nanocrystal Suspensions. *Nat. Commun.* **2016**, *7* (May), 11515.

(61) Paul, D. R. R.; Robeson, L. M. M. Polymer Nanotechnology: Nanocomposites. *Polymer (Guildf).* **2008**, *49* (15), 3187–3204.

(62) Gohardani, O.; Elola, M. C.; Elizetxea, C. Potential and Prospective Implementation of Carbon Nanotubes on next Generation Aircraft and Space Vehicles: A Review of Current and Expected Applications in Aerospace Sciences. *Prog. Aerosp. Sci.* **2014**, *70*, 42–68.

(63) Balazs, A. C.; Emrick, T.; Russell, T. P. Nanoparticle Polymer Composites: Where Two Small Worlds Meet. *Science* **2006**, *314* (5802), 1107–1110.

(64) Okada, A.; Usuki, A. Twenty Years of Polymer-Clay Nanocomposites. *Macromol. Mater. Eng.* **2006**, *291* (12), 1449–1476.

(65) Panwar, A.; Choudhary, V.; Sharma, D. K. Review: A Review: Polystyrene/clay Nanocomposites. *J. Reinf. Plast. Compos.* **2011**, *30* (5), 446–459.

(66) Mackay, M. E.; Tuteja, A.; Duxbury, P. M.; Hawker, C. J.; Van Horn, B.; Guan, Z.; Chen, G.; Krishnan, R. S. General Strategies for Nanoparticle Dispersion. *Science* **2006**, *311* (5768), 1740–1743.

(67) Kuilla, T.; Bhadra, S.; Yao, D.; Kim, N. H.; Bose, S.; Lee, J. H. Recent Advances in Graphene Based Polymer Composites. *Prog. Polym. Sci.* **2010**, *35* (11), 1350–1375.

(68) Jordan, J.; Jacob, K. I.; Tannenbaum, R.; Sharaf, M. A.; Jasiuk, I. Experimental Trends in Polymer Nanocomposites - A Review. *Mater. Sci. Eng. A* **2005**, *393*, 1–11.

(69) Azeez, A. A.; Rhee, K. Y.; Park, S. J.; Hui, D. Epoxy Clay Nanocomposites – Processing, Properties and Applications: A Review. *Compos. Part B Eng.* **2013**, *45* (1), 308–320.

(70) Abdul Khalil, H. P. S.; Bhat, A. H.; Ireana Yusra, A. F. Green Composites from Sustainable Cellulose Nanofibrils: A Review. *Carbohydr. Polym.* **2012**, *87* (2), 963–979.

(71) Stark, W. J.; Stoessel, P. R.; Wohlleben, W.; Hafner, A. Industrial Applications of

Nanoparticles. *Chem. Soc. Rev.* **2015**, *44* (16), 5793–5805.
(72) Akcora, P.; Liu, H.; Kumar, S. K.; Moll, J.; Li, Y.; Benicewicz, B. C.; Schadler, L. S.; Acehan, D.; Panagiotopoulos, A. Z.; Pryamitsyn, V.; et al. Anisotropic Self-Assembly of Spherical Polymer-Grafted Nanoparticles. *Nat. Mater.* **2009**, *8* (4), 354–359.
(73) Jancar, J.; Douglas, J. F.; Starr, F. W.; Kumar, S. K.; Cassagnau, P.; Lesser, A. J.; Sternstein, S. S.; Buehler, M. J. Current Issues in Research on Structure-Property Relationships in Polymer Nanocomposites. *Polymer (Guildf).* **2010**, *51* (15), 3321–3343.
(74) Madathingal, R. R.; Wunder, S. L. Confinement Effects of Silica Nanoparticles with Radii Smaller and Larger than Rg of Adsorbed Poly(ethylene Oxide). *Macromolecules* **2011**, *44* (8), 2873–2882.
(75) Cosgrove, T.; Grifiths, P. C.; Lloyd, P. M. Polymer Adsorption . The Effect of the Relative Sizes of Polymer and Particle. *Langmuir* **1995**, No. 8, 1457–1463.
(76) Liu, H.; Xiao, H. Adsorption of Poly(ethylene Oxide) with Different Molecular Weights on the Surface of Silica Nanoparticles and the Suspension Stability. *Mater. Lett.* **2008**, *62* (6–7), 870–873.
(77) Araki, J.; Wada, M.; Kuga, S. Steric Stabilization of a Cellulose Microcrystal Suspension by Poly (Ethylene Glycol) Grafting Steric Stabilization of a Cellulose Microcrystal Suspension by Poly (Ethylene Glycol) Grafting. *Cellulose* **2001**, No. 17, 21–27.
(78) Kan, K. H. M.; Li, J.; Wijesekera, K.; Cranston, E. D. Polymer-Grafted Cellulose Nanocrystals as pH-Responsive Reversible Flocculants. *Biomacromolecules* **2013**, *14* (9), 3130–3139.
(79) Kim, S. Y.; Meyer, H. W.; Saalwächter, K.; Zukoski, C. F. Polymer Dynamics in PEG-Silica Nanocomposites: Effects of Polymer Molecular Weight, Temperature and Solvent Dilution. *Macromolecules* **2012**, *45* (10), 4225–4237.
(80) Chazeau, L.; Cavaillé, J. Y.; Canova, G.; Dendievel, R.; Boutherin, B. Viscoelastic Properties of Plasticized PVC Reinforced with Cellulose Whiskers. *J. Appl. Polym. Sci.* **1999**, *71* (11), 1797–1808.
(81) Favier, V.; Chanzy, H.; Cavaille, J. Y. Polymer Nanocomposites Reinforced by Cellulose Whiskers. *Macromolecules* **1995**, *28* (18), 6365–6367.
(82) Favier, V.; Cavaille, J. Y.; Canova, G. R.; Shrivastava, S. C. Mechanical Percolation in Cellulose Whisker Nanocomposites. *Polym. Eng. Sci.* **1997**, *37* (10), 1732–1739.
(83) Affdl, J. C. H.; Kardos, J. L. The Halpin-Tsai Equations: A Review. *Polym. Eng. Sci.* **1976**, *16* (5), 344–352.
(84) Ouali, N.; Cavaille, J. Y.; Perez, J. Elastic, Viscoelastic and Plastic Behavior of Multiphase Polymer Blends. *Plast. Rubber Compos. Process. Appl.* **1991**, *16* (July), 55–60.
(85) Israelachvili, J. *Intermolecular and Surface Forces*; Elsevier, 2011.
(86) Feiler, A. A; Bergström, L.; Rutland, M. W. Superlubricity Using Repulsive van Der Waals Forces. *Langmuir* **2008**, *24* (6), 2274–2276.
(87) Meurk, A.; Luckham, P. F.; Bergström, L. Direct Measurement of Repulsive and Attractive van Der Waals Forces Between Inorganic Materials. *Langmuir* **1997**, *13* (13), 3896–3899.
(88) Napper, D. H. Steric Stabilization. *J. Colloid Interface Sci.* **1977**, *58* (2), 390–407.
(89) Reid, M. S.; Villalobos, M.; Cranston, E. D. Cellulose Nanocrystal Interactions Probed by Thin Film Swelling to Predict Dispersibility. *Nanoscale* **2016**, *8* (24), 12247–12257.
(90) Chen, J.; Shi, Y.; Yang, J.; Zhang, N.; Huang, T.; Chen, C.; Wang, Y.; Zhou, Z. A Simple Strategy to Achieve Very Low Percolation Threshold via the Selective Distribution of

Carbon Nanotubes at the Interface of Polymer Blends. *J. Mater. Chem.* **2012**, *22* (42), 22398.

(91) Sumita, M.; Sakata, K.; Asai, S.; Miyasaka, K.; Nakagawa, H. Dispersion of Fillers and the Electrical Conductivity of Polymer Blends Filled with Carbon Black. *Polym. Bull.* **1991**, *25* (2), 265–271.

(92) Della Volpe, C.; Maniglio, D.; Brugnara, M.; Siboni, S.; Morra, M. The Solid Surface Free Energy Calculation. *J. Colloid Interface Sci.* **2004**, *271* (2), 434–453.

(93) Biolin Scientific. *Attension Theory Note 4: Surface Free Energy - Theory and Calculations*.

(94) Shang, S. W.; Williams, J. W.; Söderholm, K. J. M. How the Work of Adhesion Affects the Mechanical Properties of Silica-Filled Polymer Composites. *J. Mater. Sci.* **1994**, *29* (9), 2406–2416.

(95) Rahmat, M.; Hubert, P. Carbon Nanotube-Polymer Interactions in Nanocomposites: A Review. *Compos. Sci. Technol.* **2011**, *72* (1), 72–84.

(96) Bracco, G.; Holst, B. *Surface Science Techniques*; 2013; Vol. 51.

(97) Cassie, A. B. D.; Baxter, S. Wettability of Porous Surfaces. *Trans. Faraday Soc.* **1944**, *40* (5), 546.

(98) Nuriel, S.; Liu, L.; Barber, A. H.; Wagner, H. D. Direct Measurement of Multiwall Nanotube Surface Tension. *Chem. Phys. Lett.* **2005**, *404* (4–6), 263–266.

(99) Barber, A. H.; Cohen, S. R.; Daniel Wagner, H. Static and Dynamic Wetting Measurements of Single Carbon Nanotubes. *Phys. Rev. Lett.* **2004**, *92* (18), 186103–1.

(100) Tran, M. Q.; Cabral, J. T.; Shaffer, M. S. P.; Bismarck, A. Direct Measurement of the Wetting Behavior of Individual Carbon Nanotubes by Polymer Melts: The Key to Carbon Nanotube-Polymer Composites. *Nano Lett.* **2008**, *8* (9), 2744–2750.

(101) Arnaudov, L. N.; Cayre, O. J.; Cohen Stuart, M. A.; Stoyanov, S. D.; Paunov, V. N. Measuring the Three-Phase Contact Angle of Nanoparticles at Fluid Interfaces. *Phys. Chem. Chem. Phys.* **2010**, *12* (2), 328–331.

(102) Owens, D. K.; Wendt, R. C. Estimation of the Surface Free Energy of Polymers. *J. Appl. Polym. Sci.* **1969**, *13* (8), 1741–1747.

(103) Hansen, C. M. 50 Years with Solubility Parameters - Past and Future. *Prog. Org. Coatings* **2004**, *51* (May), 77–84.

(104) Hildebrand, J. H.; Scott, R. L. *The Solubility of Nonelectrolytes*; American society; Dover Publications, 1964.

(105) Fried, J. R. *Polymer Science and Technology*; Chemical engineering; Prentice Hall PTR, 1995.

(106) Bergin, S. D.; Sun, Z.; Rickard, D.; Streich, P. V; Hamilton, J. P.; Coleman, J. N. Multicomponent Solubility Parameters for Single-Walled Carbon Nanotube-Solvent Mixtures. *ACS Nano* **2009**, *3* (8), 2340–2350.

(107) Gårdebjer, S.; Andersson, M.; Engström, J.; Restorp, P.; Persson, M.; Larsson, A. Using Hansen Solubility Parameters to Predict the Dispersion of Nano-Particles in Polymeric Films. *Polym. Chem.* **2016**, *7* (9), 1756–1764.

(108) Peng, S. X.; Chang, H.; Kumar, S.; Moon, R. J.; Youngblood, J. P. A Comparative Guide to Controlled Hydrophobization of Cellulose Nanocrystals via Surface Esterification. *Cellulose* **2016**.

(109) Detriche, S.; Nagy, J. B.; Mekhalif, Z.; Delhalle, J. Surface State of Carbon Nanotubes and Hansen Solubility Parameters. *J. Nanosci. Nanotechnol.* **2009**, *9* (10), 6015–6025.

(110) Detriche, S.; Zorzini, G.; Colomer, J.-F.; Fonseca, a.; Nagy, J. B. Application of the Hansen Solubility Parameters Theory to Carbon Nanotubes. *J. Nanosci. Nanotechnol.* **2008**, *8* (11), 6082–6092.

(111) Ho, D. L.; Glinka, C. J. Effects of Solvent Solubility Parameters on Organoclay Dispersions. *Chem. Mater.* **2003**, *15* (6), 1309–1312.

(112) Ham, H. T.; Choi, Y. S.; Chung, I. J. An Explanation of Dispersion States of Single-Walled Carbon Nanotubes in Solvents and Aqueous Surfactant Solutions Using Solubility Parameters. *J. Colloid Interface Sci.* **2005**, *286* (1), 216–223.

(113) Ata, S.; Yamada, T.; Hata, K. Relationship Between Primary Structure and Hansen Solubility Parameter of Carbon Nanotubes. *J. Nanosci. Nanotechnol.* **2017**, *17* (5), 3310–3315.

(114) Silveira, R. L.; Stoyanov, S. R.; Kovalenko, A.; Skaf, M. S. Cellulose Aggregation under Hydrothermal Pretreatment Conditions. *Biomacromolecules* **2016**, *17* (8), 2582–2590.

(115) Qin, X.; Xia, W.; Sinko, R.; Keten, S. Tuning Glass Transition in Polymer Nanocomposites with Functionalized Cellulose Nanocrystals through Nanoconfinement. *Nano Lett.* **2015**, *15* (10), 6738–6744.

(116) Zhao, Z.; Crespi, V. H.; Kubicki, J. D.; Cosgrove, D. J.; Zhong, L. Molecular Dynamics Simulation Study of Xyloglucan Adsorption on Cellulose Surfaces: Effects of Surface Hydrophobicity and Side-Chain Variation. *Cellulose* **2014**, *21* (2), 1025–1039.

(117) Li, L.; Pérré, P.; Frank, X.; Mazeau, K. A Coarse-Grain Force-Field for Xylan and Its Interaction with Cellulose. *Carbohydr. Polym.* **2015**, *127*, 438–450.

(118) Mazeau, K.; Charlier, L. The Molecular Basis of the Adsorption of Xylans on Cellulose Surface. *Cellulose* **2012**, *19* (2), 337–349.

(119) Eslami, H.; Behrouz, M. Molecular Dynamics Simulation of a Polyamide-66/carbon Nanotube Nanocomposite. *J. Phys. Chem. C* **2014**, *118* (18), 9841–9851.

(120) Ganesan, V.; Jayaraman, A. Theory and Simulation Studies of Effective Interactions, Phase Behavior and Morphology in Polymer Nanocomposites. *Soft Matter* **2014**, *10* (1), 13–38.

(121) Karatrantos, A.; Clarke, N.; Kröger, M. Modeling of Polymer Structure and Conformations in Polymer Nanocomposites from Atomistic to Mesoscale: A Review. *Polym. Rev.* **2016**, *56* (3), 385–428.

(122) Alian, A. R.; Kundalwal, S. I.; Meguid, S. A. Multiscale Modeling of Carbon Nanotube Epoxy Composites. *Polymer (Guildf).* **2015**, *70*, 149–160.

(123) Sheng, N.; Boyce, M. C.; Parks, D. M.; Rutledge, G. C.; Abes, J. I.; Cohen, R. E. Multiscale Micromechanical Modeling of Polymer/clay Nanocomposites and the Effective Clay Particle. *Polymer (Guildf).* **2004**, *45* (2), 487–506.

(124) Zeng, Q. H.; Yu, A. B.; Lu, G. Q. Multiscale Modeling and Simulation of Polymer Nanocomposites. *Prog. Polym. Sci.* **2008**, *33* (2), 191–269.

(125) Odegard, G. M.; Clancy, T. C.; Gates, T. S. Modeling of the Mechanical Properties of Nanoparticle/polymer Composites. *Polymer (Guildf).* **2005**, *46* (2), 553–562.

(126) Khare, K. S.; Khare, R. Effect of Carbon Nanotube Dispersion on Glass Transition in Cross-Linked Epoxy-Carbon Nanotube Nanocomposites: Role of Interfacial Interactions. *J. Phys. Chem. B* **2013**, *117* (24), 7444–7454.

(127) Bouchard, J.; Méthot, M.; Fraschini, C.; Beck, S. Effect of Oligosaccharide Deposition on the Surface of Cellulose Nanocrystals as a Function of Acid Hydrolysis Temperature. *Cellulose* **2016**.

(128) Karger-Kocsis, J.; Mahmood, H.; Pegoretti, A. Recent Advances in Fiber/matrix Interphase Engineering for Polymer Composites. *Prog. Mater. Sci.* **2015**, *73*, 1–43.
(129) Moniruzzaman, M.; Winey, K. I. Polymer Nanocomposites Containing Carbon Nanotubes. *Macromolecules* **2006**, *39* (16), 5194–5205.
(130) Habibi, Y. Key Advances in the Chemical Modification of Nanocelluloses. *Chem. Soc. Rev.* **2014**, *43* (5), 1519–1542.
(131) Bhattacharya, M. Polymer Nanocomposites-A Comparison between Carbon Nanotubes, Graphene, and Clay as Nanofillers. *Materials (Basel).* **2016**, *9* (4), 1–35.
(132) Georgakilas, V.; Kordatos, K.; Prato, M.; Guldi, D. M.; Holzinger, M.; Hirsch, A. Organic Functionalization of Carbon Nanotubes. *J. Am. Chem. Soc.* **2002**, *124* (5), 760–761.
(133) Schadler, L. S.; Kumar, S. K.; Benicewicz, B. C.; Lewis, S. L.; Harton, S. E. Designed Interfaces in Polymer Nanocomposites: A Fundamental Viewpoint. *MRS Bull.* **2007**, *32* (April), 335–340.
(134) Bansal, A.; Yang, H.; Li, C.; Cho, K.; Benicewicz, B. C.; Kumar, S. K.; Schadler, L. S. Quantitative Equivalence between Polymer Nanocomposites and Thin Polymer Films. *Nat. Mater.* **2005**, *4* (September), 693–698.
(135) Zou, H.; Wu, S.; Shen, J. Polymer/Silica Nanocomposites: Preparation, Characterization, Propertles, and Applications. *Chem. Rev.* **2008**, *108*, 3893–3957.
(136) Hyde, E. D. E. R.; Seyfaee, A.; Neville, F.; Moreno-Atanasio, R. Colloidal Silica Particle Synthesis and Future Industrial Manufacturing Pathways: A Review. *Ind. Eng. Chem. Res.* **2016**, *55* (33), 8891–8913.
(137) Stöber, W. Chemische Adsorption von Methylchlorsilanen an Kristallinem Und Amorphem Siliziumdioxyd. *Kolloid-Zeitschrift* **1956**, *149* (1), 39–46.
(138) Camenzind, A.; Caseri, W. R.; Pratsinis, S. E. Flame-Made Nanoparticles for Nanocomposites. *Nano Today* **2010**, *5* (1), 48–65.
(139) Barthel, H. Surface Interactions of Dimethylsiloxy Group-Modified Fumed Silica. *Colloids Surfaces A Physicochem. Eng. Asp.* **1995**, *101*, 217–226.
(140) Zhu, L.; Xanthos, M. Effects of Process Conditions and Mixing Protocols on Structure of Extruded Polypropylene Nanocomposites. *J. Appl. Polym. Sci.* **2004**, *93* (4), 1891–1899.
(141) Ton-That, M. T.; Perrin-Sarazin, F.; Cole, K. C.; Bureau, M. N.; Denault, J. Polyolefin Nanocomposites: Formulation and Development. *Polym. Eng. Sci.* **2004**, *44* (7), 1212–1219.
(142) Daniel, D. J.; Panneerselvam, K. Manufacturing Issues of Polypropylene Nanocomposite by Melt Intercalation Process. *Mater. Today Proc.* **2017**, *4* (2), 4032–4041.
(143) Albdiry, M.; Yousif, B.; Ku, H.; Lau, K. A Critical Review on the Manufacturing Processes in Relation to the Properties of Nanoclay/polymer Composites. *J. Compos. Mater.* **2012**, *47* (9), 1093–1115.
(144) Faucheu, J.; Gauthier, C.; Chazeau, L.; Cavaillé, J. Y.; Mellon, V.; Lami, E. B. Miniemulsion Polymerization for Synthesis of Structured Clay/polymer Nanocomposites: Short Review and Recent Advances. *Polymer (Guildf).* **2010**, *51* (1), 6–17.
(145) Pavlidou, S.; Papaspyrides, C. D. A Review on Polymer–layered Silicate Nanocomposites. *Prog. Polym. Sci.* **2008**, *33* (12), 1119–1198.
(146) Hotta, S.; Paul, D. R. Nanocomposites Formed from Linear Low Density Polyethylene and Organoclays. *Polymer (Guildf).* **2004**, *45* (22), 7639–7654.
(147) Fornes, T. .; Yoon, P. .; Hunter, D. .; Keskkula, H.; Paul, D. . Effect of Organoclay Structure on Nylon 6 Nanocomposite Morphology and Properties. *Polymer (Guildf).* **2002**,

43 (22), 5915–5933.
(148) Montenegro, J.; Vázquez-Vázquez, C.; Kalinin, A.; Geckeler, K. E.; Granja, J. R. Coupling of Carbon and Peptide Nanotubes. *J. Am. Chem. Soc.* **2014**, *136* (6), 2484–2491.
(149) Wang, S.; Humphreys, E. S.; Chung, S. Y.; Delduco, D. F.; Lustig, S. R.; Wang, H.; Parker, K. N.; Rizzo, N. W.; Subramoney, S.; Chiang, Y. M.; et al. Peptides with Selective Affinity for Carbon Nanotubes. *Nat. Mater.* **2003**, *2* (March), 196–200.
(150) Mittal, G.; Dhand, V.; Rhee, K. Y.; Park, S.-J.; Lee, W. R. A Review on Carbon Nanotubes and Graphene as Fillers in Reinforced Polymer Nanocomposites. *J. Ind. Eng. Chem.* **2015**, *21*, 11–25.
(151) Gravel, E.; Bernard, D.; Namboothiri, I.; Doris, E. Carbon Nanotubes and Heterogeneous Catalysis. *Actual. Chim.* **2015**, No. 393–394, 82–88.
(152) Monthioux, M.; Smith, B. W.; Burteaux, B.; Claye, A.; Fischer, J. E.; Luzzi, D. E. Sensitivity of Single-Wall Carbon Nanotubes to Chemical Processing: An Electron Microscopy Investigation. *Carbon N. Y.* **2001**, *39* (8), 1251–1272.
(153) Hirsch, A. Functionalization of Single-Walled Carbon Nanotubes. *Angew. Chemie - Int. Ed.* **2002**, *41* (11), 1853–1859.
(154) Song, K.; Zhang, Y.; Meng, J.; Green, E. C.; Tajaddod, N.; Li, H.; Minus, M. L. Structural Polymer-Based Carbon Nanotube Composite Fibers: Understanding the Processing-Structure-Performance Relationship. *Materials (Basel).* **2013**, *6* (6), 2543–2577.
(155) Zhu, J.; Kim, J. D.; Peng, H.; Margrave, J. L.; Khabashesku, V. N.; Barrera, E. V. Improving the Dispersion and Integration of Single-Walled Carbon Nanotubes in Epoxy Composites through Functionalization. *Nano Lett.* **2003**, *3* (8), 1107–1113.
(156) Liu, L.; Barber, A. H.; Nuriel, S.; Wagner, H. D. Mechanical Properties of Functionalized Single-Walled Carbon-Nanotube/ Poly(vinyl Alcohol) Nanocomposites. *Adv. Funct. Mater.* **2005**, *15* (6), 975–980.
(157) Bryning, M. B.; Milkie, D. E.; Islam, M. F.; Kikkawa, J. M.; Yodh, A. G. Thermal Conductivity and Interfacial Resistance in Single-Wall Carbon Nanotube Epoxy Composites. *Appl. Phys. Lett.* **2005**, *87* (16), 1–3.
(158) Sundararajan, P. R.; Singh, S.; Moniruzzaman, M. Surfactant-Induced Crystallization of Polycarbonate. *Macromolecules* **2004**, *37* (26), 10208–10211.
(159) Hsiao, A-E.; Tsai, S-Y.; Hsu, M-W.; Chang, S-J. Decoration of Multi-Walled Carbon Nanotubes by Polymer Wrapping and Its Application in MWCNT/polyethylene Composites. *Nanoscale Res. Lett.* **2012**, *7* (1), 240.
(160) Lee, H. W.; You, W.; Barman, S.; Hellstrom, S.; Lemieux, M. C.; Oh, J. H.; Liu, S.; Fujiwara, T.; Wang, W. M.; Chen, B.; et al. Lyotropic Liquid-Crystalline Solutions of High-Concentration Dispersions of Single-Walled Carbon Nanotubes with Conjugated Polymers. *Small* **2009**, *5* (9), 1019–1024.
(161) Hu, Z.; Patten, T.; Pelton, R.; Cranston, E. D. Synergistic Stabilization of Emulsions and Emulsion Gels with Water-Soluble Polymers and Cellulose Nanocrystals. *ACS Sustain. Chem. Eng.* **2015**, *3* (5), 1023–1031.
(162) Eyley, S.; Thielemans, W. Surface Modification of Cellulose Nanocrystals. *Nanoscale* **2014**, *6*, 7764–7779.
(163) Heux, L.; Chauve, G.; Bonini, C. Nonflocculating and Chiral-Nematic Self-Ordering of Cellulose Microcrystals Suspensions in Nonpolar Solvents. *Langmuir* **2000**, *16* (21), 8210–8212.
(164) Kedzior, S. A.; Marway, H. S.; Cranston, E. D. Tailoring Cellulose Nanocrystal and

Surfactant Behavior in Miniemulsion Polymerization. *Macromolecules* **2017**, *50* (7), 2645–2655.

(165) Ljungberg, N.; Cavaillé, J. Y.; Heux, L. Nanocomposites of Isotactic Polypropylene Reinforced with Rod-like Cellulose Whiskers. *Polymer (Guildf).* **2006**, *47* (18), 6285–6292.

(166) Kvien, I.; Tanem, B. S.; Oksman, K. Characterization of Cellulose Whiskers and Their Nanocomposites by Atomic Force and Electron Microscopy. *Biomacromolecules* **2005**, *6* (6), 3160–3165.

(167) Mariano, M.; Pilate, F.; de Oliveira, F. B.; Khelifa, F.; Dubois, P.; Raquez, J.-M.; Dufresne, A. Preparation of Cellulose Nanocrystal-Reinforced Poly(lactic Acid) Nanocomposites through Noncovalent Modification with PLLA-Based Surfactants. *ACS Omega* **2017**, *2* (6), 2678–2688.

(168) Cranston, E. D.; Gray, D. G. Morphological and Optical Characterization of Polyelectrolyte Multilayers Incorporating Nanocrystalline Cellulose. *Biomacromolecules* **2006**, *7* (9), 2522–2530.

(169) Wågberg, L. Polyelectrolyte Adsorption onto Cellulose Fibres. *Nord. Pulp Pap. Res. JournalPaper Res. J.* **2009**, *15* (5), 147–172.

(170) Nyström, G.; Marais, A.; Karabulut, E.; Wågberg, L.; Cui, Y.; Hamedi, M. M. Self-Assembled Three-Dimensional and Compressible Interdigitated Thin-Film Supercapacitors and Batteries. *Nat. Commun.* **2015**, *6* (May), 7259.

(171) Olszewska, A.; Valle-Delgado, J. J.; Nikinmaa, M.; Laine, J.; Österberg, M. Direct Measurements of Non-Ionic Attraction and Nanoscaled Lubrication in Biomimetic Composites from Nanofibrillated Cellulose and Modified Carboxymethylated Cellulose. *Nanoscale* **2013**, *5* (23), 11837–11844.

(172) Eronen, P.; Junka, K.; Laine, J.; Österberg, M. Interaction between Water-Soluble Polysaccharides and Native Nanofibrillar Cellulose Thin Films. *BioResources* **2011**, *6* (4), 4200–4217.

(173) Ahola, S.; Myllytie, P.; Österberg, M.; Teerinen, T.; Laine, J. Effect of Polymer Adsorption on Cellulose Nanofibril Water Binding Capacity and Aggregation. *BioResources* **2008**, *3*, 1315–1328.

(174) Junior de Menezes, A.; Siqueira, G.; Curvelo, A. A. S.; Dufresne, A. Extrusion and Characterization of Functionalized Cellulose Whiskers Reinforced Polyethylene Nanocomposites. *Polymer (Guildf).* **2009**, *50* (19), 4552–4563.

(175) Habibi, Y.; Dufresne, A. Highly Filled Bionanocomposites from Functionalized Polysaccharide Nanocrystals. *Biomacromolecules* **2008**, *9* (7), 1974–1980.

(176) Zoppe, J. O.; Peresin, M.; Habibi, Y.; Venditti, R.; Rojas, O. Reinforcing Poly(epsilon-Caprolactone) Nanofibers with Cellulose Nanocrystals. *Appl. Mater. Interfaces* **2009**, *1* (9), 1996–2004.

(177) Zoppe, J. O.; Habibi, Y.; Rojas, O. J.; Venditti, R. a; Johansson, L.-S.; Efimenko, K.; Österberg, M.; Laine, J. Poly(N-Isopropylacrylamide) Brushes Grafted from Cellulose Nanocrystals via Surface-Initiated Single-Electron Transfer Living Radical Polymerization. *Biomacromolecules* **2010**, *11* (10), 2683–2691.

(178) Kedzior, S. A.; Graham, L.; Moorlag, C.; Dooley, B. M.; Cranston, E. D. Poly(methyl Methacrylate)-Grafted Cellulose Nanocrystals: One-Step Synthesis, Nanocomposite Preparation, and Characterization. *Can. J. Chem. Eng.* **2016**, *94* (5), 811–822.

(179) Roeder, R. D.; Garcia-Valdez, O.; Whitney, R. A.; Champagne, P.; Cunningham, M. F.

Graft Modification of Cellulose Nanocrystals via Nitroxide-Mediated Polymerisation. *Polym. Chem.* **2016**, *7* (41), 6383–6390.

(180) Hatton, F. L.; Kedzior, S. A.; Cranston, E. D.; Carlmark, A. Grafting-from Cellulose Nanocrystals via Photoinduced Cu-Mediated Reversible-Deactivation Radical Polymerization. *Carbohydr. Polym.* **2017**, *157*, 1033–1040.

(181) Granqvist, N.; Liang, H.; Laurila, T.; Sadowski, J.; Yliperttula, M.; Viitala, T. Characterizing Ultrathin and Thick Organic Layers by Surface Plasmon Resonance Three-Wavelength and Waveguide Mode Analysis. *Langmuir* **2013**, *29* (27), 8561–8571.

(182) Allen, S. G.; Tanchak, O. M.; Quirk, A.; Raegen, A. N.; Reiter, K.; Whitney, R.; Clarke, A. J.; Lipkowski, J.; Dutcher, J. R. Surface Plasmon Resonance Imaging of the Enzymatic Degradation of Cellulose Microfibrils. *Anal. Methods* **2012**, *4* (10), 3238.

(183) Kontturi, K. S.; Kontturi, E.; Laine, J. Specific Water Uptake of Thin Films from Nanofibrillar Cellulose. *J. Mater. Chem. A* **2013**, *1* (43), 13655.

(184) Liu, Z.; Choi, H.; Gatenholm, P.; Esker, A. R. Quartz Crystal Microbalance with Dissipation Monitoring and Surface Plasmon Resonance Studies of Carboxymethyl Cellulose Adsorption onto Regenerated Cellulose Surfaces. *Langmuir* **2011**, *27* (14), 8718–8728.

(185) Marx, K. A. Quartz Crystal Microbalance: A Useful Tool for Studying Thin Polymer Films and Complex Biomolecular Systems at the Solution-Surface Interface. *Biomacromolecules* **2003**, *4* (5), 1099–1120.

(186) Aulin, C.; Varga, I.; Claesson, P. M.; Wågberg, L.; Lindström, T. Buildup of Polyelectrolyte Multilayers of Polyethyleneimine and Microfibrillated Cellulose Studied by in Situ Dual-Polarization Interferometry and Quartz Crystal Microbalance with Dissipation. *Langmuir* **2008**, *24* (6), 2509–2518.

(187) Holappa, S.; Kontturi, K. S.; Salminen, A.; Seppälä, J.; Laine, J. Adsorption of Hydrophobically End-Capped Poly(ethylene Glycol) on Cellulose. *Langmuir* **2013**, *29* (45), 13750–13759.

(188) Niinivaara, E.; Faustini, M.; Tammelin, T.; Kontturi, E. Water Vapor Uptake of Ultrathin Films of Biologically Derived Nanocrystals: Quantitative Assessment with Quartz Crystal Microbalance and Spectroscopic Ellipsometry. *Langmuir* **2015**, *31* (44), 12170–12176.

(189) Niinivaara, E.; Faustini, M.; Tammelin, T.; Kontturi, E. Mimicking the Humidity Response of the Plant Cell Wall by Using Two-Dimensional Systems: The Critical Role of Amorphous and Crystalline Polysaccharides. *Langmuir* **2016**, *32* (8), 2032–2040.

(190) Kittle, J. D.; Du, X.; Jiang, F.; Qian, C.; Heinze, T.; Roman, M.; Esker, A. R. Equilibrium Water Contents of Cellulose Films Determined via Solvent Exchange and Quartz Crystal Microbalance with Dissipation Monitoring. *Biomacromolecules* **2011**, *12* (8), 2881–2887.

(191) Cheng, G.; Liu, Z.; Murton, J. K.; Jablin, M.; Dubey, M.; Majewski, J.; Halbert, C.; Browning, J.; Ankner, J.; Akgun, B.; et al. Neutron Reflectometry and QCM-D Study of the Interaction of Cellulases with Films of Amorphous Cellulose. *Biomacromolecules* **2011**, *12* (6), 2216–2224.

(192) Ahola, S.; Turon, X.; Osterberg, M.; Laine, J.; Rojas, O. J. Enzymatic Hydrolysis of Native Cellulose Nano Brils and Other Cellulose Model Films: Effect of Surface Structure. *Langmuir* **2008**, *24* (9), 11592–11599.

(193) Q-Sense. *Quartz Crystal Microbalance with Dissipation - Technolgy Note*.

Chapter 3

Benchmarking Cellulose Nanocrystals: From the Laboratory to Industrial Production

It is well known that the cellulose source and hydrolysis conditions impact CNC properties. Therefore to form a basis from which CNC interactions can be understood, it is essential to have a "known starting material". In this first research chapter, CNCs extracted by sulfuric acid hydrolysis from the current North American industrial producers were extensively characterized. Morphology, colloidal stability, thermal stability, and surface chemistry were examined with reference to traditional laboratory extracted CNCs. This chapter provides the foundation to which CNC interactions can be compared and more specifically how these interactions can be expected to change when transitioning from CNCs produced in the laboratory to CNCs produced at the industrial scale.

In this chapter, all data were collected and analysed by myself except where technicians aided in the characterization, as described in the acknowledgements. The chapter was drafted by myself and later edited by my academic advisor, Dr. Emily Cranston. Dr. Marco Villalobos from Cabot Corporation was my industrial co-supervisor and provided input on research direction and feedback on the manuscript. This chapter and the supporting information (Appendix 3) is reprinted as it appears in *Langmuir*, with permission from the American Chemical Society © 2017.

Benchmarking Cellulose Nanocrystals: From the Laboratory to Industrial Production
Michael S. Reid, Marco Villalobos and Emily D. Cranston
Langmuir, **2017**, *33* (7), pp 1583–1598
DOI: 10.1021/acs.langmuir.6b03765

LANGMUIR

Invited Feature Article

pubs.acs.org/Langmuir

Benchmarking Cellulose Nanocrystals: From the Laboratory to Industrial Production

Michael S. Reid,[†] Marco Villalobos,[‡] and Emily D. Cranston*[,†]

[†]Department of Chemical Engineering, McMaster University Hamilton, Ontario, Canada L8S 4L8

[‡]Cabot Corporation, Billerica, Massachusetts 01821, United States

Supporting Information

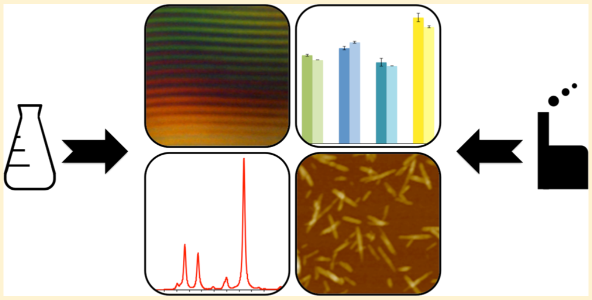

ABSTRACT: The renewability, biocompatibility, and mechanical properties of cellulose nanocrystals (CNCs) have made them an attractive material for numerous composite, biomedical, and rheological applications. However, for CNCs to shift from a laboratory curiosity to commercial applications, researchers must transition from CNCs extracted on the bench scale to material produced on an industrial scale. There are a number of companies currently producing kilogram to ton per day quantities of sulfuric acid-hydrolyzed CNCs as well as other nanocelluloses, as described herein. With the recent intensification of industrially produced CNCs and the variety of cellulose sources, hydrolysis methods, and purification procedures, the characterization of these materials becomes critical. This has further been justified by the past two decades of research that demonstrate that the CNC stability and behavior are highly dependent on the surface chemistry, surface charge density, and particle size. This work outlines key test methods that should be employed to characterize these properties to ensure a "known" starting material and consistent performance. Of the sulfuric acid-extracted CNCs examined, industrially produced material compared well with laboratory-made CNCs, exhibiting similar charge density, colloidal and thermal stability, crystallinity, morphology, and self-assembly behavior. In addition, it was observed that further purification of CNCs using Soxhlet extraction in ethanol had minimal impact on the nanoparticle properties and is unlikely to be necessary for many applications. Overall, the current standing of industrially produced CNCs is positive, suggesting that the evolution to commercial-scale applications will not be hindered by CNC production.

INTRODUCTION

In line with the growing demand for sustainable and renewable energy, the desire for "green" materials has dramatically increased over the past decade. To meet this demand, materials that take inspiration from or are directly extracted from natural resources, such as plants, mollusks, crustaceans, bacteria, and algae, have been the focus of a rapidly expanding field that seeks to include renewable materials in biomedical devices,[1] energy storage applications,[2−4] rheological modifiers,[5,6] reinforcing agents,[7−10] replacements of petroleum-based polymers,[11−14] and many other applications.[15,16] Although renewable polymeric materials (e.g., cellulose, chitin, and natural rubber) have been used for centuries, the recent "green movement" has pushed researchers to readdress many of these resources for new and innovative applications. Therefore, renewable nanomaterials make up a quickly growing field with tremendous potential. Much like other nanomaterials (e.g., graphene, carbon nanotubes, nanoclays, and metal and inorganic nanoparticles), renewable nanomaterials have high surface-area-to-volume ratios and unique nanoscale properties that are not present in macroscopic materials.[17]

As the earth's most abundant polymer, cellulose and cellulose derivatives have a long tradition in industry and have been incorporated into countless products and processes.[16] More recently, however, interest in cellulose has shifted toward nanoscale materials including cellulose nanofibrils (CNFs), bacterial nanocellulose, and cellulose nanocrystals (CNCs).[18] As first reported by Nickerson and Habrle[19] and subsequently imaged by Rånby and Ribi following the acidic hydrolysis of cotton cellulose fibers,[20] CNCs have since been extracted from a number of other natural resources including grasses, woods, algae, bacterial cellulose, and tunicate.[21] Composed of β 1−4 linked D-glucose units, linear polymer chains are arranged in a highly crystalline cellulose I structure to form high-aspect-ratio particles that are insoluble in but strongly bind water[22] and, depending on the source and extraction procedure, range from 50 to 3000 nm in length with cross sections of 3−20 nm.[23] The literature commonly presents CNCs as reinforcing agents in nanocomposites, rheological modifiers/stabilizers, and additives in biomedical devices; these and many other applications are described in a number of comprehensive review papers.[9,18,23−29] In addition to their high aspect ratio and large surface area, CNCs

Received: October 15, 2016
Revised: November 23, 2016
Published: December 1, 2016

DOI: 10.1021/acs.langmuir.6b03765
Langmuir 2017, 33, 1583−1598

have unique physical properties, such as their ability to self-assemble into chiral nematic liquid-crystalline phases,[30−33] align in magnetic[34−39] and electric fields,[40−42] and exhibit piezo-electric reponsivity.[43]

Our work on CNCs has primarily focused on developing hybrid nanomaterials such as films, aerogels, and liquid formulated products. We often play on the synergy between autoadhering polymers and surfactants with CNCs, which enables superior stabilization and enhanced mechanical properties in emulsions, gels, and foams.[6,44−50] The surface-modification routes we have developed are water-based and scalable, leading to, for example, hydrophobic, responsive, biomimetic, and cross-linkable CNCs.[51−55] Although we have targeted advanced applications such as industrial coatings,[56,57] tissue scaffolds,[6,48,50] energy storage,[2,58] water purification,[59] and food and cosmetics,[44−47] we remain committed to the thorough characterization of CNC particles and interfaces. This has included the characterization of chemical, physical, mechanical, and self-assembly properties[34,52,60−62] as well as the development of new methods to predict and assess CNC dispersions.[63,64]

Although CNCs have been extracted from a wide variety of natural cellulose sources using numerous methods,[65] CNCs obtained via sulfuric acid hydrolysis from cotton or wood have been the primary focus of both academia and industry. Commonly, CNCs are extracted by exposing cellulose to strong sulfuric acid (~64 wt %), which favorably hydrolyzes accessible disordered regions, leaving highly ordered cellulose in the form of rod-shaped particles. The strong acid hydrolysis additionally grafts anionic sulfate half esters (OSO_3^-) to the CNC surface, which electrostatically stabilize CNCs in aqueous environments. Significant research has focused on understanding and optimizing CNC extraction, and it has been found that changes to the hydrolysis conditions can greatly affect the particle dimensions, surface charge density, and overall CNC yield.[66,67]

For example, Dong et al. observed that higher temperatures and longer reaction times of hydrolysis of microcrystalline cellulose produced shorter CNCs with low aspect ratios.[68] Similarly, Beck et al. demonstrated that shorter, less polydisperse CNCs were produced from softwood pulps using longer hydrolysis times and increased acid-to-pulp ratios.[69] More recently, Dong et al. studied the yield and sulfate half ester group density of CNCs extracted from softwood pulp by analyzing the acid concentration, hydrolysis temperature, and hydrolysis time using a rotatable central composite experimental design.[70] High acid concentrations (>65 wt %) were found to produce CNCs with a sulfate half ester content upwards of 391 mmol/kg CNCs but at a significantly reduced yield (<20%). A maximum CNC yield of 66−69% with a sulfate half ester content of 241−265 mmol/kg CNC was achieved using 57−58 wt % sulfuric acid at 64−67 °C for 134−156 min.[70] This is in excellent agreement with Wang et al. and Chen et al., who obtained similar results upon extracting CNCs from bleached Kraft eucalyptus pulp.[67,71]

In addition to CNC dimensions, yield, and sulfate half ester content, a recent publication by Bouchard et al. demonstrated that the hydrolysis temperature significantly alters the by-products produced during hydrolysis and, in turn, the CNC surface.[72] CNCs extracted from bleached softwood pulp at 45 °C in 64 wt % sulfuric acid for 25 min were observed to contain nearly 12% by mass oligosaccharides that precipitate onto the CNC surface during the water quenching step of the hydrolysis reaction. These oligosaccharides, with a degree of polymerization of between 7 and 20, significantly alter the rheological, colloidal, and optical properties of the CNCs. Increasing the reaction temperature to 65 °C reduced the degree of polymerization of oligosaccharide byproducts such that they remain soluble (and thus do not precipitate on CNC surfaces) following hydrolysis. CNCs produced without oligosaccharide layers were observed to be more viscous and less colloidally stable in high-ionic-strength environments. These studies emphasize that a thorough understanding of CNC properties prior to use is critical because differences in the particle dimension and charge density can greatly affect the rheological,[73] colloidal,[74] interfacial,[75] and reinforcing properties.[76]

Along with the hydrolysis conditions, postextraction treatments such as sonication and purification can further impact the CNC properties and behavior. Beck et al. showed that the pitch of the chiral nematic phases could be controlled by varying the amount of sonication applied to CNC dispersions.[77] High-energy input was observed to increase the pitch of the chiral nematic phase and alter the reflected wavelength of dried CNC films. Similarly, Shafiei-Sabet et al. demonstrated that sonication reduced the shear viscosity of CNC dispersions at low shear rates by nearly 2 orders of magnitude.[78] Interestingly, the viscosity at high shear rates was largely unaffected by sonication. Changes to both the rheological and chiral nematic behavior are currently not fully understood but are suggested to result from the liberation of excess charged ions from the particle surface following sonication or from the precipitated oligosaccharide layer. This liberation alters the electrostatic repulsion between particles and thus the rheological behavior and self-assembly.[72]

The influence of postextraction treatment was further demonstrated by Labet and Thielemans, who showed that additional purification was needed to achieve consistent results when grafting polymers onto CNC surfaces.[79] Soxhlet extraction of freeze-dried CNCs in ethanol for 24 h improved not only the grafting density of ε-caprolactone by surface-initiated ring opening polymerization but also the reproducibility. It is proposed that Soxhlet extraction removes small molecules, including xylobiose, 1,6-anhydroglucose and vanillic acid, as well as low-molecular-weight oligosaccharides, such as those observed by Bouchard et al.,[72] that precipitate onto the CNC surface during hydrolysis while leaving the bulk of the CNC structure intact.[79] It is unclear, however, to what degree byproducts can be removed via Soxhlet extraction because the solubility of oligosaccharides decreases in ethanol and thus would remain on the particle surface.[80] Furthermore, recent molecular dynamic simulations demonstrate that oligosaccharides strongly bind to crystalline cellulose surfaces[81] and that following sonication, oligosaccharides remain on the CNC surface.[72]

The various hydrolysis conditions, postextraction treatments, and diversity of cellulose starting material highlight the need for the thorough characterization of CNCs prior to use. Additionally, it is critical that the community as a whole recognizes that CNCs produced from various sources and methods do not have the same properties and behavior. (Note that this work does not investigate CNFs. There are many industrial producers in North America, Europe, and Japan,[82,83] but comparing their materials is beyond the scope of this study.) This is particularly important because over the past decade researchers have begun to transition from CNCs traditionally made in the laboratory on the bench scale to CNCs that have been produced industrially. Ultimately, this transition must occur if commercial applications of CNCs are to be realized. To date, there has yet to be a thorough comparison of CNCs produced on the bench scale to CNCs produced commercially. Largely, CNCs produced commercially operate using proprietary technology, and often the exact cellulose source, extraction process, and purification are not entirely evident. Furthermore, as new producers enter the market and as extraction processes and cellulose sources of current producers change, there is a potential for batch-to-batch variability, which must be understood. The Canadian Standards Association has outlined test methods for assessing cellulosic nanomaterial properties, and current standards and nomenclature guidelines are in preparation by ISO and TAPPI; however, there is yet to be a direct comparison between industrial- and laboratory-scale CNCs.[84] Therefore, as the CNC community grows and industrially produced material becomes more prevalent, essential questions may be asked:

(1) Are CNCs from various producers equivalent?
(2) What are the most practical characterization methods that should be employed prior to using CNCs?
(3) When is further purification, such as Soxhlet extraction, required?
(4) If producers change the scale or starting material, what kind of changes can be expected?

Herein, we present the first detailed comparison of CNCs extracted by sulfuric acid hydrolysis on the bench scale to those produced commercially. We seek to thoroughly characterize currently available industrially produced CNCs and present the most practical methods and procedures for assessing particle dimensions, thermal and colloidal stability, and charge density such that researchers can have a known starting material prior to including CNCs in products. Additionally, we investigate how Soxhlet extraction, as a purification method, alters the CNC properties in comparison to those of the as-received material. We present clear experimental details and procedures such that new researchers and students can confidently prepare and use CNCs.

■ EXPERIMENTAL SECTION

Materials. Whatman cotton ashless filter aid was purchased from GE Healthcare Canada. Sulfuric acid was obtained from Caledon Laboratory Chemicals (Georgetown, ON, Canada). Anhydrous ethanol was purchased from Commercial Alcohols (Brampton, ON, Canada). Hydrogen peroxide and Whatman glass microfiber extraction thimbles were purchased from Sigma-Aldrich (Oakville, ON, Canada). Poly(allylamine hydrochloride) (PAH, M_w = 120 000−200 000 g/mol) was purchased from Polysciences. All chemicals were used as received. The water used was purified type I water with a resistivity of 18.2 MΩ·cm (Barnstead NANOpure DIamond system, ThermoScientific, Asheville, NC).

CNC Samples. The CNCs investigated in this work were obtained from current industrial producers of sulfuric acid-extracted CNCs operating on various industrial scales: CelluForce, Alberta Innovates Technology Futures (AITF), and the U.S. Department of Agriculture (USDA) Forest Products Laboratories (FPL) (supplied by the University of Maine) and compared to CNCs produced in our laboratory. Additionally, nanocelluloses produced by less conventional methods from American Process Inc. and Blue Goose Biorefineries were obtained and investigated to compare with traditional CNCs. All sulfuric acid-extracted CNCs samples were received in sodium form as either spray dried or freeze-dried powders or as concentrated dispersions.

CelluForce. CelluForce, the world's largest producer of CNCs with a 1 ton/day capacity, uses traditional 64 wt % sulfuric acid hydrolysis (pioneered by Dr. Derek Gray's group at McGill University and scaled up at FPInnovations, Pointe Claire, QC, Canada) to produce CNCs from bleached Kraft pulp.[31,37,68,85] Following hydrolysis CNCs are diluted, separated from residual acid, and neutralized to sodium form and spray dried.

USDA Forest Products Laboratory (FPL). CNCs are produced from strip-cut dissolving pulp via 64 wt % sulfuric acid hydrolysis for 60 min at 45 °C in an oxygen-free atmosphere in the Madison, WI pilot facility with a 10 kg/day capacity. Following hydrolysis, CNCs are diluted with reverse osmosis water and sodium chlorite is added to remove color. Finally, the acid is neutralized by the addition of sodium hydroxide. Material is fractionated and concentrated using a 20 μm membrane and sold as freeze-dried, spray-dried powders, or a dispersion.[86] The material investigated in this work was received as a 10 wt % dispersion.

Alberta Innovates Technology Futures (AITF). To investigate how changing the cellulose source and scale of production effects industrially produced CNC properties, CNCs from two different cellulose sources, cotton and wood, were supplied by AITF. Cotton-sourced CNCs were produced at a g/day capacity via traditional sulfuric acid hydrolysis and received as a freeze-dried powder (labeled AITF). Wood-based CNCs were produced on a pilot scale (kg/day capacity) from softwood dissolving pulp using 63.5 wt % sulfuric acid hydrolysis at 45 °C for 2 h. The hydrolysis was quenched with reverse osmosis water, and CNCs were neutralized to sodium form using NaOH. Samples were received in a 1.1 wt % dispersion.

Other Nanocelluloses. These materials are not strictly considered to be CNC or CNF according to the published CSA Standard[84] (and TAPPI/ISO Standards that are currently in preparation), although they possess some favorable properties of both. These nanocelluloses produced by alternative methods to the typical sulfuric acid-hydrolyzed CNCs were investigated. Although there are a number of companies selling other nanocelluloses online, we have chosen only two relatively large-scale producers of nanocellulose as a demonstration of what non-sulfuric acid-hydrolyzed CNCs may look like. This benchmarking study does not include bacterial cellulose or CNF, despite their widespread production; the same concerns exist for these materials as for CNCs but are not addressed here.

American Process Inc. American Process Inc. (API) operates a pilot-scale facility using a proprietary method called AVAP that uses SO_2 and ethanol along with mechanical treatment to liberate both CNFs and CNCs from a variety of biomass sources.[87,88] BioPlus Crystals were purchased as a 6 wt % aqueous gel and used as received.

Blue Goose Biorefineries. Blue Goose Biorefineries Inc. uses a transition-metal-catalyzed oxidative method to produce cellulose nanocrystals from a variety of biomass sources.[89] The product tested for this study is BGB Natural received as a 7.4 wt % aqueous gel. This has a mixture of fibrillar cellulose and nanomaterial. Blue Goose has since introduced a new product, BGB Ultra, that is claimed to have a more similar size distribution and crystallinity to acid-hydrolyzed CNCs but with carboxyl functional groups instead of sulfate half esters. BGB Ultra was not evaluated in this study.

Lab-Made Cellulose Nanocrystal Preparation. CNCs (denoted lab-made in the subsequent text) were prepared in the laboratory by sulfuric acid hydrolysis, as previously described.[56] Cotton Whatman ashless filter aid (40 g) was processed in 700 mL of 64 wt % sulfuric acid at 45 °C for 45 min under continuous mechanical stirring. Following hydrolysis, the reaction was quenched by 10-fold dilution with 4 °C water, and excess acid was removed by multiple rinsing and centrifugation steps. The precipitate was then diluted and dialyzed against purified water until the pH of the water from successive washes stabilized between 5 and 6 (~2 weeks). The suspension was probe sonicated (Sonifier 450, Branson Ultrasonics, Danbury, CT) continuously in an ice bath for 15 min three times at 60% output. The CNC suspensions were filtered through Whatman glass fiber filter paper and neutralized (converted to the sodium salt form) by the addition of a calculated amount of 1 mM NaOH (based on condutometric titrations). Prior to further characterization and processing, all nanocellulose material, lab-made and received from industry, was redispersed in water and lyophilized to prevent any change to the sulfate half-ester content.[90] For all subsequent analysis, CNCs were redispersed and thoroughly sonicated as needed.

Soxhlet Extraction. Cellulose material was purified via Soxhlet extraction as outlined by Labet and Thielemans.[79] Glass microfiber thimbles were soaked in 95% ethanol between 3 and 5 h and dried at 80 °C prior to extraction. Freeze-dried CNCs (ca. 0.5 g) were placed in glass microfiber extraction thimbles and Soxhlet extracted with anhydrous ethanol for 24 h. Following extraction, the material was dried at 80 °C overnight and stored over a desiccant.

Conductometric Titration. The sulfate half-ester content and thus indirectly surface charge were measured by conductometric titrations as outlined previously.[91,92] Critically, conductometric titrations must be performed on CNCs in acid form ($-OSO_3H$), and thus lab-made and industrially produced CNCs (in sodium form, $-OSO_3Na$) were treated with ion-exchange resin as outlined by Beck et al.[92] CNC dispersions (20−50 mL of ca. 0.5 wt %) were prepared by redispersing and thoroughly sonicating both as-received and Soxhlet-extracted freeze-dried CNCs. Dispersions were then passed through a 1.9 cm inner diameter glass fritted column containing 15 cm of thoroughly rinsed (>1000 mL water) Dowex Marathon C hydrogen form strong acid cation exchange resin. Between CNC samples, the column was rinsed with 300 mL of water to remove residual cellulose material. On the basis of the average $-OSO_3^-$ content of 251 mmol/kg CNC (as determined by conductometric titration), a maximum exchange of 0.5 mequiv of Na^+ ions to H^+ ions was determined for the complete set of samples. This corresponds to less than 2% of the total ion exchange capacity of the column (40.6 mequiv). Following ion exchange, conductometric titrations were performed by a diluting 2.5−5 mL dispersion of ca. 0.5 wt % CNCs in 80 mL in water. One milliliter of 100 mM NaCl solution was added to increase the conductivity to a measurable range. The conductivity and pH were continuously measured throughout the titration, and 100 μL aliquots of standardized 2 mM NaOH were added over a period of 30−45 min. The volume-corrected conductivity was plotted, from which the equivalence point was determined by the intersection of least-squares regressions from the positively and negatively sloped regions. A representative curve is presented in Figure 1. Samples were measured in triplicate, and the standard deviation is presented as the confidence interval.

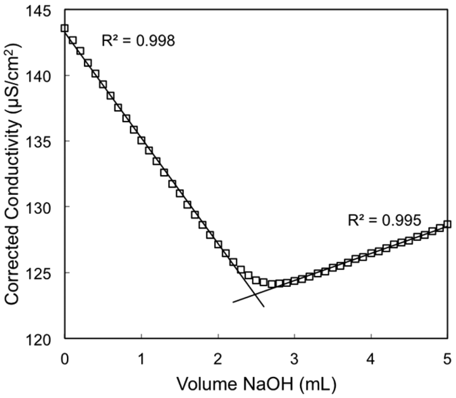

Figure 1. Representative conductometric titration curve of CNCs with NaOH showing the graphical determination of the equivalence point.

Zeta Potential. The zeta potential (related to surface potential and colloidal stability) of CNC samples was measured by assuming Smoluchowski behavior using a ZetaPlus electrophoretic mobility analyzer (Brookhaven Instruments Corp.). Note that some salt addition is necessary to get an accurate zeta potential measurement such that the double-layer thickness around CNCs is not infinite and suspensions that are unstable by eye (such as hydrophobically modified CNCs in water) will not give meaningful zeta potential readings. CNC dispersions of 0.25 wt % in 10 mM NaCl were prepared at 25 °C, and each sample was measured a total of 10 times, with each measurement composed of 15 cycles. The confidence interval (error) presented is the standard deviation of samples measured in triplicate.

Dynamic Light Scattering. The hydrodynamic apparent particle size was measured for 0.025 wt % CNC dispersions using a Malvern Zetasizer Nano particle analyzer at 20 °C (no salt added). Note that if DLS measurements are made on less concentrated samples then multiple peaks and inaccurate data may appear because of the low scattering count but that at higher concentrations particle agglomeration is promoted, which may lead to larger apparent particle sizes. Each sample was measured 15 times, and the average particle size distribution was obtained. The number average of each particle distribution was calculated, and the confidence interval presented is the standard deviation of three separate samples.

X-ray Diffraction. XRD measurements, to obtain the degree of crystallinity, were performed on freeze-dried CNCs samples using a Bruker D8 Davinci diffractometer (Bruker, USA) with a cobalt sealed tube source (λ_{avg} = 1.79026 Å), 35 kV, 45 mA with a parallel focus Goebel Mirror, Vantec 500 area detector, and 0.5 mm microslit and 0.5 mm short collimator over a 2θ range of 8−45°. Si wafer blanks were subtracted from all sample measurements. Two-dimensional area detector frames were integrated to produce diffraction patterns, which then underwent Rietveld refinement. The percent crystallinity was determined by deconvolution using the cellulose I single crystal information file (CIF) to define the peak position and a fixed amorphous peak at 24.1°. A pseudo-Voigt function with a linear background was used to fit the peak shape, and the CIF file with a March Dollase preferred orientation function model was used to fit the peak intensity. For samples that contained both cellulose I and cellulose II, the percentage of each crystal phase is presented. It is important to note that there are a number of methods described in the literature used to determine the crystallinity of cellulose and that the method used is not limited to XRD.[93−96] Furthermore, the validity and limitations of these methods and data-fitting routines are hotly debated topics that are beyond the scope of this work. Mainly XRD is reported, and the Rietveld refinement is commonly considered to be the most accurate method.[97] In a recent publication, however, Ahvenainen et al. found a good correlation with the five most common XRD fitting methods and the two-dimensional Rietveld method.[98] Moreover, within their work it is emphasized that comparison between samples and laboratories is extremely challenging. As such, the crystallinity values presented here should be taken as relative (and comparable within this study), not absolute. Using the deconvolution method presented above, we take the error in these measurements to be 3−5%.

X-ray Photoelectron Spectroscopy. XPS spectra were collected to assess the surface elemental analysis of CNCs using a Physical Electronics (PHI) Quantera II spectrometer equipped with a monochromatic Al Kα X-ray (1486.7 eV) source operated at 50 W and 15 kV. The system base pressure was no higher than 1.0×10^{-9} Torr, with an operating pressure that did not exceed 2.0×10^{-8} Torr. A pass energy of 280 eV was used to obtain all survey spectra; 26 eV was used for carbon high-resolution data, and 55 eV was used for all other high-resolution data. High-resolution C spectra allow for a distinction among the various bonding environments of carbon atoms within the sample. Excluding hydrogen, the carbon bonding environments within cellulose are carbon bound to solely carbon via single bonds, C−C (C1), carbon bound to oxygen via a single bond C−O (C2), and carbon bound to two oxygens via single bonds O−C−O (C3).

All spectra were obtained at a 45° take-off angle, and a dual-beam charge compensation system was used for the neutralization of all samples. The instrument was calibrated using a sputter-cleaned Ag surface, where the Ag $3d_{5/2}$ peak had a binding energy of 368.3 ± 0.1 eV and the full width at half-maximum for the Ag $3d_{5/2}$ peak was at least 0.52 eV. Data manipulation was performed using PHI MultiPak version 9.4.0.7 software. Measurements were performed on freeze-dried material adhered to an aluminum alloy substrate with double-sided tape.

Atomic Force Microscopy. AFM was used to measure the dimensions of CNCs and calculate the size polydispersity. Submonolayer CNC films were prepared on polished silicon wafers (MEMC Electronic Materials Sdn Bhd, Petaling Jaya, Malaysia) by spin coating 0.01 wt % CNC suspensions under N_2 gas (G3P spin-coater, Specialty Coating Systems Inc., Indianapolis, IN, USA) at 4000 rpm for 30 s with a 7 s acceleration ramp. Silicon substrates were cleaned in piranha solution (3:1 concentrated sulfuric acid/hydrogen peroxide) for 30 min, followed by continuous rinsing with purified water and drying with N_2 gas. Suspensions of 0.01 wt % were prepared by dispersing freeze-dried CNCs in water and sonicating at 60% amplitude for 30 s. To reduce the CNC aggregation on the surface, silicon substrates were spin coated

DOI: 10.1021/acs.langmuir.6b03765
Langmuir 2017, 33, 1583−1598

with a precursor layer of 0.1 wt % cationic PAH solution and rinsed (by spin-coating water) prior to CNC deposition.

AFM images were collected in alternating current (ac) mode using an Asylum MFP-3D instrument (Asylum Research, an Oxford Instrument Company, Santa Barbara, CA, USA). Images were collected in air under ambient conditions using rectangular FMR cantilevers (NanoWorld) with normal spring constants of 1.2−5.5 N/m and resonance frequencies of 60−90 kHz. Images were processed in Igor Pro 6.0 running Asylum Research AFM software (version 13.17) using a second-order flattening routine. CNC dimensions presented (cross section and length) were obtained from the analysis of a minimum of 100 particles. Confidence intervals presented are the standard deviation of the average particle dimensions measured.

Thermal Gravimetric Analysis. Thermal gravimetric analysis (TGA) was performed using a TA Instruments Q50 thermal analyzer under a constant 100 mL/min argon flow. A minimum of 1 mg of freeze-dried as-received and Soxhlet-extracted CNCs was heated to 600 °C at a heating rate of 10 °C/min.

Liquid-Crystalline Self-Assembly. The phase separation of CNC suspensions above a critical concentration of ca. 4.5 wt % into a lower chiral nematic liquid-crystalline phase and an upper isotropic phase has been well documented and furthermore implies well-dispersed individualized CNCs.[30,37,68,99] To test for this behavior, 50 mL of 1 wt % CNC suspensions was prepared from freeze-dried as-received material. Samples were thoroughly sonicated and filtered through glass microfiber filter paper and allowed to gently evaporate to ca. 5 mL with constant stirring under ambient conditions (ca. 1 week). Samples were transferred to flat capillary tubes (inner dimensions 10 × 1 mm^2) and allowed to reach equilibrium over 30 days. Photographs were taken between crossed polarizers to demonstrate phase separation. The chiral nematic texture of the anisotropic phase was imaged by polarized optical microscopy at 10-fold magnification using a Nikon Eclipse LV100POL microscope.

■ RESULTS

The CNC behavior depends on the surface charge density, crystallinity, and particle dimensions. Understanding and characterizing CNC properties is critical because the cellulose source, hydrolysis conditions, and postextraction treatment impact these properties and ultimately determine suitable applications for CNCs. As the CNC community expands, thorough characterization is crucial, particularly because industrially produced CNCs, which use proprietary technology, are beginning to replace traditionally laboratory-made CNCs. Below we compare the properties of sulfuric acid-extracted CNCs produced industrially and on the laboratory scale. Furthermore, we explore the effect of Soxhlet extraction and present the most practical methods to assess the surface charge density, colloidal and thermal stability, particle dimensions, and crystallinity.

Sulfate Half-Ester Content. The sulfate half-ester (OSO_3^-) content of CNCs extracted by sulfuric acid hydrolysis was measured by conductometric titration following dialysis and strong acid ion-exchange resin treatment; the values ranged from 206 to 335 mmol/kg of CNC in agreement with the literature,[92] as presented in Figure 2. This corresponds to 0.66−1.1 %S and 0.37−0.61 charges/nm^2 or about 1 sulfate half-ester for every 2 to 3 surface anhydroglucose units, assuming the dimensions of lab-made CNCs reported below. The broad range of OSO_3^- contents of CNCs extracted from the same process highlights the need for the careful characterization of all material prior to use. Following Soxhlet extraction in ethanol for 24 h, only minor changes in OSO_3^- content were observed, with the largest change being a 7.5% decrease in surface charge measured for FPL CNCs. Interestingly, the sulfate content increased for CNCs from CelluForce whereas it decreased for lab-made, AITF, and FPL CNCs. Because Soxhlet extraction is thought to remove residual oligomers from the particle surface and other hydrocarbon impurities,[79] formerly inaccessible OSO_3^- groups may become accessible and increase the apparent sulfate half-ester content. Conversely, if the adsorbed oligomers themselves are sulfated (which is likely), then removal would decrease the overall sulfate half-ester content.

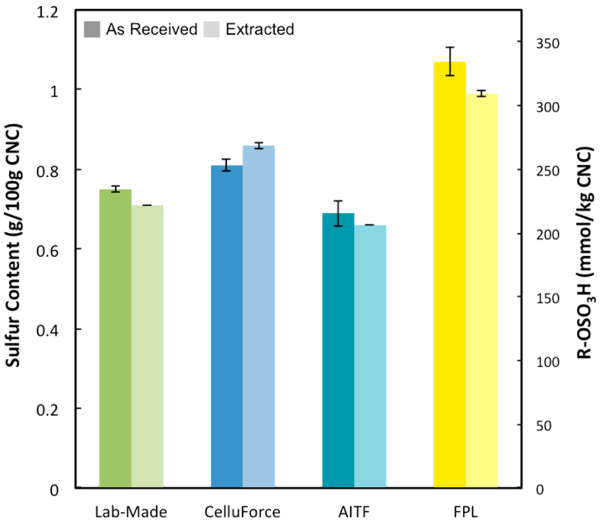

Figure 2. Sulfur content (left axis) and sulfate half-ester content (right axis) for CNCs as received (which in this case includes dialysis and ion-exchange resin treatment) and after Soxhlet extraction, as determined by conductometric titration.

Colloidal Stability. The colloidal stability of laboratory and industrially produced CNCs was assessed by zeta potential calculations from electrophoretic mobility measurements. CNCs are well known to be electrostatically stabilized by anionic sulfate half-ester groups grafted to the particle surface, and thus measuring the zeta potential provides significant insight into the behavior of CNCs in aqueous environments. Moreover, following CNC surface modification, the zeta potential is one of the primary tools used to measure the degree of modification, particularly with polymer grafting. A reduction in the (absolute value of the) potential is attributed to modification either at the ester group or other OH groups, which makes OSO_3^- groups less accessible.[46,52] Figure 3 presents the zeta potential of Na^+ form CNCs as received and following Soxhlet extraction. It is important to note that when calculating the zeta potential using the Smoluchowski or Hückel equation that assumptions are made about particle shape and behavior in an electric field. It is perhaps more accurate to report the electrophoretic mobility; however, the zeta potential is most often presented in the literature and thus is reported here. All CNCs display zeta potential values of less than −35 mV, which is significantly less than −20 mV, typically assumed to be the maximum (negative value) required for moderate colloidal stability.[100] Following Soxhlet extraction, CNCs remain stable and only a small (<5 mV) increase is observed for lab-made, AITF, and FPL CNCs. This small increase in the zeta potential corroborates well with the small decrease in the sulfate half-ester content by conductometric titration.

Particle Size and Morphology. A significant portion of particle behavior can be attributed to particle shape and morphology. For example, CNCs are ideal reinforcing materials

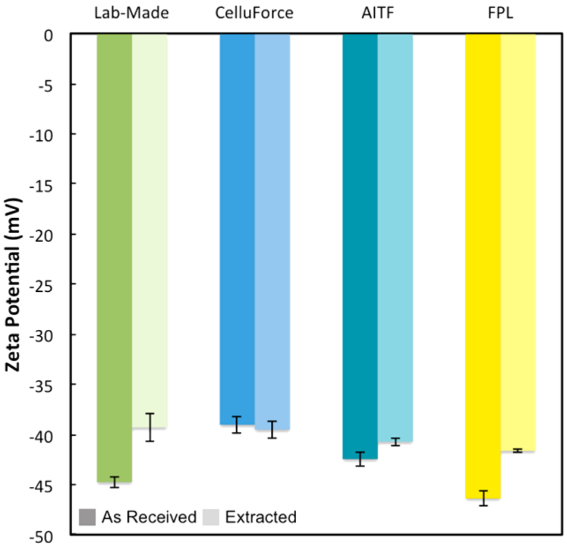

Figure 3. Zeta potential for as-received and Soxhlet-extracted CNCs in a 0.25 wt % dispersion with 10 mM NaCl.

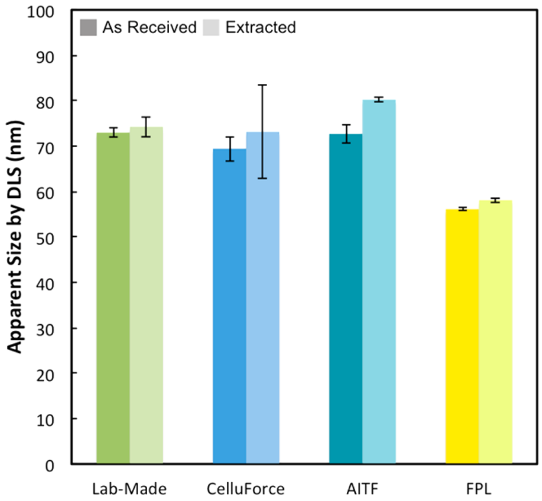

Figure 4. Apparent particle size as determined by DLS for as-received and Soxhlet-extracted CNCs in a 0.025 wt % dispersion.

because high-aspect-ratio particles reduce the volume percentage required to reach the percolation threshold.[101] Similarly, shear thinning behavior results from the high-aspect-ratio particles aligning with flow.[78] Figure 4 presents the apparent particle size of Na^+-form CNCs before and after Soxhlet extraction. Critically, DLS monitors the scattering intensity from particles undergoing Brownian motion and determines the particle size via the Stokes−Einstein relation. However, the Stokes−Einstein relation assumes that the diffusion coefficient is constant, which is not the case for rod-shaped particles such as CNCs because the diffusion constants perpendicular and parallel to the particle axis differ. As a result, particle sizes measured by DLS are not absolute. Nonetheless, DLS is an effective tool for measuring relative particle sizes and the state of dispersion of particles (if the same instrument, sample preparation, and protocol are used).

Figure 4 shows that CNCs from the various producers range in apparent particle diameter from 55 to 85 nm. Particle sizes of less than 100 nm are typical of CNCs measured by DLS and result from the assumptions discussed above.[102] Largely, particle size did not significantly change following Soxhlet extraction, with the only statistical difference observed for AITF CNCs. The increased particle size observed for AITF CNCs is likely due to particle agglomeration during Soxhlet extraction because no swelling is expected to occur.[103] Exposing CNCs to unsuitable solvents forces CNCs to strongly aggregate and increase the number of cohesive particle−particle interactions.[63] Potentially, sonication following Soxhlet extraction was insufficient to completely redisperse CNCs, resulting in CNCs with larger apparent sizes.

Although DLS provides an assessment of the relative particle size and colloidal stability, particle dimensions are more appropriately measured by microscopy, specifically transmission electron microscopy (TEM) or AFM (or a combination of DLS and microscopy[102]). Both microscopy techniques require significantly more time and sample preparation than DLS, yet the length and cross section of individual CNCs can be measured directly and meaningful statistical data can be obtained.[104,105] Figure 5 displays representative 5 μm × 5 μm AFM images of CNCs from each producer from which rod-shaped, high-aspect-ratio particles are visible. No evidence of macroscopic material was observed in any CNC samples.

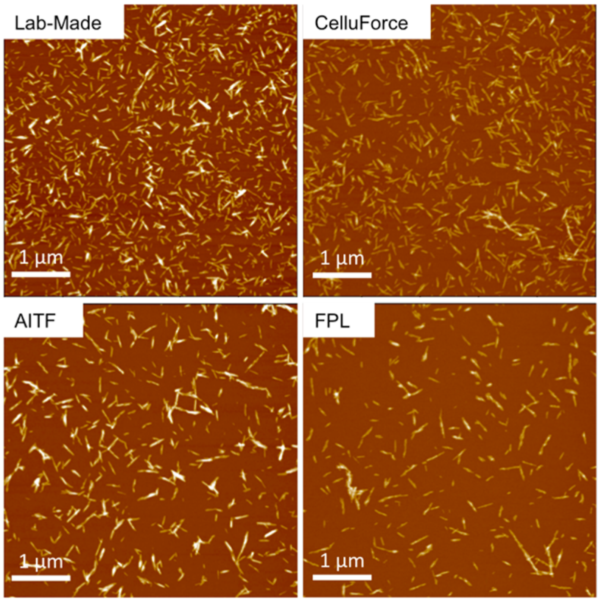

Figure 5. AFM height images of as-received CNCs from various producers.

CNC dimensions were determined by selectively measuring the length and cross section of a minimum of 100 individual particles. No particle below 20 nm was measured because tip effects convolute particle dimensions (Figure 6).[106] Similarly, aggregated CNCs were not measured because the exact boundaries of individual CNCs could not be distinguished. Finally, the cross section of the CNCs is taken as the height of the CNC in the center of the particle to avoid tip-broadening effects. The average values, including the aspect ratio, are presented in Table 1. All CNC samples exhibit a relatively narrow distribution of lengths, with the majority of particles between 100 and 200 nm. CelluForce CNCs shows the widest distribution with

DOI: 10.1021/acs.langmuir.6b03765
Langmuir 2017, 33, 1583−1598

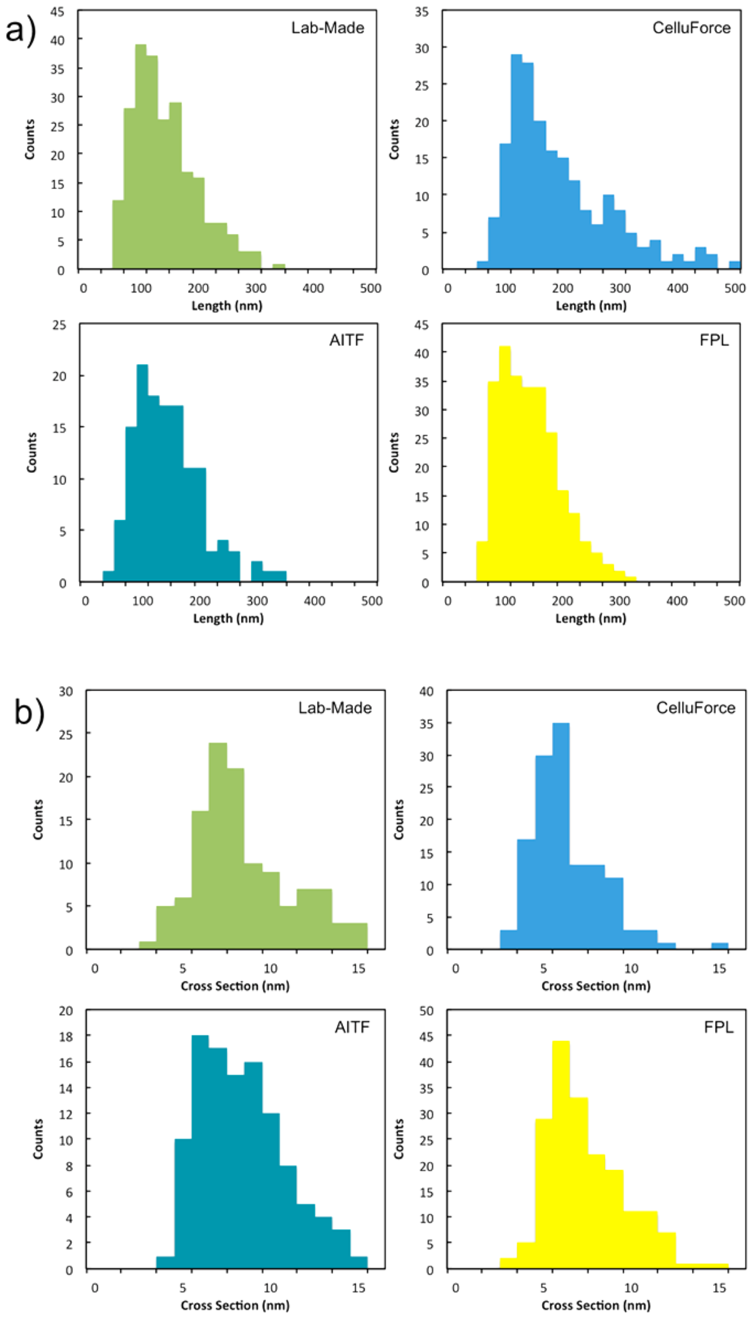

Figure 6. Particle length (a) and cross-section (b) distributions of CNCs from various producers as measured by AFM.

Table 1. Average Length, Cross Section, and Aspect Ratios of CNCs As Measured by AFM

	length (nm)	cross section (nm)	aspect ratio
lab-made	132 ± 55	8 ± 3	16
CelluForce	183 ± 88	6 ± 2	31
AITF	134 ± 56	8 ± 2	17
FPL	134 ± 52	7 ± 2	19

particles that range from 60 to 500 nm in length. Surprisingly, the length and cross section of CNCs produced by lab-made, AITF, CelluForce, and FPL were statistically equivalent, yet the apparent size measured by DLS suggested that FPL CNCs were smaller. This emphasizes the need to completely characterize all CNCs prior to use and that no single characterization method can truly access the particle behavior and properties. The cross-sectional analysis of the CNCs has a comparable distribution; however, the CNCs produced from wood sources (CelluForce and FPL) have slightly narrower particles leading to larger average aspect ratios, as expected.[69]

Crystallinity. The crystallinity of each CNC sample was assessed by XRD and is presented in Table 2. Representative diffraction patterns are located in the Supporting Information (Figures S1−S4). We again note that the appropriate method for

Table 2. Percent Crystallinity As Determined by XRD of CNCs As Received and after Soxhlet Extraction

	as received		Soxhlet extracted	
cellulose structure	I	II	I	II
lab-made	93.4		91.4	
CelluForce	89.9		88.7	
AITF	91.2		91.8	
FPL	53.9	46.1	74.2	25.8

determining the crystallinity of CNCs is a debated topic and that the values presented here are relative. CNCs from lab-made, CelluForce, and AITF exhibited purely cellulose I structure with total crystallinity ranging from 88 to 94%, in reasonable agreement with the literature.[23,51] Uniquely, CNCs from FPL could not be fit solely to cellulose I structure, consistent with previous studies,[107] and thus cellulose II was included to determine the percentage of each polymorph. The resulting fits show that FPL CNCs contain nearly equal percentages of cellulose I and cellulose II. Currently, it is unclear why FPL CNCs contain a significant portion of cellulose II; it could be present in the starting material, or it could result from exposure to high concentrations of NaOH prior to or following hydrolysis. Concentrated NaOH is known to dissolve cellulose I, such as in mercerization,[108] and the resulting dissolved cellulose polymer can precipitate onto the CNC surface in the more thermodynamically favorable structure of cellulose II. No significant change in crystallinity following Soxhlet extraction was observed for CNCs containing solely cellulose I, which is to be expected because cellulose I does not swell or dissolve in ethanol.[63] Conversely, FPL CNCs show a significant change in polymorph composition, with the percentage of cellulose I being nearly 3 times greater than the percentage of cellulose II after Soxhlet extraction and suggesting that a portion of loosely bound material, which potentially contains cellulose II, was lost.

Chemical Composition. The chemical composition of the CNCs was analyzed using XPS. Although cellulose was one of the early surfaces probed by XPS (formally referred to as ESCA[109]), the ability to quantify each type of carbon without contamination obscuring the results remains challenging.[110] Theoretically, cellulose is an excellent material for analysis because it contains only oxygen and carbon in an O/C ratio of 0.83. Furthermore, all carbon is bound to at least one oxygen, and thus only C2 and C3 should be present; see the Experimental Section for a description of carbon-type labels.[111] However, C1 carbon (C−C−C or C−C−H) is notoriously difficult to remove and is nearly always present in all measurements, even on clean gold surfaces.[112] Largely attributed to hydrocarbon contamination, clean cellulose sources contain 5−7% C1 carbon, making an absolute comparison of cellulose carbon content extremely difficult, particularly among different research laboratories and equipment. The problem is further amplified by the sample inhomogeneity, charging, and degradation/redeposition of degraded products during measurements. Nonetheless, XPS is a useful technique in determining relative changes at the particle surface, particularly when modifications contain noncarbon elements.[113] More recently, Labet and Thielmans used XPS to characterize CNCs before and after Soxhlet extraction in an effort to improve the reproducibility of CNC surface modification.[79] The quantity of C1 was used as a measure of noncellulosic material on the CNC surface. Although C1 contamination from the environment makes it difficult to determine the exact carbon percentages, a decrease of ca. 10% was observed following extraction in their work.[79]

Table 3 presents the carbon percentages and O/C ratios for CNCs as received and after Soxhlet extraction. All samples were measured under the same conditions, and we emphasize that these are relative values and that environmental contamination and charging can significantly alter percentages. Clearly, the C1 content among samples varies greatly and is larger than the accepted range of 5−7% for clean cellulose surfaces, suggesting that indeed there is contamination on the CNC surface. The source of this contamination is difficult to determine because the environmental conditions in which industry CNCs are produced are not fully known. One potential source is the containers in which CNCs are shipped because plastic containers are known to impart C1 carbon.[110] The O/C ratio for all CNCs is below the theoretical value of 0.83, again supporting the presence of noncellulosic material. After Soxhlet extraction, the relative C1 percentages decrease for lab-made, CelluForce, and AITF CNCs and remain nearly constant for FPL CNCs. Although the Soxhlet extraction reduces the overall C1 content, the effect on the O/C ratio is less clear. Lab-made CNCs increase to 0.87, higher than the theoretical value, whereas CelluForce CNCs exhibit a decrease to 0.73. Most notably are FPL CNCs, which show a dramatic reduction in O/C ratio, potentially due to the loss of cellulosic material in the form of cellulose II during extraction.

Thermal Stability. The thermal stability of industrially produced and lab-made CNCs was investigated by TGA of freeze-dried material. CNCs showed typical thermal degradation behavior[107,114] and good stability, with all as-received material maintaining at least 95% mass above 250 °C (Figure 7). The most significant difference can be seen in the char residue mass percentages (500 °C), which range from 11 to 27% for lab-made and AITF CNCs, respectively. The composition of the char residue is currently unclear but is proposed to consist of levoglucosan and low-molecular-weight hydrocarbons along with hydrogen, CO, CO_2, and H_2O.[107] Following Soxhlet extraction, the thermal stability of lab-made, CelluForce, and FPL CNCs remained unchanged (Supporting Information

Table 3. Carbon Composition As Determined by XPS of CNCs As Received and after Soxhlet Extraction along with the Oxygen/Carbon Ratio

	composition percentage							
	C1		C2		C3		O/C	
	as received	Soxhlet extracted	as received	Soxhlet extracted	as received	Soxhlet extracted	as received	Soxhlet extracted
lab-made	13.9	6.1	44.6	54.1	41.6	39.8	0.77	0.87
CelluForce	18.4	13.8	57.8	61.8	23.9	17.5	0.77	0.73
AITF	21.8	15.2	42.3	58.8	35.9	26	0.74	0.76
FPL	11.2	11.4	69.2	67.9	18.5	20.3	0.77	0.57
theoretical	0		83.3		16.7		0.83	

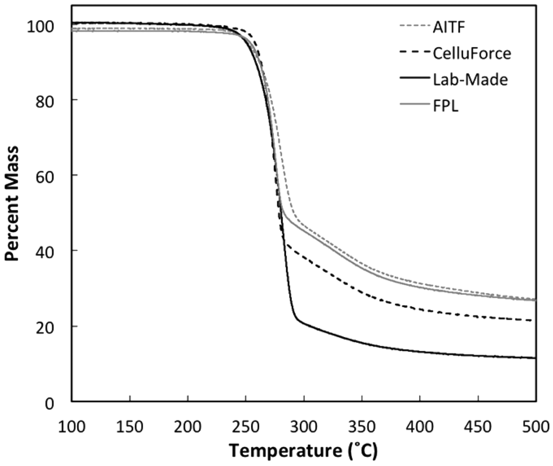

Figure 7. TGA curves of freeze-dried as-received lab-made and industrially produced CNCs.

Figures S5−S7). Conversely, Soxhlet-extracted AITF CNCs showed reduced thermal stability with 95% mass maintained only until 237 °C (Supporting Information Figure S8).

Liquid-Crystalline Properties and Self-Assembly. The self-assembly and formation of chiral nematic phases in CNC suspensions can be used as an indicator of good particle behavior. The exact onset of phase separation can indicate the average CNC size (or lack of aggregation), size distribution, surface charge, and ionic strength of the suspension.[32,37,68] Figure 8 shows (a) CNC suspensions of as-received samples at 1 wt % (below onset of phase separation), with a slight variation in translucency that is affected primarily by the average particle size and degree of agglomeration, and (b) concentrated CNC suspensions (above the onset of phase separation) after at least 10 days of self-assembly. Clear separation between the anisotropic and isotropic phases can be seen in all samples. Different volume fractions of the two phases are due to varying concentration (some material is lost during filtration), charge density, and aspect ratio of the particles. All CNCs investigated show the expected phase-separation behavior, implying good dispersion of nanoparticles and minimal contamination, which would interfere with self-assembly (salts, sugars, and polymers) in the as-received samples.

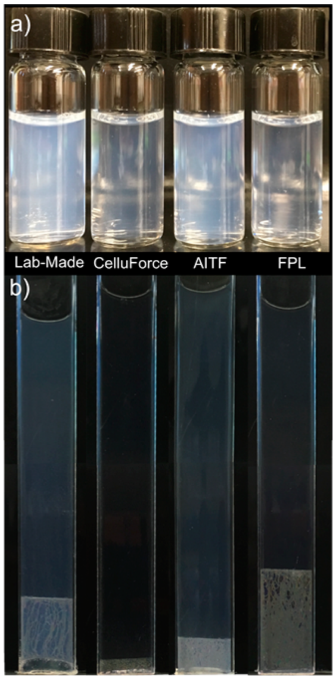

Figure 8. (a) Photographs of 1 wt % suspensions of as-received CNC samples. (b) Concentrated CNC suspensions: lab-made 8 wt %, CelluForce 3.5 wt %, AITF 8 wt %, and FPL 7 wt % after 30 days in rectangular capillary tubes imaged between cross polarizers. Note that because of sealing the capillary, the CNC dispersion does not reside directly at the bottom of the capillary.

Notably, CelluForce CNCs exhibited phase separation at significantly lower concentrations (3.5 wt %) whereas the others were all above 7 wt %. This is likely due to the higher aspect ratio of the particles (Table 1), similar to what has been observed in sulfuric acid-extracted bacterial cellulose.[115] At higher concentrations, CelluForce dispersions were observed to be completely anisotropic and kinetically arrested,[116] exhibiting no biphasic behavior. The anisotropic phase was investigated by polarized optical microscopy (POM) to confirm the presence of chiral nematic phases. Figure 9 shows that all samples display the characteristic fingerprint texture of chiral nematic liquid crystals. Because of the difference in concentration among samples, an analysis of the pitch length is not particularly relevant but generally agrees with the literature.

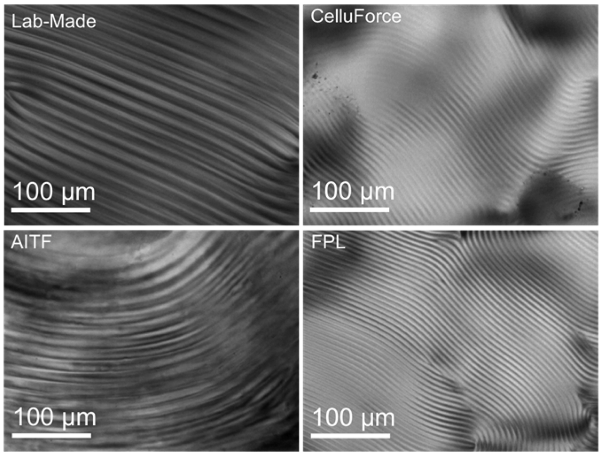

Figure 9. POM images of the anisotropic phase of as-received CNCs, showing clear fingerprint texture in all samples indicating chiral nematic liquid-crystal organization. Concentrations are lab-made 8 wt %, CelluForce 3.5 wt %, AITF 8 wt %, and FPL 7 wt %.

Effect of a Changing Cellulose Source and Production Scale. AITF CNCs investigated throughout this work were produced via bench-scale conventional sulfuric acid hydrolysis of cotton. More recently, AITF has begun to produce CNCs on the pilot scale using wood-sourced cellulose. Table 4 shows the properties of both cotton and softwood dissolving pulp-derived CNCs in which particles have identical crystallinity (Supporting Information Figure S9) and sulfate half-ester content. Small changes in the zeta potential apparent size by DLS and thermal stability (Supporting Information Figure S8) are evident but expected when transitioning to wood cellulose starting materials.

DOI: 10.1021/acs.langmuir.6b03765
Langmuir 2017, 33, 1583−1598

Table 4. Properties of AITF As-Received CNCs Derived from Cotton and Softwood Dissolving Pulp

	cellulose source	
	cotton	softwood dissolving pulp
g of S/100 g of CNC	0.69 ± 0.03	0.69 ± 0.02
R-OSO_3H mmol/kg of CNC	215 ± 10	215 ± 5
zeta potential (mV)	−42 ± 1	−34 ± 1
apparent size by DLS (nm)	73 ± 2	88 ± 16
crystallinity (%)	91	91

Additionally, Figure 10 shows that the phase separation and self-assembly properties are maintained.

Other Nanocelluloses Produced through Nonconventional Methods. In addition to the traditional sulfuric acid hydrolysis, several industrial producers are now extracting CNCs/CNFs using less-conventional methods, and there has yet to be any significant comparison with sulfuric acid-extracted CNCs. Importantly, some of these processes do not use acid hydrolysis, and as a result, no electrostatic stabilization can be expected.

American Process Inc. Figure 11 shows an optical microscopy image of BioPlus Crystals along with the appearance of a 1 wt % dispersion. Clearly, a significant portion of the material contains macroscopic fibers leading to highly turbid dispersions. The crystallinity was measured by XRD to be >85% (Supporting Information Figure S10), and AFM imaging (Figure 11 inset) shows the presence of both microscopic and nanoscale cellulose material. Importantly, because the extraction process does not graft charged groups to the nanoparticle surface, API CNCs demonstrated poor colloidal stability and settled after approximately 1 h. As such, no reliable DLS or zeta potential measurements could be obtained.

Blue Goose Biorefineries. Blue Goose Biorefineries uses a proprietary transition-metal-catalyzed oxidative process to extract highly crystalline, >90% (Supporting Information, Figure S11), carboxyl-functionalized nanocellulose material. Figure 12 shows a 1 wt % dispersion of BGB Natural along with AFM images of as-received material showing high-aspect-ratio nanofibrils with some microscopic components. No macroscopic fibers were evident by eye or optical microscopy. DLS measurements exhibit a bimodal size distribution with peaks centered at 40−50 nm and 235−272 nm (Supporting Information Figure S12), in good agreement with AFM images.

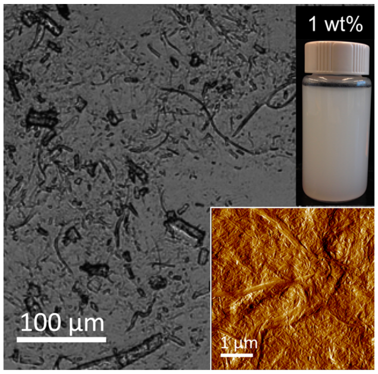

Figure 11. Optical microscopy image showing macroscopic fibers with BioPlus Crystals along with a photograph of a 1 wt % dispersion. The inset shows a 5 μm × 5 μm AFM amplitude image in which nanocellulose structures are visible.

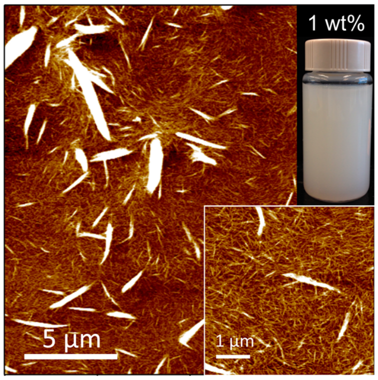

Figure 12. AFM height image of BGB Natural showing microscopic material and a 1 wt % dispersion. The inset shows 5 μm × 5 μm AFM height image.

BGB Natural particles have good colloidal stability with a zeta potential of −18 ± 1 mV.

DISCUSSION

CNC Properties from Different Producers. Overall, the sulfuric acid hydrolyzed CNCs produced industrially compare well with conventional lab-made CNCs. In all cases, sulfuric acid

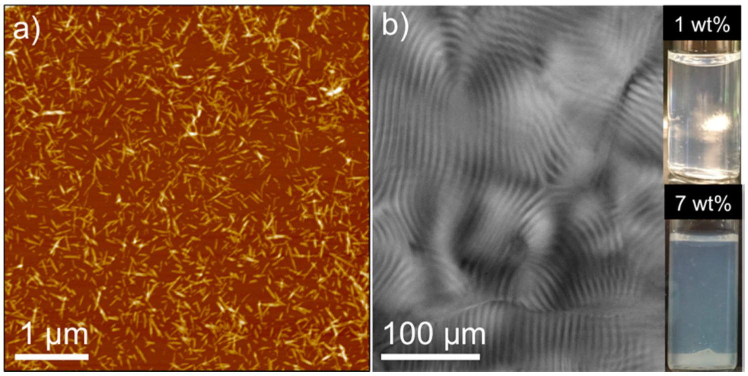

Figure 10. (a) AFM height image of AITF as-received CNCs from softwood dissolving pulp. (b) POM image of the anisotropic phase with the visual appearance of dilute and concentrated CNC suspensions.

DOI: 10.1021/acs.langmuir.6b03765
Langmuir 2017, 33, 1583−1598

hydrolysis produced high-aspect-ratio particles that were electrostatically stabilized via grafted sulfate half-ester groups. Moreover, once producers have a good feel for CNC production on the bench scale it seems that scale-up and even changes in starting cellulose material have minimal impact on the CNC chemical and physical properties. Although the CNCs investigated had similar properties, we emphasize that slight variations in these properties can have a significant effect on CNC behavior, and thorough characterization is still recommended prior to use. For example, using CNCs as rheological modifiers, reinforcing agents, or emulsion/foam stabilizers could be severely impacted such that reproducing published results with CNCs of varying properties (e.g., CNCs from different manufacturers) would present significant challenges. Below we discuss key property differences of as-received materials and the potential impact in various applications.

The sulfate half-ester content is a key factor in CNC behavior and is responsible for the colloidal stability of the particles. Notably, the sulfate half-ester content of FPL CNCs was nearly 25% greater than that of other producers (Figure 2). Interestingly, this trend is not reflected in the zeta potential or thermal stability because FPL and lab-made CNCs are equivalent. Critically, the electrophoretic mobility and ultimately the zeta potential are influenced not only by the sulfate ester content but also by the particle shape and surface morphology. Zeta potential measurements indicate that even though FPL CNCs have a higher sulfate half-ester content their mobility in an electric field is similar to that of other CNCs tested. Although a higher charge density potentially imparts superior colloidal stability, particularly in environments with elevated ionic strength, it has been shown to have a dramatic effect on how particles behave at interfaces. Kalashnikova et al. demonstrated that the charge density plays a major role in how effective CNCs are as Pickering emulsion stabilizers, leaning toward lower-charged CNCs for more stable emulsions.[117]

CNC behavior at an interface is dependent not only on the surface charge density but also on the particle aspect ratio. In a follow-up publication, Kalashnikova et al. further demonstrated that the coverage and behavior of oil-in-water emulsions were heavily influenced by the particle aspect ratio.[75] Using shorter particles as stabilizing agents produced more individualized droplets whereas long CNC-bridged droplets created network-like emulsions. The aspect ratio not only affects the interfacial behavior but also impacts the rheological properties,[73] reinforcing capability,[76] and packing of CNCs.[118] Particles with higher aspect ratios form gels and percolated networks at significantly lower concentrations than do shorter particles, potentially reducing the amount of material required for specific applications. Again, this highlights that thorough characterization is needed because cellulose source and extraction procedures impact the aspect ratio as evidenced by CelluForce CNCs, which have a significantly larger aspect ratio.

We emphasize that microscopy is an essential tool for characterization because DLS measurements, although giving relative particle sizes and distributions, do not convey a true particle shape, dimensions, and size distribution. Clear evidence of this is seen when analyzing the dimensions of FPL CNCs as dispersions and in the dry state. DLS measurements suggest that FPL CNCs are more than 10 nm smaller than other CNCs (Figure 4); however, AFM analysis of both the length and cross section show that FPL CNCs are equivalent to other producers. However, DLS does suggest that FPL CNCs have a higher diffusion constant, which is perhaps a result of cellulose II precipitating on the surface and reducing the fuzziness that is sometimes attributed to oligosaccharides on the CNC surface.[72]

A critical feature of CNCs is the cellulose I crystal structure. Cellulose I is known not to swell, and thus CNCs are expected to maintain their size and morphology in a variety of solvents and matrices.[101] Additionally, the high elastic modulus and potential reinforcing capabilities of CNCs are largely attributed to the rigid cellulose I crystal structure, and thus highly crystalline materials are desired for these applications. CNCs produced by lab-made, CelluForce, and AITF are highly crystalline, with cellulose I percentages upwards of ca. 90% being in good agreement with previous literature values. Most notable in the crystallinity measurements is the presence of cellulose II within FPL CNCs, which has been observed previously.[107] Although we can only postulate as to the source of cellulose II, we suggest that a portion of the cellulose I structure was at least partially dissolved in NaOH and subsequently regenerated/precipitated onto the CNC surface into the cellulose II polymorph. We note the dissolving pulp used in the production of FPL CNC as a possible source of cellulose II, and they suggest that the NaOH concentrations used in CNC production are below the threshold for mercerization. Currently, the presence of cellulose II with FPL material appears to have little impact on the particle behavior because it maintains a good colloidal stability, aspect ratio, and self-assembly.

Both industrially produced and bench-scale CNCs show good thermal stability up to 250 °C, suggesting that incorporating CNCs into drilling fluids and polymer composites via melt mixing is feasible for all as-received CNCs. However, sulfate half-ester groups do fall off with heating and over time,[90] and this work implies that the quantity of sulfate esters is not directly linked to the CNC thermal stability within the range investigated. Although not tested in this work, we emphasize that the rate of heating (i.e., incorporating directly into a polymer melt vs a gradual temperature increase) along with the bound moisture content is related to discoloration and remains poorly understood.

Biphasic behavior and, more specifically, the formation of anisotropic chiral nematic structures above a critical concentration is an emblem of good CNC behavior and is of great interest as structured color templates for cosmetics, anticounterfeit, and optical applications.[119] The formation of these structures in all of the CNCs investigated is an advantage for future applications. However, despite the many academic demonstrations and control of CNC self-assembly in magnetic[34−39] and electric fields,[40−42] the exploitation of this behavior in a commercially relevant and scalable processes remains to be seen.

Soxhlet Extraction. Generally, Soxhlet extraction had a minimal effect on CNC properties. Only minor changes in the sulfate half-ester content, zeta potential, and apparent particle size were observed for all CNCs. Where these values differ, it is believed that CNC behavior, such as colloidal stability, remains relatively unchanged. For example, the zeta potential of lab-made and FPL CNCs increased by ca. −5 mV following Soxhlet extraction; however, the particles remain highly anionic and stable with zeta potentials of ca. −40 mV. This trend is similarly reflected in the sulfate ester content where the largest decrease of 7.5% was observed for FPL CNCs. The apparent particle diameter as measured by DLS indicates that the particle dimensions are largely unchanged following Soxhlet extraction and any increase in size is attributed to aggregation following exposure to ethanol.

Although we believe that the bulk colloidal, thermal, and interfacial behavior of the CNCs will remain unchanged following Soxhlet extraction, this is not to say that Soxhlet extraction is not sometimes a prerequisite. The recent publication by Bouchard et al.[72] clearly demonstrates that bound oligosaccharides are very much impacted by the exact hydrolysis conditions. Some applications may need these and other byproducts to be removed to improve efficiency and reproducibility. Experiments that have demonstrated extreme sensitivity to purification protocols include grafting small molecules to CNCs (and polymer grafting[79]) and particularly when studying CNCs as model cellulose films: open film assembly on different substrates is strongly reliant on Soxhlet extraction for repeatable experiments.[120]

The most significant impact of Soxhlet extraction observed in this work was in the crystal structure of FPL CNCs. Prior to extraction, as-received material had nearly a 1:1 ratio of cellulose I and cellulose II polymorphs. Following extraction, the cellulose II content significantly decreased, yielding a cellulose I to cellulose II ratio of 3:1 and suggesting that cellulose II is lost during purification. Additionally, because of the decrease in sulfate ester content and zeta potential, a portion of the cellulose II is presumably sulfated. We note, however, that the loss of cellulose II does not significantly affect the CNC behavior because only minor changes in the apparent particle size and zeta potential were observed.

X-ray Photoelectron Spectroscopy. Soxhlet extraction is proposed to remove residual hydrolysis byproducts and oligomers from the CNC surface. Labet and Thielemans showed that following Soxhlet extraction the overall functionalization and reproducibility of ring-opening polymerization on CNCs was improved.[79] Although Soxhlet extraction improves functionalization, quantifying the purity of CNCs is challenging, particularly via XPS. Notably, any residual oligomers or hydrolysis byproducts that have precipitated onto the CNC surface will be primarily composed of cellulosic materials, chemically equivalent to CNCs. Moreover, clean cellulose filter paper has been shown to contain 5−7% aliphatic C1 carbon, and storing samples in glass, aluminum, plastic, or cellophane can dramatically reduce the reproducibility.[110] This is particularly noteworthy for industrially produced CNCs because the various handling steps and shipping containers are unknown. As a result, we discourage the use of XPS for baseline CNC characterization but recognize its importance for examining nanocellulose modified with noncarbon/oxygen-only compounds.

Other Nanocelluloses. Nanocelluloses produced by American Process Inc. and Blue Goose Biorefineries, although highly crystalline with a significant nanocomponent, show important differences in appearance and properties compared to CNCs extracted by sulfuric acid hydrolysis. Most notable is the presence of macroscopic fibers in American Process Inc. BioPlus Crystals. These large-scale fibers will dramatically affect the rheological, colloidal, and mechanical properties of the material, which could be positive for some applications (i.e., composites) but detrimental to others and ultimately should not be classified as CNCs. From our perspective, the work we have published on emulsions, hydrogels, aerogels, thin films, and composites would not give the same results if API nanocellulose was used. Conversely, BGB Natural particles, although containing a bimodal distribution of both nanocellulose and fibrillar cellulose, showed no evidence of macroscopic material and demonstrated better colloidal stability with a zeta potential of −18 ± 1 mV. We additionally note that Blue Goose Biorefineries reports that their more recent product, BGB Ultra, although not investigated in this work, has a similar size distribution and optical properties to those of sulfuric acid-extracted CNCs. The various products being produced from nanocellulose suppliers again highlight the need for thorough characterization prior to CNC use.

■ CONCLUSION

This work presents the first detailed analysis and comparison of laboratory and industrially produced sulfuric acid-extracted CNCs and seeks to answer the following questions:

Are CNCs from Various Producers Equivalent? Overall, industrially produced CNCs from CelluForce, Alberta Innovates Technology Futures, and the USDA Forest Products Laboratories compare well with CNCs extracted on a bench scale, with all material containing highly crystalline, high-aspect-ratio nano-only CNCs. However, differences in the sulfate half-ester content, colloidal stability, crystallinity, and morphology do exist. These properties must be fully characterized prior to use because they can significantly impact particle behavior.

Nanocelluloses produced by nontraditional processes investigated in this work, including American Process Inc. BioPlus Crystals and Blue Goose Biorefineries BGB Natural, although containing highly crystalline nanocellulose material, exhibit behavior and properties that differ significantly from those of sulfuric acid-extracted CNCs. Additionally, the materials tested in this work cannot be considered in the same light as CNCs because they contain microscopic and macroscopic components.

What Are the Most Practical Characterization Methods That Should Be Employed Prior to Using CNCs? This work has shown that changes to the cellulose source and hydrolysis conditions can significantly impact CNC properties and behavior. As such, we emphasize that CNCs must be thoroughly characterized to ensure that their performance is consistent. For the majority of applications, we recommend at the minimum conductometric titrations, zeta potential measurements, XRD, dynamic light scattering, and microscopy (either AFM or TEM) to characterize the sulfate half-ester content, colloidal stability, crystallinity, and particle morphology. In applications in which CNCs are being surface modified, such as through polymer grafting, we further suggest including XPS before and after modification; however, quantitative analysis remains difficult. We additionally note that as CNC applications increase in scale, extensive characterization will become onerous and industrial-scale quality assurance/control protocols must be developed.

Is Further Purification, Such As Soxhlet Extraction, Required? Our investigation shows that Soxhlet extraction does not significantly impact the core properties or behavior of CNCs. Although minor changes were observed for the sulfate half-ester content and zeta potential, particles remain highly negatively charged and colloidally stable. Moreover, quantifying the cleanliness remains extremely challenging. The most notable change following Soxhlet extract was observed in the crystallinity of FPL CNCs; however, the particle physical properties did not change significantly.

If Producers Change the Scale and Starting Material, Then What Kind of Changes Can We Expect? As cellulose sources and production scales change, obtaining identical material from industrial producers could be challenging and is worth watching out for. Moreover, as CNC technology continues to develop we can expect a variety of nanocellulose grades from industrial producers with different properties and morphologies such as Blue Goose Biorefineries BGB Natural and BGB Ultra. Currently, batch-to-batch variability will likely result in minor

DOI: 10.1021/acs.langmuir.6b03765
Langmuir 2017, 33, 1583−1598

differences in particle dimensions and sulfate half-ester content. Nonetheless, transitioning between cellulose sources and increasing the production scale yielded comparable CNCs, as evident from cotton- and wood-based CNCs from AITF.

Ultimately, for the CNC community to continue to grow and for commercial applications to be realized, industrially produced CNCs are needed. Overall, this investigation demonstrates that with proper characterization the transition from laboratory scale to industrial CNCs should be met with optimism. Current producers of sulfuric acid-extracted CNCs are generating material with comparable particle dimensions and properties to those that have been investigated in the past.

■ ASSOCIATED CONTENT

Supporting Information

The Supporting Information is available free of charge on the ACS Publications website at DOI: 10.1021/acs.langmuir.6b03765.

> X-ray diffraction patterns and thermal gravimetric analysis profiles of as-received and Soxhlet-extracted cellulose nanocrystals produced in the laboratory and on the industrial scale (PDF)

■ AUTHOR INFORMATION

Corresponding Author

*E-mail: ecranst@mcmaster.ca.

ORCID

Emily D. Cranston: 0000-0003-4210-9787

Notes

The authors declare no competing financial interest.

Biographies

Michael S. Reid is a Ph.D. candidate in chemical engineering at McMaster University. He received his Honors B.Sc. degree in chemical physics (2009) from the University of Guelph and his M.Sc. in chemistry (2012) from the University of Alberta. Since joining the Cranston research group, his primary research interests include interfacial engineering, plant-based colloids, and sustainable nanocomposite materials.

Marco Villalobos is the ATC Technology Director and Global Applications Development Director at Cabot Corporation. He previously held R&D Manager positions at BASF and S.C. Johnson Polymer. His B.Sc. is in Chemical Engineering from the National University of Mexico, and he obtained both his M.Eng (1989) and Ph.D. (1993) in Chemical Engineering from McMaster University. His expertise is in the development and commercialization of new products and applications via market driven innovation with research interests in elastomers, plastics, composites, coatings, toners, adhesives, displays, inks, and batteries.

Emily D. Cranston is an associate professor in chemical engineering at McMaster University. She received her Honors B.Sc. degree in chemistry at McGill University and her Ph.D. in materials chemistry (2008) in the group of Dr. Derek G. Gray, also at McGill University. She was a postdoctoral researcher at the Royal Institute of Technology in Sweden before returning to Canada in 2011. She is the Vice-Chair of the TAPPI Nanotechnology Division and recipient of the 2016 KINGFA Young Investigator's Award from the American Chemical Society's Cellulose and Renewable Materials Division. Cranston's research focuses on the design and characterization of sustainable nanocomposites and hybrid materials from cellulose and biobased nanoparticles.

■ ACKNOWLEDGMENTS

Funding from the Natural Sciences and Engineering Research Council of Canada and the Industrial Postgraduate Scholarship Program sponsored by Cabot Corporation is gratefully acknowledged. The authors also thank Richard Berry at CelluForce, Alan Rudie at the USDA Forest Products Laboratory, Behzad Ahvazi and Christophe Danumah at Alberta Innovates Technology Futures, and Sean McAlpine at Blue Goose Biorefineries. We thank Professors R. Pelton, A. Guarne, and J. Moran-Mirabal for sharing equipment to characterize CNCs. We thank Victoria

Jarvis as part of the McMaster Analytical X-ray Diffraction Facility for her time and expertise. Additionally, the Biointerfaces Institute and the Brockhouse Institute for Materials Research at McMaster University are acknowledged for support and equipment.

REFERENCES

(1) Sionkowska, A. Current Research on the Blends of Natural and Synthetic Polymers as New Biomaterials: Review. *Prog. Polym. Sci.* **2011**, *36* (9), 1254−1276.

(2) Yang, X.; Shi, K.; Zhitomirsky, I.; Cranston, E. D. Cellulose Nanocrystal Aerogels as Universal 3D Lightweight Substrates for Supercapacitor Materials. *Adv. Mater.* **2015**, *27* (40), 6104−6109.

(3) Nyström, G.; Marais, A.; Karabulut, E.; Wågberg, L.; Cui, Y.; Hamedi, M. M. Self-Assembled Three-Dimensional and Compressible Interdigitated Thin-Film Supercapacitors and Batteries. *Nat. Commun.* **2015**, *6* (May), 7259.

(4) Nyström, G.; Fernández-Ronco, M. P.; Bolisetty, S.; Mazzotti, M.; Mezzenga, R. Amyloid Templated Gold Aerogels. *Adv. Mater.* **2016**, *28* (3), 472−478.

(5) Xie, F.; Halley, P. J.; Avérous, L. Rheology to Understand and Optimize Processibility, Structures and Properties of Starch Polymeric Materials. *Prog. Polym. Sci.* **2012**, *37* (4), 595−623.

(6) Yang, X.; Bakaic, E.; Hoare, T.; Cranston, E. D. Injectable Polysaccharide Hydrogels Reinforced with Cellulose Nanocrystals: Morphology, Rheology, Degradation, and Cytotoxicity. *Biomacromolecules* **2013**, *14* (12), 4447−4455.

(7) La Mantia, F. P.; Morreale, M. Green Composites: A Brief Review. *Composites, Part A* **2011**, *42* (6), 579−588.

(8) Siqueira, G.; Bras, J.; Dufresne, A. Cellulosic Bionanocomposites: A Review of Preparation, Properties and Applications. *Polymers (Basel, Switz.)* **2010**, *2* (4), 728−765.

(9) Eichhorn, S. J.; Baillie, C. A.; Zafeiropoulos, N.; Mwaikambo, L. Y.; Ansell, M. P.; Dufresne, A.; Entwistle, K. M.; Herrera-Franco, P. J.; Escamilla, G. C.; Groom, L.; et al. Current International Research into Cellulosic Fibres and Composites. *J. Mater. Sci.* **2001**, *36*, 2107−2131.

(10) Faruk, O.; Bledzki, A. K.; Fink, H. P.; Sain, M. Biocomposites Reinforced with Natural Fibers: 2000−2010. *Prog. Polym. Sci.* **2012**, *37* (11), 1552−1596.

(11) Liu, X.; Wang, Y.; Yu, L.; Tong, Z.; Chen, L. Thermal Degradation and Stability of Starch under Different Processing Conditions. *Starch-Stärke* **2013**, *65*, 48−60.

(12) Liu, H.; Xie, F.; Yu, L.; Chen, L.; Li, L. Thermal Processing of Starch-Based Polymers. *Prog. Polym. Sci.* **2009**, *34* (12), 1348−1368.

(13) Pillai, C. K. S.; Paul, W.; Sharma, C. P. Chitin and Chitosan Polymers: Chemistry, Solubility and Fiber Formation. *Prog. Polym. Sci.* **2009**, *34* (7), 641−678.

(14) Rinaudo, M.; Ã, M. R. Chitin and Chitosan: Properties and Applications. *Prog. Polym. Sci.* **2006**, *31* (7), 603−632.

(15) Gallezot, P. Conversion of Biomass to Selected Chemical Products. *Chem. Soc. Rev.* **2012**, *41* (4), 1538−1558.

(16) Klemm, D.; Heublein, B.; Fink, H. P.; Bohn, A. Cellulose: Fascinating Biopolymer and Sustainable Raw Material. *Angew. Chem., Int. Ed.* **2005**, *44* (22), 3358−3393.

(17) Schaefer, D. W.; Justice, R. S. How Nano Are Nanocomposites? *Macromolecules* **2007**, *40* (24), 8501−8517.

(18) Klemm, D.; Kramer, F.; Moritz, S.; Lindström, T.; Ankerfors, M.; Gray, D. G.; Dorris, A. Nanocelluloses: A New Family of Nature-Based Materials. *Angew. Chem., Int. Ed.* **2011**, *50*, 5438−5466.

(19) Nickerson, R. F.; Habrle, J. a. Cellulose Intercrystalline Structure. *Ind. Eng. Chem.* **1947**, *39* (11), 1507−1512.

(20) Ranby, B. G.; Ribi, E. Uber Den Feinbau Zellulose. *Experientia* **1950**, *6*, 12−14.

(21) Brinchi, L.; Cotana, F.; Fortunati, E.; Kenny, J. M. Production of Nanocrystalline Cellulose from Lignocellulosic Biomass: Technology and Applications. *Carbohydr. Polym.* **2013**, *94* (1), 154−169.

(22) Medronho, B.; Romano, A.; Miguel, M. G.; Stigsson, L.; Lindman, B. Rationalizing Cellulose (in)solubility: Reviewing Basic Physicochemical Aspects and Role of Hydrophobic Interactions. *Cellulose* **2012**, *19*, 581−587.

(23) Moon, R. J.; Martini, A.; Nairn, J.; Simonsen, J.; Youngblood, J. Cellulose Nanomaterials Review: Structure, Properties and Nanocomposites. *Chem. Soc. Rev.* **2011**, *40* (7), 3941−3994.

(24) Azizi Samir, M. A. S.; Alloin, F.; Dufresne, A. Review of Recent Research into Cellulosic Whiskers, Their Properties and Their Application in Nanocomposite Field. *Biomacromolecules* **2005**, *6* (2), 612−626.

(25) Eichhorn, S. J.; Dufresne, A.; Aranguren, M.; Marcovich, N. E.; Capadona, J. R.; Rowan, S. J.; Weder, C.; Thielemans, W.; Roman, M.; Renneckar, S.; et al. Review: Current International Research into Cellulose Nanofibres and Nanocomposites. *J. Mater. Sci.* **2010**, *45* (1), 1−33.

(26) Habibi, Y.; Lucia, L. A.; Rojas, O. J. Cellulose Nanocrystals: Chemistry, Self-Assembly, and Applications. *Chem. Rev.* **2010**, *110* (6), 3479−3500.

(27) Habibi, Y. Key Advances in the Chemical Modification of Nanocelluloses. *Chem. Soc. Rev.* **2014**, *43* (5), 1519−1542.

(28) Mariano, M.; El Kissi, N.; Dufresne, A. Cellulose Nanocrystals and Related Nanocomposites: Review of Some Properties and Challenges. *J. Polym. Sci., Part B: Polym. Phys.* **2014**, *52*, 791−806.

(29) Zhu, H.; Luo, W.; Ciesielski, P. N.; Fang, Z.; Zhu, J. Y.; Henriksson, G.; Himmel, M. E.; Hu, L. Wood-Derived Materials for Green Electronics, Biological Devices, and Energy Applications. *Chem. Rev.* **2016**, *116* (16), 9305−9374.

(30) Revol, J. F.; Bradford, H.; Giasson, J.; Marchessault, R. H.; Gray, D. G. Helicoidal Self-Ordering of Cellulose Microfibrils in Aqueous Suspension. *Int. J. Biol. Macromol.* **1992**, *14* (3), 170−172.

(31) Dong, X. M.; Kimura, T.; Revol, J.-F.; Gray, D. G. Effects of Ionic Strength on the Isotropic−Chiral Nematic Phase Transition of Suspensions of Cellulose Crystallites. *Langmuir* **1996**, *12* (8), 2076−2082.

(32) Dong, X. M.; Gray, D. G. Effect of Counterions on Ordered Phase Formation in Suspensions of Charged Rodlike Cellulose Crystallites. *Langmuir* **1997**, *13* (8), 2404−2409.

(33) Lagerwall, J. P. F.; Schütz, C.; Salajkova, M.; Noh, J.; Hyun Park, J.; Scalia, G.; Bergström, L. Cellulose Nanocrystal-Based Materials: From Liquid Crystal Self-Assembly and Glass Formation to Multifunctional Thin Films. *NPG Asia Mater.* **2014**, *6* (1), e80.

(34) De France, K. J.; Yager, K. G.; Hoare, T.; Cranston, E. D. Cooperative Ordering and Kinetics of Cellulose Nanocrystal Alignment in a Magnetic Field. *Langmuir* **2016**, *32* (30), 7564−7571.

(35) Frka-Petesic, B.; Sugiyama, J.; Kimura, S.; Chanzy, H.; Maret, G. Negative Diamagnetic Anisotropy and Birefringence of Cellulose Nanocrystals. *Macromolecules* **2015**, *48* (24), 8844−8857.

(36) Pullawan, T.; Wilkinson, A. N.; Eichhorn, S. J. Influence of Magnetic Field Alignment of Cellulose Whiskers on the Mechanics of All-Cellulose Nanocomposites. *Biomacromolecules* **2012**, *13* (8), 2528−2536.

(37) Revol, J.-F.; Godbout, L.; Dong, X.-M.; Gray, D. G.; Chanzy, H.; Maret, G. Chiral Nematic Suspensions of Cellulose Crystallites; Phase Separation and Magnetic Field Orientation. *Liq. Cryst.* **1994**, *16* (1), 127−134.

(38) Song, G.; Kimura, F.; Kimura, T.; Piao, G. Orientational Distribution of Cellulose Nanocrystals in a Cellulose Whisker as Studied by Diamagnetic Anisotropy. *Macromolecules* **2013**, *46* (22), 8957−8963.

(39) Kim, D. H.; Song, Y. S. Rheological Behavior of Cellulose Nanowhisker Suspension under Magnetic Field. *Carbohydr. Polym.* **2015**, *126*, 240−247.

(40) Csoka, L.; Hoeger, I. C.; Peralta, P.; Peszlen, I.; Rojas, O. J. Dielectrophoresis of Cellulose Nanocrystals and Alignment in Ultrathin Films by Electric Field-Assisted Shear Assembly. *J. Colloid Interface Sci.* **2011**, *363* (1), 206−212.

(41) Frka-Petesic, B.; Jean, B.; Heux, L. First Experimental Evidence of a Giant Permanent Electric-Dipole Moment in Cellulose Nanocrystals. *EPL (Europhysics Lett.* **2014**, *107* (2), 28006.

(42) Bordel, D.; Putaux, J.-L.; Heux, L. Orientation of Native Cellulose in an Electric Field. *Langmuir* **2006**, *22* (11), 4899−4901.

(43) Csoka, L.; Hoeger, I. C.; Rojas, O. J.; Peszlen, I.; Pawlak, J. J.; Peralta, P. N. Piezoelectric Effect of Cellulose Nanocrystals Thin Films. *ACS Macro Lett.* **2012**, *1* (7), 867−870.

(44) Hu, Z.; Patten, T.; Pelton, R.; Cranston, E. D. Synergistic Stabilization of Emulsions and Emulsion Gels with Water-Soluble Polymers and Cellulose Nanocrystals. *ACS Sustainable Chem. Eng.* **2015**, *3* (5), 1023−1031.

(45) Hu, Z.; Cranston, E. D.; Ng, R.; Pelton, R. Tuning Cellulose Nanocrystal Gelation with Polysaccharides and Surfactants. *Langmuir* **2014**, *30* (10), 2684−2692.

(46) Hu, Z.; Ballinger, S.; Pelton, R.; Cranston, E. D. Surfactant-Enhanced Cellulose Nanocrystal Pickering Emulsions. *J. Colloid Interface Sci.* **2015**, *439*, 139−148.

(47) Hu, Z.; Marway, H. S.; Kasem, H.; Pelton, R.; Cranston, E. D. Dried and Redispersible Cellulose Nanocrystal Pickering Emulsions. *ACS Macro Lett.* **2016**, *5*, 185−789.

(48) Chau, M.; De France, K. J.; Kopera, B.; Machado, V. R.; Rosenfeldt, S.; Reyes, L.; Chan, K. J. W.; Förster, S.; Cranston, E. D.; Hoare, T.; et al. Composite Hydrogels with Tunable Anisotropic Morphologies and Mechanical Properties. *Chem. Mater.* **2016**, *28* (10), 3406−3415.

(49) Hu, Z.; Xu, R.; Cranston, E. D.; Pelton, R. Stable Aqueous Foams from Cellulose Nanocrystals and Methyl Cellulose. *Biomacromolecules* **2016**, DOI: 10.1021/acs.biomac.6b01641.

(50) De France, K. J.; Chan, K. J. W.; Cranston, E. D.; Hoare, T. Enhanced Mechanical Properties in Cellulose Nanocrystal−Poly(oligoethylene Glycol Methacrylate) Injectable Nanocomposite Hydrogels through Control of Physical and Chemical Cross-Linking. *Biomacromolecules* **2016**, *17* (2), 649−660.

(51) Kedzior, S. a.; Graham, L.; Moorlag, C.; Dooley, B. M.; Cranston, E. D. Poly(methyl Methacrylate)-Grafted Cellulose Nanocrystals: One-Step Synthesis, Nanocomposite Preparation, and Characterization. *Can. J. Chem. Eng.* **2016**, *94* (5), 811−822.

(52) Kan, K. H. M.; Li, J.; Wijesekera, K.; Cranston, E. D. Polymer-Grafted Cellulose Nanocrystals as pH-Responsive Reversible Flocculants. *Biomacromolecules* **2013**, *14* (9), 3130−3139.

(53) Rivkin, A.; Abitbol, T.; Nevo, Y.; Verker, R.; Lapidot, S.; Komarov, A.; Veldhuis, S. C.; Zilberman, G.; Reches, M.; Cranston, E. D.; et al. Bionanocomposite Films from Resilin-CBD Bound to Cellulose Nanocrystals. *Ind. Biotechnol.* **2015**, *11*, 44−58.

(54) Yang, X.; Cranston, E. D. Chemically Cross-Linked Cellulose Nanocrystal Aerogels with Shape Recovery and Superabsorbent Properties. *Chem. Mater.* **2014**, *26* (2), 6016−6025.

(55) Abitbol, T.; Marway, H.; Cranston, E. D. Surface Modification of Cellulose Nanocrystals with Cetyltrimethylammonium Bromide. *Nord. Pulp Pap. Res. J.* **2014**, *29* (1), 046−057.

(56) Cranston, E. D.; Gray, D. G. Morphological and Optical Characterization of Polyelectrolyte Multilayers Incorporating Nanocrystalline Cellulose. *Biomacromolecules* **2006**, *7* (9), 2522−2530.

(57) Abitbol, T.; Prevo, B. G.; Galli, C.; Choudhary, S.; et al. Comparison of Nanocrystalline Cellulose and Fumed Silica in Latex Coatings. *Green Mater.* **2014**, *2*, 206−221.

(58) Shi, K.; Yang, X.; Cranston, E. D.; Zhitomirsky, I. Efficient Lightweight Supercapacitor with Compression Stability. *Adv. Funct. Mater.* **2016**, *26* (35), 6437−6445.

(59) Zhu, H.; Yang, X.; Cranston, E. D.; Zhu, S. Flexible and Porous Nanocellulose Aerogels with High Loadings of Metal-Organic Framework Particles for Separations Applications. *Adv. Mater.* **2016**, *28* (35), 7652−7765.

(60) Gill, U.; Sutherland, T.; Himbert, S.; Rheinstädter, M.; Cranston, E. D.; Moran-Mirabal, J. M. Beyond Buckling: Humidity-Independent Measurement of the Mechanical Properties of Green Nanocomposite Films. *Small* **2016**, submitted.

(61) Cranston, E. D.; Gray, D. G.; Rutland, M. W. Direct Surface Force Measurements of Polyelectrolyte Multilayer Films Containing Nanocrystalline Cellulose. *Langmuir* **2010**, *26* (22), 17190−17197.

(62) Sato, T.; Ali, M. M.; Pelton, R.; Cranston, E. D. DNA Stickers Promote Polymer Adsorption onto Cellulose. *Biomacromolecules* **2012**, *13* (10), 3173−3180.

(63) Reid, M. S.; Villalobos, M.; Cranston, E. D. Cellulose Nanocrystal Interactions Probed by Thin Film Swelling to Predict Dispersibility. *Nanoscale* **2016**, *8* (24), 12247−12257.

(64) Abitbol, T.; Palermo, A.; Moran-Mirabal, J. M.; Cranston, E. D. Fluorescent Labeling and Characterization of Cellulose Nanocrystals with Varying Charge Contents. *Biomacromolecules* **2013**, *14* (9), 3278−3284.

(65) Sacui, I. a.; Nieuwendaal, R. C.; Burnett, D. J.; Stranick, S. J.; Jorfi, M.; Weder, C.; Foster, E. J.; Olsson, R. T.; Gilman, J. W. Comparison of the Properties of Cellulose Nanocrystals and Cellulose Nanofibrils Isolated from Bacteria, Tunicate, and Wood Processed Using Acid, Enzymatic, Mechanical, and Oxidative Methods. *ACS Appl. Mater. Interfaces* **2014**, *6* (9), 6127−6138.

(66) Hamad, W. Y.; Hu, T. Q. Structure-Process-Yield Interrelations in Nanocrystalline Cellulose Extraction. *Can. J. Chem. Eng.* **2010**, *88* (3), 392−402.

(67) Chen, L.; Wang, Q.; Hirth, K.; Baez, C.; Agarwal, U. P.; Zhu, J. Y. Tailoring the Yield and Characteristics of Wood Cellulose Nanocrystals (CNC) Using Concentrated Acid Hydrolysis. *Cellulose* **2015**, *22* (3), 1753−1762.

(68) Dong, X. M.; Revol, J.-F.; Gray, D. G. Effect of Microscystallite Preparation Conditions on the Formation of Colloid Crystals of Cellulose. *Cellulose* **1998**, *5* (1), 19−32.

(69) Beck-Candanedo, S.; Roman, M.; Gray, D. G. Effect of Reaction Conditions on the Properties and Behavior of Wood Cellulose Nanocrystal Suspensions. *Biomacromolecules* **2005**, *6* (2), 1048−1054.

(70) Dong, S.; Bortner, M. J.; Roman, M. Analysis of the Sulfuric Acid Hydrolysis of Wood Pulp for Cellulose Nanocrystal Production: A Central Composite Design Study. *Ind. Crops Prod.* **2016**, *93*, 76−87.

(71) Wang, Q.; Zhao, X.; Zhu, J. Y. Kinetics of Strong Acid Hydrolysis of a Bleached Kraft Pulp for Producing Cellulose Nanocrystals (CNCs). *Ind. Eng. Chem. Res.* **2014**, *53* (27), 11007−11014.

(72) Bouchard, J.; Méthot, M.; Fraschini, C.; Beck, S. Effect of Oligosaccharide Deposition on the Surface of Cellulose Nanocrystals as a Function of Acid Hydrolysis Temperature. *Cellulose* **2016**, *23*, 3555.

(73) Wu, Q.; Meng, Y.; Wang, S.; Li, Y.; Fu, S.; Ma, L.; Harper, D. Rheological Behavior of Cellulose Nanocrystal Suspension: Influence of Concentration and Aspect Ratio. *J. Appl. Polym. Sci.* **2014**, *131* (15), 40525−40533.

(74) Cherhal, F.; Cousin, F.; Capron, I. Influence of Charge Density and Ionic Strength on the Aggregation Process of Cellulose Nanocrystals in Aqueous Suspension, as Revealed by Small-Angle Neutron Scattering. *Langmuir* **2015**, *31* (20), 5596−5602.

(75) Kalashnikova, I.; Bizot, H.; Bertoncini, P.; Cathala, B.; Capron, I. Cellulosic Nanorods of Various Aspect Ratios for Oil in Water Pickering Emulsions. *Soft Matter* **2013**, *9* (3), 952.

(76) Rusli, R.; Shanmuganathan, K.; Rowan, S. J.; Weder, C.; Eichhorn, S. J. Stress Transfer in Cellulose Nanowhisker Composites-Influence of Whisker Aspect Ratio and Surface Charge. *Biomacromolecules* **2011**, *12* (4), 1363−1369.

(77) Beck, S.; Bouchard, J.; Berry, R. Controlling the Reflection Wavelength of Iridescent Solid Films of Nanocrystalline Cellulose. *Biomacromolecules* **2011**, *12*, 167−172.

(78) Shafiei-Sabet, S.; Hamad, W. Y.; Hatzikiriakos, S. G. Rheology of Nanocrystalline Cellulose Aqueous Suspensions. *Langmuir* **2012**, *28* (49), 17124−17133.

(79) Labet, M.; Thielemans, W. Improving the Reproducibility of Chemical Reactions on the Surface of Cellulose Nanocrystals: ROP of E-Caprolactone as a Case Study. *Cellulose* **2011**, *18* (3), 607−617.

(80) Akpinar, O.; McGorrin, R. J.; Penner, M. H. Cellulose-Based Chromatography for Cellooligosaccharide Production. *J. Agric. Food Chem.* **2004**, *52* (13), 4144−4148.

(81) Peri, S.; Muthukumar, L.; Nazmul Karim, M.; Khare, R. Dynamics of Cello-Oligosaccharides on a Cellulose Crystal Surface. *Cellulose* **2012**, *19* (6), 1791−1806.

(82) Future Markets Inc. *The Global Market for Nanocellulose to 2020*; 2013.

(83) Microfibrillar Cellulose Project from Borregaard Gets EU Funding. *BioPlast. Mag.* **2016**.

(84) Canadian Standards Association. *Cellulosic Nanomaterials — Test Methods for Characterization (CSA Z5100-14)*; 2014.

(85) Sarma, S. J.; Ayadi, M.; Brar, S. K.; Berry, R. Sustainable Commercial Nanocrystalline Cellulose Manufacturing Process with Acid Recycling. *Carbohydr. Polym.* **2017**, *156*, 26−33.

(86) Houtman, C. Technoeconomic Analysis of Commercial-Scale CNC Production. *TAPPI Nano* **2016**.

(87) Nelson, K.; Retsina, T. Innovative Nanocellulose Process Breaks the Cost Barrier. *TAPPI J.* **2014**, *13* (5), 19−23.

(88) Nelson, K.; Retsina, T.; Iakovlev, M.; van Heiningen, A.; Deng, Y.; Shatkin, J. A.; Mulyadi, A. *Materials Research for Manufacturing*; Springer: Cham, 2016; Vol. *224*.

(89) Blue Goose Biorefineries Inc. http://bluegoosebiorefineries.com/ (accessed Sept 1, 2016).

(90) Beck, S.; Bouchard, J. Auto-Catalyzed Acidic Desulfation of Cellulose Nanocrystals. *Nord. Pulp Pap. Res. J.* **2014**, *29* (01), 006−014.

(91) Abitbol, T.; Kloser, E.; Gray, D. G. Estimation of the Surface Sulfur Content of Cellulose Nanocrystals Prepared by Sulfuric Acid Hydrolysis. *Cellulose* **2013**, *20* (2), 785−794.

(92) Beck, S.; Méthot, M.; Bouchard, J. General Procedure for Determining Cellulose Nanocrystal Sulfate Half-Ester Content by Conductometric Titration. *Cellulose* **2015**, *22* (1), 101−116.

(93) Agarwal, U. P.; Ralph, S. a.; Reiner, R. S.; Baez, C. Probing Crystallinity of Never-Dried Wood Cellulose with Raman Spectroscopy. *Cellulose* **2016**, *23* (1), 125−144.

(94) Nishiyama, Y.; Langan, P.; Chanzy, H. Crystal Structure and Hydrogen-Bonding System in Cellulose Ibeta from Synchrotron X-Ray and Neutron Fiber Diffraction. *J. Am. Chem. Soc.* **2002**, *124* (31), 9074−9082.

(95) Park, S.; Baker, J. O.; Himmel, M. E.; Parilla, P. a; Johnson, D. K. Cellulose Crystallinity Index: Measurement Techniques and Their Impact on Interpreting Cellulase Performance. *Biotechnol. Biofuels* **2010**, *3* (1), 10.

(96) French, A. D.; Santiago Cintrón, M. Cellulose Polymorphy, Crystallite Size, and the Segal Crystallinity Index. *Cellulose* **2013**, *20* (1), 583−588.

(97) Driemeier, C.; Calligaris, G. a. Theoretical and Experimental Developments for Accurate Determination of Crystallinity of Cellulose I Materials. *J. Appl. Crystallogr.* **2011**, *44* (1), 184−192.

(98) Ahvenainen, P.; Kontro, I.; Svedström, K. Comparison of Sample Crystallinity Determination Methods by X-Ray Diffraction for Challenging Cellulose I Materials. *Cellulose* **2016**, *23* (2), 1073−1086.

(99) Edgar, C. D.; Gray, D. G. Influence of Dextran on the Phase Behavior of Suspensions of Cellulose Nanocrystals. *Macromolecules* **2002**, *35* (19), 7400−7406.

(100) Bhattacharjee, S. DLS and Zeta Potential – What They Are and What They Are Not? *J. Controlled Release* **2016**, *235*, 337−351.

(101) Garboczi, E. J.; Snyder, K. a.; Douglas, J. F.; Thorpe, M. F. Geometrical Percolation Threshold of Overlapping Ellipsoids. *Phys. Rev. E: Stat. Phys., Plasmas, Fluids, Relat. Interdiscip. Top.* **1995**, *52* (1), 819−828.

(102) Boluk, Y.; Danumah, C. Analysis of Cellulose Nanocrystal Rod Lengths by Dynamic Light Scattering and Electron Microscopy. *J. Nanopart. Res.* **2014**, *16* (1), 2174.

(103) Maurer, R. J.; Sax, A. F.; Ribitsch, V. Moleular Simulation of Surface Reorganization and Wetting in Crystalline Cellulose I and II. *Cellulose* **2013**, *20*, 25−42.

(104) Lahiji, R. R.; Xu, X.; Reifenberger, R.; Raman, A.; Rudie, A.; Moon, R. J. Atomic Force Microscopy Characterization of Cellulose Nanocrystals. *Langmuir* **2010**, *26* (6), 4480−4488.

(105) Brinkmann, A.; Chen, M.; Couillard, M.; Jakubek, Z. J.; Leng, T.; Johnston, L. J. Correlating Cellulose Nanocrystal Particle Size and Surface Area. *Langmuir* **2016**, *32*, 6105.

(106) Postek, M. T.; Vladar, A.; Dagata, J.; Farkas, N.; Ming, B.; Wagner, R.; Raman, A.; Moon, R. J.; Sabo, R.; Wagner, T. H.; et al. Development of the Metrology and Imaging of Cellulose Nanocrystals. *Meas. Sci. Technol.* **2011**, *22* (2), 024005.

(107) Peng, Y.; Gardner, D. J.; Han, Y.; Kiziltas, A.; Cai, Z.; Tshabalala, M. a. Influence of Drying Method on the Material Properties of Nanocellulose I: Thermostability and Crystallinity. *Cellulose* **2013**, *20* (5), 2379−2392.

(108) Langan, P.; Nishiyama, Y.; Chanzy, H. X-Ray Structure of Mercerized Cellulose II at 1 Å Resolution. *Biomacromolecules* **2001**, *2* (2), 410−416.

(109) Dorris, G. M.; Gray, D. G. The Surface Analysis of Paper and Wood Fibers by ESCA (Electron Spectroscopy for Chemical Analysis). I. Application to Cellulose and Lignin. *Cellul. Chem. Technol.* **1978**, *12*, 9−23.

(110) Johansson, L. S.; Campbell, J. M. Reproducible XPS on Biopolymers: Cellulose Studies. *Surf. Interface Anal.* **2004**, *36* (8), 1018−1022.

(111) Edgar, C. D.; Gray, D. G. Smooth Model Cellulose I Surfaces from Nanocrystal Suspensions. *Cellulose* **2003**, *10*, 299−306.

(112) King, D. Oxidation of Gold by Ultraviolet Light and Ozone at 25 C. *J. Vac. Sci. Technol., A* **1995**, *13*, 1247−1253.

(113) Zoppe, J. O.; Habibi, Y.; Rojas, O. J.; Venditti, R. a; Johansson, L.-S.; Efimenko, K.; Österberg, M.; Laine, J. Poly(N-Isopropylacrylamide) Brushes Grafted from Cellulose Nanocrystals via Surface-Initiated Single-Electron Transfer Living Radical Polymerization. *Biomacromolecules* **2010**, *11* (10), 2683−2691.

(114) Camarero Espinosa, S.; Kuhnt, T.; Foster, E. J.; Weder, C. Isolation of Thermally Stable Cellulose Nanocrystals by Phosphoric Acid Hydrolysis. *Biomacromolecules* **2013**, *14* (4), 1223−1230.

(115) Hirai, A.; Inui, O.; Horii, F.; Tsuji, M. Phase Separation Behavior in Aqueous Suspensions of Bacterial Cellulose Nanocrystals Prepared by Sulfuric Acid Treatment. *Langmuir* **2009**, *25* (1), 497−502.

(116) Honorato-Rios, C.; Kuhnhold, A.; Bruckner, J.; Dannert, R.; Lagerwall, J. P. Equilibrium Liquid Crystal Phase Diagrams and Detection of Kinetic Arrest in Cellulose Nanocrystal Suspensions. *Front. Mater.* **2016**, *3* (21), 1−13.

(117) Kalashnikova, I.; Bizot, H.; Cathala, B.; Capron, I. Modulation of Cellulose Nanocrystals Amphiphilic Properties to Stabilize Oil/water Interface. *Biomacromolecules* **2012**, *13* (1), 267−275.

(118) Uetani, K.; Yano, H. Semiquantitative Structural Analysis of Highly Anisotropic Cellulose Nanocolloids. *ACS Macro Lett.* **2012**, *1* (6), 651−655.

(119) Giese, M.; Blusch, L. K.; Khan, M. K.; MacLachlan, M. J. Functional Materials from Cellulose-Derived Liquid-Crystal Templates. *Angew. Chem., Int. Ed.* **2015**, *54* (10), 2888−2910.

(120) Niinivaara, E.; Faustini, M.; Tammelin, T.; Kontturi, E. Water Vapor Uptake of Ultrathin Films of Biologically Derived Nanocrystals: Quantitative Assessment with Quartz Crystal Microbalance and Spectroscopic Ellipsometry. *Langmuir* **2015**, *31* (44), 12170−12176.

Appendix 3: Chapter 3 Supporting Information

Crystallinity

X-ray Diffraction. XRD measurements, to obtain the degree of crystallinity, were performed on freeze dried CNCs samples using a Bruker D8 DAVINCI diffractometer (Bruker USA) with a cobalt sealed tube source (λ_{avg} = 1.79026 Å), 35 kV, 45 mA with a parallel focus Goebel Mirror, Vantec 500 area detector, and 0.5 mm micro-slit and 0.5 mm short collimator over a 2θ range of 8-45˚. Si wafer blanks were subtracted from all sample measurements. Two dimensional area detector frames were integrated to produce diffraction patterns, which then underwent Rietveld refinement. Percent crystallinity was determined by deconvolution using the cellulose I single crystal information file (CIF) to define peak position and a fixed amorphous peak at 24.1˚. A pseudo-voigt function with linear background was used to fit peak shape and the CIF file with a March Dollase preferred orientation function model was used to fit peak intensity. For samples that contained both cellulose I and cellulose II structures the percentage of each crystal phase is presented. It is important to note that there are a number of methods described in the literature used to determine the crystallinity of cellulose and is not only limited to XRD.[1–4] Furthermore, the validity and limitations of these methods and data fitting routines is a hotly debated topic and is beyond the scope of this work. Largely XRD is reported and the Rietveld refinement commonly considered to be the most accurate method.[5–7] In a recent publication however, Ahvenainen *et al.* found good correlation with the five most common XRD fitting methods and the two dimensional Rietveld method.[8] Moreover, within their work it is emphasized that comparison between samples and laboratories is extremely challenging. As such the crystallinity values presented here should be taken as relative (and comparable within this study) not absolute. Using the deconvolution method presented above the error in these measurements is taken to be 3-5%.

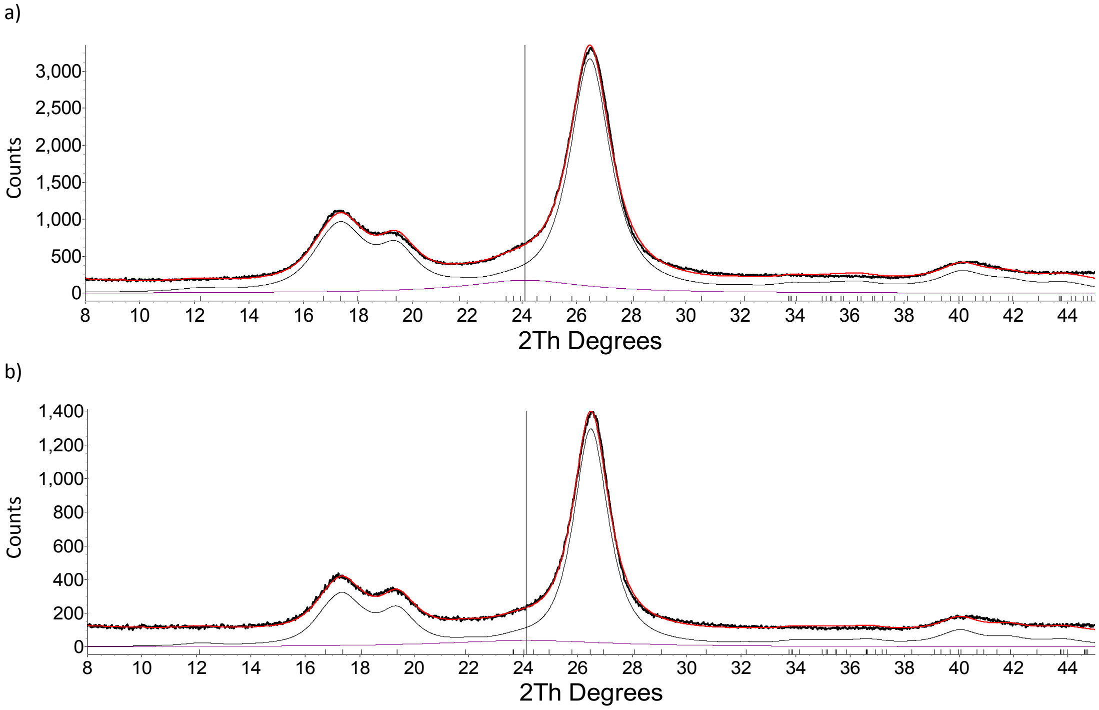

Figure S1: XRD spectra of AITF CNCs **a)** as received and **b)** Soxhlet extracted in ethanol for 24 h.

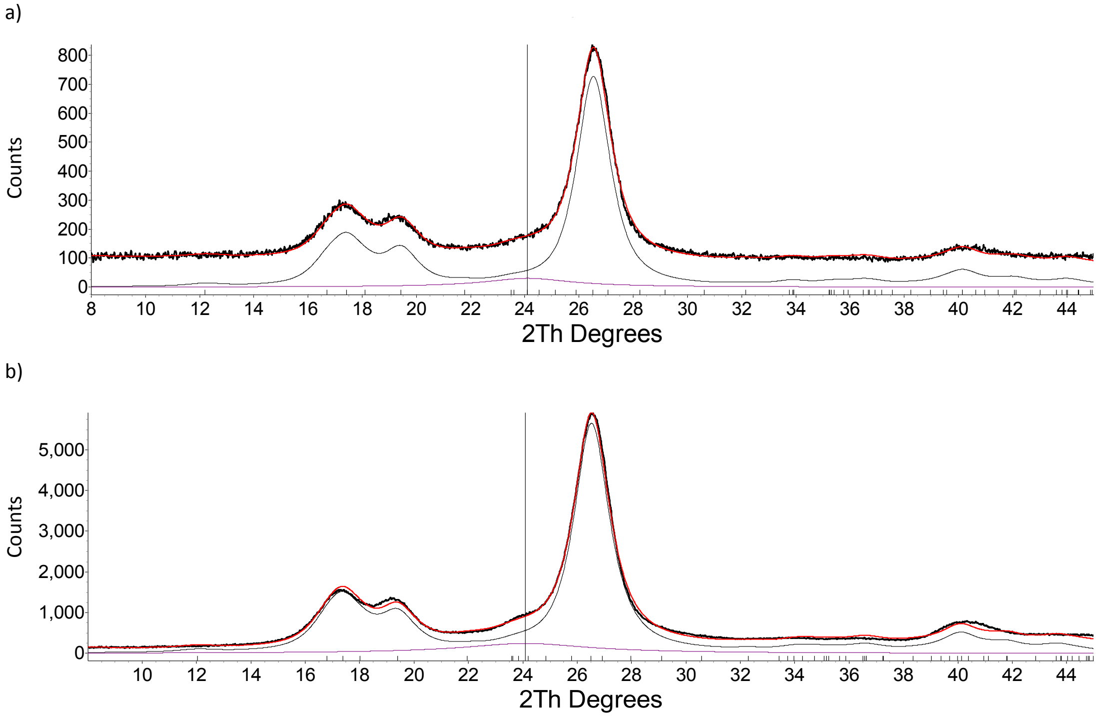

Figure S2: XRD spectra of Lab-Made CNCs **a)** as received and **b)** Soxhlet extracted in ethanol for 24 h.

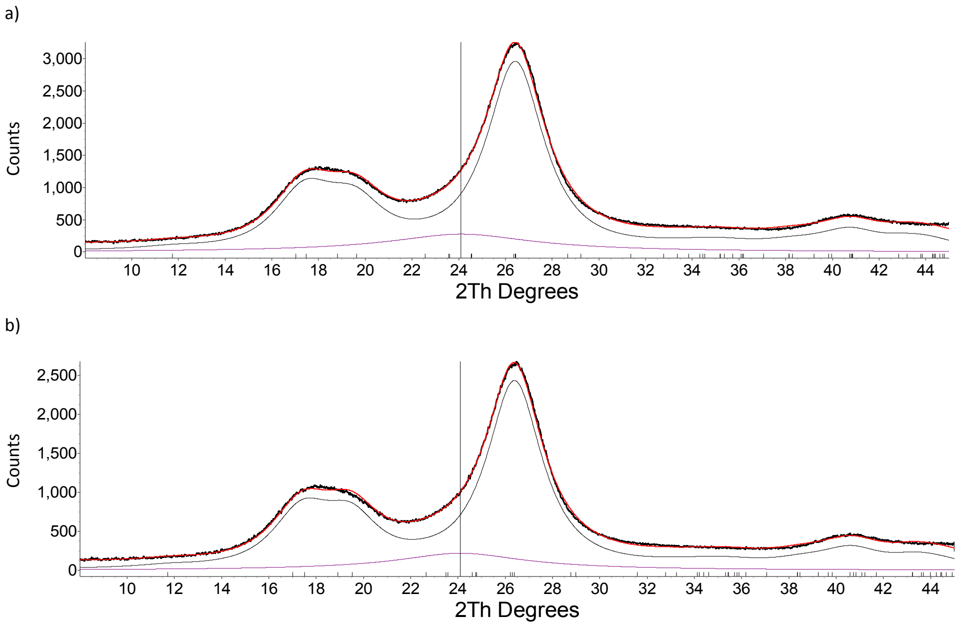

Figure S3: XRD spectra of CelluForce CNCs **a)** as received and **b)** Soxhlet extracted in ethanol for 24 h.

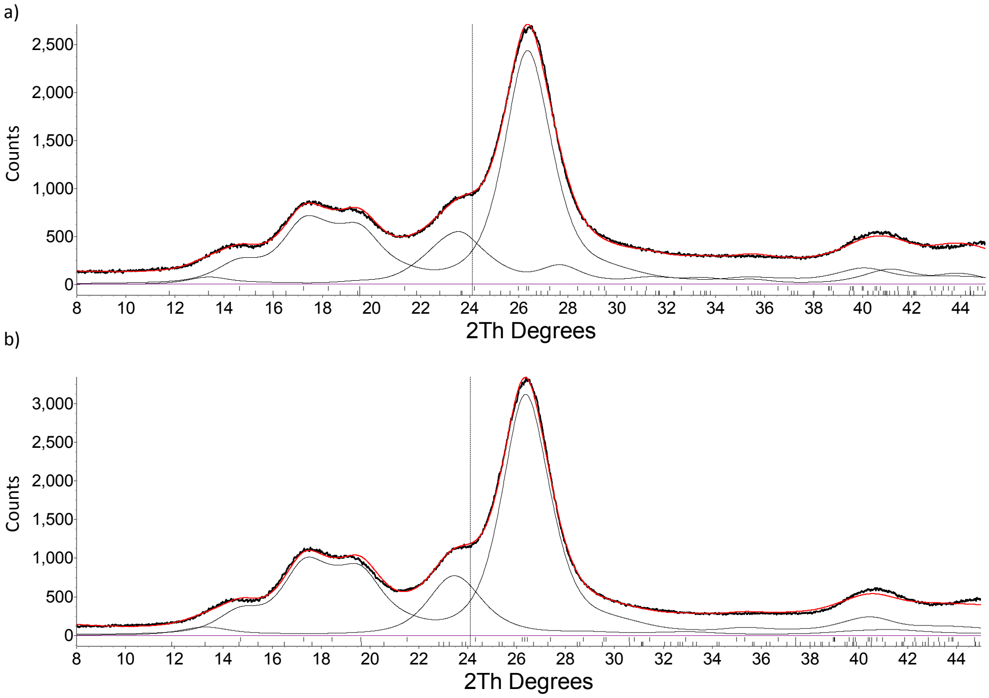

Figure S4: XRD spectra of FPL CNCs **a)** as received and **b)** Soxhlet extracted in ethanol for 24 h.

Thermal Stability

Thermal Gravimetric Analysis. Thermal gravimetric analysis (TGA) was performed using TA Instruments Q50 thermal analyzer under a constant 100 mL/min argon flow. A minimum of 1 mg of freeze-dried as received and Soxhlet extracted CNCs were heated to 600˚C at heating rate of 10˚C/min.

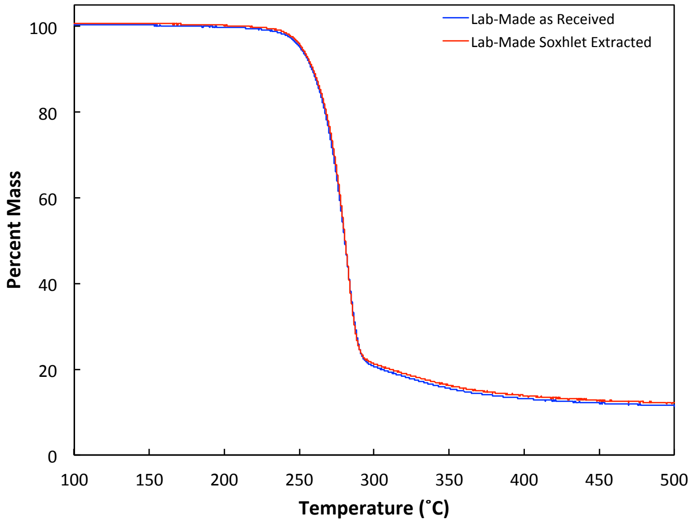

Figure S5: TGA curves of as received and Soxhlet extracted Lab-Made CNCs.

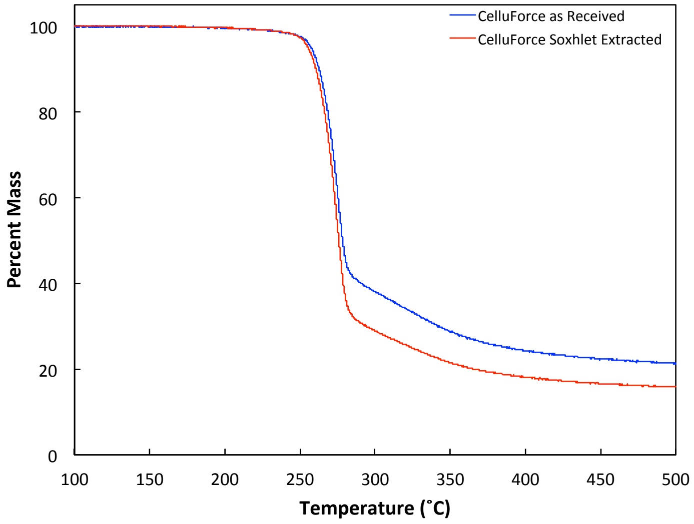

Figure S6: TGA curves of as received and Soxhlet extracted CelluForce CNCs.

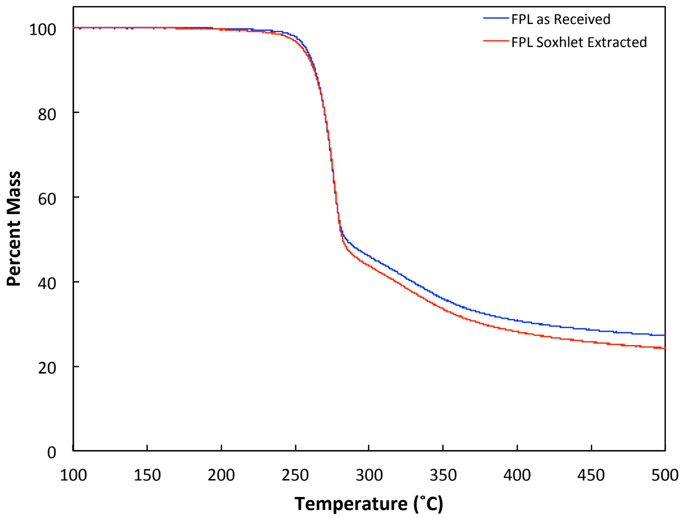

Figure S7: TGA curves of as received and Soxhlet extracted FPL CNCs.

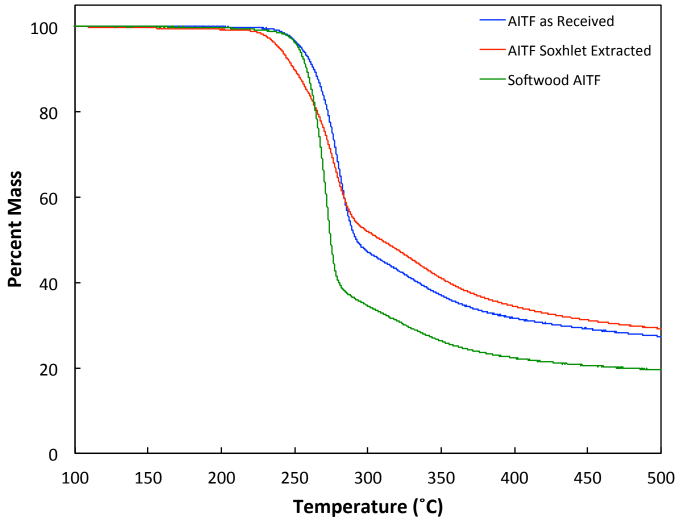

Figure S8: TGA curves of as received and Soxhlet extracted cotton AITF CNCs and as received softwood AITF CNCs.

Changing Source and Production Scale

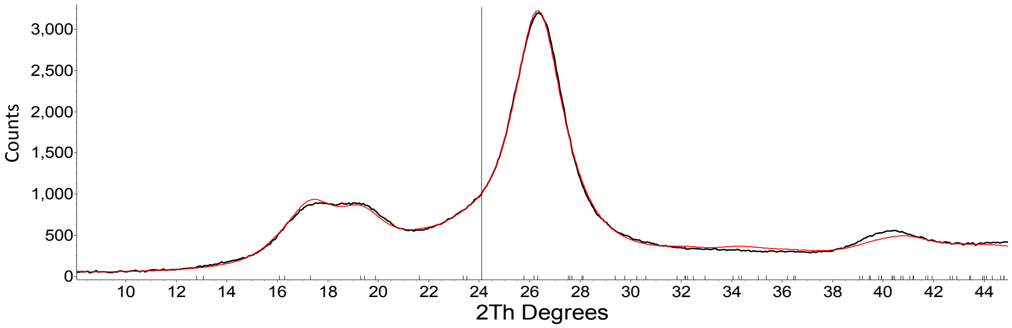

Figure S9: XRD spectra of as received AITF CNCS extracted from bleached softwood pulp.

Other Nanocellulose Producers

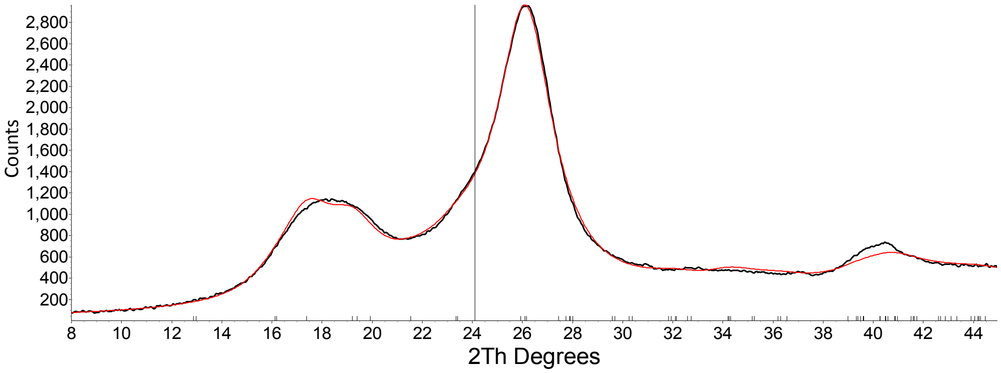

Figure S10: XRD spectra of as received API's BioPlus™ Crystals

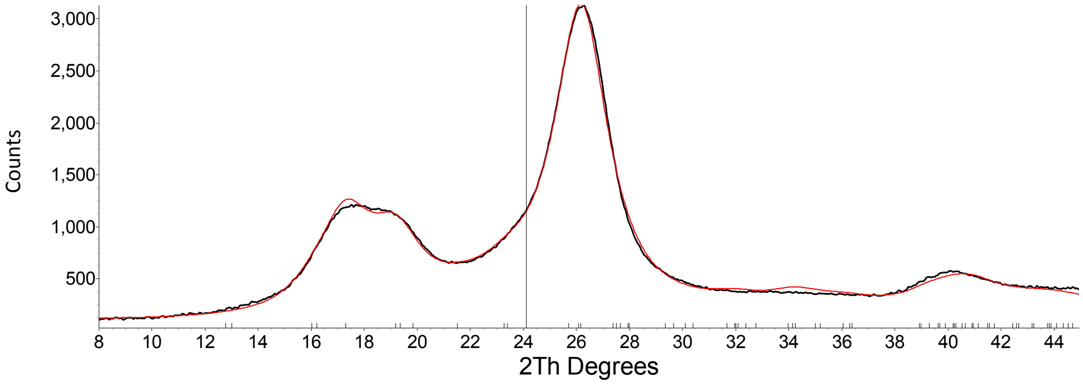

Figure S11: XRD spectra of as received Blue Goose Biorefineries BGB Natural™ nanocellulose

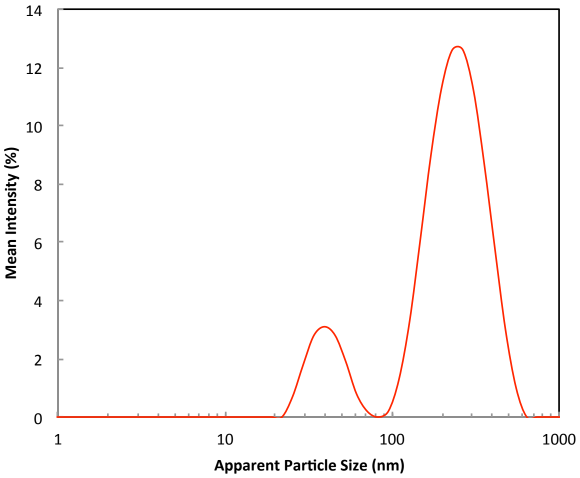

Figure S12: Apparent particle size distribution of Blue Goose Biorefineries BGB Natural™ as measured by DLS

References

(1) Agarwal, U. P.; Ralph, S. a.; Reiner, R. S.; Baez, C. Probing Crystallinity of Never-Dried Wood Cellulose with Raman Spectroscopy. *Cellulose* **2016**, *23* (1), 125–144.
(2) Nishiyama, Y.; Langan, P.; Chanzy, H. Crystal Structure and Hydrogen-Bonding System in Cellulose Ibeta from Synchrotron X-Ray and Neutron Fiber Diffraction. *J. Am. Chem. Soc.* **2002**, *124* (31), 9074–9082.
(3) Park, S.; Baker, J. O.; Himmel, M. E.; Parilla, P. a; Johnson, D. K. Cellulose Crystallinity Index: Measurement Techniques and Their Impact on Interpreting Cellulase Performance. *Biotechnol. Biofuels* **2010**, *3* (1), 10.
(4) French, A. D.; Santiago Cintrón, M. Cellulose Polymorphy, Crystallite Size, and the Segal Crystallinity Index. *Cellulose* **2013**, *20* (1), 583–588.
(5) Driemeier, C.; Calligaris, G. a. Theoretical and Experimental Developments for Accurate Determination of Crystallinity of Cellulose I Materials. *J. Appl. Crystallogr.* **2011**, *44* (1), 184–192.
(6) Oliveira, R. P.; Driemeier, C. CRAFS: A Model to Analyze Two-Dimensional X-Ray Diffraction Patterns of Plant Cellulose. *J. Appl. Crystallogr.* **2013**, *46* (4), 1196–1210.
(7) Driemeier, C. Two-Dimensional Rietveld Analysis of Celluloses from Higher Plants. *Cellulose* **2014**, *21* (2), 1065–1073.
(8) Ahvenainen, P.; Kontro, I.; Svedström, K. Comparison of Sample Crystallinity Determination Methods by X-Ray Diffraction for Challenging Cellulose I Materials. *Cellulose* **2016**, *23* (2), 1073–1086.

Chapter 4

Cellulose Nanocrystal Interactions Probed by Thin Film Swelling to Predict Dispersibility

In the previous chapter it was established that although there are differences between industrially produced CNCs, generally they compare well to those produced in the laboratory. As a result, it can be expected that knowledge obtained from studying laboratory produced CNCs can be readily translated to commercially available materials. Building upon this understanding, this chapter presents a new surface plasmon resonance spectroscopy-based platform to examine the forces that govern CNC particle-particle interactions in various solvents. Thin CNC films are used to mimic the highly aggregated state of CNCs which is found in spray dried or freeze dried CNC powders. Since commercial CNCs are most often sold/shipped as dry powders it is important to understand what interactions must be overcome to disperse CNCs.

In this chapter, the experimental design and implementation was my own. All data were collected and analysed by myself. The chapter was drafted by myself and later edited by my academic advisor, Dr. Emily Cranston. Dr. Marco Villalobos from Cabot Corporation was my industrial co-supervisor and provided input on research direction and feedback on the manuscript. This chapter and supporting information (Appendix 4) is reprinted as it appears in *Nanoscale*, with permission from the Royal Chemical Society © 2016.

Cellulose Nanocrystal Interactions Probed by Thin Film Swelling to Predict Dispersibilty
Michael S. Reid, Marco Villalobos and Emily D. Cranston
Nanoscale, **2016**, *8,* pp 12247-12257
DOI: 10.1039/C6NR01737A

Nanoscale

PAPER

View Article Online
View Journal | View Issue

Cite this: *Nanoscale*, 2016, **8**, 12247

Cellulose nanocrystal interactions probed by thin film swelling to predict dispersibility†

Michael S. Reid,[a] Marco Villalobos[b] and Emily D. Cranston*[a]

Received 1st March 2016,
Accepted 27th May 2016

DOI: 10.1039/c6nr01737a

www.rsc.org/nanoscale

The production of well-dispersed reinforced polymer nanocomposites has been limited due to poor understanding of the interactions between components. Measuring the cohesive particle–particle interactions and the adhesive particle–polymer interactions is challenging due to nanoscale dimensions and poor colloidal stability of nanoparticles in many solvents. We demonstrate a new cohesive interaction measurement method using cellulose nanocrystals (CNCs) as a model system; CNCs have recently gained attention in the composites community due to their mechanical strength and renewable nature. Multi-wavelength surface plasmon resonance spectroscopy (SPR) was used to monitor the swelling of CNC thin films to elucidate the primary forces between CNCs. This was achieved by measuring swelling *in situ* in water, acetone, methanol, acetonitrile, isopropanol, and ethanol and relating the degree of swelling to solvent properties. Films swelled the most in water where we estimate 1.2–1.6 nm spacings between CNCs (or 4–6 molecular layers of water). Furthermore, a correlation was found between film swelling and the solvent's Hildebrand solubility parameter (R^2 = 0.9068). The hydrogen bonding component of the solubility parameters was more closely linked to swelling than the polar or dispersive components. The films remained intact in all solvents, and using DLVO theory we have identified van der Waals forces as the main cohesive interaction between CNCs. The trends observed suggest that solvents (and polymers) alone are not sufficient to overcome CNC–CNC cohesion and that external energy is required to break CNC agglomerates. This work not only demonstrates that SPR can be used as a tool to measure cohesive particle–particle interactions but additionally advances our fundamental understanding of CNC interactions which is necessary for the design of cellulose nanocomposites.

Introduction

Despite recent advances, reinforced polymeric nano-composites (apart from elastomeric systems) are still in their infancy. Cost, poor particle dispersibility and limited load transfer between the phases have been major stumbling blocks within the field. The variety of matrices and particles available requires specific application design, however, ultimately both the mechanical and thermal properties of nanocomposites are governed by the balance between cohesive particle–particle and adhesive particle–polymer interactions.[1] Indeed Akcora *et al.* were able to predict and control nanoparticle assembly in polystyrene matrices by altering the cohesive and adhesive interactions within the composite.[2] Grafting increasingly dense polymer chains onto the nanoparticles reduced particle–particle interactions and assembly shifted from spherical aggregates to sheets to strings and finally individually dispersed nanoparticles. (Herein we define cohesion as the interaction between nanoparticles of the same material in contrast to the traditional definition of cohesion being within a material; this is also used in the powder and composites materials community.[3]) Advancing the field of reinforced nanocomposites requires methods to extract and predict these interactions in a variety of systems.

Cellulose nanocrystals (CNCs) are an abundant and sustainable rod-shaped nanomaterial that has recently been used in biomedical devices,[4–6] as rheological modifiers,[7,8] emulsion stabilizers[9–12] and many other composite applications.[13–17] Depending on the cellulose source (*e.g.*, wood, cotton, bacteria, algae or tunicate) CNCs range from 100–1000 nm in length and 5–20 nm in cross-section and are commonly extracted through sulfuric acid hydrolysis.[16,18,19] Although, applications span several fields, the potential for CNCs to act as reinforcing agents in polymer matrices is widely discussed.[15] Analytical models and experimental measurements report a longitudinal

---

[a] *Department of Chemical Engineering, McMaster University, Hamilton, Ontario, Canada L8S 4L8. E-mail: ecranst@mcmaster.ca*
[b] *Cabot Corporation, Billerica, MA 01821, USA*

† Electronic supplementary information (ESI) available: Details regarding CNC purification and characterization, XPS data of raw and extracted CNCs, AFM images of dry CNC films, fitting of SPR data and layer parameters, AFM images of water swollen CNC films, reference Hildebrand and Hansen solubility parameters for solvents tested, description of DLVO calculations. See DOI: 10.1039/c6nr01737a

Young's modulus that ranges from 56–220 GPa and a density of 1.5–1.6 g cm^{-1}.[3,15]

Currently, the major hurdle limiting CNC reinforced nanocomposites is the hydrophilic nature of the particles. High density of surface hydroxyl groups limits the compatibility with hydrophobic polymers leading to CNC aggregation and limited mechanical improvement. Furthermore, in the dried form (spray dried or freeze dried), CNCs can form strong agglomerates (sometimes attributed to hydrogen bonding)[20] which are not easily overcome when CNCs are added to molten polymers or compounded using organic solvents.[21–23] A significant amount of work has aimed to improve particle–polymer adhesion by esterification, silylation, urethanization, amidation, as well as grafting polymers to and from the CNC surface.[24] Regardless of the CNC surface chemistry, the ability to extract and predict particle–particle and particle–polymer interactions in composites remains challenging due to nanoscale dimensions and poor colloidal stability in non-aqueous environments.

The objective of this work is to probe cohesive particle–particle interactions of sodium-form sulfuric acid-hydrolyzed CNCs, which are currently the type of CNCs most widely available commercially[25] and as such, are the most industrially relevant for future CNC nanocomposite production. To this end, supported CNC thin films were swollen in various liquids to probe solvent uptake and particle–particle spacing. We find that the films swell in all solvents tested, the most in water and the least in acetone (with intermediate swelling observed for alcohols and acetonitrile), and in all cases films are held together by van der Waals forces. While qualitatively this is expected based on past fibre/cellulose studies, we believe that this is the first direct and quantitative report of probing CNC–CNC interactions and comparing water and non-aqueous solvents.

Cellulose thin films have been commonly used to examine adhesion, adsorption and swelling of regenerated cellulose, cellulose nanofibrils and CNCs in water.[26–33] With respect to pure CNC films, Kittle *et al.*[32] observed that swollen films contain 75% water by mass, nearly three times greater than earlier measurements by Aulin *et al.*[30] Rationalizing the disparity between these measurements is challenging but is suggested to be due to the initial state of hydration in the film.[32] In the most recent study, Niinivaara *et al.* monitored CNC film swelling in humid environments by quartz crystal microbalance with dissipation (QCM-D) and spectroscopic ellipsometry.[33] They deduced that hydrated CNCs retain a 2 nm water layer around each CNC particle. While these works provide critical insight into CNC film swelling in aqueous environments, there remains poor agreement across studies and a lack of understanding of these interactions in non-aqueous liquid media.

Our work uses surface plasmon resonance spectroscopy (SPR) which is less common than ellipsometry and QCM-D, and is an optical technique that monitors the intensity of a laser beam reflected off a plasmonic surface (gold or silver); we show here that it offers quantitative insight into the interactions between nanoparticles, in a straightforward way. Unlike most other techniques, SPR is capable of tracking *in situ* the transition from the dry to the liquid swollen state. SPR is regularly used as a biosensor to measure adsorption or desorption (and binding kinetics) and although it has been used to probe various cellulose surfaces in aqueous environments[34–44] some SPR instrumentation is more suited to materials science investigations, such as the equipment used here, where film thickness and density are obtained from optical fitting of SPR reflectivity over a large angular range. This is in contrast to instruments that only work over a small angular range and, for example, cannot be used in media with different refractive indices (n) from water. Despite the fact that full angle SPR can operate in a number of solvents, the operational range for our films is generally limited to solvents with refractive indices below n = 1.4, excluding typical wettability test solvents, such as methylene iodide (n = 1.530).

In a recent study also based on SPR, Kontturi *et al.* monitored water content of highly porous cellulose nanofibril films, which when swollen contained over 50% water, agreeing with parallel QCM-D measurements.[29] Importantly, the authors note that sample heterogeneity within the cellulose nanofibril film made SPR measurements and data fitting very challenging. Here we test smooth and uniform CNC films in a variety of suitable SPR solvents: water, acetone, methanol, acetonitrile, isopropanol, and ethanol, and although they do not represent common hydrophobic polymers in terms of their solubility parameters (*i.e.*, polyethylene or polystyrene), they do mimic polymers aimed towards biodegradable composites and biomedical applications such as poly(vinyl alcohol), poly(lactic acid) and poly(vinyl pyrrolidone).

This paper presents SPR (with supporting results from atomic force microscopy, AFM) as a novel method to probe cohesive particle–particle interactions through film swelling and relate nanoparticle dispersibility to Hildebrand and Hansen solubility parameters. We believe this technique and our approach is applicable to other nanoparticle systems and can offer significant insight for nanoparticle dispersion and nanocomposite design. The study of CNC films specifically, differs from studying the properties of individualized CNCs in aqueous suspension[18,45] or in polar-organic solvents[46] as CNC interactions within the film are expected to represent aggregated dried CNCs which is the commercially available format. Overall, we demonstrate that CNC particle–particle interactions are strong and are dominated by hydrogen bonding and attractive van der Waals forces.

Experimental

Materials

Whatman cotton ashless filter aid was purchased from GE Healthcare Canada. Sulfuric acid, methanol, acetone, acetonitrile and isopropanol were all obtained from Caledon Laboratory Chemicals (Georgetown, ON, Canada). Anhydrous ethanol was purchased from Commercial Alcohols (Brampton, ON, Canada). Hydrogen peroxide was purchased from Sigma Aldrich (Oakville, ON, Canada). All chemicals were used as received. Water used was purified Type I water with a resistivity of 18.2 MΩ cm (Barnstead NANOpure DIamond system, ThermoScientific, Asheville, NC).

Sulfuric acid hydrolysis of CNCs

CNCs were prepared by sulfuric acid hydrolysis, as previously described.[47] Briefly, 40 g of cotton Whatman ashless filter aid was digested in 700 mL of 64 wt% sulfuric acid at 45 °C for 45 min under continuous mechanical stirring. Immediately following hydrolysis, the mixture was diluted 10-fold with 4 °C water to quench the reaction. The suspension was centrifuged at 6000 rpm for 10 min four times to remove excess acid. The precipitate was then diluted and dialysed against water until the pH stabilized (~2 weeks). The suspension was sonicated (Sonifier 450, Branson Ultrasonics, Danbury, CT) continuously in an ice bath for 15 min three times at 60% output. The CNC suspensions were neutralized (converted to the sodium salt form) by the addition of an appropriate amount of 1 mM NaOH and then lyophilized for storage. Although work has shown that CNCs can adsorb organic material during production and from the environment[48] we observed an insignificant reduction in the aliphatic carbon composition for spin coated CNC films before and after soxhlet extraction (ESI Table S1†). We believe that environmental contamination during sample preparation cannot be avoided and as a result, CNCs used in this study were not purified further following dialysis. The CNC dimensions were 4–15 nm by 50–306 nm, measured by AFM of 100 particles with an average cross section and length of 8 nm and 122 nm respectively. The surface sulfate half ester content was 0.7% sulfur by mass corresponding to approximately 0.41 charge groups per nm^2 of CNC surface area as determined by conductometric titration with NaOH.[49]

Film preparation

CNC films were prepared on polished Si wafers (MEMC Electronic Materials Sdn Bhd, Petaling Jaya, Malaysia) or SiO_2 coated SPR sensors (BioNavis, Ylöjärvi, Finland) by spin coating under N_2 gas (G3P Spincoat, Specialty Coating Systems Inc. Indianapolis, USA) at 4000 rpm for 30 s with a 7 s ramp. Prior to deposition, all surfaces were cleaned in a piranha solution (3 : 1 concentrated sulfuric acid to hydrogen peroxide) for 30 min, followed by continuous rinsing with purified water and drying by a stream of N_2 gas. Suspensions were prepared by dispersing freeze dried CNCs in water and sonicating at 60% amplitude for 30 s. Film thicknesses were controlled by varying the CNC suspension concentration between 1 and 3 wt%. Following spin coating, films were heat treated at 80 °C for 8 hours (overnight) to remove water from the film. Films were then gently rinsed with purified water and heat treated again for 8 hours. We believe that this procedure removes loosely bound CNCs from the surface and improves the overall stability of the film by removing excess water, which increases particle–particle interaction by replacing water–CNC hydrogen bonds with CNC–CNC hydrogen bonds as discussed by Beck *et al.*[21] Additionally we propose this procedure helps to eliminate radial ordering of CNCs which may occur during spin coating (as evidenced by AFM imaging).

Atomic force microscopy

AFM images were collected in alternating current (AC) mode using an Asylum MFP-3D instrument (Asylum Research an Oxford Instrument Company, Santa Barbara, CA). Images of dry films were collected in air under ambient conditions. Rectangular FMR cantilevers (NanoWorld) with normal spring constants of 1.2–5.5 N m^{-1} and resonant frequencies of 60–90 kHz were used for all morphological and scratch height measurements. Root-mean-squared (rms) roughness was calculated by averaging 25 1 μm × 1 μm areas over a 5 μm × 5 μm image. The thickness of dry CNC films was determined by *in situ* AFM scratch height analysis. Scratching was performed using the AFM tip in contact mode (with a set point of *ca.* 1 V or 200 nN) to gently remove CNCs from the surface over a 1 μm × 1 μm area. The force used was sufficient to displace CNCs but leave the underlying SiO_2 substrate undamaged. The scratched area was reimaged (5 μm × 5 μm) in AC mode, using the same tip used to scratch, to obtain the cross sectional profile. Images were processed in Igor Pro 6.0 running Asylum Research AFM software (version 13.17) using a second order flatten routine, excluding the scratched region. Thicknesses were measured by taking the average height difference from the top of the CNC film and the underlying substrate.

Swollen films were measured in purified water using an open fluid cell. Prior to swelling, dry films were scratched as described above and the cross section was measured. Water was then introduced and the system was allowed to equilibrate (~30 min). The previously scratched areas were then reimaged (5 μm × 5 μm) and the height of the film was determined. Film thickness values reported are from three separate films and images were processed in the same fashion as dry films and the data error bars represent the standard deviation of the initial film thickness.

Surface plasmon resonance

Full angle (40°–77°) SPR curves were collected using a SPR Navi™ 200 (BioNavis, Ylöjärvi, Finland). Laser wavelengths of 785 nm and 670 nm with a spot size of 500 μm × 500 μm were simultaneously used to continuously monitor dry and swollen CNC films. Films were swollen under constant solvent flow rates of 100 μL min^{-1} at 25 °C and allowed to equilibrate for 30 min. Within the flow cell an O-ring confines the film in the *xy* (lateral) plane and thus films are assumed to only swell in the *z*-direction (vertical to the sensor surface). Experimental SPR curves were fit by the Fresnel equations using recursion formalism and assuming parallel slab geometry with the free software Winspall 3.01 (Max-Planck Institute for Polymer Research, Mainz, Germany). We note that the SPR signal is averaged over the laser spot and that film roughness and thickness will vary over the sensor surface (surface roughness by AFM is 5.7 nm over 1 μm^2). While the precision in the SPR curve fitting and the relative changes in thickness are indeed at the angstrom level, the overall accuracy in thickness is likely in the nanometer range.

The refractive index (n) and the thickness (d) of dry CNC films were independently determined following the multi-wavelength SPR approach as described by Granqvist *et al.*[50] It is well known that when optically fitting layer parameters the n and d correlate to each other and form a n–d continuum of possible solutions, but by employing both 670 nm and 785 nm wavelengths simultaneously, two sets of n–d continua are established from which a unique solution for n and d can be obtained. Bare SiO_2 sensors were initially modeled to determine background layer parameters and n–d continua were calculated by modeling CNC film thickness for refractive indices between 1.30 and 1.55 with 0.005 intervals. Plotting the two continua on the same axis determined the intersection point and solutions for n and d. Assuming CNC films behave as Cauchy materials, when used, the chromatic dispersion relation ($\mathrm{d}n/\mathrm{d}\lambda$) of pure cellulose was taken to be 0.0271 μm^{-1} and used to shift the 670 nm continuum.[29,51] Notably $\mathrm{d}n/\mathrm{d}\lambda$ for air was considered negligible. Both shifted and non-shifted continua displayed intersection points and the difference between the two is taken as the uncertainty in the fitting and is discussed below. Within this study, the multi-wavelength approach was only applied to dry CNC films. The refractive index of CNCs is reported to range from 1.51 [32] to 1.62 [47] and is taken as $n_{\mathrm{CNC}} = 1.55$ within this work.

Optical theory and thin film analysis. *In situ* film swelling has been extensively studied by optical techniques, in particular *via* ellipsometry.[33,52] However, extracting parameters such as thickness, refractive index and volume fraction of swollen films remains challenging and can contain a significant degree of error. For example, failure to account for the change in free volume within polymer films can lead to thickness errors in excess of 100% when using an effective medium approximation.[53] Additionally, depending on the penetrant, swelling can occur following either constant or volume additive regimes convoluting which optical models are appropriate.[54] Considering the volume additive regime: as the film swells the volume fraction of the swollen material decreases, reducing the effective refractive index of the system. As a result, an inverse relationship develops between film thickness and refractive index. This was successfully employed by Erdoğan *et al.* who measured polymer film swelling *via* solvent vapour sorption using fixed angle SPR.[55–57] In their study, the ratios of the volume (V) and optical intensity (I) from the initial to the equilibrium swollen state were inversely proportional according to eqn (1):

$$\frac{V_{\mathrm{Eq}}}{V_t} = \frac{I_t}{I_{\mathrm{Eq}}} \tag{1}$$

where subscripts, t and Eq refer to the film at time, t, and at equilibrium, respectively. It is important to note that because the refractive index of solvent vapour does not differ significantly from air the bulk refractive index of the system remains constant. As a result, angular shifts in the SPR peak are relatively small (<1°) and fixed angle SPR is applicable.[55] When liquid swelling agents are used the bulk refractive index of the system radically changes, significantly shifting the SPR peak position (>25°). Full angle SPR measurements are capable of accounting for large angular changes and thus swelling information can be extracted. In the present study, the significant increase in angular position often shifted the 670 nm SPR peak outside the measurable range, eliminating the possibility for a multi-wavelength approach. As a result, CNC films were characterized by the difference in angular position of the 785 nm SPR peak and total internal reflectance peak (TIR) in an adapted form of eqn (1):

$$\frac{V_{\mathrm{Eq}}}{V_0} = \frac{\Delta\theta_0}{\Delta\theta_{\mathrm{Eq}}} \tag{2}$$

where $\Delta\theta_0$ and $\Delta\theta_{\mathrm{Eq}}$ are the difference between the SPR peak and TIR angles for the initial dry and swollen films, respectively. Critically, $\Delta\theta_{\mathrm{Eq}}$ must be corrected to account for the solvent refractive index to isolate angular shifts due to CNC film swelling alone; contrary to the common description of SPR it is not just the TIR that shifts when the media refractive index changes but the SPR peak as well. Fig. 1 presents modeled (dashed line) and experimentally measured $\Delta\theta_{\mathrm{Eq}}$ values for a bare SiO_2 coated SPR sensor in various solvents. Within the range explored, there is a linear increase of $\Delta\theta_{\mathrm{Eq}}$ with solvent refractive index. This phenomenon is rarely discussed in literature and to our knowledge Fig. 1 is the first explicit presentation of this effect.[58] Failure to subtract solvent effects from $\Delta\theta_{\mathrm{Eq}}$ would artificially increase the perceived swelling in thin films.

Results

CNC films in air

The thickness and morphology of CNC thin films in air were measured by AFM and SPR (Fig. 2) to compare the results of physical *versus* optical methods.

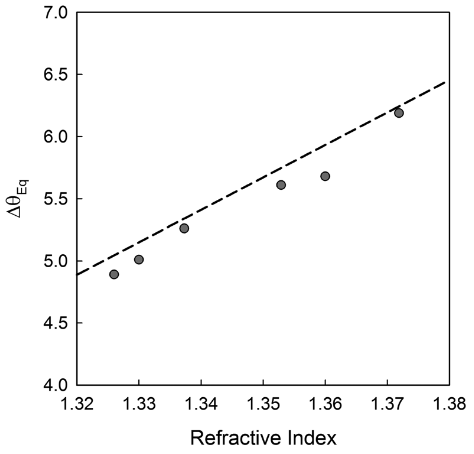

Fig. 1 Experimental (circles) and modeled (dashed line) shift in SPR angle with solvent refractive index.

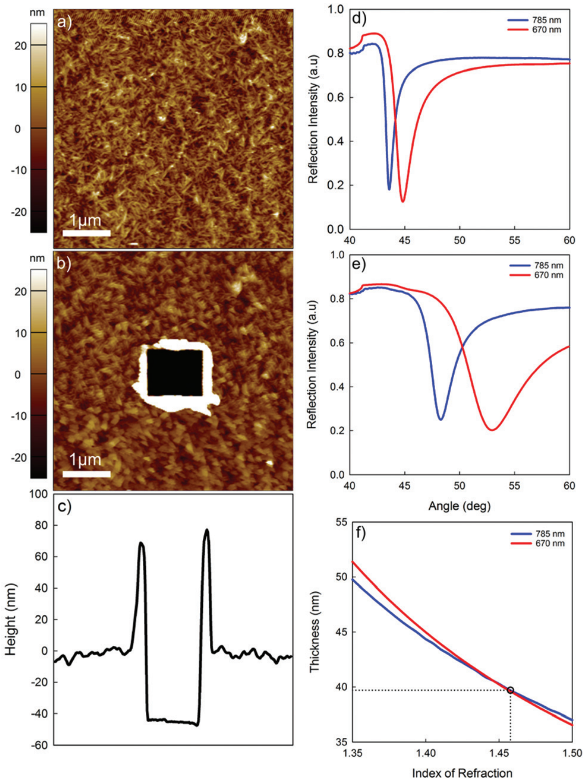

Fig. 2 AFM height image of (a) a dry CNC film after the "heat treat–rinse–heat treat" procedure, (b) scratched CNC film, and (c) cross section height analysis of scratched image used to determine film thickness. SPR spectrum of (d) bare SiO_2 substrate and (e) dry CNC film. Wavelength crossover (f) displays an index of refraction of 1.4578 and a thickness of 39.7 nm.

AFM images showed that complete, uniform films were produced with an average roughness of 5.7 ± 0.4 nm (Fig. 2a). Additionally, Fig. 2a shows that the CNC films are isotropic in the *xy* plane, indicating that the alignment often observed in spin coated CNC films has been eliminated due to the "heat treat-rinse-heat treat" protocol.[47,59,60] Fig. 2b and c present the scratched AFM image and the average cross sectional analysis of the film, respectively. The scratched image shows that CNCs have been removed from the substrate and that the displaced CNCs have built-up in the region immediately surrounding the scratched area. Amplitude and phase images indicate that no CNCs remain in the scratched region (ESI Fig. S1†) and an average film thickness of 40 ± 5 nm, corresponding to 4–5 CNC layers, was calculated as the height difference between the bare substrate and the unaffected CNC film region.

Similarly, CNC films were characterized by multi-wavelength SPR,[50] (Fig. 2d and e) and data were fit following the Fresnel equations by adjusting the thickness (d), refractive index (n) and extinction coefficient (k) of each layer using Winspall software (see ESI Fig. S2 and S3† for layer model parameters). Fig. 2d displays characteristic features of a typical full angle SPR curve for a clean sensor, which includes an increase in reflected light intensity at 41° due to the TIR and a significant reduction in intensity at the SPR angle. Fig. 2e displays the same features however, the SPR peak has shifted to higher angles due to the presence of CNCs at the sensor surface.[29] In addition, the breadth of the SPR peak increases following CNC deposition indicating that the roughness at the air interfaces has increased, correlating with AFM roughness measurements.[34]

Fig. 2f presents the n–d continuum from which d and n of the film were determined. Assuming the chromatic dispersion ($dn/d\lambda$) is negligible, an intersection point is observed at d = 39.7 nm and n = 1.458 correlating well with AFM thickness measurements. Applying the average $dn/d\lambda$ value of 0.0271 μm^{-1} used by Kontturi *et al.*[29] the layer parameters shifted to d = 39.1 nm and n = 1.466. It is important to note that the $dn/d\lambda$ value was determined for pure cellulose, the structure of which was not specified and potentially contains both amorphous and crystalline material,[51] thus it is unclear if this value can be directly applied to CNCs which are composed of crystalline cellulose I.[59] Additionally, the porous nature of the films suggests the $dn/d\lambda$ cannot be modeled simply as a single phase but as a weighted average between air and cellulose. As such, the difference between the values with and without the $dn/d\lambda$ factor is taken to be the uncertainty in the film thickness and effective refractive index, yielding parameters of d = 39.7 ± 0.6 nm and n = 1.458 ± 0.008.

Because the CNC films are not free standing and are very thin, calculating the density is challenging. However, the effective refractive index of 1.458 indicates that the films contain a high density of CNCs (n_{CNC} = 1.55) and Braun and Pilon showed volume averaging theory (VAT) can be used to calculate the porosity (ϕ) for non-adsorbing nanoporous thin films according to eqn (3):[61]

$$n_{film} = \sqrt{(1-\phi)n_C^2 + \phi n_D^2} \tag{3}$$

where n_{film}, n_C, and n_D are the refractive indices of the film, continuous phase and discontinuous phase, respectively. In the dry state, CNCs are in physical contact and are assumed to be the continuous phase thus $n_C = n_{CNC}$. Rearranging eqn (3), the composition of the spin coated CNC film was calculated to be 20 ± 2% air and 80 ± 2% CNC by volume. This is in excellent agreement with similarly prepared CNC films by Niinivaara *et al.*[33]

CNC film swelling

CNC films were swollen *in situ* in the SPR by introducing various solvents under constant flow; the films remained stable throughout all measurements and no material was lost as evidenced by rinsing and drying at the end of each experiment to ensure the same SPR profile in air (*i.e.*, Fig. 2e) was obtained. While adsorbed atmospheric water may be present in the CNC films, all measurements were performed under the same conditions and all solvents tested are miscible with water thus we expect the surface of the particles to participate in a solvent exchange over the 30 min swelling period. Fig. 3 pre-

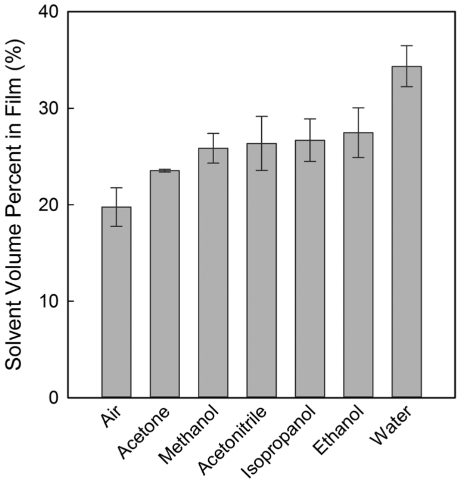

Fig. 3 Percent volume of solvent in swollen CNC films.

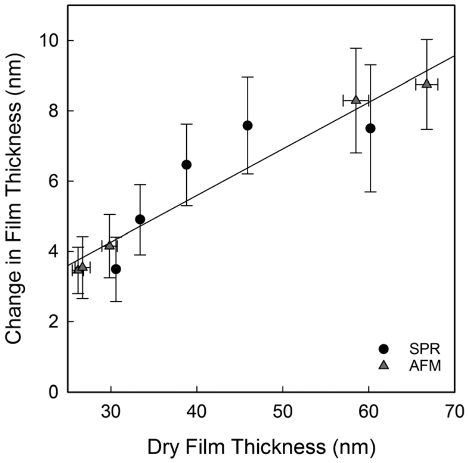

Fig. 4 Change in CNC film thickness in water measured by SPR and AFM. Solid line is included as a guide for the eye.

sents the volume fraction of air or solvent in dry and swollen films, respectively, as measured by SPR. Intuitively, water exhibits the highest volume fraction of solvent within swollen films due to the hydrophilic nature of CNCs. Less space within the CNC films is created by swelling in non-aqueous solvents with the volume fraction increasing in the order of acetone, methanol, acetonitrile, isopropanol, and ethanol. A Student's *t*-test indicates that swelling in methanol, acetonitrile, isopropanol and ethanol is statistically equivalent. All swelling values differ from acetone ($p > 0.2$) and water ($p > 0.05$). The extent of swelling and the trends with respect to common physical parameters/constants are discussed further below.

To support SPR swelling measurements, AFM scratch height analysis was used to physically measure CNC film thickness, first in air (similar to Fig. 2) and then in water using an open fluid cell, allowing the films to swell until equilibrium (ESI Fig. S4 and S5†). SPR swollen film thicknesses were calculated by assuming the volume increases only in the vertical direction. The SPR data error bars are calculated from the uncertainty in the volume percentage determined from the multi-wavelength SPR approach and leads to larger uncertainty in thicker films. Fig. 4 presents the change in film thickness (from dry to liquid environments) for CNC films with different starting thicknesses as measured by SPR and AFM. Plotting the percentage change in film thickness indicates that film swelling is statistically independent of starting film thickness (ESI S5†). Over a range of dry film thicknesses (25–70 nm) the volume increased by an average of 13.5 ± 0.4% measured by AFM and 14 ± 2% by SPR. This highlights that the two methods correspond closely, and that swelling needs to be normalized by dry film thickness (which is already done for data presented in Fig. 3). We also note that as indicated by Fält *et al.*[62] it is difficult to avoid tip penetration during wet AFM imaging, but the agreement supports the interpretation of both techniques and that the volume fraction of CNC films can be measured by SPR using an inverse relationship with $\Delta\theta$. These results imply that this data processing approach can be extended to other solvents.

As a final test, water-swollen CNC films were monitored by SPR under increasing flow rates. The SPR peak angle exhibited no change for flow rates of 100–500 μL min^{-1}, equivalent to shear stress of 0.3–1.4 dyne per cm^2 (data not shown).[63] This indicates that despite the large swelling of CNC films in water, it is not possible to partially or fully remove the CNCs from the substrate using the magnitude of shear available within the SPR instrument. Additionally, this measurement was conducted over a period of 2 hours from which negligible change in film thickness was observed after 30 min.

Discussion

Particle dispersibility ultimately depends on the balance between adhesive particle–solvent or particle–polymer and cohesive particle–particle interactions. Here we present a method to measure CNC cohesion by looking at nanoparticle separation in a variety of solvents in which the particles are not colloidally stable. The results presented above indicate that CNC–CNC cohesive interactions remain strong in all of the solvents tested, as none of the films delaminated upon exposure to liquid. However, the interactions between particles can be partially screened which leads to film swelling. We believe that the CNC films studied here are a reasonable model for CNC agglomerates which may be present during nanocomposite compounding and measurement of the cohesive interactions will prove useful for future formulation development. We emphasize that CNCs are insoluble in the solvents used here, however the interpretation of solubility parameters as "dispersibility parameters" for insoluble nanoparticles combined with SPR swelling will allow us to rationalize and predict CNC–CNC cohesive interactions in aqueous and non-aqueous environments.

Film swelling and solubility parameters

Due to the hydrophilic nature of cellulose, swelling in water is of great interest[26] and as expected, water was found to swell CNC films the most (followed by alcohols, acetonitrile, and acetone). Although cellulose fibers are known to swell in water, experimental[64] and theoretical[65] work has demonstrated that solvent does not penetrate the cellulose I crystal structure of CNCs. As such, we assume that CNC films swell by increasing inter-particle spacing and not by increasing the size of individual particles. We predict that CNC film swelling follows two distinct steps: firstly, solvent rapidly penetrates the film through the porous structure (capillary action), filling the voids. Subsequent swelling occurs as solvent enthalpically wets CNC surfaces and continues to fill, and create new space between CNC particles. The new space created increases the thickness and total volume of the film by reducing cohesive particle–particle interactions. For solvents with hydrogen bonding capabilities, this wetting replaces the majority of particle–particle hydrogen bonds with particle–solvent hydrogen bonds.[66]

Water-swollen CNC films were determined to have a total thickness increase of 14 ± 2% compared to the dry state. In contrast, films in non-aqueous solvents all showed a minimal change in volume; acetone increased the film volume by only 4% and methanol, acetonitrile, isopropanol and ethanol increased the volume by 6–8%. There is no apparent correlation with the solvent dielectric constants which are 20.7, 32.7, 37.5, 17.9, and 24.5 for acetone, methanol, acetonitrile, isopropanol, and ethanol, respectively. This is similarly reflected in the lack of trend with cellulose-solvent Hamaker constants (approximated using Lifshitz theory, ESI Fig. S6a†), suggesting that swelling is not dependent on solvent shielding of van der Waals forces. Moreover, no trend corresponding to solvent molecular size was observed, eliminating any explanation based on sterics/solvation forces, and suggesting that the chemical nature of the solvent is responsible for interrupting particle–particle interactions and overall film swelling.

Swollen films contain 25 ± 2 wt% water, in good agreement with QCM-D measurements of similar swollen CNC films studied by Aulin *et al.*[30] and Niinivaara *et al.*[33] (assuming a CNCs density of 1.55 g cm^{-3}).[15] In contrast, Kittle *et al.* determined water content of CNC films to be nearly triple this value at 74 wt% *via* QCM-D.[32] Similar results were observed in low-density cellulose nanofibril films studied by Kontturi *et al.*[29] Currently it is unclear as to why this discrepancy in the literature exists but highlights that film structure and the initial state of hydration can significantly alter swelling behaviour of nanocellulose films. The agreement of this work and similarly prepared CNC films by Aulin *et al.* and Niinivaara *et al.* supports our interpretation of SPR data and additionally the validity of SPR as useful tool in film swelling studies of nanoparticle systems.

To understand the dominant chemical properties that influence film swelling we turned to solubility parameters; the Hildebrand solubility parameter has long been used to predict solvation and polymer-solvent interactions based on cohesive energy density,[67] and it may offer insight into insoluble particle–solvent interactions as well. Fig. 5 indicates that there is a correlation (R^2 = 0.9068) between solvent volume fraction taken up by the film and the Hildebrand solubility parameter; essentially, the larger the solubility parameter, the greater the particle–particle spacing (*i.e.*, more swelling). This correlation is stronger than that between film swelling and solvent surface tension (see ESI Fig. S6b†) as well as Hamaker constants and dielectric constants, described above. Hildebrand solubility parameters, however, do not provide information about which solvent characteristics are responsible for interrupting cohesive CNC–CNC interactions.[68] For example, the cohesive energy density does not suggest why acetonitrile, a non-hydrogen bonding solvent, equally swells CNC films as ethanol, a hydrogen bonding solvent. To this end we used the Hansen solubility parameters, which separate the Hildebrand solubility parameter into its respective dispersive, polar, and hydrogen bonding components, as a measure of effective solvent properties. Although swelling observed in methanol, acetonitrile, isopropanol and ethanol are statistically within the same range, plotting individual volume percentages against the Hansen solubility parameters helps' establish general trends in solvent parameters (see ESI Table S2† for theoretical Hildebrand and Hansen solubility parameters). Fig. 6 presents the relationship between the solvent volume fraction in swollen CNC films and the components of the Hansen solubility parameters. Film swelling has a weak correlation to the dispersive and polar components (Fig. 6a and b) however swelling does increase with an increase in the hydrogen bonding component (R^2 = 0.8154, Fig. 6c). This is attributed to the abundance of hydrogen bonding sites at the CNC surface and that in liquid CNC–CNC hydrogen bonds are understood to be replaced with CNC–solvent hydrogen bonds. Despite this trend, this does not demonstrate why acetonitrile is as

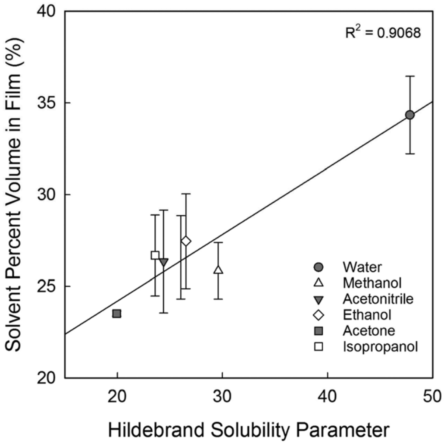

Fig. 5 Percent volume of solvent in swollen CNC film *versus* Hildebrand solubility parameters. Line represents linear regression best fit with correlation coefficient, R^2 = 0.9068.

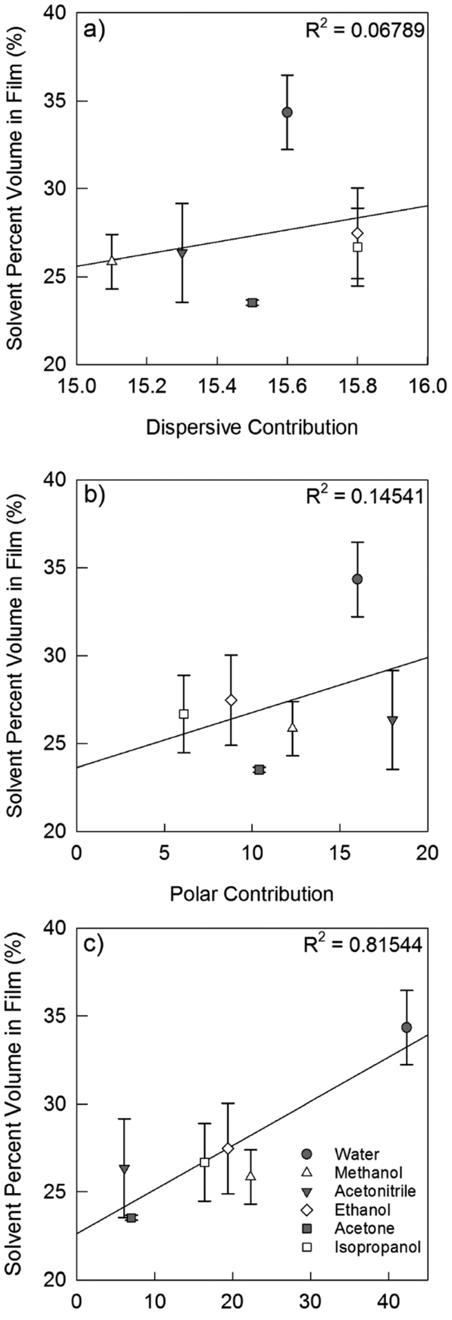

Fig. 6 Percent volume of solvent in swollen CNC films for (a) dispersive, (b) polar and (c) hydrogen bonding Hansen solubility parameters. Lines represent linear regression best fits with correlation coefficient, R^2. The legend in (c) applies to all figures, (a)–(c).

effective as ethanol. Although there is a lack of agreement overall with polar component of the Hansen solubility parameters, the large polarity (and dielectric constant) of acetonitrile indicates that it can interrupt cohesive particle–particle interaction without hydrogen bonding. Additionally, we observe that acetone with poor hydrogen bonding capabilities and low polarity does not effectively increase the volume of the films contrasting water with high polarity and hydrogen bonding. Extending this to nanocomposites, we suggest that agglomerates will persist in non-polar polymer matrices incapable of hydrogen bonding, such as polyethylene, even under high shear possibly because of the inability for the polymer to effectively interrupt cohesive particle–particle interactions.[22] Melt processed CNC/polyvinyl alcohol composites have been reported with improved CNC dispersibility and mechanical performance suggesting that the polymer's ability to form hydrogen bonds is critical.[69]

Film stability and particle–particle spacing

Strong, attractive van der Waals forces between high aspect ratio nanoparticles at nanometer separations are well documented to be responsible for aggregates and agglomerates in nano-composites,[70,71] and we believe we have explicitly demonstrated that this is also the case for CNCs, as discussed below. Because CNC films remain stable throughout the swelling measurements even after CNC–CNC hydrogen bonds have been replaced with CNC–solvent hydrogen bonds we recognize that other short range forces are responsible for the strong particle–particle cohesion. Within swollen CNC films, the largest volume increase observed was 14 ± 2% or a 5.6 ± 0.6 nm thickness increase (assuming that all swelling occurs in the vertical direction due to the O-ring clamp used in the experimental setup which restricts lateral swelling) for a 40 nm thick CNC film in water. Assuming CNCs lay flat in distinct layers and have a square prism geometry with an average cross section of 8 nm, the volume increase in swollen films can be equated to a 1.2–1.6 nm vertical spacing between each CNC (when distributed evenly) which is in excellent agreement with CNC films swollen in humid environments.[33] This spacing is significantly greater than any hydrogen bonding length and is large enough to contain 4–6 molecular layers of water.

We suggest that wetting of the CNC surface induces hydration forces, which are sufficient to overcome van der Waals forces over this narrow spacing. Forces at these separations (<2 nm) have been measured by Pashley and Israelachvili to extend *ca.* 1.7 nm from mica surfaces or 6–7 molecular layers in good agreement with the work presented here.[72] Since we expect no physical entanglements between rigid rod-like particles, beyond a spacing of 1.6 nm hydration effects at the CNC surface cannot overcome attractive forces and thus indicate that van der Waals forces are likely responsible for holding the films intact. Exploring this, the crossed and parallel configuration geometries of CNCs (approximated as cylinders) were averaged and Fig. 7 presents simulated van der Waals attraction, electrostatic double layer repulsion, and the total combined contributions (*i.e.*, DLVO) interaction potential profiles (details in ESI†). The van der Waals contribution was calculated using a Hamaker constant of 8 × 10^{-21} J as measured by Bergström *et al.* for cellulose in water.[73] Electrostatic double layer repulsion between CNCs was calculated fol-

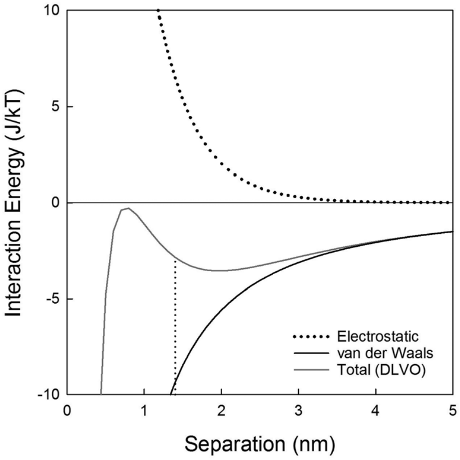

Fig. 7 Simulated average attractive van der Waals energy between crossed and parallel CNCs in 0.35 M aqueous medium, the electrostatic double layer repulsion, and the total (DLVO) interaction energy as a function of nanoparticle separation. The vertical dashed line shows the average particle separation observed from the CNC swelling experiments.

lowing Buining *et al.*[74] assuming constant surface potential and using a surface potential for CNCs of −18 mV as measured by Stiernstedt *et al.*[75] We note that the surface potential has a significant impact on the calculated interaction energy and is detailed further in the ESI.† Importantly, the ionic strength due to Na^+ counterions within the swollen CNC film was calculated to be 0.35 M based on the sulfate half ester content of the CNCs and water occupying 34% of the film volume (divided by 2 because only the counterions are mobile). At high ionic strengths, as is the case within the CNC film, the onset of electrostatic repulsion occurs at small separations (<3 nm) where attractive van der Waals forces are larger in magnitude and thus dominate. In fact, at no point does the combined DLVO interaction reach repulsive energies since the ionic strength at the initial stages of swelling is even larger than the completely swollen CNC films. (See ESI Fig. S7† for visualization of the effect of ionic strength in this range on DLVO interaction energy.)

The largest CNC particle–particle spacing we observe experimentally due to swelling is 1.6 nm which is well within the attractive DLVO regime according to Fig. 7. At the average CNC spacing of 1.4 nm (dotted line, Fig. 7), DLVO forces are greater than the average kinetic energy of $3kT/2$ (where k is the Boltzmann constant and T is temperature in kelvin). This implies that CNCs do not have sufficient thermal energy to overcome the attractive forces holding them together which demonstrates why external energy, such as sonication, is needed to fully disperse freeze dried or spray dried CNCs in water.[21] As the electrostatic double layer forces play a minor role at these particle–particle separations and ionic strengths, we attribute CNC particle cohesion in the wet state primarily to van der Waals forces.

We can furthermore extend the trend in Fig. 5 to predict a Hildebrand "dispersibility" parameter for CNCs based on DLVO theory: if CNCs must be separated by more than 5 nm to overcome the attractive regime ($>-3kT/2$) this implies a swelling of over 50% solvent volume in the film. This would correspond to a Hildebrand parameter of 150 $MPa^{1/2}$ for CNCs which is significantly greater than water (47.8 $MPa^{1/2}$), and much larger than common hydrophobic polymers (ESI Table S2†). While this result exemplifies the difficulties associated with dispersing particles in nanocomposites these SPR swelling measurements can be easily extended to predict the dispersibility of surface modified CNCs as well as other types of nanoparticles.

Conclusion

In summary, this work demonstrates that SPR as a technique is capable of probing particle–particle cohesion at the nanometer scale in a variety of solvents. Specifically CNC–CNC particle interactions were explored *via* film swelling in aqueous and non-aqueous solvents. The hydrogen bonding ability of the solvent was observed to be the most correlated factor (albeit a weak correlation) in film swelling however, highly polar acetonitrile was equally effective as alcohols at screening interparticle interactions. Film swelling is proposed to occur as the solvent fills the porous structure of the film followed by enthalpic wetting of individual CNCs. This wetting replaces CNC–CNC hydrogen bonds with CNC–solvent hydrogen bonds and interrupts cohesive particle–particle interactions. In all solvents, the van der Waals forces between CNC particles maintained the particle–particle cohesion and the overall stability of the CNC films. The largest spacing observed suggests 4–6 molecular layers of water are present between each CNC, in excellent agreement with QCM-D measurements of CNCs in humid environments.[33] From this work we predict that to produce well-dispersed CNC nanocomposites (with unmodified CNCs), polymers likely require hydrogen bonding or polar components that can interrupt CNC–CNC bonding and the input of external energy must be sufficient to overcome van der Waals forces.

Acknowledgements

Funding from the Natural Sciences and Engineering Research Council of Canada, Industrial Postgraduate Scholarship program sponsored by Cabot Corporation is gratefully acknowledged. The authors also thank S. Kedzior, H. Marway, K. De France, D. LeClair and L. Poole for useful discussions. Professors R. Pelton, A. Guarne and J. Moran-Mirabal are thanked for sharing equipment to characterize CNCs and prepare films. The Biointerfaces Institute and the Brockhouse Institute for Materials Research at McMaster University are acknowledged for support and equipment.

References

1 J. Jancar, J. F. Douglas, F. W. Starr, S. K. Kumar, P. Cassagnau, A. J. Lesser, S. S. Sternstein and M. J. Buehler, *Polymer*, 2010, **51**, 3321–3343.
2 P. Akcora, H. Liu, S. K. Kumar, J. Moll, Y. Li, B. C. Benicewicz, L. S. Schadler, D. Acehan, A. Z. Panagiotopoulos, V. Pryamitsyn, V. Ganesan, J. Ilavsky, P. Thiyagarajan, R. H. Colby and J. F. Douglas, *Nat. Mater.*, 2009, **8**, 354–359.
3 V. Khoshkava and M. R. Kamal, *Biomacromolecules*, 2013, **14**, 3155–3163.
4 J. O. Zoppe, M. Peresin, Y. Habibi, R. Venditti and O. Rojas, *Appl. Mater. Interfaces*, 2009, **1**, 1996–2004.
5 X. Yang, E. Bakaic, T. Hoare and E. D. Cranston, *Biomacromolecules*, 2013, **14**, 4447–4455.
6 J. Harris, A. Hess, S. Rowan, C. Weder, C. Zorman, D. Tyler and J. Capadona, *J. Neural Eng.*, 2011, **8**, 046010.
7 E. E. Ureña-Benavides, G. Ao, V. A. Davis and C. L. Kitchens, *Macromolecules*, 2011, **44**, 8990–8998.
8 Q. Wu, Y. Meng, S. Wang, Y. Li, S. Fu, L. Ma and D. Harper, *J. Appl. Polym. Sci.*, 2014, 40525.
9 S. Tasset, B. Cathala, H. Bizot and I. Capron, *RSC Adv.*, 2014, **4**, 893.
10 J. O. Zoppe, R. A. Venditti and O. J. Rojas, *J. Colloid Interface Sci.*, 2012, **369**, 202–209.
11 G. Sèbe, F. Ham-Pichavant and G. Pecastaings, *Biomacromolecules*, 2013, **14**, 2937–2944.
12 Z. Hu, S. Ballinger, R. Pelton and E. D. Cranston, *J. Colloid Interface Sci.*, 2014, **439**, 139–148.
13 S. J. Eichhorn, A. Dufresne, M. Aranguren, N. E. Marcovich, J. R. Capadona, S. J. Rowan, C. Weder, W. Thielemans, M. Roman, S. Renneckar, W. Gindl, S. Veigel, J. Keckes, H. Yano, K. Abe, M. Nogi, A. N. Nakagaito, A. Mangalam, J. Simonsen, A. S. Benight, A. Bismarck, L. A. Berglund and T. Peijs, *J. Mater. Sci.*, 2009, **45**, 1–33.
14 S. J. Eichhorn, *Soft Matter*, 2011, **7**, 303.
15 M. Mariano, N. El Kissi and A. Dufresne, *J. Polym. Sci., Part B: Polym. Phys.*, 2014, **52**, 791–806.
16 R. J. Moon, A. Martini, J. Nairn, J. Simonsen and J. Youngblood, *Chem. Soc. Rev.*, 2011, **40**, 3941–3994.
17 S. J. Eichhorn, C. A. Baillie, N. Zafeiropoulos, L. Y. Mwaikambo, M. P. Ansell, A. Dufresne, K. M. Entwistle, P. J. Herrera-Franco, G. C. Escamilla, L. Groom, M. Hughes, C. Hill, T. G. Rials and P. M. Wild, *J. Mater. Sci.*, 2001, **36**, 2107–2131.
18 J. F. Revol, H. Bradford, J. Giasson, R. H. Marchessault and D. G. Gray, *Int. J. Biol. Macromol.*, 1992, **14**, 170–172.
19 Y. Habibi, L. A. Lucia and O. J. Rojas, *Chem. Rev.*, 2010, **110**, 3479–3500.
20 X. M. Dong and D. G. Gray, *Langmuir*, 1997, **13**, 2404–2409.
21 S. Beck, J. Bouchard and R. Berry, *Biomacromolecules*, 2012, **13**, 1486–1494.
22 A. Junior de Menezes, G. Siqueira, A. A. S. Curvelo and A. Dufresne, *Polymer*, 2009, **50**, 4552–4563.
23 N. Lin and A. Dufresne, *Macromolecules*, 2013, **46**, 5570–5583.
24 Y. Habibi, *Chem. Soc. Rev.*, 2014, **43**, 1519–1542.
25 *The Global Market for Nanocellulose to 2020*, Future Markets Inc., 2013.
26 E. Kontturi, T. Tammelin and M. Österberg, *Chem. Soc. Rev.*, 2006, **35**, 1287–1304.
27 Z. Hu, E. D. Cranston, R. Ng and R. Pelton, *Langmuir*, 2014, **30**, 2684–2692.
28 C. V. Cerclier, A. Guyomard-Lack, F. Cousin, B. Jean, E. Bonnin, B. Cathala and C. Moreau, *Biomacromolecules*, 2013, **14**, 3599–3609.
29 K. S. Kontturi, E. Kontturi and J. Laine, *J. Mater. Chem. A*, 2013, **1**, 13655.
30 C. Aulin, S. Ahola, P. Josefsson, T. Nishino, Y. Hirose, M. Österberg and L. Wågberg, *Langmuir*, 2009, **25**, 7675–7685.
31 F. Jiang, J. Kittle, X. Tan, A. Esker and M. Roman, *Langmuir*, 2013, **29**, 3280–3291.
32 J. D. Kittle, X. Du, F. Jiang, C. Qian, T. Heinze, M. Roman and A. R. Esker, *Biomacromolecules*, 2011, **12**, 2881–2887.
33 E. Niinivaara, M. Faustini, T. Tammelin and E. Kontturi, *Langmuir*, 2015, **31**, 12170–12176.
34 A. N. Raegen, K. Reiter, A. Dion, A. J. Clarke, J. Lipkowski and J. R. Dutcher, *Anal. Chem.*, 2014, **86**, 3346–3354.
35 Z. Liu, H. Choi, P. Gatenholm and A. R. Esker, *Langmuir*, 2011, **27**, 8718–8728.
36 X. Liu, D. Wu, S. Turgman-Cohen, J. Genzer, T. W. Theyson and O. J. Rojas, *Langmuir*, 2010, **26**, 9565–9574.
37 S. G. Allen, O. M. Tanchak, A. Quirk, A. N. Raegen, K. Reiter, R. Whitney, A. J. Clarke, J. Lipkowski and J. R. Dutcher, *Anal. Methods*, 2012, **4**, 3238.
38 O. Grigoray, H. Wondraczek, E. Heikkilä, P. Fardim and T. Heinze, *Carbohydr. Polym.*, 2014, **111**, 280–287.
39 K. Junka, J. Guo, I. Filpponen, J. Laine and O. J. Rojas, *Biomacromolecules*, 2014, **15**, 876–881.
40 H. Orelma, I. Filpponen, L. S. Johansson, J. Laine and O. J. Rojas, *Biomacromolecules*, 2011, **12**, 4311–4318.
41 H. Orelma, L. O. Morales, L.-S. Johansson, I. C. Hoeger, I. Filpponen, C. Castro, O. J. Rojas and J. Laine, *RSC Adv.*, 2014, **4**, 51440–51450.
42 H. Orelma, T. Teerinen, L. S. Johansson, S. Holappa and J. Laine, *Biomacromolecules*, 2012, **13**, 1051–1058.
43 S. Ahola, J. Salmi, L. S. Johansson, J. Laine and M. Österberg, *Biomacromolecules*, 2008, **9**, 1273–1282.
44 S. E. Gradwell, S. Renneckar, A. R. Esker, T. Heinze, P. Gatenholm, C. Vaca-Garcia and W. Glasser, *C. R. Biol.*, 2004, **327**, 945–953.
45 X. Dong, T. Kimura, J. Revol and D. G. Gray, *Langmuir*, 1996, 2076–2082.
46 D. Viet, S. Beck-Candanedo and D. G. Gray, *Cellulose*, 2006, **14**, 109–113.
47 E. D. Cranston and D. G. Gray, *Biomacromolecules*, 2006, **7**, 2522–2530.
48 M. Labet and W. Thielemans, *Cellulose*, 2011, **18**, 607–617.
49 S. Beck, M. Méthot and J. Bouchard, *Cellulose*, 2014, **22**, 101–116.

50 N. Granqvist, H. Liang, T. Laurila, J. Sadowski, M. Yliperttula and T. Viitala, *Langmuir*, 2013, **29**, 8561–8571.

51 S. N. Kasarova, N. G. Sultanova, C. D. Ivanov and I. D. Nikolov, *Opt. Mater.*, 2007, **29**, 1481–1490.

52 W. Ogieglo, H. Wormeester, K.-J. Eichhorn, M. Wessling and N. E. Benes, *Prog. Polym. Sci.*, 2015, **42**, 42–78.

53 W. Ogieglo, H. Wormeester, M. Wessling and N. E. Benes, *Polymer*, 2014, **55**, 1737–1744.

54 B. W. Rowe, B. D. Freeman and D. R. Paul, *Macromolecules*, 2007, **40**, 2806–2813.

55 M. Erdoğan, I. Capan, C. Tarimci and A. K. Hassan, *J. Colloid Interface Sci.*, 2008, **323**, 235–241.

56 M. Erdoğan, R. Çapan and F. Davis, *Sens. Actuators, B*, 2010, **145**, 66–70.

57 Z. Ozbek, M. Erdoğan and R. Capan, *Sens. Actuators, B*, 2014, **196**, 328–335.

58 T. Akimoto, S. Sasaki, K. Ikebukuro and I. Karube, *Appl. Opt.*, 1999, **38**, 4058–4064.

59 C. D. Edgar and D. G. Gray, *Cellulose*, 2003, **10**, 299–306.

60 E. D. Cranston and D. G. Gray, *Colloids Surf., A*, 2008, **325**, 44–51.

61 M. M. Braun and L. Pilon, *Thin Solid Films*, 2006, **496**, 505–514.

62 S. Fält, L. Wågberg and E. L. Vesterlind, *Langmuir*, 2003, **19**, 7895–7903.

63 T. Viitala, H. Liang, M. Gupta, T. Zwinger, M. Yliperttula and A. Bunker, *J. Colloid Interface Sci.*, 2012, **378**, 251–259.

64 H. Hatakeyama and T. Hatakeyama, *Thermochim. Acta*, 1998, **308**, 3–22.

65 R. J. Maurer, A. F. Sax and V. Ribitsch, *Cellulose*, 2013, **20**, 25–42.

66 M. Ioelovich, *Sci. Isreal Technol. Adv.*, 2011, **13**, 35–44.

67 C. M. Hansen, *Prog. Org. Coat.*, 2004, **51**, 77–84.

68 L. A. Errede, *Macromolecules*, 1986, **1525**, 1522–1525.

69 W. Zhang, X. He, C. Li, X. Zhang, C. Lu, X. Zhang and Y. Deng, *Cellulose*, 2014, **21**, 485–494.

70 Y. Y. Huang and E. M. Terentjev, *Polymers*, 2012, **4**, 275–295.

71 V. Singh, D. Joung, L. Zhai, S. Das, S. I. Khondaker and S. Seal, *Prog. Mater. Sci.*, 2011, **56**, 1178–1271.

72 R. M. Pashley and J. N. Israelachvili, *J. Colloid Interface Sci.*, 1984, **101**, 511–523.

73 L. Bergström, S. Stemme, T. Dahlfors, H. Arwin and L. Ödberg, *Cellulose*, 1999, **6**, 1–13.

74 P. Buining, A. Philipse and H. Lekkerkerker, *Langmuir*, 1994, 2106–2114.

75 J. Stiernstedt, N. Nordgren, L. Wågberg, H. Brumer, D. G. Gray and M. W. Rutland, *J. Colloid Interface Sci.*, 2006, **303**, 117–123.

Appendix 4: Chapter 4 Supporting Information

Purification of CNCs

Soxhlet Extraction. Following CNC extraction, the presence of impurities at the CNC surface was investigated by purifying ca. 1 g of freeze dried material via soxhlet extraction according to Labet and Thielemans.[1] Freeze dried CNCs were extracted in ethanol for 24 h and oven-dried at 80˚C overnight. Extracted CNCs were then used to produce spin-coated films.

Film Preparation. CNC films were prepared on polished Si wafers (MEMC Electronic Materials Sdn Bhd, Petaling Jaya, Malaysia) or SiO_2 coated SPR sensors (BioNavis, Ylöjärvi, Finland) by spin coating under N_2 gas (G3P Spincoat, Specialty Coating Systems Inc. Indianapolis, USA) at 4000 rpm for 30 s with a 7 s ramp. Prior to deposition, all surfaces were cleaned in a piranha solution (3:1 concentrated sulfuric acid to hydrogen peroxide) for 30 min, followed by continuous rinsing with purified water and drying by a stream of N_2 gas. Film thicknesses were controlled by varying the CNC suspension concentration between 1 and 3 wt.%. Following spin coating, films were annealed at 80˚C for 8 hours (overnight). Films were then gently rinsed with purified water and annealed again for 8 hours. We believe that this procedure removes loosely bound surface CNCs and helps to eliminate radial ordering of CNCs which may occur during spin coating (as evidenced by AFM imaging).

X-Ray Photoelectron Spectroscopy (XPS). CNC spin coated films and freeze dried material were analyzed by XPS. XPS spectra were recorded using a Physical Electronics (PHI) Quantera II spectrometer equipped with a Al anode source for X-ray generation and a quartz crystal monochromator for focusing the generated X-rays. A monochromatic Al K-α X-ray (1486.7 eV) source was operated at 50W 15kV. The system base pressure was no higher than 1.0 x 10-9 Torr, with an operating pressure that did not exceed 2.0 x10-8 Torr. A pass energy of 280 eV was used to obtain all survey spectra and 26 eV was used for Carbon high resolution data and 55 eV for all other high resolution data. All spectra were obtained at 45˚ take off angles, and a dual beam charge compensation system was used for neutralization of all samples. The instrument was calibrated using a sputter-cleaned piece of Ag, where the Ag 3d5/2- peak had a binding energy of 368.3 ± 0.1 eV and full width at half maximum for the Ag 3d-5/2 peak was at least 0.52 eV. Data manipulation was performed using PHI MultiPak Version 9.4.0.7 software.

Table S1: X-ray photoelectron spectroscopy (XPS) carbon composition from deconvoluted high resolution C1 peak for raw and extracted CNC material prepare by spin coating and freeze drying.

		Carbon Composition from Deconvoluted C1 Peak (%)			
Preparation	**State**	**C-C**	**C-O-C**	**O-C-O**	**O-C=O**
Spin Coated	Raw	12.2	67.9	18.9	1.0
	Extracted	11.2	66.5	21.9	0.4
Freeze Dried	Raw	13.9	44.6	41.6	0.0
	Extracted	6.1	54.1	39.8	0.0

Analysis of Dry CNC Films

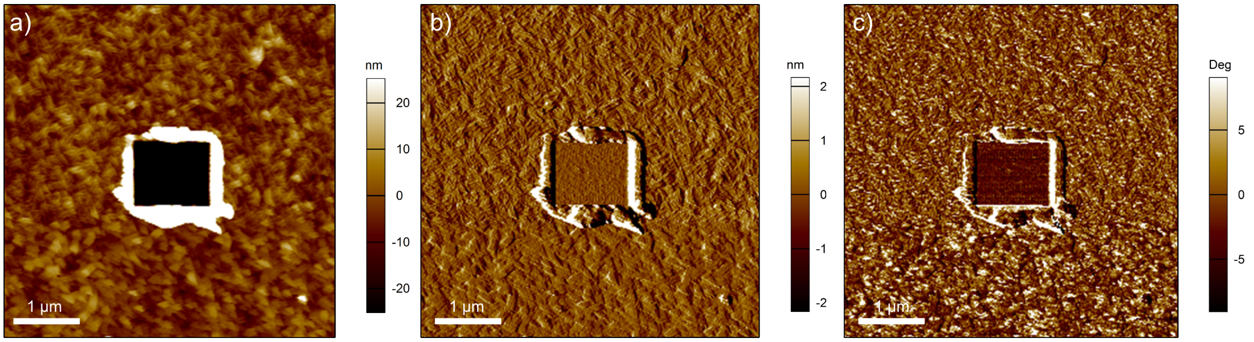

Figure S1: Representative AFM scratch height analysis images displaying the (a) height, (b) amplitude and (c) phase channels.

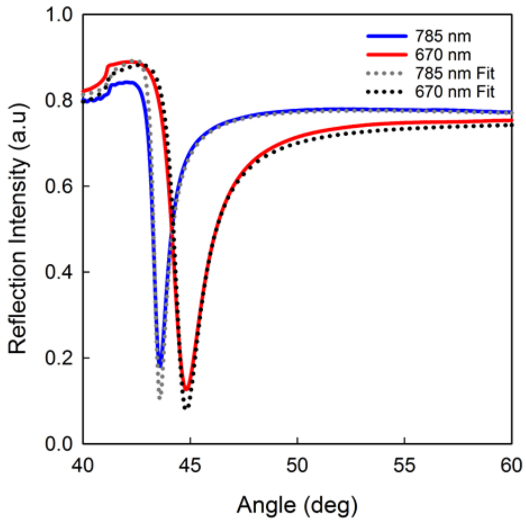

	d (nm)	n(785)	k(785)	n(670)	k(670)
Glass	inf	1.5162	0	1.5192	0
Cr	1.43	3.4035	2.9198	2.3235	1.5498
Au	48.9	0.2695	4.7610	0.2695	3.8610
SiO_2	13.6	1.5775	0	1.5765	0
Air	inf	1	0	1	0
Glass	inf	1.5162	0	1.5192	0

Figure S2: SPR curve and layer parameters for fit of bare SiO_2 sensor in air.

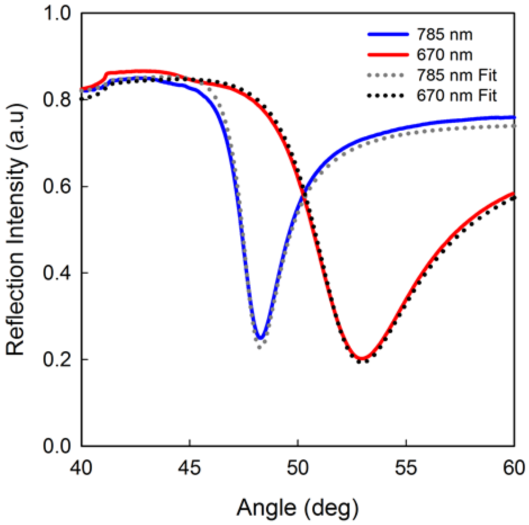

	d (nm)	n(785)	k(785)	n(670)	k(670)
Glass	inf	1.5180	0	1.5202	0
Cr	2.03	2.9250	4.1000	2.9234	1.0598
Au	48.5	0.1614	4.8090	0.2667	3.9017
SiO_2	13.7	1.575	0	1.5725	0
CNC	39.7	1.4578	0.025	1.4578	0.045
Air	inf	1	0	1	0

Figure S3: SPR curve and layer parameters for fit of a dry CNC film in air.

Scratch Height Analysis of Water Swollen Films

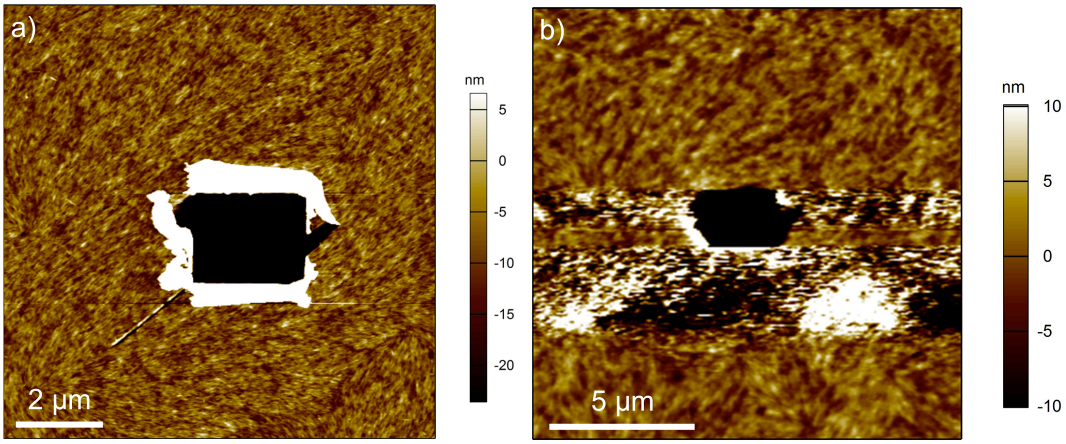

Figure S4: AFM height images of scratched images of a (a) dry CNC film in air and a (b) swollen CNC film in water.

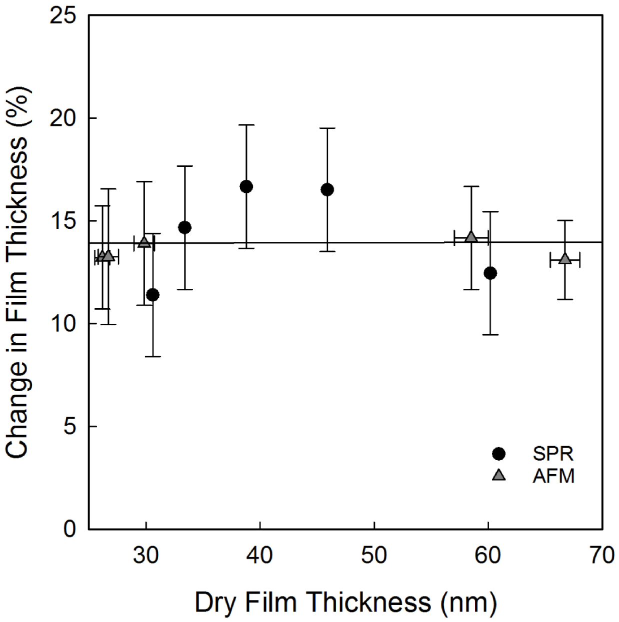

Figure S5: Change in CNC film thickness in water measured by SPR and AFM. Solid line included to guide the eye.

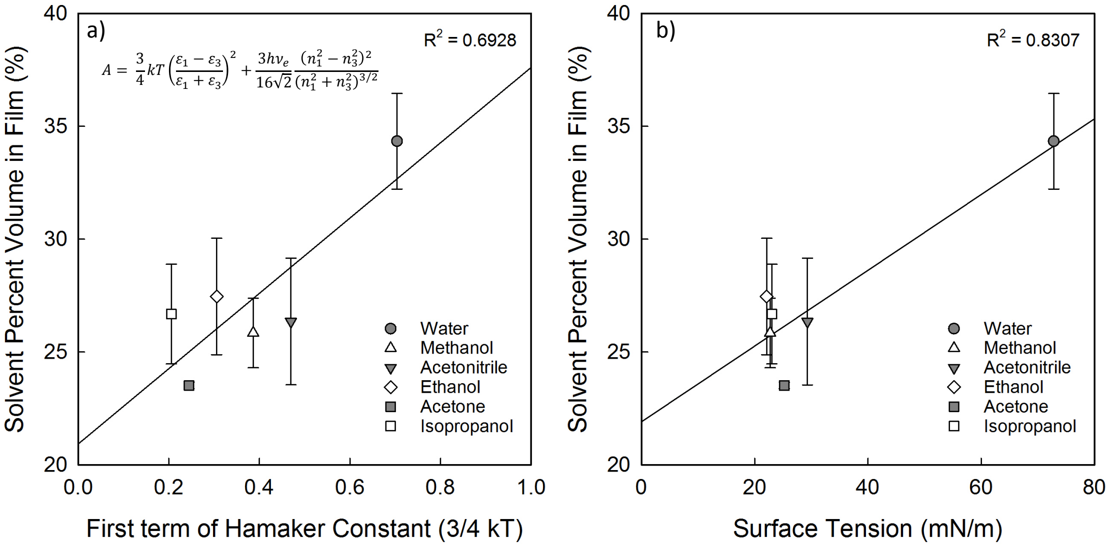

Figure S6: Solvent percent in film plotted against a) the first term in the Hamaker constant for two identical phases across a medium as calculated from Israelachvili.[2] and b) surface tension of the solvents tested.

Solvent Parameters

Table S2: Hildebrand and Hansen Solubility Parameters from reference [3] or otherwise listed.

Solvent	Hildebrand Solubility Parameter	Hansen Solubility Parameters		
		Dispersive	Polar	Hydrogen Bonding
Water	47.84	15.6	16.0	42.3
Methanol	29.61	15.1	12.3	22.3
Acetonitrile	24.40	15.3	18.0	6.1
Ethanol	26.52	15.8	8.8	19.4
Acetone	19.94	15.5	10.4	7.0
Isopropanol	23.58	15.8	6.1	16.4
Polyethylene	18.1	18.0	0	2.0
Polystyrene	20.1	18.6	6.0	4.5
Poly(vinyl alcohol)	29.2	15.0	17.2	17.8
Poly(vinyl pyrrolidone)[4]	24.3	18.8	13.4	7.5
Poly(lactic acid)[5]	21.2	17.5	9.5	7.3

DLVO Calculations

Repulsive parallel (${V_R}^P$) and crossed (${V_R}^C$) interaction energies were calculated following Buining *et al.*[6]

$$ {V_R}^P = 64(\pi)^{1/2} nkT\gamma^2 L \frac{(\kappa R)^{1/2}}{\kappa^2} \exp{(-\kappa D)} $$

$$ {V_R}^C = 128\pi nkT\gamma^2 \frac{a}{\kappa^2} \exp{(-\kappa D)} $$

with

$$ \gamma = \tanh{(\frac{e\psi_o}{4kT})} $$

where n is the number density of ions calculated for a monovalent salt in ultra pure water (1×10^{-7} M), k is the Boltzmann constant, T is temperature, κ is the Debye length, R and L are the radius and length of the CNC respectively, D is the particle spacing, e is the charge of an electron and ψ_o is the CNC surface potential (-18 mV Ref. [7]).

Attractive van der Waals potentials (V_A) were calculated from Israelachvili.[2]

$$V_A{}^P = \frac{-AL}{12\sqrt{2}D^{3/2}}\left(\frac{R_1 R_2}{R_1 + R_2}\right)^{1/2}$$

$$V_A{}^C = \frac{-A\sqrt{R_1 R_2}}{6D}$$

Where A is the Hamaker constant (8×10^{-21} J Ref. [8]) and for CNCs $R_1 = R_2$.

The parallel and crossed conformations were averaged and used to calculate the total potential:

$$V_T = V_R + V_A$$

The effect of altering the ionic strength (0.5 M and 1 M) and particle surface potential (-20 mV, -30 mV and -50 mV) are presented in Figure S7 and Figure S8 respectively. The ionic strength of the film was determined to be 350 mM based on the sulfur content of the CNC particles and the volume percent (~35%) of water with the film. Additionally, we assume only the counter ions are mobile within the film as the sulfate esters are chemically bound to the CNC surface. The particle surface potential has a significant impact on the calculated interaction energy. Experimentally this value for CNCs was measured to be -18 mV by Stiernstedt *et al.* and was used unless other wise stated.

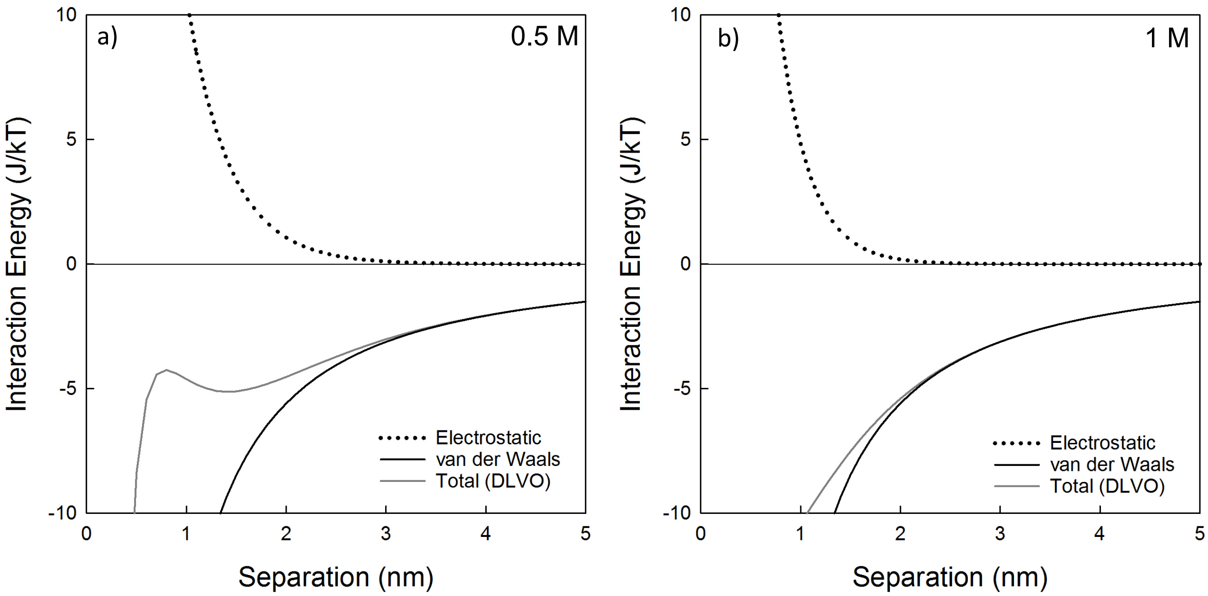

Figure S7: Simulated average attractive van der Waals energy between crossed and parallel CNCs in water, the electrostatic double layer repulsion, and the total (DLVO) interaction energy as a function of nanoparticle separation in solutions with ionic strength of a) 0.5 M and b) 1 M with particle surface potential of -18 mV.

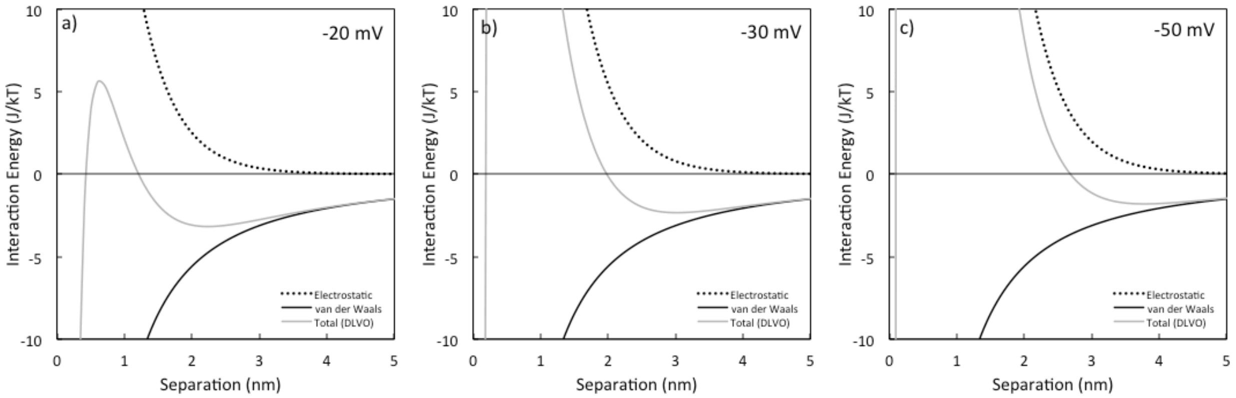

Figure S8: Simulated average attractive van der Waals energy between crossed and parallel CNCs in water, the electrostatic double layer repulsion, and the total (DLVO) interaction energy as a function of nanoparticle separation in a 350 mM solution with varying surface potentials of a) -20 mV b) -30 mV and c) -50 mV

References

(1) Labet, M.; Thielemans, W. Improving the Reproducibility of Chemical Reactions on the Surface of Cellulose Nanocrystals: ROP of ε-Caprolactone as a Case Study. *Cellulose* **2011**, *18* (3), 607–617.
(2) Israelachvili, J. *Intermolecular & Surface Forces*; Academic Press: San Diego, 1992.
(3) Hansen, C. M. *Hansen Solubility Parameters: A User's Handbook*, 2nd ed.; CRC Press, 2007.
(4) Li, L.; Jiang, Z.; Xu, J.; Fang, T. Predicting Poly(vinyl Pyrrolidone)'s Solubility Parameter and Systematic Investigation of the Parameters of Electrospinning with Response Surface Methodology. *J. Appl. Polym. Sci.* **2014**, *131* (11), n/a-n/a.
(5) Sato, S.; Gondo, D.; Wada, T.; Kanehashi, S.; Nagai, K. Effects of Various Liquid Organic Solvents on Solvent-Induced Crystallization of Amorphous Poly(lactic Acid) Film. *J. Appl. Polym. Sci.* **2013**, *129* (3), 1607–1617.
(6) Buining, P.; Philipse, A.; Lekkerkerker, H. Phase Behavior of Aqueous Dispersions of Colloidal Boehmite Rods. *Langmuir* **1994**, No. 9, 2106–2114.
(7) Stiernstedt, J.; Nordgren, N.; Wågberg, L.; Brumer, H.; Gray, D. G.; Rutland, M. W. Friction and Forces between Cellulose Model Surfaces: A Comparison. *J. Colloid Interface Sci.* **2006**, *303* (1), 117–123.
(8) Bergström, L.; Stemme, S.; Dahlfors, T.; Arwin, H.; Ödberg, L. Spectroscopic Ellipsometry Characterization and Estimation of the Hamaker Constant of Cellulose. *Cellulose* **1999**, *6* (1), 1–13.

Chapter 5

Effect of Ionic Strength and Surface Charge Density on the Kinetics of Cellulose Nanocrystal Thin Film Swelling

The previous chapter described a new surface plasmon resonance spectroscopy-based platform for the measurement of particle-particle interactions, where van der Waals forces were observed to be the dominant force between CNCs. Moreover, it was shown that thin, particle only, films can serve as good analogs for dried CNC aggregates. CNC films swelled most in aqueous environments (compared to organic solvents and alcohols) but remained in tack during the measurement without any redispersion of CNCs. In this chapter, this technique is extended to investigate the rate of film swelling in aqueous environments as a function of CNC surface chemistry and solution ionic strength. It is established that, while the total thickness of the films is independent of surface charge density, the rate of swelling scales with osmotic pressure.

In this chapter film swelling data collection and analysis was performed by myself. Stephanie Kedzior was responsible for CNC surface modification and dynamic light scattering measurements. The chapter was drafted by myself and later edited by Stephanie Kedzior and my academic advisor, Dr. Emily Cranston. Dr. Marco Villalobos from Cabot Corporation was my industrial co-supervisor and provided technical guidance. This chapter is reprinted as it appears in *Langmuir*, with permission from the American Chemical Society © 2017.

Effect of Ionic Strength and Surface Charge Density on the Kinetics of Cellulose Nanocrystal Thin Film Swelling
Michael S. Reid, Stephanie A. Kedzior, Marco Villalobos and Emily D. Cranston
Langmuir, ASAP
DOI: 10.1021/acs.langmuir.7b01740

LANGMUIR
Article
pubs.acs.org/Langmuir

Effect of Ionic Strength and Surface Charge Density on the Kinetics of Cellulose Nanocrystal Thin Film Swelling

Michael S. Reid,[†] Stephanie A. Kedzior,[†] Marco Villalobos,[‡] and Emily D. Cranston*,[†]

[†]Department of Chemical Engineering, McMaster University, Hamilton, Ontario, Canada L8S 4L8
[‡]Cabot Corporation, Billerica, Massachusetts 01821, United States

Supporting Information

ABSTRACT: This work explores cellulose nanocrystal (CNC) thin films (<50 nm) and particle−particle interactions by investigating film swelling in aqueous solutions with varying ionic strength (1−100 mM). CNC film hydration was monitored *in situ* via surface plasmon resonance, and the kinetics of liquid uptake were quantified. The contribution of electrostatic double-layer forces to film swelling was elucidated by using CNCs with different surface charges (anionic sulfate half ester groups, high and low surface charge density, and cationic trimethylammonium groups). Total water uptake in the thin films was found to be independent of ionic strength and surface chemistry, suggesting that in the aggregated state van der Waals forces dominate over double-layer forces to hold the films together. However, the *rate* of swelling varied significantly. The water uptake followed Fickian behavior, and the measured diffusion constants decreased with the ionic strength gradient between the film and the solution. This work highlights that nanoparticle interactions and dispersion are highly dependent on the state of particle aggregation and that the rate of water uptake in aggregates and thin films can be tailored based on surface chemistry and solution ionic strength.

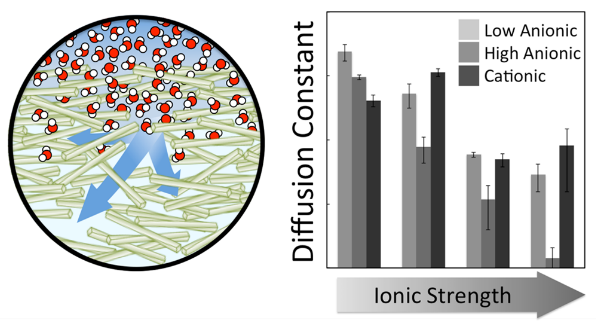

■ INTRODUCTION

Spurred by the global desire for green, renewable, and sustainable technologies, nanocellulose research has rapidly expanded over the past two decades.[1−3] Not only limited to academia, the number of patents citing cellulose nanocrystals (CNCs), cellulose micro/nanofibrils, and bacterial cellulose has similarly increased.[4,5] Although current commercial use of nanocellulose is limited, potential applications range from foods and cosmetics to polymer nanocomposites and cements.[1] Regardless of the application, maintaining well-dispersed, individualized particles (or fibrils) is critical as aggregation significantly reduces surface area, increases the percolation threshold, and often negates any nanoscale advantage.[6,7] As a result, the development of nanocellulose-based products necessitates well-dispersed nanomaterials on an industrial scale.

Because nanocellulose has a high density of surface hydroxyl groups, and generally forms stable colloidal suspensions in water (due to the presence of grafted charged surface groups), the most immediate applications will likely be aqueous based or aqueous processed materials. Within many envisioned products, nanocellulose will be combined with surfactants and/or polymers requiring thorough understanding of their effect on particle dispersion. Moreover, applications such as cement, concrete, and drilling fluids contain high concentrations of metal ions, silicates, and other salts, all of which can limit dispersibility and cause aggregation.[6,8] Nanocellulose behavior in high ionic strength environments is particularly challenging since colloidal stability is dependent on electrostatic repulsion between charged surface groups, such as the sulfate half esters that are grafted during the sulfuric acid hydrolysis production method.[9−11]

A significant amount of work has investigated nanocellulose behavior in various ionic strength media as both dispersions[12−14] and thin films.[15] Cherhal et al. monitored CNC aggregation by small-angle neutron scattering and showed that CNC aggregation occurs rapidly upon the addition of NaCl.[16] The densities of the CNC aggregates were independent of ionic strength but influenced by CNC surface charge. Aggregates formed using neutral CNCs (<0.01 e/nm^2) were more dense than those with surface sulfate half ester groups (0.16 e/nm^2). More recently, Phan-Xuan et al. investigated CNC aggregation in aqueous media containing mono-, di-, and trivalent metallic ions via small-angle X-ray scattering.[17] In agreement with Cherhal et al., similar aggregate density was observed for monovalent salts; however, not only did multivalent ions induce aggregation more efficiently, but aggregate density scaled with ionic strength.[17] Importantly, the critical aggregation concentration did not directly correlate with the Schulze−Hardy law, suggesting that other interactions (i.e., hydrophobic interactions) play a non-negligible role. This is

Received: May 23, 2017
Revised: July 10, 2017
Published: July 11, 2017

DOI: 10.1021/acs.langmuir.7b01740
Langmuir XXXX, XXX, XXX−XXX

potentially due to the amphiphilic nature of CNCs as observed by the propensity for particles to aggregate along their hydrophobic edge even at low concentrations.[18−20]

The current industrial producers of sulfuric acid hydrolyzed CNCs deliver material as either spray-dried or freeze-dried powders. This is not only economical from a shipping perspective but additionally improves the chemical stability of CNCs during storage.[21] In the dry state, CNCs are highly aggregated and must be fully dispersed within the desired application media to achieve good mechanical, rheological, and optical properties. As a result, understanding how dry, aggregated CNCs swell and disperse is of great interest. Beck et al. investigated the dispersibility dried CNC powders following evaporation, freeze-drying, and spray-drying and showed that the counterion of the sulfate half ester group significantly influenced CNC dispersibility.[22] Within their work, dried acid form CNCs ($-OSO_3H$) remained highly aggregated upon rehydration, whereas CNCs with monovalent alkali metal counterions (i.e., $-OSO_3Na$) showed good dispersibility. It is proposed that the metal counterion interrupts the interparticle hydrogen bonds that form upon drying, leading to more readily dispersible material. Similar hydrogen bonding interference has been suggested to occur when cellulose nanofibrils are freeze-dried in the presence of NaCl.[23]

Although previous works have investigated nanocellulose dispersibility,[24−27] the rate of hydration and swelling of aggregates has not been thoroughly investigated. The initial state of aggregation (i.e., parallel or crossed rod packing, density, pore size/morphology, etc.) within dry materials is typically unknown, as the drying method (freeze-drying, spray-drying, evaporation, etc.)[22,26,28] greatly impacts structure. This makes comparison of data between research groups challenging, as the geometry-dependent forces and diffusion rates differ between materials.

Cellulose thin films can serve as an excellent model system and have been extensively used to investigate nanocellulose behavior in both multilayer films and "cellulose-only" systems.[15] A significant amount of work has investigated the optical properties,[29] enzymatic degradation,[30−32] adhesion,[33−35] adsorption,[36−40] mechanical properties,[41] and swelling[42−47] of cellulose-based thin films. However, unlike macroscopic cellulose fibers,[48] there has yet to be any significant study examining the *kinetics* of CNC thin film swelling and its relationship to dispersibility. As a result, we ask: what are the interparticle forces and mechanisms that govern CNC thin film swelling in water, and how does particle surface chemistry and media ionic strength impact the time scale of this process? To address these questions, we present the first investigation that examines the rate of CNC film swelling using surface plasmon resonance spectroscopy (SPR). Confined CNC thin films (<50 nm) with varying surface chemistry and charge density were monitored following exposure to aqueous solutions of 1−100 mM NaCl. Continuous measurement of the films from the dry to the wet state demonstrated that the swelling rate increased with the ionic strength gradient between the film and the solution. However, the total water uptake in the film showed no statistically significant trend with ionic strength or surface chemistry. The results and methodologies of this work, while focused toward CNC thin films, can be applied to other dried nanoparticle systems (that can be deposited uniformly) and highlight the challenges associated with swelling and dispersing dried nanoparticle aggregates.

■ EXPERIMENTAL SECTION

Materials. Whatman cotton ashless filter aid was obtained from GE Healthcare Canada. Sulfuric acid and sodium hydroxide were purchased from Caledon Laboratory Chemicals (Georgetown, ON, Canada). Hydrogen peroxide, sodium chloride, and 2,3-epoxypropyltrimethylammonium chloride (EPTMAC) were purchased from Sigma-Aldrich (Oakville, ON, Canada). All chemicals were used as received. Water used throughout this work was purified Type I water with a resistivity of 18.2 MΩ·cm (Barnstead NANOpure DIamond system, Thermo Scientific, Asheville, NC).

Sulfuric Acid Hydrolysis of CNCs. CNCs were prepared by conventional sulfuric acid hydrolysis in which 40 g of Whatman cotton ashless filter aid was digested in 700 mL of 64 wt % sulfuric acid at 45 °C for 45 min under continuous stirring.[49] Following hydrolysis, the reaction was quenched by diluting the mixture in 7 L of 4 °C water. The suspension was then centrifuged for 10 min at 6000 rpm, from which the supernatant was decanted and replaced with water. This process was repeated until the suspension remained turbid following centrifugation. The precipitate was then dialyzed against water until the pH stabilized (~2 weeks changing water daily). The suspension was sonicated (Sonifier 450, Branson Ultrasonics, Danbury, CT) continuously in an ice bath for 15 min three times at 60% output. CNC suspensions were neutralized by the addition of an appropriate amount of 1 mM NaOH and freeze-dried for storage. Sulfate half ester content on the CNC surface (i.e., surface charge density) was measured by conductometric titration with NaOH according to Beck et al.[50] Unmodified CNCs are denoted HS-CNCs for "high sulfate content CNCs".

Desulfation of CNCs. HS-CNCs were partially desulfated by adding an equal volume of 3 M NaOH to a 10 wt % CNC suspension. The mixture was added to an oil bath at 65 °C and allowed to proceed for 5 h. Upon completion of the reaction, it was dialyzed against purified water until a neutral pH was obtained. Subsequently, CNC suspensions were neutralized by the addition of an appropriate amount of 1 mM NaOH and freeze-dried for storage. The resulting CNCs were denoted as LS-CNCs for "low sulfate content CNCs".

Cationic Functionalization of CNCs. Cationic CNCs (CAT-CNCs) were prepared following previous literature[51] using LS-CNCs as a starting material. The pH of a 2 wt % LS-CNC suspension was adjusted to 13.2 using NaOH. The suspension was then added to a 65 °C oil bath and EPTMAC was added at a 1:16 CNC:EPTMAC weight ratio dropwise under constant stirring. The reaction proceeded for 5 h and was then quenched and dialyzed against purified water until a neutral pH was obtained. CAT-CNC suspensions were then freeze-dried for storage.

Elemental Analysis. HS-CNCs, LS-CNCs, and CAT-CNCs were freeze-dried, and elemental analysis was performed by Micro Analysis Inc. (Wilmington, DE). The materials were combusted in a pure oxygen environment, and ion chromatography was used to quantify elemental composition. HS-CNCs and LS-CNCs were analyzed for sulfur, and CAT-CNCs were analyzed for sulfur and nitrogen. The results presented are an average of three independent measurements. Additionally, the sulfur content of HS-CNC and LS-CNC was measured via conductometric titrations and is presented in Supporting Information Table S1.

Zeta Potential. Zeta potential measurements were performed on 0.1 wt % CNC suspensions with 10 mM added NaCl using a Zeta Potential ZetaPlus Analyzer (Brookhaven, USA).

Film Preparation for SPR Measurements. SiO_2-coated SPR sensors (BioNavis, Ylöjärvi, Finland) were cleaned in a piranha solution (3:1 concentrated sulfuric acid to hydrogen peroxide) for 30 min, followed by continuous rinsing with purified water and drying by a stream of N_2. CNC suspensions were prepared by dispersing freeze-dried CNCs in purified water and sonicating at 60% amplitude for 30 s. CNC thin films (<50 nm thick) were prepared on the cleaned SPR sensors by spin-coating a 2−3 wt % CNC suspension under N_2 gas (G3P Spincoat, Specialty Coating Systems Inc., Indianapolis, IN) at 4000 rpm for 30 s with a 7 s acceleration ramp. Spin-coated films were

DOI: 10.1021/acs.langmuir.7b01740
Langmuir XXXX, XXX, XXX−XXX

Table 1. Apparent Particle Size Measured by DLS, Zeta Potential, Elemental Mass Percentages of Sulfur and Nitrogen, and Calculated Inherent Ionic Strength from Anionic and Cationic Groups within Each Film

	apparent particle size (nm)	zeta potential (mV)	mass sulfur (%)	mass nitrogen (%)	anionic ionic strength (mM)	cationic ionic strength (mM)
LS-CNC	57 ± 5	−32 ± 2	0.46 ± 0.05	0	450 ± 50	0
HS-CNC	57 ± 1	−33 ± 5	0.70 ± 0.05	0	680 ± 50	0
CAT-CNC	68 ± 1	+33 ± 2	0.49 ± 0.04	0.55 ± 0.01	480 ± 40	1220 ± 20

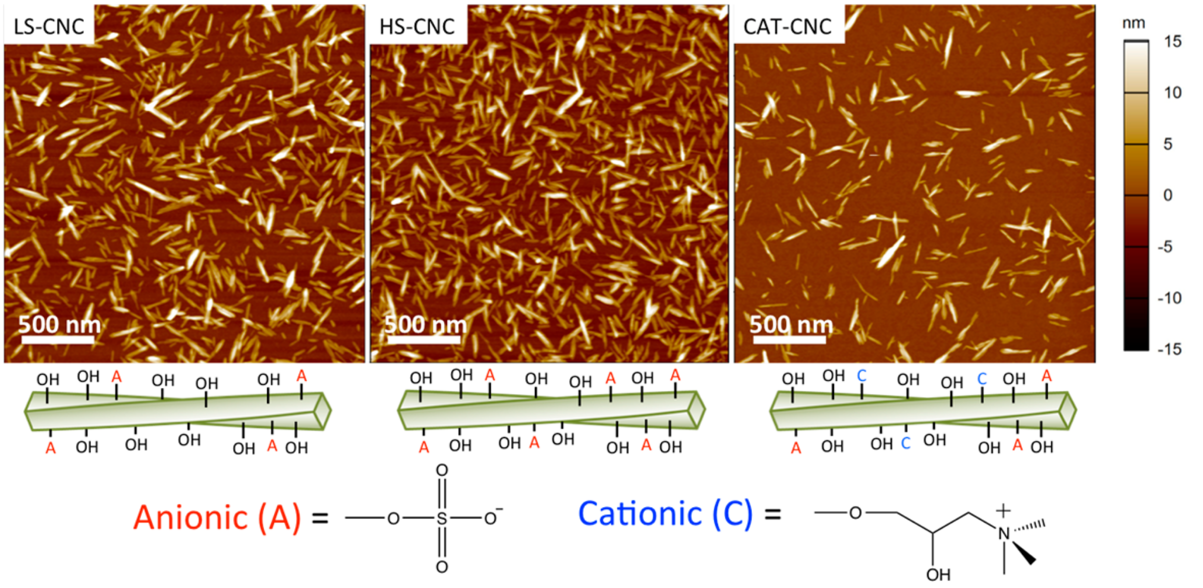

Figure 1. 2.5 μm × 2.5 μm AFM height images of LS-CNCs, HS-CNCs, and CAT-CNCs along with schematic representation of the surface chemistry of each particle (not drawn to scale).

heat treated at 80 °C for 12 h, gently rinsed with purified water, and heat-treated again overnight.

Atomic Force Microscopy (AFM). AFM images were collected using an Asylum MFP-3D instrument (Asylum Research, an Oxford Instrument Company, Santa Barbara, CA) in alternating current (ac) mode under ambient conditions. Surfaces were imaged using rectangular FMR cantilevers (NanoWorld) with normal spring constants of 1.2−5.5 N/m and resonant frequencies of 60−90 kHz. Images were processed in Igor Pro 6.0 running Asylum Research AFM software (version 13.17) using a second-order flatten routine.

Dynamic Light Scattering (DLS). Hydrodynamic diameter, i.e., "apparent particle size", of CNCs in 1, 10, 50, and 100 mM NaCl was measured for suspensions of 0.025 wt % using a Malvern Zetasizer Nano particle analyzer at 20 °C. Samples were measured 24 h after the addition of NaCl. Following initial measurements, samples were dialyzed for 1 week against purified water (water changes 2 times a day) to remove NaCl and sonicated at 60% amplitude for 10 s to disperse loosely bound material. Samples were then filtered using a Pall Acrodisc glass fiber syringe filter with a nominal pore size of 1 μm to remove metal particles, which are released from the sonicator probe. The apparent particle size was measured again to examine irreversible aggregation. All samples were measured 15 times, and the average particle size distribution was obtained. The number-average of each particle distribution was calculated, and the confidence interval presented is the standard deviation from three separate samples.

Surface Plasmon Resonance (SPR). Full angle (40°−77°) SPR curves at 670 and 785 nm were collected using a multiparametric MP-SPR Navi 200 (BioNavis, Ylöjärvi, Finland). Using the 785 nm laser wavelength, films were monitored *in situ* from the dry to the wet state (see Supporting Information Figure S1 for representative raw data). Films were swollen under constant flow of 100 μL/min of 1, 10, 50, and 100 mM NaCl at 25 °C and allowed to equilibrate for a minimum of 30 min (see Figure S2 for longer equilibration time data). SPR curves were fit using the free software Winspall 3.01 (Max-Planck Institute for Polymer Research, Mainz, Germany) based on the Fresnel equations and recursion formalism. Prior to swelling, the refractive index of dry CNC films (n_{film}) was determined to range from 1.453 to 1.463 via the wavelength crossover method (see Figure S3), yielding an average index of refraction of n_{film} = 1.458. Taking the refractive index of CNCs to be n_{CNC} = 1.55, dry film porosity (V_d) was determined to be 20 ± 1% using optical volume averaging theory as outlined previously.[47] Assuming swelling occurs as interparticle spacing increases perpendicular to surface, the percent volume of water within swollen films (V_s) and thus the film thickness was determined by

$$V_s = \frac{\Delta\theta_d}{\Delta\theta_s} V_d \tag{1}$$

where $\Delta\theta_d$ and $\Delta\theta_s$ are the difference between the SPR peak and total internal reflection angle for the initial dry and swollen films, respectively. Notably $\Delta\theta_s$ is corrected for water angular shifts.[47] Swelling profiles are plotted as the ratio of $\Delta\theta_t/\Delta\theta_0$ where $\Delta\theta_t$ is the angular value at time t and $\Delta\theta_0$ is the angular value upon the introduction of swelling media (see Figure S1). The average of a minimum of three swelling measurements is shown, and the confidence interval is presented as the standard deviation.

■ RESULTS AND DISCUSSION

CNC Properties. The density of sulfate half ester groups on the surface of sulfuric acid extracted CNCs varies between producers[11] and is well-known to impact colloidal properties such as rheology,[52] interface stabilizing ability,[53] and particle self-assembly.[54] Although significant work has investigated how charge and charge density influence colloidal behavior, no work has been done to examine how surface charge affects swelling rates of CNC thin films. To this end, we prepared thin films using CNCs with a (relatively) low density of surface $-OSO_3^-$ groups (LS-CNCs), a high density of $-OSO_3^-$ groups (HS-CNCs), and cationic trimethylammonium surface groups (CAT-CNCs) and examined swelling in aqueous media of varying ionic strength (see Table 1 for CNC chemical composition and Table S1 for calculated surface charge densities).

All CNCs prepared were between 51 and 366 nm in length and 4 to 14 nm in cross section as measured by AFM (Figure 1). LS-CNCs and CAT-CNCs were prepared from HS-CNCs and showed no significant change in particle morphology or aspect ratio following treatment (i.e., desulfation and cationization, respectively), and only minor aggregation was observed for CAT-CNCs by DLS (Table 1). Elemental analysis indicated that nearly a third of the sulfate groups were removed for LS-CNCs yet all CNCs remained colloidally stable according to zeta potential measurements (Table 1). Comparatively, CAT-CNCs exhibited a positive zeta potential supporting that cationic groups were successfully grafted to the CNC surface. Importantly, although CAT-CNCs had a net positive surface charge, elemental analysis indicated that both anionic and cationic groups were present on the particle surface (Table 1). As a result, we expect that when CAT-CNCs are in contact (as is the case in thin films), ionic bridging between particles may occur[51] and potentially lead to irreversible aggregation, impacting film swelling and dispersibility.

To examine ionic bridging, DLS was used to monitor CNC aggregation and redispersibility following the addition and removal of NaCl from colloidal suspensions (Figure 2). Both types of anionic CNCs demonstrated good colloidal stability in 1 and 10 mM NaCl solutions; however, above 50 mM NaCl, LS-CNCs showed significantly more aggregation, indicating that electrostatic repulsion between LS-CNCs was greatly suppressed. Upon the removal of NaCl by dialysis, and probe sonication to redisperse the CNCs, the initial particle size of LS-CNCs and HS-CNCs is recovered, indicating that aggregation is completely reversible (Figure 2b), which is expected for CNCs with only anionic surface groups. In contrast, CAT-CNCs show a stronger tendency to aggregate (Figure 2a), with notable aggregation occurring in 10 mM NaCl and up. Upon the removal of NaCl, highly aggregated material (>1 μm) remains, particularly for the CAT-CNCs in 100 mM NaCl, indicating that irreversible aggregation has occurred. While it is difficult to quantify the extent of ionic bridging between CAT-CNCs, we expect this phenomenon to occur when particles are forced together during the spin-coating process that is used to prepare the thin films for swelling experiments.

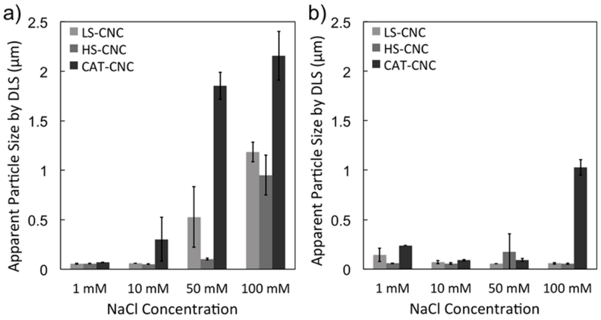

Figure 2. Apparent particle size as measured by DLS for (a) CNCs in various concentrations of NaCl and (b) the same samples measured following dialysis and sonication.

Film Structure. Spin-coated CNC films are uniform, thin (<50 nm), porous structures that are composed of tightly packed CNCs; the films are stable in both aqueous and nonaqueous solvents.[47] CNCs within the film are no longer colloidally stable and are considered to be in physical contact, that is, with particle spacings that can be approximated as 0 nm. Prior to swelling, all films were measured via multiwavelength SPR and found to have an index of refraction that ranges from 1.453 to 1.463 (see Figure S3). Using volume averaging theory,[55] the average film porosity for all films was determined to be 20 ± 1%, indicating that CNC content within the films is consistent regardless of CNC surface chemistry. This is to say that the ratio of cellulose to air in each film is the same for all CNC films examined. We envision CNC film structure similar to randomly packed high aspect ratio rods, however, with higher density than theoretically predicted due to the polydispersity of the CNC particles and the forces experienced during spin-coating.[56] The internal structure (i.e., pore size, pore size distribution), however, cannot be specifically determined via SPR or AFM and is likely impacted by surface charge. Nonetheless, CNCs within the film are highly aggregated and serve as a good analogue for dried aggregates with particle spacing of ca. 0 nm.

Because of the anionic (and cationic) surface groups, CNC aggregates and thin films contain a high density of charged species, from both grafted surface groups and their counterions. As a result, the CNC thin films used here have an inherent ionic strength that alters osmotic pressure and influences swelling and dispersion behavior. Under the assumption that all counterions are accessible, Table 1 shows the approximated inherent ionic strength of CNC films calculated from the percent sulfur and nitrogen on each CNC (see sample calculation in the Supporting Information). While DLS shows that ionic bridging occurs in CAT-CNC films, we cannot explicitly determine to what degree this impacts the overall ionic strength of the film. As a result, the ionic strengths from both anionic and cationic groups are presented in Table 1 for CAT-CNCs.

Water Diffusion into CNC Thin Films. To provide insight into the diffusion of water within CNC aggregates, uniform thin films were monitored via SPR during swelling from the dry to the wet state. Our previous work showed that under continuous flow of aqueous and nonaqueous solvents CNC thin films remain stable throughout swelling experiments and return to their original state following drying[47] (this is also the case for the experiments presented here; see Figure S4). Swelling of particle-only films occurs as water penetrates interparticle space (CNCs do not swell themselves[42,46,47]), increasing particle−particle spacing, which we propose is analogous to the initial stages of particle dispersion from dried aggregates. We emphasize that CNCs within the thin films prepared cannot be considered as colloidally stable and that initially particles are in physical contact with each other.

Figure 3 shows normalized representative swelling profiles, measured by SPR for HS-CNC films upon the introduction of aqueous NaCl solutions, where film swelling is observed as a reduction in SPR angular values (LS-CNC and CAT-CNC profiles are provided in Figure S5). Clearly, ionic strength impacts not only the shape of the swelling profile but also the

DOI: 10.1021/acs.langmuir.7b01740

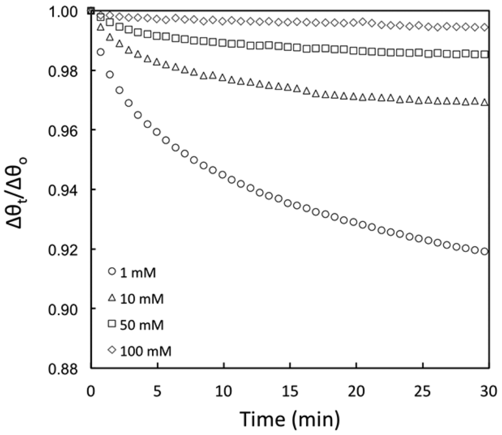

Figure 3. Swelling profiles of HS-CNC films measured by SPR. Curves are normalized to the angular shift immediately following NaCl solution addition. Representative raw swelling profiles are shown in Figure S7.

angular change; 1 and 100 mM NaCl elicit the largest and smallest angular changes, respectively. Films were allowed to equilibrate for a minimum of 30 min, after which no significant change to film volume was observed (see Figure S2 for longer equilibration times). The volume of water in the swollen films is ca. 30–40% (calculated by eq 1, see Experimental Section), equating to an increase of 4–8 nm for a 40 nm thick CNC film. No statistically relevant trend in total water uptake with ionic strength or surface charge density is observed (Figure 4). The idea that total swelling is independent of ionic strength is in good agreement with Cherhal et al., who found that for CNCs with a constant surface charge density aggregate density (i.e., particle spacing) was independent of ionic strength above a critical salt concentration (~2 mM).[16]

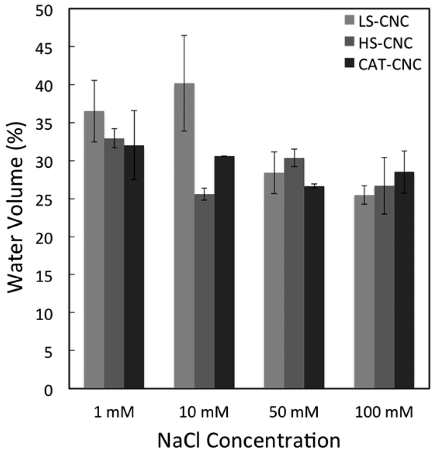

Figure 4. Calculated volume of water within the CNC films in various concentrations of NaCl after 30 min of swelling determined from SPR profiles. Film porosity is taken as 20% (i.e., the volume of air in the films initially).

It is somewhat counterintuitive, however, that films with different surface charge densities all swell to similar degrees or that the particle–particle spacing within CNC films is equivalent after swelling (as indicated in Figure 4). We propose that this is due to the fact that within a dry film, prior to swelling, CNCs are in physical contact and particle spacing is ca. 0 nm—introducing water increases particle spacing, however, within the precision of our measurements; all water uptake values correspond to a final CNC–CNC spacing of 1–2 nm, and this spacing is still within the van der Waals dominated region of the DLVO curve (see Supporting Information for DLVO approximations and plots in Figure S6). As a result, electrostatic repulsion does not play a significant role, making particle spacing and film thickness independent of surface charge density and ionic strength. As a result, within our thin films, electrostatic repulsion between particles does not effectively overcome van der Waals forces; thus, LS-CNCs and HS-CNCs exhibit similar changes in film volume and water uptake.

This thin film swelling behavior clearly differs from macroscopic fiber and biocomposite material swelling, which is known to depend on surface charge density and added salt, but these materials are heterogeneous in morphology and chemical composition and often change dimensions over visible length scales. The CNC films studied here are purely composed of highly crystalline cellulose I and are homogeneous and due to their ultrathin nature may be influenced by substrate and/or confinement effects. Most importantly, CNCs are in physical contact with no other components to separate them. The swelling determined here is also close to the resolution limit of most techniques which is likely why these are the first measurements of their kind. As such, we believe that the equivalent swelling observed for all of our films is reasonable for this system but that further work would be required to comment on the swelling tendencies of micro- or macroscopic hybrid CNC materials.

Although ionic strength has little impact on overall particle–particle spacing, swelling kinetics and water diffusion rates within the CNC films do vary significantly with ionic strength (Figure 3). To determine the nature of diffusion, thin films are considered to have uniform slab geometry with dimensions of 2 mm × 7 mm (dictated by the SPR flow cell) × <50 nm thick yielding an aspect ratio, which can exhibit one-dimensional diffusion behavior. Adapting the generalized empirical equation detailed by Ritger and Peppas,[57] we calculate the diffusion exponent (n) of time (t) via

$$\frac{V_t}{V_0} = \frac{\Delta\theta_0}{\Delta\theta_t} = kt^n \qquad (2)$$

where k is a constant related to the structure of the film; V_0 and V_t are the volume of water within the film immediately following injection and at time t, respectively. Within their pivotal work, Ritger and Peppas outlined that under an early time solution ($M_t/M_0 < 0.50$ where M is the mass of solvent in the film) Fickian diffusion is defined by $n = 0.5$ and non-Fickian diffusion as $0.5 < n < 1.0$ (see Figure S8). Figure 5 shows that all CNC films exhibited nearly Fickian behavior with mean diffusion exponents ranging from 0.47 to 0.60.

Minor deviation from Fickian diffusion, particularly in the early stages of swelling, is expected to result from the porous structure and the nature of swelling within the film. First, water rapidly fills large open pores, expelling air, via a non-Fickian process that is expected to follow a time dependency that scales as $n > 0.5$. Simultaneously, narrow channels and pores between tightly packed particles present a confined geometry that can slow water diffusion through the film. At the extreme, water diffusion can approach the single file limit with diffusion

DOI: 10.1021/acs.langmuir.7b01740

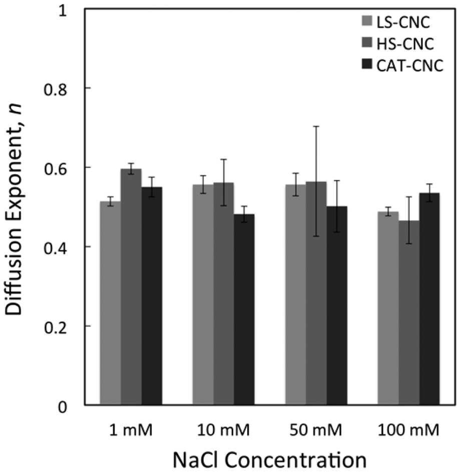

Figure 5. Calculated diffusion exponents via eq 2 for CNC film swelling in NaCl solutions.

exponents $n < 0.5$.[58,59] However, as swelling progresses, particle−particle spacing rapidly increases and non-Fickian behavior yields to Fickian diffusion. Although it is unclear to what extent these processes influence diffusion, the overall behavior of swelling reflects that of Fickian diffusion. Similar to the film thickness change upon water uptake, the *mechanism* of water diffusion is not impacted by CNC surface chemistry/charge density or the ionic strength of the swelling medium.

Under the assumption of Fickian behavior, we calculated the water diffusion constants (D) by adapting work from Erdoğan et al. to liquid swelling media:[60]

$$\frac{V_t}{V_0} = \frac{\Delta\theta_0}{\Delta\theta_t} = 4\sqrt{\frac{D}{\pi a_{\mathrm{d}}}}\,t^{1/2} \tag{3}$$

where a_{d} is the initial dry film thickness. In the Fickian regime, diffusion constants for both LS-CNC and HS-CNC films decreased with increasing ionic strength (Figure 6). This behavior is attributed to the decreasing ionic strength gradient between the aqueous solution and the anionic CNC film.

Specifically, at low salt concentrations (1 mM NaCl) the osmotic pressure in the films is large, and correspondingly, larger diffusion constants were measured. In contrast, concentrated salt solutions (100 mM NaCl) led to a smaller concentration gradient and thus slower diffusion (with a fairly linear trend between low and high salt concentrations for anionic CNCs). Contradicting this, the diffusion constants for LS-CNC films are consistently larger than HS-CNC films despite LS-CNCs having lower charge density and a smaller osmotic pressure. This suggests structural differences between the films. We rationalize these structural differences by considering the process of film formation from CNC suspensions: during spin-coating, dispersed CNCs are forced together to form aggregates, which are then deposited on the SPR sensor surface. The surface charge density impacts aggregation from the dispersed state and thus LS-CNC are expected to form more dense aggregates in accordance with Cherhal et al.[16] Because all dry CNC films have equivalent total porosity (i.e., all films contain 20% air and 80% CNCs), films containing denser aggregates must have larger pores (or channels) between groups of CNCs. We propose that diffusion rates in LS-CNC films are larger because the films have larger pores between CNCs, and vice versa (this proposed structure is shown schematically in Figure 7). While we infer that these channels contribute to the rate of swelling, we propose that the film volume increases only as particle−particle spacing increases. As a result, water uptake by larger pores, void of CNCs, may increase the rate of swelling but does not contribute significantly to the total swollen thickness. Nonetheless, both LS-CNC and HS-CNC films follow similar trends over the concentration range examined, suggesting that the swelling mechanism and forces within the films are comparable.

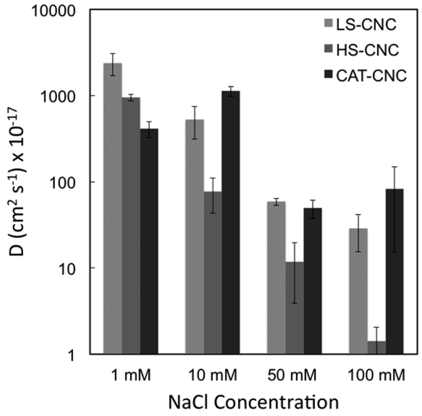

Figure 6. Diffusion constants calculated from eq 3 for water in CNC films measured from SPR swelling experiments in NaCl solutions.

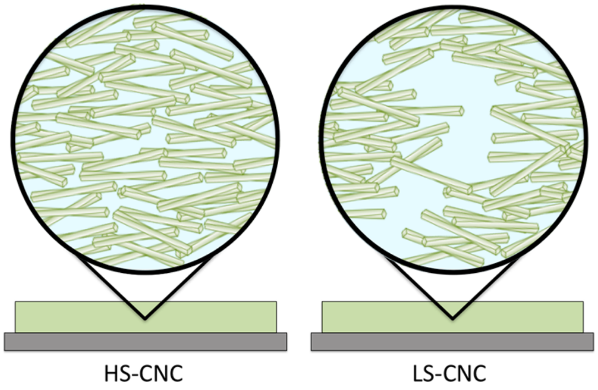

Figure 7. Schematic representation of proposed structural difference between dry HS-CNC and LS-CNC films which both have 20% porosity according to SPR measurements. LS-CNC films are depicted with larger pores (or channels) because the spin-coating process used to create the films likely induces denser CNC aggregates (less electrostatic repulsion), which leads to larger diffusion constants during swelling (not drawn to scale).

In contrast, CAT-CNC film swelling exhibits two distinct diffusion regimes with a transition occurring between 10 and 50 mM NaCl. Above this point, swelling in both 50 and 100 mM NaCl yields statistically equivalent diffusion constants indicating that ionic strength does not influence the rate of film swelling. While it is unclear to the cause of this behavior, and the role of ionic bridging, the presence of both anionic and cationic groups clearly impact the swelling rate. Nonetheless, similar to LS-CNCs, the magnitudes of the diffusion coefficients for CAT-CNCs are mostly larger than HS-CNCs, which suggests that there are structural differences between the

DOI: 10.1021/acs.langmuir.7b01740

films. Much like LS-CNCs, DLS measurements indicate that CAT-CNCs are less colloidally stable than HS-CNCs and likely form denser aggregates during spin-coating, leading to faster swelling kinetics due to larger pores or channels. These findings become critical when considering formulating CNCs into various aqueous applications. For example, because diffusion within thin films (and aggregates) is the most rapid in low ionic strength media, CNCs should be incorporated prior to salt, ionic surfactant, or polyelectrolyte addition.

■ CONCLUSIONS

This work examines the swelling kinetics of CNC thin films when exposed to aqueous media of varying ionic strength. In general, when aggregated (as thin films or dry particles), CNCs must overcome strong attractive particle−particle interactions to be dispersed. Understanding the balance between attractive van der Waals and repulsive double-layer forces in the aggregated state is essential to achieving well-dispersed colloidal systems, regardless of the particle type. Unlike spray-dried and freeze-dried aggregates, CNC thin films are uniform and flat, allowing for quantitative analysis of film volume and water diffusion using *in situ* SPR to measure changes from the dry to the wet state.

In response to the scientific questions outlined in the Introduction "what are the interparticle forces and mechanisms that govern CNC thin film swelling in water, and how does particle surface chemistry and media ionic strength impact the time scale of this process?", we conclude that particle−particle spacing in swollen CNC films was found to be independent of surface charge density and ionic strength, indicating that van der Waals forces dominate the particle−particle interactions that hold the films together. This suggests that when dispersing freeze-dried or spray-dried aggregates, double-layer forces alone are not sufficient to fully disperse particles and that external energy is needed to fully disperse CNCs in both high and low ionic strength media.

CNC film swelling is driven by osmotic pressure and water uptake follows Fickian diffusion. Critically, the diffusion *rate* was significantly impacted by film surface charge density and ionic strength. Diffusion of water into the films was the most rapid in low ionic strength media where the ionic strength gradient between the film and the solution was the greatest. Diffusion rates were also inferred to be affected by structural differences in the films; we propose that denser CNC aggregates (formed during film formation and drying) have larger pores/channels *between* aggregates, which leads to a faster influx of water. Because of the tight particle−particle packing in CNC thin films, we expect these results to be readily translatable to dried CNC aggregates and will aid in the formulation of aqueous CNC products containing salts, ionic surfactants, and polyelectrolytes. Moreover, this methodology can be generally applied as a tool to examine swelling and interparticle forces of many other dried nanoparticle systems.

■ ASSOCIATED CONTENT

Ⓢ Supporting Information

The Supporting Information is available free of charge on the ACS Publications website at DOI: 10.1021/acs.langmuir.7b01740.

> Representative SPR curves of CNC films during swelling, swelling profile of CNC film over 12 h, determination of CNC film parameters via SPR wavelength crossover method, SPR curves before and after swelling, and representative swelling profiles for all films examined; calculation of the ionic strength, DLVO interactions, and diffusion exponent within the film (PDF)

■ AUTHOR INFORMATION

Corresponding Author

*E-mail ecranst@mcmaster.ca (E.D.C.).

ORCID

Michael S. Reid: 0000-0002-0999-6671
Emily D. Cranston: 0000-0003-4210-9787

Notes

The authors declare no competing financial interest.

■ ACKNOWLEDGMENTS

Funding from the Natural Sciences and Engineering Research Council of Canada, Industrial Postgraduate Scholarship program sponsored by Cabot Corporation is gratefully acknowledged. Professors R. Pelton, A. Guarne, and J. Moran-Mirabal are thanked for sharing equipment to characterize CNCs. Additionally, the Biointerfaces Institute and the Brockhouse Institute for Materials Research at McMaster University are acknowledged for support and equipment.

■ REFERENCES

(1) Klemm, D.; Kramer, F.; Moritz, S.; Lindström, T.; Ankerfors, M.; Gray, D. G.; Dorris, A. Nanocelluloses: A New Family of Nature-Based Materials. *Angew. Chem., Int. Ed.* **2011**, *50*, 5438−5466.

(2) Moon, R. J.; Martini, A.; Nairn, J.; Simonsen, J.; Youngblood, J. Cellulose Nanomaterials Review: Structure, Properties and Nanocomposites. *Chem. Soc. Rev.* **2011**, *40* (7), 3941−3994.

(3) Oksman, K.; Aitomäki, Y.; Mathew, A. P.; Siqueira, G.; Zhou, Q.; Butylina, S.; Tanpichai, S.; Zhou, X.; Hooshmand, S. Review of the Recent Developments in Cellulose Nanocomposite Processing. *Composites, Part A* **2016**, *83*, 2−18.

(4) Charreau, H.; Foresti, M. L.; Vazquez, A. Nanocellulose Patents Trends: A Comprehensive Review on Patents on Cellulose Nanocrystals, Microfibrillated and Bacterial Cellulose. *Recent Pat. Nanotechnol.* **2013**, *7* (1), 56−80.

(5) Reid, M. S.; Villalobos, M.; Cranston, E. D. The Role of Hydrogen Bonding in Non-Ionic Polymer Adsorption to Cellulose Nanocrystals and Silica Colloids. *Curr. Opin. Colloid Interface Sci.* **2017**, *29*, 76−82.

(6) Cao, Y.; Zavattieri, P.; Youngblood, J.; Moon, R.; Weiss, J. The Relationship between Cellulose Nanocrystal Dispersion and Strength. *Constr. Build. Mater.* **2016**, *119*, 71−79.

(7) Kedzior, S. A.; Graham, L.; Moorlag, C.; Dooley, B. M.; Cranston, E. D. Poly(methyl Methacrylate)-Grafted Cellulose Nanocrystals: One-Step Synthesis, Nanocomposite Preparation, and Characterization. *Can. J. Chem. Eng.* **2016**, *94* (5), 811−822.

(8) Molnes, S. N.; Torrijos, I. P.; Strand, S.; Paso, K. G.; Syverud, K. Sandstone Injectivity and Salt Stability of Cellulose Nanocrystals (CNC) dispersions—Premises for Use of CNC in Enhanced Oil Recovery. *Ind. Crops Prod.* **2016**, *93*, 152−160.

(9) Fall, A. B.; Lindström, S. B.; Sundman, O.; Ödberg, L.; Wågberg, L. Colloidal Stability of Aqueous Nanofibrillated Cellulose Dispersions. *Langmuir* **2011**, *27* (18), 11332−11338.

(10) Israelachvili, J. *Intermolecular & Surface Forces*; Academic Press: San Diego, CA, 1992.

(11) Reid, M. S.; Villalobos, M.; Cranston, E. D. Benchmarking Cellulose Nanocrystals: From the Laboratory to Industrial Production. *Langmuir* **2017**, *33* (7), 1583−1598.

(12) Shafiei-Sabet, S.; Hamad, W. Y.; Hatzikiriakos, S. G. Ionic Strength Effects on the Microstructure and Shear Rheology of

Cellulose Nanocrystal Suspensions. *Cellulose* **2014**, *21* (5), 3347−3359.

(13) González-Labrada, E.; Gray, D. G. Viscosity Measurements of Dilute Aqueous Suspensions of Cellulose Nanocrystals Using a Rolling Ball Viscometer. *Cellulose* **2012**, *19* (5), 1557−1565.

(14) Dong, X. M.; Kimura, T.; Revol, J.-F.; Gray, D. G. Effects of Ionic Strength on the Isotropic−Chiral Nematic Phase Transition of Suspensions of Cellulose Crystallites. *Langmuir* **1996**, *12* (8), 2076−2082.

(15) Kontturi, E.; Tammelin, T.; Österberg, M. Cellulose–Model Films and the Fundamental Approach. *Chem. Soc. Rev.* **2006**, *35*, 1287−1304.

(16) Cherhal, F.; Cousin, F.; Capron, I. Influence of Charge Density and Ionic Strength on the Aggregation Process of Cellulose Nanocrystals in Aqueous Suspension, as Revealed by Small-Angle Neutron Scattering. *Langmuir* **2015**, *31* (20), 5596−5602.

(17) Phan-Xuan, T.; Thuresson, A.; Skepö, M.; Labrador, A.; Bordes, R.; Matic, A. Aggregation Behavior of Aqueous Cellulose Nanocrystals: The Effect of Inorganic Salts. *Cellulose* **2016**, *23* (6), 3653−3663.

(18) Uhlig, M.; Fall, A.; Wellert, S.; Lehmann, M.; Prévost, S.; Wågberg, L.; von Klitzing, R.; Nyström, G. Two-Dimensional Aggregation and Semidilute Ordering in Cellulose Nanocrystals. *Langmuir* **2016**, *32* (2), 442−450.

(19) Kalashnikova, I.; Bizot, H.; Cathala, B.; Capron, I. Modulation of Cellulose Nanocrystals. Amphiphilic Properties to Stabilize Oil/Water Interface. *Biomacromolecules* **2012**, *13* (1), 267−275.

(20) Silveira, R. L.; Stoyanov, S. R.; Kovalenko, A.; Skaf, M. S. Cellulose Aggregation under Hydrothermal Pretreatment Conditions. *Biomacromolecules* **2016**, *17* (8), 2582−2590.

(21) Beck, S.; Bouchard, J. Auto-Catalyzed Acidic Desulfation of Cellulose Nanocrystals. *Nord. Pulp Pap. Res. J.* **2014**, *29* (1), 006−014.

(22) Beck, S.; Bouchard, J.; Berry, R. Dispersibility in Water of Dried Nanocrystalline Cellulose. *Biomacromolecules* **2012**, *13*, 1486−1494.

(23) Missoum, K.; Bras, J.; Belgacem, M. N. Water Redispersible Dried Nanofibrillated Cellulose by Adding Sodium Chloride. *Biomacromolecules* **2012**, *13* (12), 4118−4125.

(24) Cheng, D.; Wen, Y.; Wang, L.; An, X.; Zhu, X.; Ni, Y. Adsorption of Polyethylene Glycol (PEG) onto Cellulose Nano-Crystals to Improve Its Dispersity. *Carbohydr. Polym.* **2015**, *123*, 157−163.

(25) Butchosa, N.; Zhou, Q. Water Redispersible Cellulose Nanofibrils Adsorbed with Carboxymethyl Cellulose. *Cellulose* **2014**, *21* (6), 4349−4358.

(26) Peng, Y.; Gardner, D. J.; Han, Y. Drying Cellulose Nanofibrils: In Search of a Suitable Method. *Cellulose* **2012**, *19* (1), 91−102.

(27) Khoshkava, V.; Kamal, M. R. Effect of Drying Conditions on Cellulose Nanocrystal (CNC) Agglomerate Porosity and Dispersibility in Polymer Nanocomposites. *Powder Technol.* **2014**, *261*, 288−298.

(28) Peng, Y.; Gardner, D. J.; Han, Y.; Kiziltas, A.; Cai, Z.; Tshabalala, M. a. Influence of Drying Method on the Material Properties of Nanocellulose I: Thermostability and Crystallinity. *Cellulose* **2013**, *20* (5), 2379−2392.

(29) Cranston, E. D.; Gray, D. G. Birefringence in Spin-Coated Films Containing Cellulose Nanocrystals. *Colloids Surf., A* **2008**, *325* (1−2), 44−51.

(30) Cerclier, C. V.; Guyomard-Lack, A.; Cousin, F.; Jean, B.; Bonnin, E.; Cathala, B.; Moreau, C. Xyloglucan-Cellulose Nanocrystal Multilayered Films: Effect of Film Architecture on Enzymatic Hydrolysis. *Biomacromolecules* **2013**, *14*, 3599−3609.

(31) Cheng, G.; Liu, Z.; Murton, J. K.; Jablin, M.; Dubey, M.; Majewski, J.; Halbert, C.; Browning, J.; Ankner, J.; Akgun, B.; et al. Neutron Reflectometry and QCM-D Study of the Interaction of Cellulases with Films of Amorphous Cellulose. *Biomacromolecules* **2011**, *12* (6), 2216−2224.

(32) Jiang, F.; Kittle, J. D.; Tan, X.; Esker, A. R.; Roman, M. Effects of Sulfate Groups on the Adsorption and Activity of Cellulases on Cellulose Substrates. *Langmuir* **2013**, *29* (10), 3280−3291.

(33) Cranston, E. D.; Gray, D. G.; Rutland, M. W. Direct Surface Force Measurements of Polyelectrolyte Multilayer Films Containing Nanocrystalline Cellulose. *Langmuir* **2010**, *26* (22), 17190−17197.

(34) Stiernstedt, J.; Nordgren, N.; Wågberg, L.; Brumer, H.; Gray, D. G.; Rutland, M. W. Friction and Forces between Cellulose Model Surfaces: A Comparison. *J. Colloid Interface Sci.* **2006**, *303* (1), 117−123.

(35) Notley, S. M.; Pettersson, B.; Wågberg, L. Direct Measurement of Attractive van Der Waals' Forces between Regenerated Cellulose Surfaces in an Aqueous Environment. *J. Am. Chem. Soc.* **2004**, *126*, 13930−13931.

(36) Eronen, P.; Junka, K.; Laine, J.; Österberg, M. Interaction between Water-Soluble Polysaccharides and Native Nanofibrillar Cellulose Thin Films. *BioResources* **2011**, *6* (4), 4200−4217.

(37) Benselfelt, T.; Cranston, E. D.; Ondaral, S.; Johansson, E.; Brumer, H.; Rutland, M. W.; Wågberg, L. Adsorption of Xyloglucan onto Cellulose Surfaces of Different Morphologies: An Entropy-Driven Process. *Biomacromolecules* **2016**, *17* (9), 2801−2811.

(38) Holappa, S.; Kontturi, K. S.; Salminen, A.; Seppälä, J.; Laine, J. Adsorption of Hydrophobically End-Capped Poly(ethylene Glycol) on Cellulose. *Langmuir* **2013**, *29* (45), 13750−13759.

(39) Saarinen, T.; Österberg, M.; Laine, J. Adsorption of Polyelectrolyte Multilayers and Complexes on Silica and Cellulose Surfaces Studied by QCM-D. *Colloids Surf., A* **2008**, *330*, 134−142.

(40) Liu, Z.; Choi, H.; Gatenholm, P.; Esker, A. R. Quartz Crystal Microbalance with Dissipation Monitoring and Surface Plasmon Resonance Studies of Carboxymethyl Cellulose Adsorption onto Regenerated Cellulose Surfaces. *Langmuir* **2011**, *27* (14), 8718−8728.

(41) Cranston, E. D.; Eita, M.; Johansson, E.; Netrval, J.; Salajková, M.; Arwin, H.; Wågberg, L.; Salajkov, M.; Arwin, H.; Lars, W. Determination of Young's Modulus for Nanofibrillated Cellulose Multilayer Thin Films Using Buckling Mechanics. *Biomacromolecules* **2011**, *12* (4), 961−969.

(42) Niinivaara, E.; Faustini, M.; Tammelin, T.; Kontturi, E. Water Vapor Uptake of Ultrathin Films of Biologically Derived Nanocrystals: Quantitative Assessment with Quartz Crystal Microbalance and Spectroscopic Ellipsometry. *Langmuir* **2015**, *31* (44), 12170−12176.

(43) Niinivaara, E.; Faustini, M.; Tammelin, T.; Kontturi, E. Mimicking the Humidity Response of the Plant Cell Wall by Using Two-Dimensional Systems: The Critical Role of Amorphous and Crystalline Polysaccharides. *Langmuir* **2016**, *32* (8), 2032−2040.

(44) Aulin, C.; Ahola, S.; Josefsson, P.; Nishino, T.; Hirose, Y.; Österberg, M.; Wågberg, L. Nanoscale Cellulose Films with Different Crystallinities and Mesostructures–Their Surface Properties and Interaction with Water. *Langmuir* **2009**, *25* (13), 7675−7685.

(45) Ahola, S.; Salmi, J.; Johansson, L. S.; Laine, J.; Österberg, M. Model Films from Native Cellulose Nanofibrils. Preparation, Swelling, and Surface Interactions. *Biomacromolecules* **2008**, *9*, 1273−1282.

(46) Kittle, J. D.; Du, X.; Jiang, F.; Qian, C.; Heinze, T.; Roman, M.; Esker, A. R. Equilibrium Water Contents of Cellulose Films Determined via Solvent Exchange and Quartz Crystal Microbalance with Dissipation Monitoring. *Biomacromolecules* **2011**, *12* (8), 2881−2887.

(47) Reid, M. S.; Villalobos, M.; Cranston, E. D. Cellulose Nanocrystal Interactions Probed by Thin Film Swelling to Predict Dispersibility. *Nanoscale* **2016**, *8* (24), 12247−12257.

(48) Hubbe, M. A.; Venditti, R. A.; Rojas, O. J. What Happens To Cellulosic Fibers During Papermaking and Recycling? A Review. *BioResources* **2007**, *2*, 739−788.

(49) Revol, J.-F.; Bradford, H.; Giasson, J.; Marchessault, R. H.; Gray, D. Helicoidal Self-Ordering of Cellulose Microfibrils in Aqudous Suspension. *Int. J. Biol. Macromol.* **1992**, *14*, 170−172.

(50) Beck, S.; Méthot, M.; Bouchard, J. General Procedure for Determining Cellulose Nanocrystal Sulfate Half-Ester Content by Conductometric Titration. *Cellulose* **2015**, *22*, 101−116.

(51) Hasani, M.; Cranston, E. D.; Westman, G.; Gray, D. G. Cationic Surface Functionalization of Cellulose Nanocrystals. *Soft Matter* **2008**, *4* (11), 2238.

(52) Shafeiei-Sabet, S.; Hamad, W. Y.; Hatzikiriakos, S. G. Influence of Degree of Sulfation on the Rheology of Cellulose Nanocrystal Suspensions. *Rheol. Acta* **2013**, *52* (8–9), 741–751.

(53) Kalashnikova, I.; Bizot, H.; Cathala, B.; Capron, I. Modulation of Cellulose Nanocrystals Amphiphilic Properties to Stabilize Oil/water Interface. *Biomacromolecules* **2012**, *13* (1), 267–275.

(54) Dong, X.; Revol, J.; Gray, D. G. Effect of Microcrystallite Preparation Conditions on the Formation of Colloid Crystals of Cellulose. *Cellulose* **1998**, *5*, 19–32.

(55) Braun, M. M.; Pilon, L. Effective Optical Properties of Non-Absorbing Nanoporous Thin Films. *Thin Solid Films* **2006**, *496* (2), 505–514.

(56) Williams, S. R.; Philipse, A. P. Random Packings of Spheres and Spherocylinders Simulated by Mechanical Contraction. *Phys. Rev. E: Stat. Phys., Plasmas, Fluids, Relat. Interdiscip. Top.* **2003**, *67*, 51301.

(57) Ritger, P. L.; Peppas, N. A. A Simple Equation for Description of Solute Release I. Fickian and Non-Fickian Release from Non-Swellable Devices in the Form of Slabs, Spheres, Cylinders or Discs. *J. Controlled Release* **1987**, *5* (1), 23–36.

(58) Lucena, D.; Tkachenko, D. V.; Nelissen, K.; Misko, V. R.; Ferreira, W. P.; Farias, G. A.; Peeters, F. M. Transition from Single-File to Two-Dimensional Diffusion of Interacting Particles in a Quasi-One-Dimensional Channel. *Phys. Rev. E - Stat. Nonlinear, Soft Matter Phys.* **2012**, *85* (3), 1–12.

(59) Kumar, A. V. A. Crossover from Normal Diffusion to Single-File Diffusion of Particles in a One-Dimensional Channel: LJ Particles in Zeolite Zsm-22. *Mol. Phys.* **2015**, *113* (11), 1306–1310.

(60) Erdoğan, M.; Capan, I.; Tarimci, C.; Hassan, A. K. Modeling of Vapor Sorption in Polymeric Film Studied by Surface Plasmon Resonance Spectroscopy. *J. Colloid Interface Sci.* **2008**, *323* (2), 235–241.

DOI: 10.1021/acs.langmuir.7b01740
Langmuir XXXX, XXX, XXX–XXX

Appendix 5: Chapter 5 Supporting Information

Table S1: Mass percentages of sulfur and nitrogen on CNCs measured by conductometric titration and elemental analysis (combustion followed by ion chromatography, performed by Micro Analysis Inc.) and calculated estimate of the CNC surface charge density.

	Mass Sulfur (%) Titration	Mass Sulfur (%) Elemental	Mass Nitrogen (%) Elemental	Surface Charge Density* (charges/nm^2)
LS-CNC	0.50 ± 0.02	0.46 ± 0.05	-	0.26
HS-CNC	0.71 ± 0.02	0.70 ± 0.05	-	0.40
CAT-CNC	-	0.49 ± 0.04	0.55 ± 0.01	0.28† / 0.71‡

*Calculated from titration (and elemental for CAT-CNC) and average CNC dimensions of 122 × 8 nm.
†Surface charge density for contribution from sulfate half esters.
‡Surface charge density contribution from hydroxypropyltrimethylammonium groups.

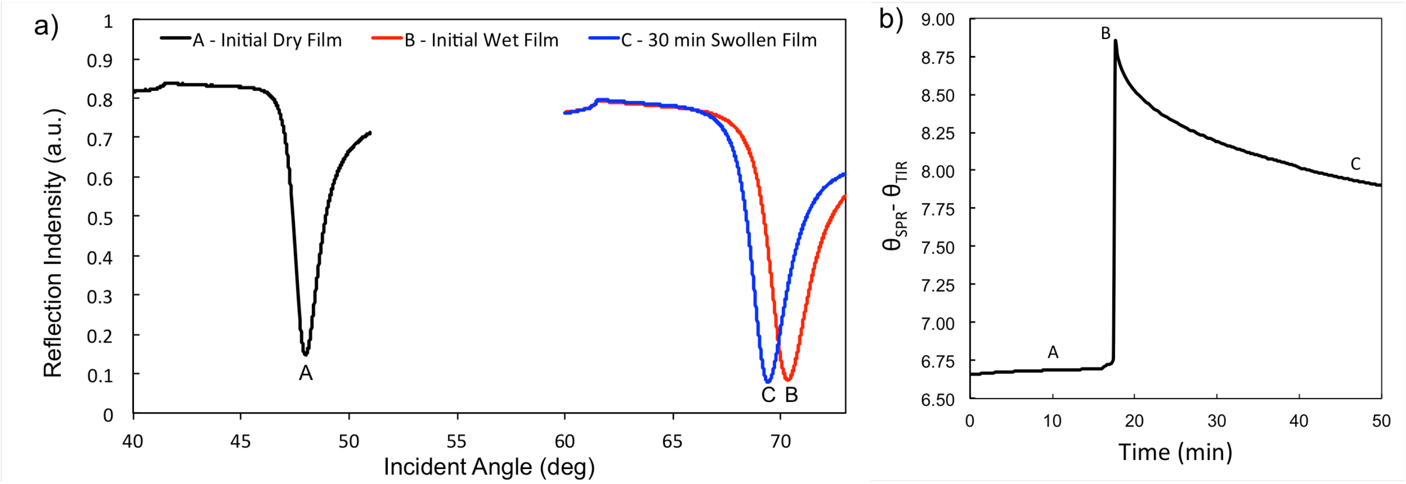

Figure S1: a) Representative SPR curves for LS-CNC in 1 mM NaCl showing angular positions for dry films, initially wet films and completely swollen films. **b)** SPR swelling profile (or sensogram) displaying the angular change over time, where θ_o and θ_t in *Equation 2* are repsented by the anglular positions of curves collected at *B* and B→C respectively. Note that $\Delta\theta_o$ and $\Delta\theta_t$ are corrected for angular shift due the presence of water.[1] See Figure S8 for details of the graphical use of *Equation 2*.

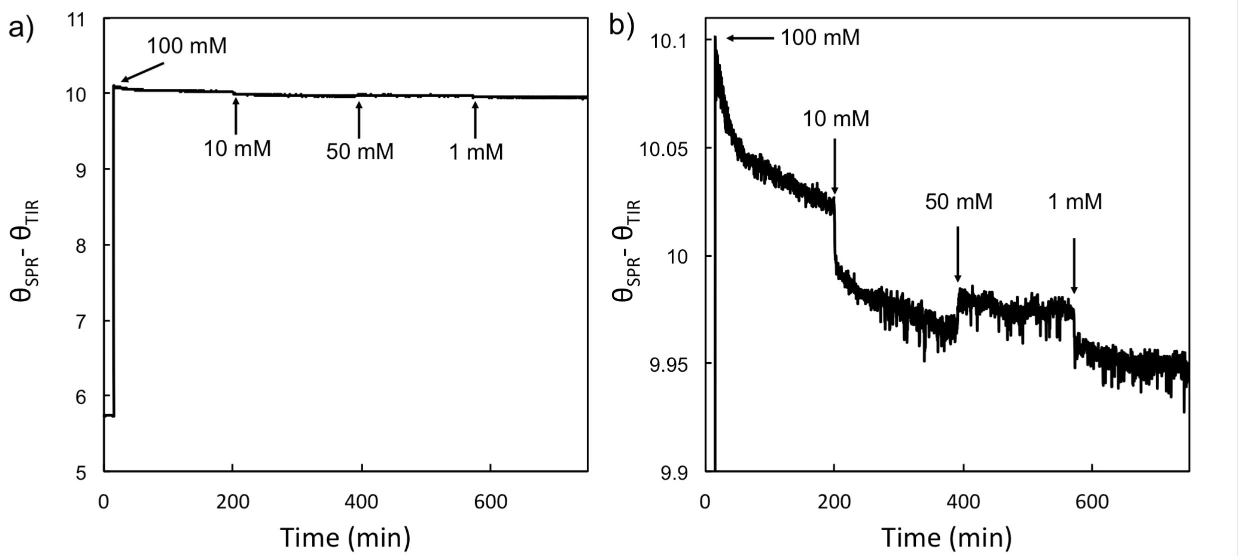

Figure S2: **a)** Raw swelling profile for HS-CNCs over 12 hours with the introduction of varying ionic strength media. **b)** The same data with a rescaled y-axis to show details of swelling after injection of media. We consider a change of <0.05˚ over a period of 10 min to be insignificant, and the result of instrument drift.

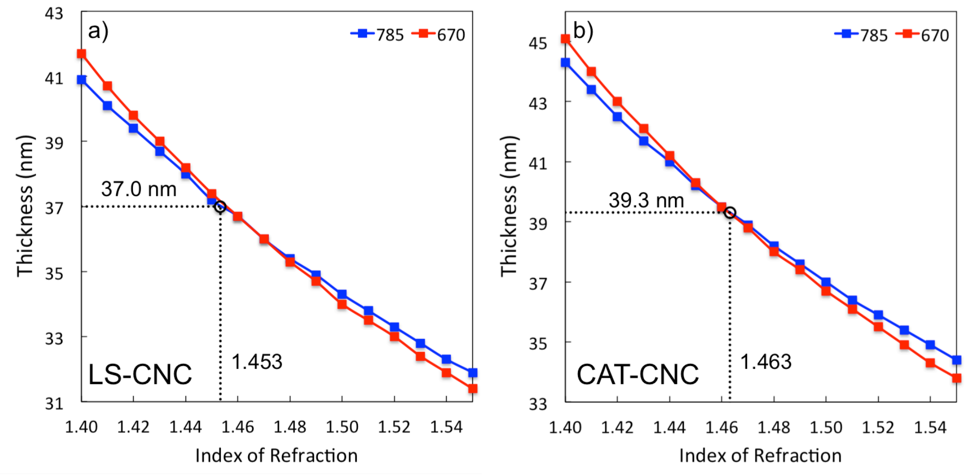

c)

Layer	Thickness (nm)	*n* (785 nm)	*n* (670 nm)	*k* (785 nm)	*k* (670 nm)
Glass	-	1.5151	1.5190	0	0
Cr	1.3	3.1294	3.0834	3.448	3.350
Au	47	0.1490	0.1377	4.783	3.782
SiO_2	13.3	1.5387	1.5415	0	0
CNC	-	-	-	0.02	0.03
Air	-	1.0	-	-	-

Figure S3: Determination of the thickness and refractive index of (a) LS-CNC and (b) CAT-CNC films via the wavelength crossover method as outlined by Granqvist *et al.*[2] and (c) the fitted layer parameters.

Sample calculation for the ionic strength of CNC films for HS-CNCs

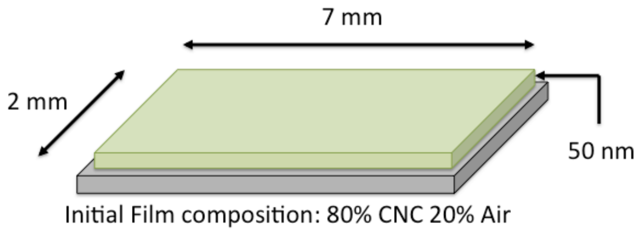

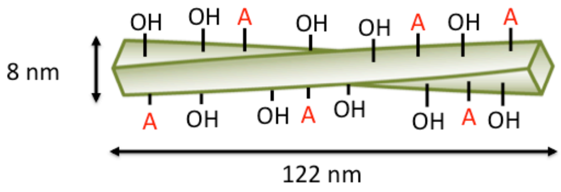

Flow cell dimensions: **2 mm** x **7 nm**
Surface area of one CNC: **4032 nm^2**
Volume of one CNC: **7808 nm^3**

Density of CNCs: **1.55 g/cm^3**
Surface area/gram CNC: **3.33×10^{20} nm^2/gCNC**
Sulfur percentage: **0.007 gS/g CNC**

Charges per gram CNC = (6.022×10^{23} mol) / (32 gS/mol)x(0.007 gS/gCNC) = **1.33×10^{20} e^-/gCNC**
Charge per area = (1.33×10^{20} e^-/gCNC)/(3.33×10^{20} nm^2/gCNC) = **0.4 e^-/nm^2**

Total volume of film (100%): 7×10^{14} nm^3 = **7×10^{-10} L**
Volume of “accessible space” (20%): 1.4×10^{14} = **1.4×10^{-10} L**

Number of CNCs in total film: **8.97×10^{10}**
Number of CNCs in porous film (80%): **7.17×10^{10}**
Surface area in porous film: **2.89×10^{14} nm^2**

Number of charges in film: (2.89×10^{14} nm^2) x (0.4 e^-/nm^2) = **1.16×10^{14} e^-**
Moles of charge in film: (1.16×10^{14} e^-) / (6.022×10^{23} e^-/mol) = **1.93×10^{-10} mol**

Since $–OSO_3^-$ groups are bound, we consider only mobile Na^+ counterions in the solution contribute to the ionic strength where $[Na^+] = [–OSO_3^-]$:

$$I = \frac{1}{2}\sum_{i=1}^{\infty} c_1 z_i^2$$

$$I_{film} = \frac{1}{2}\left[\frac{1.93 \times 10^{-10}\ mol}{7.1 \times 10^{10}\ L}\right]$$

$$I_{film} = 0.678\ mol/L$$

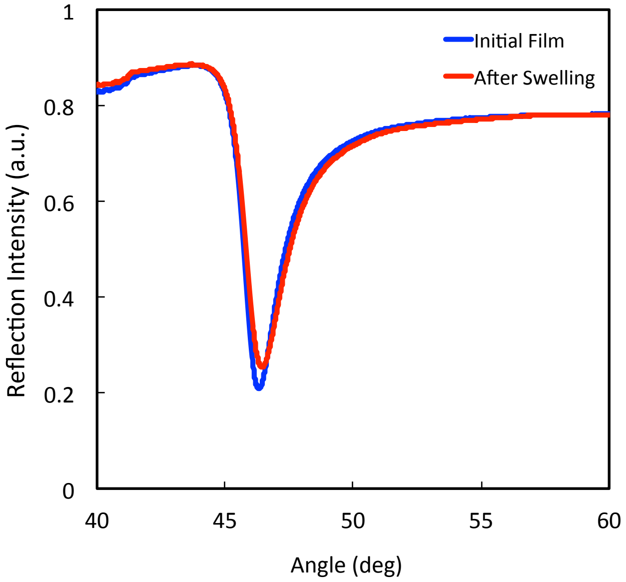

Figure S4: Representative SPR curve for 785 nm wavelength laser of the HS-CNC film before and after swelling in 10 mM NaCl.

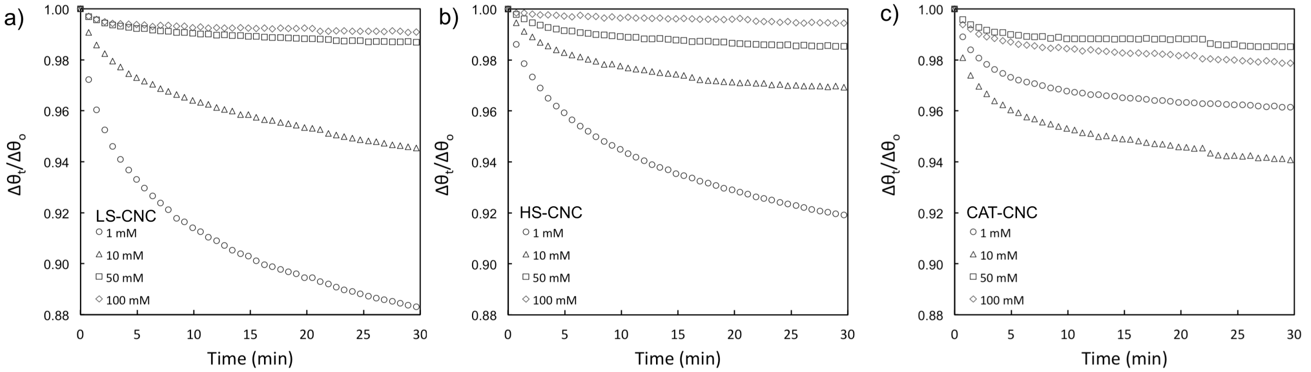

Figure S5: Normalized representative swelling profiles for (a) LS-CNC, (b) HS-CNC and (c) CAT-CNC in various concentrations of NaCl.

DLVO calculations

Repulsive parallel (${V_R}^P$) and crossed (${V_R}^C$) interaction energies were calculated following Buining *et al.*[3]

$$ {V_R}^P = 64(\pi)^{1/2} nkT\gamma^2 L \frac{(\kappa R)^{1/2}}{\kappa^2} \exp{(-\kappa D)} $$

$$ {V_R}^C = 128\pi nkT\gamma^2 \frac{a}{\kappa^2} \exp{(-\kappa D)} $$

with

$$\gamma = \tanh\left(\frac{e\psi_o}{4kT}\right)$$

where n is the number density of ions within the film, k is the Boltzmann constant, T is temperature, κ is the Debye length, R and L are the radius and length of the CNC respectively, D is the particle spacing, e is the charge of an electron and $\psi_o$is the CNC surface potential.

For the number density of ions in the film, the maximum can be considered as the sum of the ionic strength of the film and the ionic strength of the media. Thus for LS-CNC films n = 450 mM + 100 mM = 550 mM = 6.7 × 10^{26} ions/m^3. At the minimum limit, we can consider the ionic strength of the film to be the sole contributor of ions and thus n = 450 mM = 5.4 × 10^{26} ions/m^3.

For the surface potential of CNCs, previous works have reported values of ψ_o= -18 mV, which is typical for sulfuric acid hydrolyzed CNCs.[4] However, because in this work we examine both unmodified (HS-CNC) and desulfated (LS-CNC) we calculate DLVO interactions within reasonable upper and lower bounds of ψ_o= -10 mV and ψ_o= -20 mV.

Attractive van der Waals potentials (V_A) were calculated from Israelachvili.[5]

$${V_A}^P = \frac{-AL}{12\sqrt{2}D^{3/2}}\left(\frac{R_1R_2}{R_1+R_2}\right)^{1/2}$$

$${V_A}^C = \frac{-A\sqrt{R_1R_2}}{6D}$$

Where A is the Hamaker constant (8 × 10^{-21} J Ref. [6]) and for CNCs $R_1 = R_2$.

The parallel and crossed conformations were averaged for both the attractive and repulsive contributions:

$$({V_R}^P + {V_R}^C)/2 = V_R$$

$$({V_A}^P + {V_A}^C)/2 = V_A$$

and used to calculate the total potential:

$$V_T = V_R + V_A$$

The total DLVO interaction calculated for LS-CNC and HS-CNC films is presented in Figure S6 for all upper and lower bounds. DLVO interactions at a spacing of 1 – 2 nm are dominated by attractive van der Waals forces, for all ionic strengths (ion number densities) and surface potentials within the films.

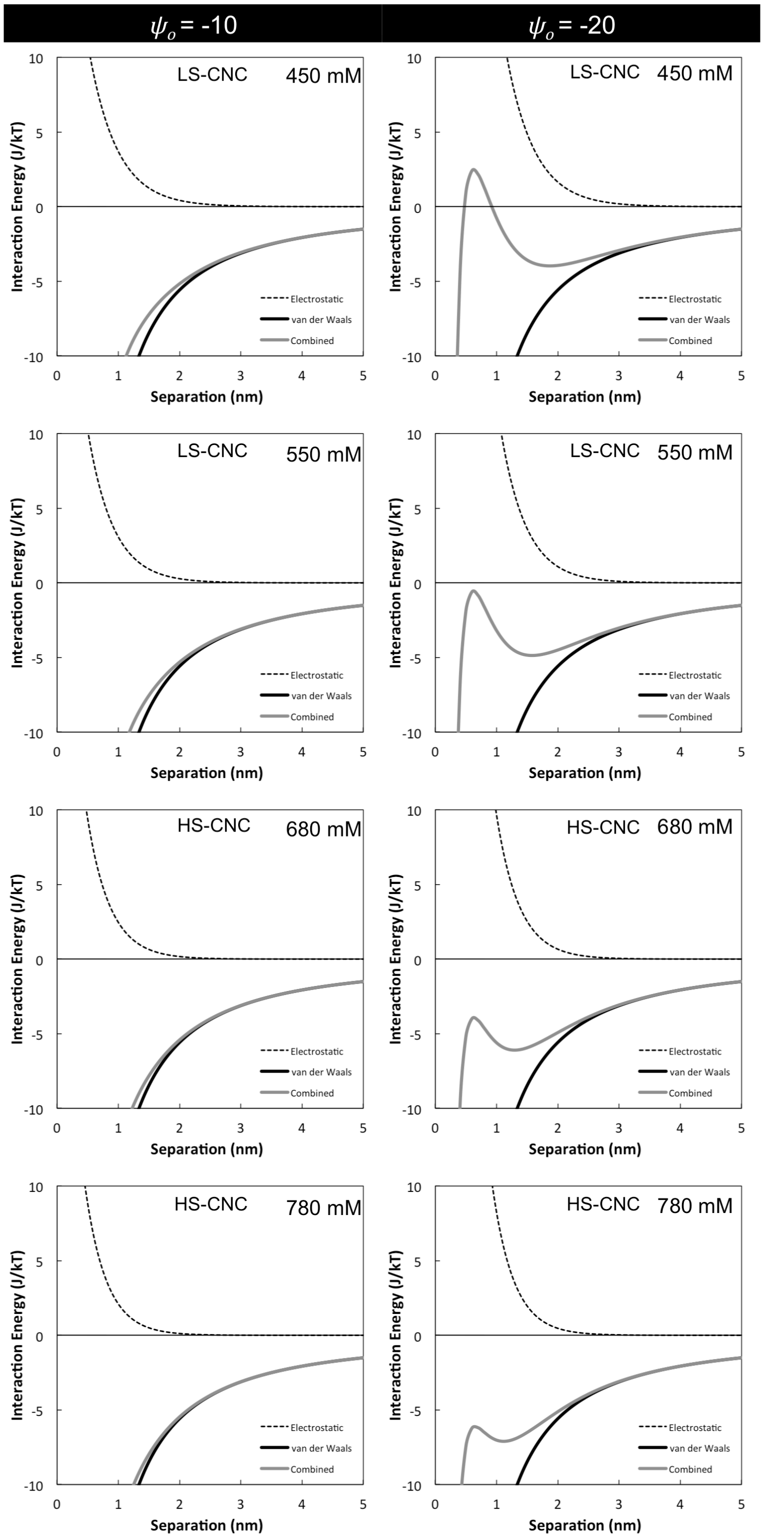

Figure S6: Total DLVO interaction (averaged for crossed and parallel geometries) for LS-CNC and HS-CNCs films with a porosity of 20%. Calculations show DLVO curves for surface potential of -10 mV (left) and -20 mV (right) at various ionic strengths within the film**.**

Surface plasmon resonance data and diffusion coefficients

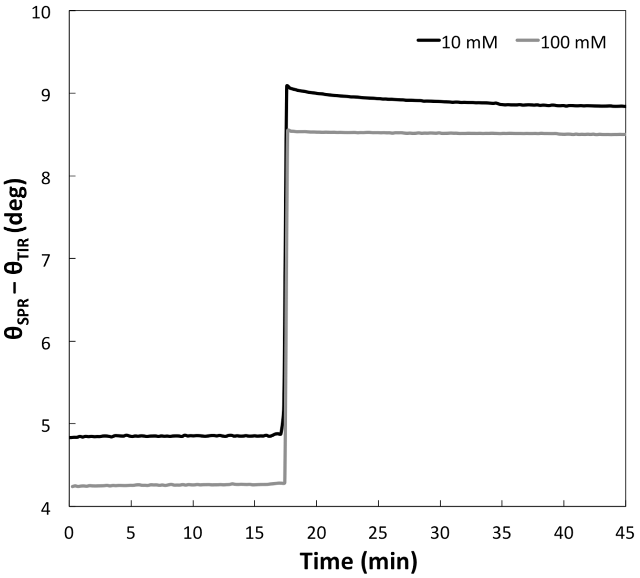

Figure S7: Representative raw swelling profiles for HS-CNC in 10 and 100 mM NaCl with injection occurring at 17 min. Initial angular values differ due to different initial film thicknesses. Swelling curves in Figure S5 are generated by normalizing data to the angular value immediately following water injection.

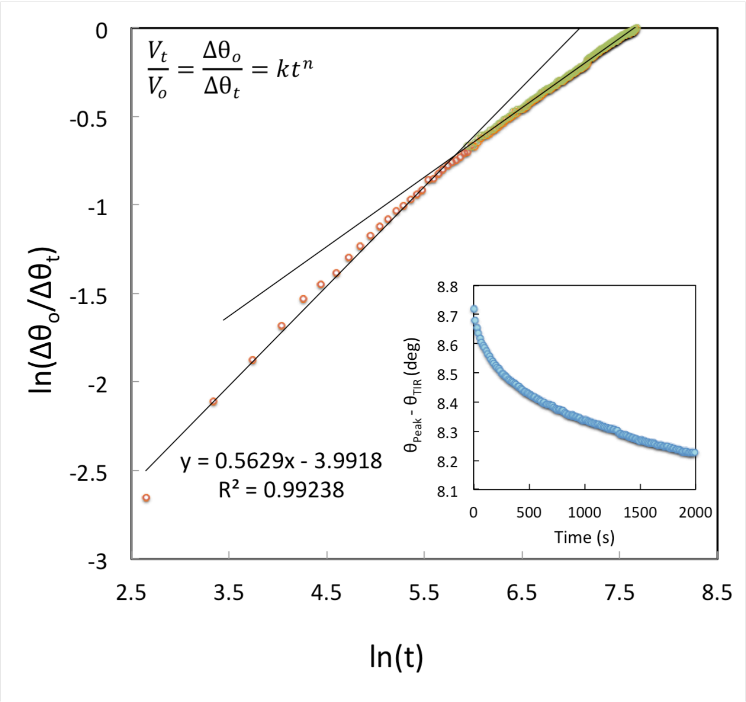

Figure S8: Representative plot showing diffusion exponent analysis for an early time solution of LS-CNC in 10 mM NaCl. Inset shows raw data as measured by the SPR

References:

(1) Reid, M. S.; Villalobos, M.; Cranston, E. D. Cellulose Nanocrystal Interactions Probed by Thin Film Swelling to Predict Dispersibility. *Nanoscale* **2016**, *8* (24), 12247–12257.

(2) Granqvist, N.; Liang, H.; Laurila, T.; Sadowski, J.; Yliperttula, M.; Viitala, T. Characterizing Ultrathin and Thick Organic Layers by Surface Plasmon Resonance Three-Wavelength and Waveguide Mode Analysis. *Langmuir* **2013**, *29* (27), 8561–8571.

(3) Buining, P.; Philipse, A.; Lekkerkerker, H. Phase Behavior of Aqueous Dispersions of Colloidal Boehmite Rods. *Langmuir* **1994**, No. 9, 2106–2114.

(4) Stiernstedt, J.; Nordgren, N.; Wågberg, L.; Brumer, H.; Gray, D. G.; Rutland, M. W. Friction and Forces between Cellulose Model Surfaces: A Comparison. *J. Colloid Interface Sci.* **2006**, *303* (1), 117–123.

(5) Israelachvili, J. *Intermolecular & Surface Forces*; Academic Press: San Diego, 1992.

(6) Bergström, L.; Stemme, S.; Dahlfors, T.; Arwin, H.; Ödberg, L. Spectroscopic Ellipsometry Characterization and Estimation of the Hamaker Constant of Cellulose. *Cellulose* **1999**, *6* (1), 1–13.

Chapter 6

Non-Ionic Polymer Adsorption to Cellulose Nanocrystals and Silica Colloids

The previous two research chapters established that particle-particle interactions in CNC systems are governed by van der Waals forces. As an essential next step, this chapter investigates polymer adsorption to CNC surfaces to build a deeper understanding of particle-polymer interactions and dispersibility in nanocomposites. Polyethylene glycol is used as a model linear polymer to investigate the role of hydrogen bonding during polymer adsorption: two systems are compared directly, namely CNCs and fumed silica (which is a well-described particle system in the literature). This chapter finds that although there is an abundance of hydroxyl groups on the surface of CNCs, polyethylene glycol does not adsorb to cellulose in aqueous environments. The new experiments with polyethylene glycol and CNCs are further discussed and compared to previous reports in the literature investigating non-ionic polymer adsorption to nanocellulose. This review highlights that hydrogen bonding plays a minor role and that polymer adsorption, in most cases, is entropically-driven.

The work within this chapter is composed of two sections: Firstly, an investigation of polyethylene glycol adsorption to CNC surfaces in aqueous environments compared to polyethylene glycol/fumed silica interactions. Second, a review of the current understanding of non-ionic polymer adsorption to CNC surfaces and the role of hydrogen bonding is presented. In the first section, the data were collected by myself with the assistance of Heera Marway and Camila Moran-Hidalgo who both aided in QCM-D data collection. All data analysis was performed by myself. The first section of this chapter was drafted by myself and later edited by my academic advisor, Dr. Emily Cranston. For the review article, the manuscript was written by myself with assistance from my co-supervisors, Dr. Emily Cranston and Dr. Marco Villalobos. The first portion of this chapter has been published in the journal *Cellulose* and reprinted with permission from *Springer* © 2017. The second is published in the journal *Current Opinion in Colloid & Interface Science* and is reprinted with permission from *Elsevier* © 2017.

Section 1:
Comparison of Polyethylene Glycol Adsorption to Nanocellulose Versus Fumed Silica in Water

Michael S. Reid, Heera S. Marway, Camila Moran-Hidalgo, Marco Villalobos and Emily D. Cranston

Cellulose, **2017**

DOI: 10.1007/s10570-017-1482-8

Section 2:
The Role of Hydrogen Bonding in Non-Ionic Polymer Adsorption to Cellulose Nanocrystals and Silica Colloids

Michael S. Reid, Marco Villalobos and Emily D. Cranston

Current Opinion in Colloid & Interface Science, **2017**, *29,* pp 76–82

DOI: 10.1016/j.cocis.2017.03.005

Cellulose
DOI 10.1007/s10570-017-1482-8

ORIGINAL PAPER

Comparison of polyethylene glycol adsorption to nanocellulose versus fumed silica in water

Michael S. Reid · **Heera S. Marway** · **Camila Moran-Hidalgo** ·
Marco Villalobos · **Emily D. Cranston**

Received: 17 June 2017 / Accepted: 29 August 2017

Abstract The recent intensification of industrially produced cellulose nanocrystals (CNCs) and cellulose nanofibrils has positioned nanocelluloses as promising materials for many water-based products and applications. However, for nanocelluloses to move beyond solely an academic interest, a thorough understanding of their interaction with water-soluble polymers is needed. In this work, we address a conflicting trend in literature that suggests polyethylene glycol (PEG) adsorbs to CNC surfaces by comparing the adsorption behaviour of PEG with CNCs versus fumed silica. While PEG is known to have strong hydrogen bonding tendencies and holds water tightly, it is sometimes (we believe erroneously) presumed that PEG binds to cellulose through hydrogen bonding in aqueous media. To test this assumption, the adsorption of PEG to CNCs and fumed silica (both in the form of particle films and in aqueous dispersions) was examined using quartz crystal microbalance with dissipation, isothermal titration calorimetry, rheology and dynamic light scattering. For all PEG molecular weights (300–10,000 g/mol) and concentrations (100–10,000 ppm) tested, strong rapid adsorption was found with fumed silica, whereas no adsorption to CNCs was observed. We conclude that unlike silanols, the hydroxyl groups on the surface of CNCs do not readily hydrogen bond with the ether oxygen in the PEG backbone. As such, this work along with previous papermaking literature supports the opinion that PEG does *not* adsorb to cellulose surfaces.

Keywords Cellulose nanocrystals · Polyethylene glycol · Adsorption phenomena · QCM-D · Fumed silica

Introduction

Polymer behaviour at interfaces remains a prevailing topic in the fields of chemistry, physics, biology, and engineering. Unlike small molecules, polymer flexibility leads to complex and fascinating behaviour driven by entropic and/or enthalpic processes (Fleer et al. 1998). Understanding the mechanisms of polymer adsorption is critical for the development of many antifouling, wastewater and composite applications, to name just a few.

Electronic supplementary material The online version of this article (doi:10.1007/s10570-017-1482-8) contains supplementary material, which is available to authorized users.

M. S. Reid · H. S. Marway · C. Moran-Hidalgo ·
E. D. Cranston (✉)
Department of Chemical Engineering, McMaster
University, Hamilton, ON L8S 4L8, Canada
e-mail: ecranst@mcmaster.ca

M. Villalobos
Cabot Corporation, Billerica, MA 01821, USA

Cellulose nanocrystals (CNCs) are sustainable rod-shaped nanoparticles that have promising mechanical, optical and rheological properties (Klemm et al. 2011; Moon et al. 2011). Recent intensification of industrially produced CNCs has made them widely available and has drawn considerable interest in the literature (Reid et al. 2017b, c). Composed of β(1–4) linked D-glucose units, linear cellulose polymer chains form crystalline high aspect ratio particles that have been used as emulsion/foam stabilizers (Kalashnikova et al. 2012, et al. 2013; Hu et al. 2016), adsorbents (He et al. 2013; Yu et al. 2016), reinforcing fillers in cement (Cao et al. 2015) and polymer composites (Mariano et al. 2014; Oksman et al. 2016), and many other applications (Grishkewich et al. 2017). Typically extracted from wood, cotton, and other higher order plants, CNCs are commonly produced via sulfuric acid hydrolysis, which grafts anionic sulfate half ester groups to the particle surface imparting colloidal stability (Habibi et al. 2010). This along with the abundance of surface hydroxyl groups and the global desire for green processes, imply that water based applications are an area where CNCs can have a significant and immediate impact. As such, thorough understanding of water-soluble polymer adsorption onto the surface of CNCs is of critical importance.

In addition to the numerous fundamental studies investigating CNC self-assembly (Revol et al. 1992; Edgar and Gray 2002; Gray and Mu 2015; Honorato-Rios et al. 2016), thin film behaviour (Kontturi et al. 2007; Hoeger et al. 2011; Niinivaara et al. 2015) and colloidal stability (Dong et al. 1996; Viet et al. 2006; Gårdebjer et al. 2016), there exists nearly a century of papermaking research from which parallels can be drawn and should not be overlooked (Biermann 1996). Notably the adsorption of polyelectrolytes (specifically cationic polymers) and non-ionic polymers to cellulose fibers has been well documented (Ishimaru and Lindström 1984), and exploited, for example, in flocculants (Hubbe 2007), wet adhesives (Gustafsson et al. 2016), and sizing agents (Biermann 1996). Electrostatics and the release of bound counterions drives polyelectrolyte adsorption which yields strong polymer adsorption to cellulose (Wågberg 2000), and more recently has been used to design hybrid nanocellulose films for potential biomedical, optical and coatings applications, based on layer-by-layer assembly (Martin and Jean 2014).

Non-ionic polymer adsorption is less well-understood, however the adsorption of polysaccharides, specifically hemicelluloses and cellulose derivatives are of growing interest, as they are hydrogen bonding polymers that are commonly found in papermaking (Eronen et al. 2011; Sundman 2014; Hu et al. 2014, 2015; Benselfelt et al. 2016). While often chemically similar, variations between adsorbing and non-adsorbing polysaccharides suggests a complex set of driving forces for adsorption that can include entropic (e.g., release of bound water) and enthalpic pathways, and/or co-crystallization or precipitation of polymers/oligomers on cellulose surfaces (Laine et al. 2000; Lopez et al. 2010; Kargl et al. 2012; Bouchard et al. 2016; Benselfelt et al. 2016). Not only limited to polysaccharides, many other synthetic linear and branched non-ionic polymers and have been reported to adsorb to cellulose surfaces (Holappa et al. 2013; Hatton et al. 2015; Kontturi et al. 2017), implying that if PEG does not absorb to cellulose it is really an exception to most polymers. Because of the numerous adsorption behaviours observed between cellulose and non-ionic polymers, studying model polymer-particle systems is useful for isolating specific interactions.

Polyethylene glycol (PEG), also known as polyethylene oxide and polyoxyethylene (where the latter two are conventionally used for PEG > 20,000 g/mol), is a simple linear water-soluble polymer, which is known to adsorb to surfaces via hydrogen bonding and is used in numerous cosmetic, pharmaceutical and industrial engineering applications (Knop et al. 2010). PEG–cellulose interactions have long been studied in the wood and papermaking industries as stabilizing agents, retention aids and as probe molecules, amongst others. For example, PEG of varying molecular weights (200–20,000 g/mol) has been used in solute exclusion measurements, pioneered by Stone and Scallan (1967), to investigate the accessible surface area and pore size distribution of swollen cellulose fibers (Aggebrandt and Samuelson 1964; Tarkow et al. 1966; Stone and Scallan 1967). Critically PEG, and other polymers, are selected as probe molecules such that no significant interactions occur between the polymer and cellulose and that polymer diffusion and retention is equivalent to water (or other solvents) (Karimi and Taherzadeh 2016). Additionally, PEG has been used to improve dimensional and moisture stability within wood products however, because PEG does not absorb to cellulose, polymers must be cross-linked within the product to prevent leaching (Trey et al. 2010; de Cuadro et al. 2015).

In papermaking, early work by Pelton and co-workers showed high molecular weight PEG (10^5–10^7 g/mol) to be an effective flocculating agent for some mechanical pulps (Pelton et al. 1980, 1981; Xiao et al. 1996). In these works PEG adsorption only occurred for unwashed pulps or upon the addition of lignin or phenolic containing co-factors, suggesting that PEG does not adsorb to pure cellulose fibers. This was supported by Lindström and Glad-Nordmark, who, when examining PEG adsorption to various wood pulps (Lindström and Glad-Nordmark 1983), as well as microcrystalline cellulose (Lindström and Glad-Nordmark 1984), reported that phenolic and/or catechol residues, present in lignin containing pulps (or by the addition of tannic acid), were required for PEG adsorption. When these compounds were removed or chemically modified (by methylation or acetylation) no PEG adsorption was observed. It is proposed that the PEG adsorption to pulps occurs via hydrogen bonding between the ether oxygen and the hydroxyl groups of phenols and catechol groups. As a result, from a wood products and papermaking perspective it is accepted that PEG does not adsorb to cellulose (macroscopic) fibers in aqueous environments.

The rapid growth of nanocellulose research has led to many conflicting results in the literature, some of which propose that PEG *does* adsorb to cellulose surfaces (Bardet et al. 2015; Cheng et al. 2015; Oguzlu and Boluk 2017). For example Cheng et al. (2015) demonstrated that incorporating PEG ($M_w = 400$–10,000 g/mol) into CNC dispersions, followed by freeze drying, led to a CNC + PEG powder with improved re-dispersibility which was proposed to be due to a brush-like structure of PEG adsorbed to CNCs via hydrogen bonding in water. In another study, Bardet et al. (2015) stated that low molecular weight PEG ($M_w = 200$ g/mol) irreversibly adsorbed to CNC thin films from solution via hydrogen bonding, as measured by quartz crystal microbalance with dissipation monitoring (QCM-D). Most recently, Oguzlu and Boluk (2017), reported adsorption of high molecular weight PEG ($M_w = 600{,}000$ g/mol) to CNC surfaces in the dispersed state based on polarized optical microscopy and electrophoretic mobility; however, no increase in CNC particle size was measured by transmission electron microscopy and NMR indicated that depletion effects caused particle aggregation, similar to previous papermaking studies (Hubbe et al. 2009).

In contrast to these recent works that suggests PEG adsorbs to cellulose, many studies have suggested the opposite. For example, investigations of PEG containing triblock copolymers (Li et al. 2011; Holappa et al. 2013), and polymers containing PEG pendant (or brush) groups (De France et al. 2016), propose that PEG does *not* adsorb to cellulose, and in fact PEG inhibits polymer adsorption. In these studies, adsorption of amphiphilic polymers is proposed to occur via hydrophobic interactions whereby the hydrophobic portion of the polymer adsorbs to CNCs to limit water interactions (Holappa et al. 2013). Moreover, larger PEG side chains on a hydrophobic acrylic polymer backbone, reduced the overall polymer adsorption to CNC films despite an increase in hydrogen bonding sites (De France et al. 2016). Lastly, PEG has been covalently end-grafted to CNCs and shown to offer steric stabilization and improved colloidal stability in water and non-aqueous solvents, suggesting that PEG adopts an extended morphology and preferentially interacts with the liquid environment and not the cellulose surface (Araki et al. 2001; Kloser and Gray 2010).

Unlike nanocellulose, PEG adsorption to silica particles and silica surfaces has been thoroughly studied and is well understood (Kim et al. 2012). Silica particles produced via liquid or pyrogenic processes have numerous commercial, pharmaceutical and industrial applications, including as additives to increase filler content and retention aids in papermaking (Hyde et al. 2016). Adsorption of PEG to silica occurs via hydrogen bonding between surface silanol groups and the ether oxygen within the PEG backbone. Critically, surface silanols have a pK_a that ranges from 4.5 to 8.5 depending on Si coordination (Leung et al. 2009), and are sufficiently acidic to behave as Brønsted acids from which strong hydrogen bonds are formed with the PEG ether oxygen, a Lewis base (Rubio and Kitchener 1976; Mathur and Moudgil 1997). The subsequent adsorption yields a 1–2 nm thick rigid, glassy polymer layer on the silica surface regardless of molecular weight or concentration (Kim et al. 2012).

Considering the acidity (or lack thereof) of cellulose's surface alcohol groups ($pK_a = 13$) (Bhattacharyya and Rohrer 2012), PEG–cellulose hydrogen bonding is not expected. However, due to the conflicting results in the literature, currently it is unclear whether (1) nanoscale physical effects, (2) the presence of anionic sulfate ester groups, or (3) the amphiphilic nature of crystalline CNCs, may somehow promote PEG adsorption. As a result, the goal of this work is to answer the question: "Does polyethylene glycol adsorb to cellulose nanocrystals in aqueous environments?" To address this, we systematically investigated PEG adsorption to CNCs both as dispersed particles in water, and as thin films submerged in water, over a range of PEG molecular weights and concentrations. We directly compare polymer adsorption behaviour with CNCs to that of fumed silica, whereby silica is used as a reference/control due to its known strong hydrogen bonding interaction with PEG. We believe this work provides fundamental insight into non-ionic polymer adsorption to cellulose surfaces, and clarifies conflicting reports in the nanocellulose literature.

Experimental

Materials

Whatman cotton ashless filter aid was purchased from GE Healthcare Canada. Sulfuric acid, was obtained from Caledon Laboratory Chemicals (Georgetown, ON, Canada). Polyethylene glycol $M_w = 300$ g/mol (PEG300), polyethylene glycol $M_w = 1000$ g/mol (PEG1000) and 2-hydroxyethyl cellulose $M_w = 90{,}000$ g/mol (HEC) with a molar substitution of 2.5 were purchased from Sigma Aldrich (Oakville, ON, Canada). Polyethylene glycol $M_w = 6000$ g/mol (PEG6000) and polyethylene glycol $M_w = 10{,}000$ g/mol (PEG10000) were purchased from Fluka Analytica. CAB-O-SIL® M-5 fumed silica was received from Cabot Corporation (Billerica, MA). All chemicals were used as received. Water used was purified Type I water with a resistivity of 18.2 MΩ cm (Barnstead NANOpure DIamond system, ThermoScientific, Asheville, NC).

Cellulose nanocrystal preparation

CNCs used in this study were prepared by conventional sulfuric acid hydrolysis, as previously described (Reid et al. 2016). 40 g of cotton Whatman ashless filter aid was hydrolyzed in 700 mL of 64 wt% sulfuric acid at 45 °C for 45 min under continuous mechanical stirring. The reaction was quenched by a tenfold dilution with 4 °C water and excess acid was removed by multiple rinsing and centrifugation steps. Dispersions were diluted and dialyzed against ultra pure water until pH of the water from successive washes stabilized between 5 and 6 (~2 weeks with daily water changes). The CNC dispersion was probe sonicated (Sonifier 450, Branson Ultrasonics, Danbury, CT) continuously in an ice bath for 15 min three times at 60% maximum amplitude. CNC dispersions were filtered through Whatman glass fiber filter paper, neutralized (pH 6–7) by the addition of 1 mM NaOH and lyophilized. As such, all CNCs are in the sodium form (with Na^+ as the surface sulfate half ester counterion) and dried sodium-form CNCs are known to redisperse well upon rehydration and sonication because the Na^+ interferes with cellulose–cellulose hydrogen bonding (Beck et al. 2012).

Quartz crystal microbalance with dissipation (QCM-D)

Thin CNC and fumed silica films were prepared as described previously (Reid et al. 2016). Briefly, 3 wt% dispersions were spin coated onto piranha cleaned (3:1 concentrated sulfuric acid to hydrogen peroxide) silicon dioxide coated QCM-D sensors. Films were dried at 80 °C overnight, gently rinsed with water, and dried overnight again. All measurements were performed using a Q-Sense E4 (distributed by Biolin Scientific for Q-Sense, Sweden) under constant 100 µL/min flow. Prior to adsorption, films were equilibrated in water for a minimum of 8 h to establish a stable baseline and as such minimum particle loss is expected during adsorption and rinsing steps of QCM-D measurements. PEG ($M_w = 300$–$10{,}000$ g/mol) solutions with concentrations of 1000 ppm and 10,000 ppm were introduced and allowed to adsorb until a plateau was reached ($\Delta f < 1$ Hz over 1800 s period). Films were then rinsed with water to remove loosely bound material. Due to the drift in frequency over long time periods in the QCM-D experiments, we conservatively estimate the limit of detection as 0.1 mg/m^2. All experiments were run at least two times, with adsorption to CNC surfaces run in triplicate. Representative normalized QCM-D profiles of the third overtone are presented.

Isothermal titration calorimetry (ITC)

Titrations were performed using a Nano ITC low-volume system (TA Instruments–Waters LLC, Newcastle, DE) at 25 °C under constant 350 rpm stirring. Experiments consisted of 20 successive 2.5 μL additions of 0.5 wt% (500 ppm) PEG (M_w = 300–10,000 g/mol) solution to 300 μL of 1 wt% particle dispersion. Heat signals were processed using NanoAnalyze software (TA Instruments–Waters LLC, Newcastle, DE). The heat of dilution was measured (and subtracted from the heat of adsorption) by titrating PEG solutions into ultra pure water containing no particles. Data from the first injection was disregarded to omit errors associated with the diffusion of titrant into the calorimetric cell as is typical of ITC experiments (Chiad et al. 2009).

Rheological measurements

Steady state shear viscosity measurements were performed using an ATS RheoSystem Stresstech HR rheometer on CNC/polymer dispersions in the semi-dilute regime, using stainless steel cone and plate geometry. 5 wt% CNC dispersions were prepared with varying concentrations of HEC and PEG300 and PEG10000 and measured in triplicate, with representative curves presented.

Dynamic light scattering (DLS)

Apparent particle size was measured for 0.025 wt% colloid dispersions containing 100–10,000 ppm PEG (M_w = 300–10,000 g/mol) using a Malvern Zetasizer Nano particle analyzer at 20 °C (no salt added). Each measurement consisted of 15 measurement cycles and the average particle size distribution was determined. The uncertainty is presented as the standard deviation of three separate sample measurements. Following initial measurement, dispersions with and without PEG were dried at 80 °C overnight. Particles were then re-dispersed by adding a volume equivalent to the original dispersion, gently shaking and allowing the dispersions to equilibrate for 48 h. Particle size was then re-measured (without sonication). Note that for fumed silica dispersions after rehydration, macroscopic material was visible by eye and thus were not suitable for DLS measurements.

Results and discussion

Polymer adsorption in this work was investigated over a range of low molecular weight PEG polymers to avoid crystallization effects and significant molecular entanglement that can increase adsorption not specific to particle surface chemistry. All PEG adsorption studies were performed in ultra pure water as the presence of ions can reduce the available binding sites of PEG, limiting polymer segment interactions and adsorption (Kalasin and Santore 2016). Critically, this work investigates polymer adsorption in water using a variety of techniques which probe adsorption to both thin films and dispersed particles.

Thin films

QCM-D is a label free, surface sensitive technique that measures the change in mass per unit area by monitoring the shift in frequency (Δf) of a resonating quartz crystal during binding/adsorption/desorption events and has been extensively used to monitor polymer adsorption to thin films (Eronen et al. 2011). In addition to measuring the change in frequency, some QCM instruments monitor the dissipation (ΔD), or energy lost per oscillation cycle, which provides insight into the rigidity of bound polymer layers.

Figure 1 shows representative frequency and dissipation curves for PEG10000 adsorption at 1000 ppm for both fumed silica and CNC films. Additional QCM-D adsorption profiles for lower molecular weight PEG are provided in the Supporting Information, Figs. S1–S4. While the absolute magnitude of the frequency shift is dependent on the thickness and surface area of the film, clear differences in kinetics and adsorption behaviour can be seen for fumed silica versus CNCs. PEG10000 adsorption to fumed silica is rapid, reaching a plateau of ca. −17 Hz immediately following polymer addition, indicating both strong adsorption and saturation of the silica film agreeing with previous QCM-D (Saigal et al. 2013), and ellipsometry measurements (Malmsten et al. 1992). Following rinsing (at ca. 3000 s), the frequency shifts to ca. −10 Hz as loosely bound polymer is removed from the surface.

In contrast, slow adsorption is observed for CNC films, reaching a soft plateau of ca. −11 Hz after 5000 s (Fig. 1a). Similar behaviour is observed for lower molecular weight PEG at 1000 ppm

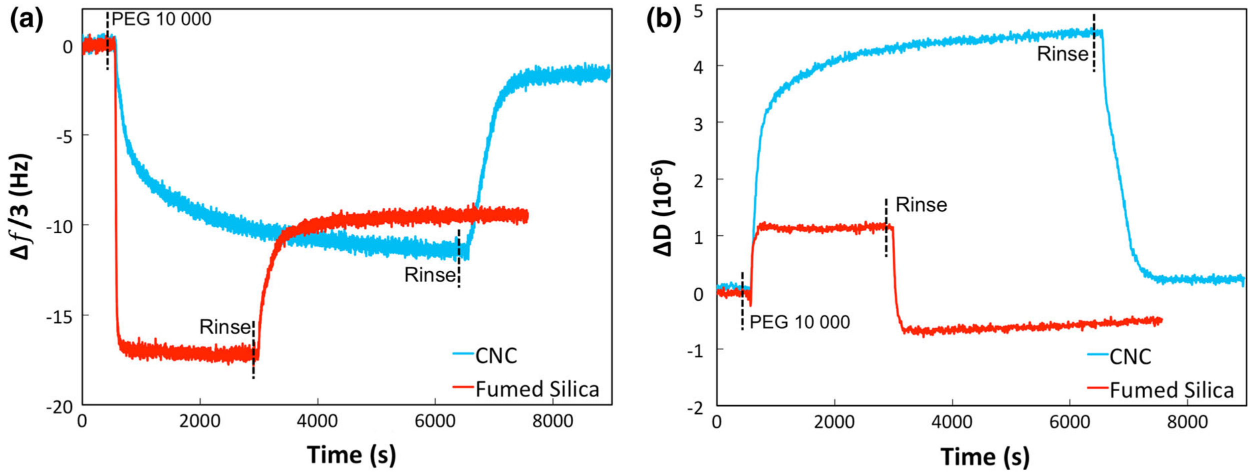

Fig. 1 QCM-D data of the third overtone showing the change in **a** frequency and **b** dissipation as a function of time for PEG 10,000 at 1000 ppm. After reaching a stable baseline (5 min) PEG solution is injected and allowed to continuously flow over the sensor until a plateau is observed. At that point, a water rinse is started until a second plateau is reached

(Supporting Information Fig. S3) however, we note that in 10,000 ppm PEG solutions, frequency and dissipation shifts are more rapid, indicating quick polymer saturation at the film surface. The slow adsorption behaviour in 1000 ppm PEG solutions shows poor PEG affinity for CNC films in comparison to silica. Moreover, due to the porous structure of CNC films (Reid et al. 2016), we note that PEG can potentially diffuse into the film increasing the total mass but not as the result of PEG–cellulose adsorption.

The lack of PEG adsorption to CNCs is exemplified after rinsing, whereby the frequency returns to ca. 0 Hz indicating that all polymer has been removed from the CNC film. This is in contrast to Bardet et al. (2015) who reported that low molecular weight PEG adsorbs to CNCs during QCM-D experiments. We note however, that the films studied by Bardet et al. (2015) were prepared in situ using a cationic polyethyleneimine (PEI) adhesion layer to anchor an "open" CNC film prepared in situ on the QCM-D sensor. We suggest that the PEG adsorption was more likely due to hydrogen bonding with PEI's amine groups as opposed to an interaction with cellulose (Utsuno and Uludağ 2010). The films used here do not have underlying polymer adhesion layers, fully coat the sensor and are much thicker; as such, interactions can only occur between PEG and CNCs. The lack of PEG on the surface of CNC films following rinsing shows that PEG does not adsorb to CNC films.

QCM-D dissipation profiles similarly show rapid and slow changes during PEG adsorption on fumed silica and CNCs, respectively (Fig. 1b). After rinsing, fumed silica films maintain dissipation values less than 10% of the frequency shift which indicate rigid polymer adsorption and allows for the calculation of adsorbed mass using the Sauerbrey equation (Aulin et al. 2008). Although the rigidity of the CNC film is less apparent, for comparison we calculate the adsorbed mass using the same method. Table 1 presents the total mass per area of adsorbed PEG on CNC and fumed silica films, before and after rinsing, for all molecular weights and concentrations of PEG tested. Importantly, the mass of PEG adsorbed, determined by QCM-D, includes the water bound to PEG, (which is significant) and thus the numbers in Table 1 are considered "hydrated" values—the dry mass would be closer to 50% of the wet mass assuming a known/unchanging number of water molecules bound to each PEG repeat unit (Huang and Nishinari 2001). Note that a negative mass indicates that (Δf) was greater than zero after rinsing and thus a percentage of the film was lost from the sensor surface.

Table 1 shows that while the adsorbed mass for PEG300 and PEG1000 are similar between the films, significantly more polymer adsorbs to fumed silica at higher molecular weights (i.e., PEG6000 and PEG10000). Furthermore, adsorbed mass after rinsing is independent of concentration, indicating that the fumed silica surface becomes saturated in good agreement with Kim et al. (2012). Interestingly, only PEGs that have molecular weights above the molecular weight of entanglement (M_e), which for PEG is

Table 1 Adsorbed mass with the standard deviation of separate adsorption measurements before and after rinsing as calculated by the Sauerbrey equation

Molar mass (g/mol)	Adsorbed mass before rinse (mg/m^2)				Adsorbed mass after rinse (mg/m^2)			
	Fumed silica		CNC		Fumed silica		CNC	
	1000 ppm	10,000 ppm	1000 ppm	10,000 ppm	1000 ppm	10,000 ppm	1000 ppm	10,000 ppm
300	0.6 ± 0.4	2.1 ± 0.2	0.6 ± 0.2	2.3 ± 0.1	0.0 ± 0.1	0.1 ± 0.1	−0.1 ± 0.4	0.2 ± 0.1
1000	1.3 ± 0.3	3.4 ± 0.1	1.7 ± 0.1	2.7 ± 0.9	0.0 ± 0.1	−0.2 ± 0.3	0.1 ± 0.3	0.2 ± 0.3
6000	2.3 ± 0.9	5.5 ± 0.1	1.2 ± 0.2	2.2 ± 0.1	1.2 ± 0.6	1.2 ± 0.2	0.2 ± 0.5	0.1 ± 0.2
10,000	2.7 ± 0.4	4.2 ± 0.4	0.6 ± 0.1	1.5 ± 0.4	1.4 ± 0.3	1.1 ± 0.7	0.1 ± 0.1	−0.2 ± 0.3

~3000 g/mol, have substantial adsorption to silica after rinsing. Although, we do not expect molecular entanglement to be needed for adsorption, particularly in the dilute regime investigated here, the mass values in Table 1 potentially suggest that polymer flexibility plays a role in PEG adsorption at silica film surfaces. We note however, that Kim et al. (2012) have shown that in dispersion, PEG adsorption occurs regardless of PEG molecular weight and the thickness of the subsequent adsorbed glassy polymer is 1–2 nm. Although not specifically examined in this work, the differences in adsorbed mass potentially demonstrates different conformational requirements for adsorption to a particle film versus particles in dispersion.

The mass of adsorbed PEG on silica is consistent with previously reported adsorption densities for all PEG polymers over M_e (Madathingal and Wunder 2011). However, we note that varying surface chemistry and surface area (SA) between silica particles can make direct comparison of results difficult. For example Madathingal and Wunder (2011). showed that PEG (M_w = 100,000 g/mol) adsorption varied from 0.21 to 1.13 mg/m^2 for silica particles with diameters of 15 and 100 nm respectively. This fact convolutes trends within literature, particularly when analyzing the effect of polymer molecular weight. Low molecular weight PEG adsorption densities of 0.58 mg/m^2 (SA = 50 m^2/g) (Esumi et al. 2001), and 0.70 mg/m^2 (SA = 3.26 m^2/g) (Zaman 2000), have been reported for 10,000 g/mol and 7500 g/mol PEG, respectively. Similar densities have been found for high molecular weight PEG ($>1 \times 10^6$ g/mol) with Rubio and Kitchener (1976) and Mathur and Moudgil (1997) reporting 0.7 mg/m^2 (SA = 171 m^2/g) and 0.8 mg/m^2 (SA = 3.18 m^2/g), respectively. Looking specifically at 10 nm silica particles with a SA of 251 m^2/g, adsorption densities of 0.23, 0.28, 0.30 and 0.31 mg/m^2 were reported for 50,000, 150,000, 500,000 and 1,000,000 g/mol PEG respectively (Liu and Xiao 2008). More significant increases were reported for silica particles with a SA of 17.6 m^2/g, in which adsorption densities of 0.40, 0.51 and 0.74 mg/m^2 were observed for 10,000, 100,000 and 600,000 g/mol PEG respectively (Esumi et al. 1998). Although, adsorption density clearly increases with molecular weight, significant changes are only observed over several orders of magnitude and thus it is reasonable that PEG6000 and PEG10000 exhibit similar adsorption densities on fumed silica films.

In contrast to fumed silica, Table 1 shows that PEG does not adsorb to CNC films as the adsorbed PEG mass after rinsing is not significantly different from zero. Although the mass of the CNC films initially increases in the presence of PEG solutions, we propose that this is the result of non-specific polymer interactions with the film and potential polymer diffusion into the film's porous structure [25–40% pores by volume in water (Reid et al. 2016, 2017a)], and is not due to PEG–cellulose adsorption.

Particle dispersions

While QCM-D quantitatively measures the (wet) mass of polymer adsorbed to a film, it is not directly obvious how/if polymer adsorption differs for a film of particles compared to individual particles in dispersion. As such, we monitored the heat of adsorption by isothermal titration calorimetry for fumed silica and CNCs mixed with aqueous PEG solutions, investigated changes in rheological behaviour of CNC dispersions in PEG solutions, and measured particle size following redispersion of dried CNC + PEG dispersions via dynamic light scattering.

Isothermal titration calorimetry and heat of adsorption

ITC was performed by injecting small aliquots of PEG solution into fumed silica and CNC dispersions. By monitoring the release (exothermic) or absorption (endothermic) of heat resulting from polymer–particle interactions, we can obtain further insight into PEG behavior at particle surfaces. Figure 2 presents the raw data collected for the injection of PEG6000 from which clear differences between injecting into water (Fig. 2a), fumed silica (Fig. 2b) and CNCs (Fig. 2c) can be seen. Subtracting the heat of dilution (PEG into water) and integrating, the molar heat of injection (ΔH) can be determined (Fig. 3). For fumed silica, all PEG molecular weights clearly demonstrate an exothermic process indicative of strong hydrogen bonding and an enthalpically driven adsorption process (Chiad et al. 2009). In contrast, no significant exothermic processes were observed for CNC dispersions, suggesting that no PEG–CNC hydrogen bonds (or other strong bonds) are formed. Additionally, if PEG adsorption occurred by an entropic process, such as the release of structured solvent, we would expect to observe an endothermic process, as is the case for XG adsorption (Lopez et al. 2010). The fact that for all PEG molecular weights, the adsorption ΔH for CNCs is nearly two orders of magnitude less than for fumed silica indicates that there is no significant enthalpic interaction between the PEG and CNCs in dispersion.

Rheology

Fumed silica is extensively used as a rheological modifier and is well-known to have shear thickening properties making it useful for many coatings, adhesives and functional fluid applications (Cabot Corporation 2016). The rheological properties of PEG and fumed silica dispersions have been thoroughly investigated in both the dilute and concentrated regimes (Raghavan et al. 2000; Zhang and Archer 2002; Khandavalli and Rothstein 2014; Hasanzadeh et al. 2015). Adsorbed polymers increase the effective volume fraction of particles and can form network-like structures dramatically impacting rheological

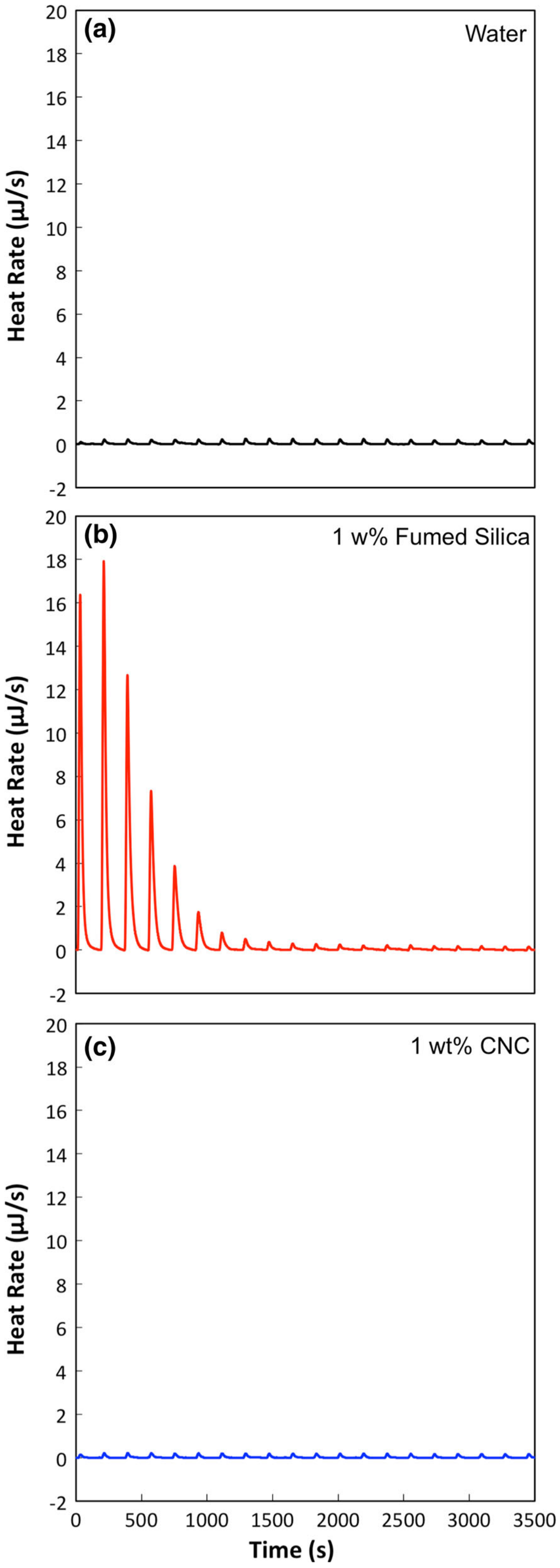

◀**Fig. 2** Raw ITC data for the injection of 0.5 wt% PEG6000 into 300 µL of **a** water and 1 wt% dispersions of **b** fumed silica and **c** CNC. Injection volume was 2.5 µL

properties of dispersions (Zhang and Archer 2002). The rheological behaviour of PEG-silica dispersions is complex and beyond the scope of this work but is well summarized elsewhere (Khandavalli and Rothstein 2014).

Similarly, the rheological properties of CNCs in aqueous dispersions have been studied (Ureña-Benavides et al. 2011; Shafiei-Sabet et al. 2012; Noroozi et al. 2013; Lu et al. 2014; Shafiei-Sabet et al. 2014), but only a few have probed the rheological behaviour with added polymers (Ben Azouz et al. 2012; Boluk et al. 2012; Oguzlu et al. 2016). In work investigating melt processed CNC composites, the viscosity of polymer solutions containing very high molecular weight PEG (5×10^6 g/mol), was shown to decrease with CNC concentration (Ben Azouz et al. 2012). In contrast, incorporating hydroxyethyl cellulose (HEC) and carboxymethyl cellulose into CNC dispersions, has been shown to dramatically increase the apparent viscosity although two contradicting mechanisms are presented in the literature (Boluk et al. 2012; Oguzlu et al. 2016). Boluk et al. (2012) proposed that increased viscosity of CNC dispersions upon the addition of HEC is not due to polymer adsorption but is the result of depletion effects causing weak CNC flocculation. In contrast, Hu et al. (2014) have shown that HEC ($M_w > 250{,}000$ g/mol) adsorbs to CNC thin films via QCM-D, suggesting that changes to rheological behaviour are the result of polymer adsorption and indicate that depletion flocculation is not occurring. In dispersion, ordered CNC nematic gels were readily formed upon the addition of HEC, and justified as an increase in CNC “apparent” volume fraction resulting from HEC adsorption.

Under the assumption that HEC *does* adsorb to cellulose, rheological behaviour of CNCs with PEG300 and PEG10000 was investigated and compared to CNC + HEC dispersions. We note that both the molecular weight (90,000 g/mol) and concentration (<0.15 wt%) of HEC are below the critical overlap concentration (Hu et al. 2014), and we do not expect gelation to occur at these dilute concentrations during rheological measurements. Moreover, shear viscosity of polymer-only solutions are nearly an order of magnitude less than CNC dispersions (Supporting Information Fig. S5) and any increase in viscosity is expected to result from polymer adsorption. Figure 4 shows that at concentrations as low as 0.05 wt%, HEC increases the shear viscosity of the CNC dispersion due to polymer adsorption and the increased “apparent” volume fraction of the particles. In contrast, PEG300 and PEG10000 at concentrations of 1 wt% insignificantly impact rheological properties suggesting that the CNC volume fraction (or particle size) remains constant. As a result, viscosity

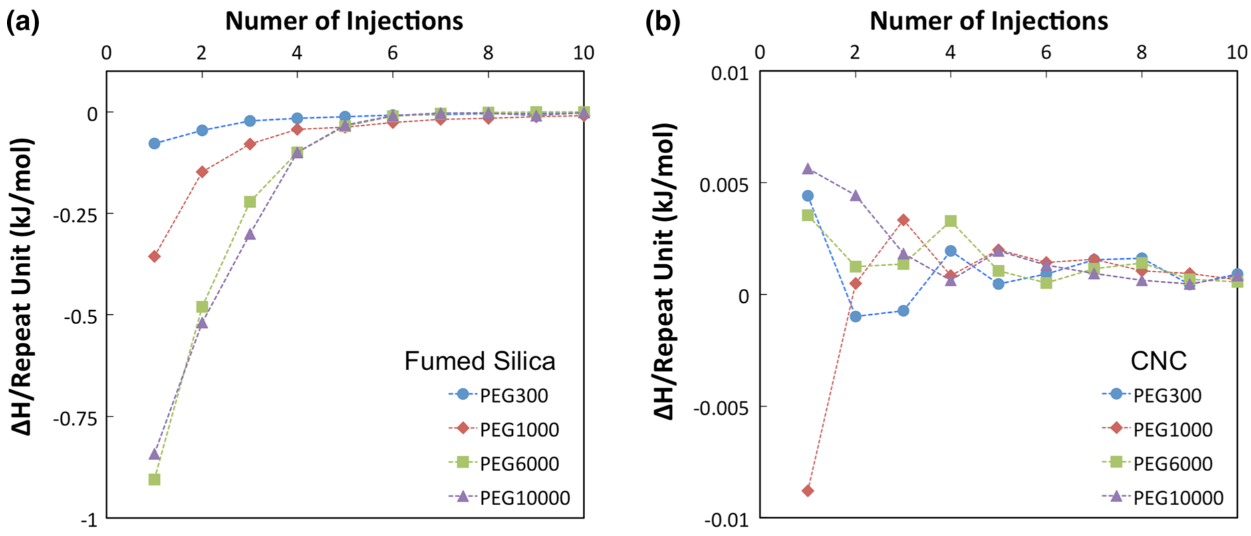

Fig. 3 Molar heat of injection for the addition of PEG to **a** fumed silica and **b** CNC dispersions. ΔH is normalized to the moles of PEG repeat units per injection. Note that ΔH for CNC dispersions is ca. 10^2 less than fumed silica

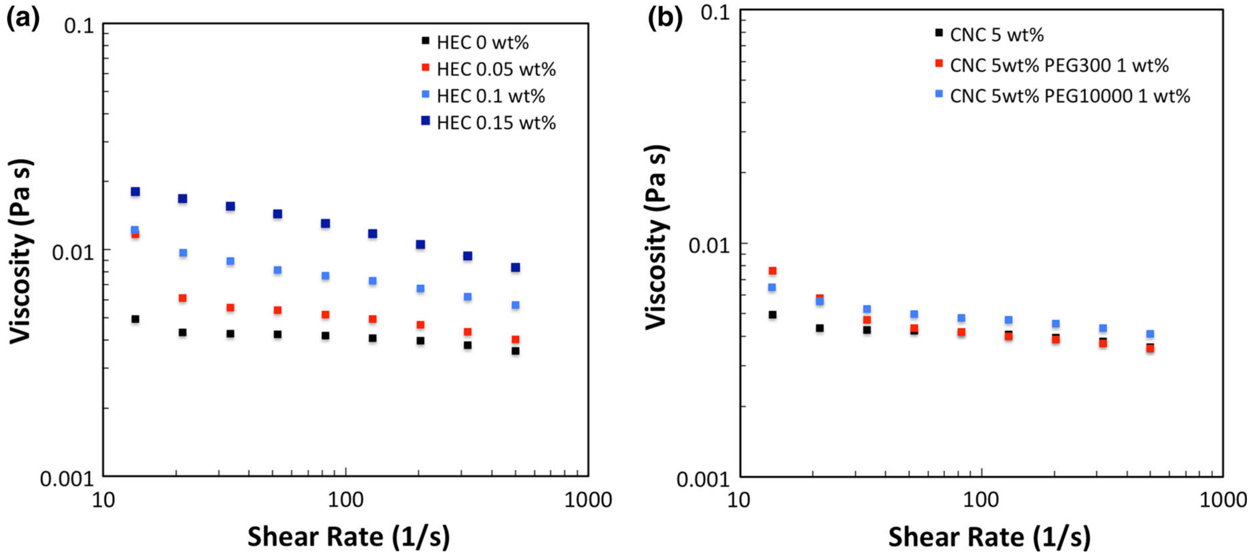

Fig. 4 Steady state shear viscosity as a function of shear rate for 5 wt% CNC dispersions with **a** HEC and **b** PEG300 and PEG10000

measurements further indicate that PEG does not adsorb to CNC particle surfaces in aqueous environments.

Dynamic light scattering and redispersion of dried particles with PEG

Apparent particle size of fumed silica and CNCs in aqueous solutions of PEG was measured by DLS. These mixtures were dried and rehydrated to measure particle size following redispersion. Critically, DLS assumes Brownian motion of spherical particles during analysis. CNCs and fumed silica are rod-like and fractal-shaped particles, respectively, and thus sizes should be taken as "apparent" and only relative changes considered. Additionally, following the the largest radius of gyration of PEG in aqueous environments is taken to be 4.7 nm for PEG10000, nearly two orders of magnitude smaller than fumed silica and CNCs, and thus free PEG is expected to be an insignificant source of light scattering (Devanand and Selser 1991). Finally, the viscosity of polymer solutions containing 10000 ppm PEG10000 were statistically equivalent to that of pure water and thus is not expected to impact the diffusion of particles in dispersion or the DLS measurement.

For all PEG concentrations and molecular weights examined, no statistically significant increase in particle size is observed for fumed silica mixed with PEG before drying (Supporting Information Fig. S6). This agrees with previous reports and indicates that PEG tightly conforms to the surface of the silica particle and does not extend into the bulk of the dispersion (Malmsten et al. 1992). This is supported by the low dissipation values measured in QCM-D implying a flat and rigid adsorbed morphology (Fig. 1). Importantly, because silica particles remain well dispersed with no significant increase in particle size, DLS measurements show that PEG does not lead to aggregation or bridging within the concentration regimes investigated, which is in good agreement with previous studies (Kim et al. 2012).

Upon drying the dispersions of fumed silica mixed with PEG (the same ones as measured in Supporting Information Fig. S6), the powders could not be redispersed and macroscopic aggregates of PEG/silica were visible by eye after rehydration. Evaporating dispersions increases the volume fraction of particles and PEG through a threshold concentration where polymer entanglement and particle bridging can occur (Kim et al. 2012). PEG is a well-known flocculant for fumed silica sols and has been shown to be effective at molecular weights as low as 6000 g/mol (Eisenlauer et al. 1980). Polymer bridging in highly concentrated regimes can lead to network formation creating irreversible aggregates maintained by strong PEG-silica hydrogen bonds. Rehydration does not effectively interrupt particle–polymer interactions and yields highly aggregated material with particle sizes too large for analysis by DLS.

Similar to fumed silica, CNCs show no significant change in particle size when mixed with PEG solutions (Supporting Information Fig. S6). CNCs in water and in all PEG solutions tested had an apparent DLS size of 77 ± 2 nm. This is in contrast to Bardet et al. (2015) who report an average increase in CNC size from 105 ± 5 to 122 ± 10 nm in aqueous solutions of PEG200. It is unclear why such a significant increase is observed in their work but does suggest the presence of PEG multilayers on the CNC surface or particle aggregation.

In contrast to silica, we dried CNC dispersions with and without PEG and found that PEG improved the redispersibility of CNCs upon rehydration (Fig. 5). This agrees with previous work by Cheng et al. (2015) but based on the new evidence provided herein, we believe an entirely different mechanism is at play than the hydrogen bonded PEG "brush" structure on CNCs that they suggest. We propose that upon drying, PEG hinders CNC-CNC interactions limiting short-range attractive van der Waals forces and hydrogen bonding between particles; this can be envisioned to be similar to polymer intercalation of clays. For the *dried* CNC + PEG dispersions, which are void of water, we expect that PEG does hydrogen bond with the CNC particle surface, as has been measured via infrared spectroscopy in dried PEG/CNC composites (Xu et al. 2013) and by differential scanning calorimetry in model PEG/cellulose films (Kondo and Sawatari 1994). Upon rehydration however, PEG–CNC hydrogen bonds are replaced by PEG-water and CNC-water hydrogen bonds yielding dissolved polymer and dispersed CNC particles.

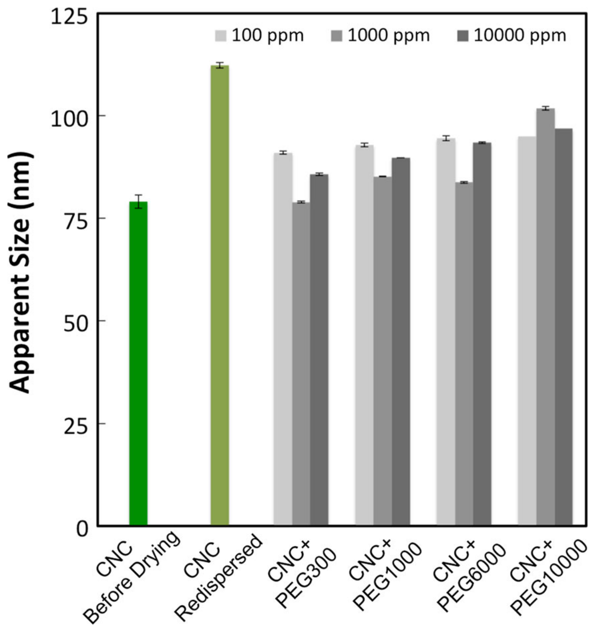

Fig. 5 Apparent particle size of CNCs before drying along with redispersed CNCs mixed with PEG following drying and rehydration (without sonication) as measured by DLS

This is supported by the fact that for CNCs dried with PEG300 at 1000 ppm, particle sizes measured by DLS were the same before and after drying indicating that PEG effectively interrupted the strong forces between CNC particles that lead to irreversible aggregation upon drying. Moreover, for molecular weights below 10,000 g/mol, 1000 ppm (the middle concentration tested) yields the least aggregated particles. Although the particle sizes over the range of PEG concentrations investigated only differ on the order of 10%, this indicates that there may be an ideal PEG concentration that should be added to CNC dispersions to optimize redispersion. We suggest that below the 1000 ppm threshold, there is insufficient PEG to effectively interrupt CNC–CNC interactions leading to more aggregated particles. Above the threshold, there is a greater potential for PEG to self-associate and exclude CNCs, again resulting in aggregated particles.

While it is not the primary focus of this work, self-association of CNCs at high PEG concentrations could result from depletion effects that occur as the dispersion evaporates and polymer concentration increases. Concentrated solutions of high molecular weight PEG have been shown to cause depletion flocculation of cellulose fibers in paper making (Hubbe et al. 2009), and analogous effects could drive CNC aggregation during drying. Increasing PEG molecular weight yields larger CNC particle sizes as shown previously, further indicating that depletion effects cannot be ignored in concentrated polymer solutions (i.e., during drying) (Cheng et al. 2015). However, particle sizes in this work are significantly smaller than previous redispersion studies making it difficult to deconvolute minor aggregation and polymer adsorption, which potentially occurs in the dried state. Regardless of PEG molecular weight or concentration, CNC + PEG dispersions showed relatively good redispersibility and we postulate that polymer–particle interactions that occur in the dry state are reversed upon hydration, unlike with fumed silica + PEG dispersions.

Conclusions

This work compared the adsorption of PEG to fumed silica versus CNCs, in the form of both thin films and dispersed particles. Low molecular weight PEG was investigated as a simple non-ionic water-soluble linear polymer for which hydrogen bonding is understood to be the primary mechanism of adsorption in aqueous environments. Indeed, PEG adsorption to silica has been shown to occur via hydrogen bonding between surface silanol groups (which have relatively low pK_a's and behave as Brønsted acids) and the ether oxygen of the PEG backbone which acts as the Lewis base (Mathur and Moudgil 1997). All measurements in this work supported strong enthalpically-driven PEG adsorption to silica due to this hydrogen bonding.

On the other hand, PEG did not adsorb to CNC films or dispersed particles and did not increase the viscosity of CNC dispersions. However, PEG *was* effective in physically screening cellulose–cellulose interactions when PEG + CNC dispersions were dried, allowing for improved redispersibility because of the reversibility of PEG–CNC interactions upon rehydration. Therefore, in the presence of water, it appears that cellulose prefers to hydrogen bond with water over highly hydrogen bonding capable polymers, like PEG. Thus, only previous reports of strong PEG–CNC interactions in *dried* materials remain convincing (Azizi Samir et al. 2004; Changsarn et al. 2011; Xu et al. 2013).

To address the proposed question "Does polyethylene glycol adsorb to cellulose nanocrystals in aqueous environments?" this work supports the conclusion that PEG does *not* adsorb to CNCs. This agrees with previous papermaking research (Lindström and Glad-Nordmark 1983), and implies that nanoscale effects, anionic sulfate half ester groups, particle crystallinity or the amphiphilic nature of CNCs do not cause CNCs to interact with PEG differently than macroscopic cellulose fibers. The comparison between silica and CNCs shows that highly hydroxylated surfaces do not all behave similarly in aqueous environments and highlights that multiple characterization techniques allow for deeper insight into polymer–particle interactions, which we believe will aid in the design and use of CNCs in water-based applications.

Acknowledgments Funding from the Natural Sciences and Engineering Research Council of Canada, Industrial Postgraduate Scholarship program sponsored by Cabot Corporation is gratefully acknowledged. We additionally acknowledge Cabot Corporation for their donation of CAB-O-SIL® M-5 fumed silica. Professors R. Pelton, A. Guarne, R. Epand and J. Moran-Mirabal are thanked for sharing equipment to characterize CNCs. Additionally, the Biointerfaces Institute and the Brockhouse Institute for Materials Research at McMaster University are acknowledged for support and equipment.

References

Aggebrandt LG, Samuelson O (1964) Penetration of water-soluble polymers into cellulose fibers. J Appl Polym Sci 8:2801–2812. doi:10.1002/app.1964.070080625

Araki J, Wada M, Kuga S (2001) Steric stabilization of a cellulose microcrystal suspension by poly(ethylene glycol) grafting. Langmuir 17:21–27. doi:10.1021/la001070m

Aulin C, Varga I, Claesson PM et al (2008) Buildup of polyelectrolyte multilayers of polyethyleneimine and microfibrillated cellulose studied by in situ dual-polarization interferometry and quartz crystal microbalance with dissipation. Langmuir 24:2509–2518. doi:10.1021/la7032884

Azizi Samir MAS, Alloin F, Sanchez JY, Dufresne A (2004) Cellulose nanocrystals reinforced poly(oxyethylene). Polymer (Guildf) 45:4149–4157. doi:10.1016/j.polymer.2004.03.094

Bardet R, Belgacem N, Bras J (2015) Flexibility and color monitoring of cellulose nanocrystal iridescent solid films using anionic or neutral polymers. ACS Appl Mater Interfaces 7:4010–4018. doi:10.1021/am506786t

Beck S, Bouchard J, Berry R (2012) Dispersibility in water of dried nanocrystalline cellulose. Biomacromol 13:1486–1494. doi:10.1021/bm300191k

Ben Azouz K, Ramires EC, Van den Fonteyne W et al (2012) Simple method for the melt extrusion of a cellulose nanocrystal reinforced hydrophobic polymer. ACS Macro Lett 1:236–240. doi:10.1021/mz2001737

Benselfelt T, Cranston ED, Ondaral S et al (2016) Adsorption of xyloglucan onto cellulose surfaces of different morphologies: an entropy-driven process. Biomacromol 17:2801–2811. doi:10.1021/acs.biomac.6b00561

Bhattacharyya L, Rohrer JS (eds) (2012) Applications of ion chromatography for pharmaceutical and biological products. Wiley, Hoboken

Biermann CJ (1996) Stock preparation and additives for papermaking. In: Handbook of pulping and papermaking, 2nd edn. Elsevier/Academic Press, London, pp 190–208. doi:10.1016/B978-012097362-0/50012-1

Boluk Y, Zhao L, Incani V (2012) Dispersions of nanocrystalline cellulose in aqueous polymer solutions: structure formation of colloidal rods. Langmuir 28:6114–6123. doi:10.1021/la2035449

Bouchard J, Méthot M, Fraschini C, Beck S (2016) Effect of oligosaccharide deposition on the surface of cellulose nanocrystals as a function of acid hydrolysis temperature. Cellulose 23:3555–3567. doi:10.1007/s10570-016-1036-5

Cabot Corporation (2016) Hydrophilic Fumed Silica. http://www.cabotcorp.com/solutions/products-plus/fumed-metal-oxides/hydrophilic. Accessed 11 Oct 2016

Cao Y, Zavaterri P, Youngblood J et al (2015) The influence of cellulose nanocrystal additions on the performance of cement paste. Cem Concr Compos 56:73–83. doi:10.1016/j.cemconcomp.2014.11.008

Changsarn S, Mendez JD, Shanmuganathan K et al (2011) Biologically inspired hierarchical design of nanocomposites based on poly(ethylene oxide) and cellulose nanofibers. Macromol Rapid Commun 32:1367–1372. doi:10.1002/marc.201100183

Cheng D, Wen Y, Wang L et al (2015) Adsorption of polyethylene glycol (PEG) onto cellulose nano-crystals to improve its dispersity. Carbohydr Polym 123:157–163. doi:10.1016/j.carbpol.2015.01.035

Chiad K, Stelzig SH, Gropeanu R et al (2009) Isothermal titration calorimetry: a powerful technique to quantify interactions in polymer hybrid systems. Macromolecules 42:7545–7552. doi:10.1021/ma9008912

de Cuadro P, Belt T, Kontturi KS et al (2015) Cross-linking of cellulose and poly(ethylene glycol) with citric acid. React Funct Polym 90:21–24. doi:10.1016/j.reactfunctpolym.2015.03.007

De France KJ, Chan KJW, Cranston ED, Hoare T (2016) Enhanced mechanical properties in cellulose nanocrystal–poly(oligoethylene glycol methacrylate) injectable nanocomposite hydrogels through control of physical and chemical cross-linking. Biomacromol 17:649–660. doi:10.1021/acs.biomac.5b01598

Devanand K, Selser JC (1991) Asymptotic behavior and long-range interactions in aqueous solutions of poly (ethylene oxide). Macromolecules 24:5943–5947. doi:10.1021/ma00022a008

Dong XM, Kimura T, Revol J-F, Gray DG (1996) Effects of ionic strength on the isotropic–chiral nematic phase transition of suspensions of cellulose crystallites. Langmuir 12:2076–2082. doi:10.1021/la950133b

Edgar CD, Gray DG (2002) Influence of dextran on the phase behavior of suspensions of cellulose nanocrystals. Macromolecules 35:7400–7406. doi:10.1021/ma0204195

Eisenlauer J, Killmann E, Korn M (1980) Stability of colloidal silica (aerosil) hydrosols. II. Influence of the pH value and the adsorption of polyethylene glycols. J Colloid Interface Sci 74:120–135. doi:10.1016/0021-9797(80)90176-9

Eronen P, Junka K, Laine J, Österberg M (2011) Interaction between water-soluble polysaccharides and native nanofibrillar cellulose thin films. BioResources 6:4200–4217

Esumi K, Iitaka M, Koide Y (1998) Simultaneous adsorption of poly(ethylene oxide) and cationic surfactant at the silica/water interface. J Colloid Interface Sci 208:178–182. doi:10.1006/jcis.1998.5819

Esumi K, Nakaie Y, Sakai K, Torigoe K (2001) Adsorption of poly(ethyleneglycol) and poly(amidoamine)dendrimer from their mixtures on alumina/water and silica/water interfaces. Colloids Surfaces A Physicochem Eng Asp 194:7–12. doi:10.1016/S0927-7757(00)00788-3

Fleer GJ, Cohen Stuart MA, Scheutjens JMHM et al (1998) Polymers at interfaces. Chapman & Hall, Illistrate

Gårdebjer S, Andersson M, Engström J et al (2016) Using ansen solubility parameters to predict the dispersion of nano-particles in polymeric films. Polym Chem 7:1756–1764. doi:10.1039/C5PY01935D

Gray DG, Mu X (2015) Chiral nematic structure of cellulose nanocrystal suspensions and films; polarized light and atomic force microscopy. Materials (Basel) 8:7873–7888. doi:10.3390/ma8115427

Grishkewich N, Mohammed N, Tang J, Tam KC (2017) Recent advances in the application of cellulose nanocrystals. Curr Opin Colloid Interface Sci 29:32–45. doi:10.1016/j.cocis.2017.01.005

Gustafsson E, Pelton R, Wågberg L (2016) Rapid development of wet adhesion between carboxymethylcellulose modified cellulose surfaces laminated with polyvinylamine adhesive. ACS Appl Mater Interfaces 8:24161–24167. doi:10.1021/acsami.6b05673

Habibi Y, Lucia LA, Rojas OJ (2010) Cellulose nanocrystals: chemistry, self-assembly, and applications. Chem Rev 110:3479–3500. doi:10.1021/cr900339w

Hasanzadeh M, Mottaghitalab V, Rezaei M (2015) Rheological and viscoelastic behavior of concentrated colloidal suspensions of silica nanoparticles: a response surface methodology approach. Adv Powder Technol 26:1570–1577. doi:10.1016/j.apt.2015.08.011

Hatton FL, Malmström E, Carlmark A (2015) Tailor-made copolymers for the adsorption to cellulosic surfaces. Eur Polym J 65:325–339. doi:10.1016/j.eurpolymj.2015.01.026

He X, Male KB, Nesterenko PN et al (2013) Adsorption and desorption of methylene blue on porous carbon monoliths and nanocrystalline cellulose. ACS Appl Mater Interfaces 5:8796–8804. doi:10.1021/am403222u

Hoeger I, Rojas OJ, Efimenko K et al (2011) Ultrathin film coatings of aligned cellulose nanocrystals from a convective-shear assembly system and their surface mechanical properties. Soft Matter 7:1957. doi:10.1039/c0sm01113d

Holappa S, Kontturi KS, Salminen A et al (2013) Adsorption of hydrophobically end-capped poly(ethylene glycol) on cellulose. Langmuir 29:13750–13759. doi:10.1021/la402494m

Honorato-Rios C, Kuhnhold A, Bruckner J et al (2016) Equilibrium liquid crystal phase diagrams and detection of kinetic arrest in cellulose nanocrystal suspensions. Front Mater 3:1–13. doi:10.3389/fmats.2016.00021

Hu Z, Cranston ED, Ng R, Pelton R (2014) Tuning cellulose nanocrystal gelation with polysaccharides and surfactants. Langmuir 30:2684–2692. doi:10.1021/la404977t

Hu Z, Patten T, Pelton R, Cranston ED (2015) Synergistic stabilization of emulsions and emulsion gels with water-soluble polymers and cellulose nanocrystals. ACS Sustain Chem Eng 3:1023–1031. doi:10.1021/acssuschemeng.5b00194

Hu Z, Xu R, Cranston ED, Pelton RH (2016) Stable aqueous foams from cellulose nanocrystals and methyl cellulose. Biomacromol 17:4095–4099. doi:10.1021/acs.biomac.6b01641

Huang L, Nishinari K (2001) Interaction between poly(ethylene glycol) and water as studied by differential scanning calorimetry. J Polym Sci Part B: Polym Phys 39:496–506.

doi:10.1002/1099-0488(20010301)39:5<496:AID-POLB1023>3.0.CO;2-H

Hubbe MA (2007) Flocculation and redispersion of cellulosic fiber suspensions: a review of effects of hydrodynamic shear and polyelectrolytes. BioResources 2:296–331

Hubbe MA, Nanko H, McNeal MR (2009) Retention aid polymer interactions with cellulosic surfaces and suspensions: a review. BioResources 4:850–906

Hyde EDER, Seyfaee A, Neville F, Moreno-Atanasio R (2016) Colloidal silica particle synthesis and future industrial manufacturing pathways: a review. Ind Eng Chem Res 55:8891–8913. doi:10.1021/acs.iecr.6b01839

Ishimaru Y, Lindström T (1984) Adsorption of water-soluble, nonionic polymers onto cellulosic fibers. J Appl Polym Sci 29:1675–1691. doi:10.1002/app.1984.070290521

Kalashnikova I, Bizot H, Cathala B, Capron I (2012) Modulation of cellulose nanocrystals amphiphilic properties to stabilize oil/water interface. Biomacromol 13:267–275. doi:10.1021/bm201599j

Kalashnikova I, Bizot H, Bertoncini P et al (2013) Cellulosic nanorods of various aspect ratios for oil in water Pickering emulsions. Soft Matter 9:952. doi:10.1039/c2sm26472b

Kalasin S, Santore MM (2016) Near-surface motion and dynamic adhesion during silica microparticle capture on a polymer (solvated PEG) brush via hydrogen bonding. Macromolecules 49:334–343. doi:10.1021/acs.macromol.5b01977

Kargl R, Mohan T, Bračič M et al (2012) Adsorption of carboxymethyl cellulose on polymer surfaces: evidence of a specific interaction with cellulose. Langmuir 28:11440–11447. doi:10.1021/la302110a

Karimi K, Taherzadeh MJ (2016) A critical review on analysis in pretreatment of lignocelluloses: degree of polymerization, adsorption/desorption, and accessibility. Bioresour Technol 203:348–356. doi:10.1016/j.biortech.2015.12.035

Khandavalli S, Rothstein JP (2014) Extensional rheology of shear-thickening fumed silica nanoparticles dispersed in an aqueous polyethylene oxide solution. J Rheol (NY) 58:411–431. doi:10.1122/1.4864620

Kim SY, Meyer HW, Saalwächter K, Zukoski CF (2012) Polymer dynamics in PEG-silica nanocomposites: effects of polymer molecular weight, temperature and solvent dilution. Macromolecules 45:4225–4237. doi:10.1021/ma300439k

Klemm D, Kramer F, Moritz S et al (2011) Nanocelluloses: a new family of nature-based materials. Angew Chemie Int Ed 50:5438–5466. doi:10.1002/anie.201001273

Kloser E, Gray DG (2010) Surface grafting of cellulose nanocrystals with poly(ethylene oxide) in aqueous media. Langmuir 26:13450–13456. doi:10.1021/la101795s

Knop K, Hoogenboom R, Fischer D, Schubert US (2010) Poly(ethylene glycol) in drug delivery: pros and cons as well as potential alternatives. Angew Chemie Int Ed 49:6288–6308. doi:10.1002/anie.200902672

Kondo T, Sawatari C (1994) Intermolecular hydrogen bonding in cellulose/poly(ethylene oxide) blends: thermodynamic examination using 2,3-di-O- and 6-O-methylcelluloses as cellulose model compounds. Polymer (Guildf) 35:4423–4428. doi:10.1016/0032-3861(94)90102-3

Kontturi E, Johansson L, Kontturi K (2007) Cellulose nanocrystal submonolayers by spin coating. Langmuir 23:9674–9680

Kontturi KS, Biegaj K, Mautner A et al (2017) Noncovalent surface modification of cellulose nanopapers by adsorption of polymers from aprotic solvents. Langmuir 33:5707–5712. doi:10.1021/acs.langmuir.7b01236

Laine J, Lindström T, Glad-Nordmark G, Risinger G (2000) Studies on topochemical modification of cellulosic fibres. Part 1. Chemical conditions for the attachment of carboxymethyl cellulose onto fibres. Nord Pulp Pap Res J 15:520–526. doi:10.3183/NPPRJ-2000-15-05-p520-526

Leung K, Nielsen I, Criscenti L (2009) Elucidating the bimodal acid–base behavior of the water–silica interface from first principles. J Am Chem Soc 131:18358–18365. doi:10.1021/ja906190t

Li Y, Liu H, Song J et al (2011) Adsorption and association of a symmetric PEO–PPO–PEO triblock copolymer on polypropylene, polyethylene, and cellulose surfaces. ACS Appl Mater Interfaces 3:2349–2357. doi:10.1021/am200264r

Lindström T, Glad-Nordmark G (1983) Selective adsorption, flocculation, and fractionation of wood pulps with polyethyleneoxide. J Colloid Interface Sci 94:404–411. doi:10.1016/0021-9797(83)90280-1

Lindström T, Glad-Nordmark G (1984) Flocculation of latex and cellulose dispersions by means of transient polymer networks. Colloids Surf 8:337–351. doi:10.1016/0166-6622(84)80128-6

Liu H, Xiao H (2008) Adsorption of poly(ethylene oxide) with different molecular weights on the surface of silica nanoparticles and the suspension stability. Mater Lett 62:870–873. doi:10.1016/j.matlet.2007.06.079

Lopez M, Bizot H, Chambat G et al (2010) Enthalpic studies of xyloglucan–cellulose interactions. Biomacromol 11:1417–1428. doi:10.1021/bm1002762

Lu A, Hemraz U, Khalili Z, Boluk Y (2014) Unique viscoelastic behaviors of colloidal nanocrystalline cellulose aqueous suspensions. Cellulose 21:1239–1250. doi:10.1007/s10570-014-0173-y

Madathingal RR, Wunder SL (2011) Confinement effects of silica nanoparticles with radii smaller and larger than Rg of adsorbed poly(ethylene oxide). Macromolecules 44:2873–2882. doi:10.1021/ma1021693

Malmsten M, Linse P, Cosgrove T (1992) Adsorption of PEO–PPO–PEO block copolymers at silica. Macromolecules 25:2474–2481. doi:10.1021/ma00035a028

Mariano M, El Kissi N, Dufresne A (2014) Cellulose nanocrystals and related nanocomposites: review of some properties and challenges. J Polym Sci Part B: Polym Phys 52:791–806. doi:10.1002/polb.23490

Martin C, Jean B (2014) Nanocellulose/polymer multilayered thin films: tunable architectures towards tailored physical properties. Nord Pulp Pap Res J 29:19–30

Mathur S, Moudgil BM (1997) Adsorption mechanism(s) of poly(ethylene oxide) on oxide surfaces. J Colloid Interface Sci 196:92–98. doi:10.1006/jcis.1997.5192

Moon RJ, Martini A, Nairn J et al (2011) Cellulose nanomaterials review: structure, properties and nanocomposites. Chem Soc Rev 40:3941–3994. doi:10.1039/c0cs00108b

Niinivaara E, Faustini M, Tammelin T, Kontturi E (2015) Water vapor uptake of ultrathin films of biologically derived nanocrystals: quantitative assessment with quartz crystal microbalance and spectroscopic ellipsometry. Langmuir 31:12170–12176. doi:10.1021/acs.langmuir.5b01763

Noroozi N, Grecov D, Shafiei-Sabet S (2013) Estimation of viscosity coefficients and rheological functions of nanocrystalline cellulose aqueous suspensions. Liq Cryst 41:56–66. doi:10.1080/02678292.2013.834081

Oguzlu H, Boluk Y (2017) Interactions between cellulose nanocrystals and anionic and neutral polymers in aqueous solutions. Cellulose 24:131–146. doi:10.1007/s10570-016-1096-6

Oguzlu H, Danumah C, Boluk Y (2016) The role of dilute and semi-dilute cellulose nanocrystal (CNC) suspensions on the rheology of carboxymethyl cellulose (CMC) solutions. Can J Chem Eng 94:1841–1847. doi:10.1002/cjce.22597

Oksman K, Aitomäki Y, Mathew AP et al (2016) Review of the recent developments in cellulose nanocomposite processing. Compos Part A Appl Sci Manuf 83:2–18. doi:10.1016/j.compositesa.2015.10.041

Pelton RH, Allen LH, Nugent HM (1980) Survey of potential retention aids for newsprint manufacture. Pulp Pap Can 81(54–56):58

Pelton RH, Allen LH, Nugent HM (1981) Novel dual-polymer retention aids for newsprint and groundwood specialties. Tappi 64:89–92

Raghavan SR, Walls HJ, Khan SA (2000) Rheology of silica dispersions in organic liquids: new evidence for solvation forces dictated by hydrogen bonding. Langmuir 16:7920–7930. doi:10.1021/la991548q

Reid MS, Villalobos M, Cranston ED (2016) Cellulose nanocrystal interactions probed by thin film swelling to predict dispersibility. Nanoscale 8:12247–12257. doi:10.1039/C6NR01737A

Reid MS, Kedzior SA, Villalobos M, Cranston ED (2017a) Effect of ionic strength and surface charge density on the kinetics of cellulose nanocrystal thin film swelling. Langmuir. doi:10.1021/acs.langmuir.7b01740

Reid MS, Villalobos M, Cranston ED (2017b) Benchmarking cellulose nanocrystals: from the laboratory to industrial production. Langmuir 33:1583–1598. doi:10.1021/acs.langmuir.6b03765

Reid MS, Villalobos M, Cranston ED (2017c) The role of hydrogen bonding in non-ionic polymer adsorption to cellulose nanocrystals and silica colloids. Curr Opin Colloid Interface Sci 29:76–82. doi:10.1016/j.cocis.2017.03.005

Revol JF, Bradford H, Giasson J et al (1992) Helicoidal self-ordering of cellulose microfibrils in aqueous suspension. Int J Biol Macromol 14:170–172

Rubio J, Kitchener J (1976) The mechanism of adsorption of poly(ethylene oxide) flocculant on silica. J Colloid Interface Sci 57:132–142. doi:10.1016/0021-9797(76)90182-X

Saigal T, Riley JK, Golas PL et al (2013) Poly(ethylene oxide) star polymer adsorption at the silica/aqueous interface and displacement by linear poly(ethylene oxide). Langmuir 29:3999–4007. doi:10.1021/la305085a

Shafiei-Sabet S, Hamad WY, Hatzikiriakos SG (2012) Rheology of nanocrystalline cellulose aqueous suspensions. Langmuir 28:17124–17133. doi:10.1021/la303380v

Shafiei-Sabet S, Hamad WY, Hatzikiriakos SG (2014) Ionic strength effects on the microstructure and shear rheology of cellulose nanocrystal suspensions. Cellulose 21:3347–3359. doi:10.1007/s10570-014-0407-z

Stone JE, Scallan AM (1967) The effect of component removal upon the porous structure of the cell wall of wood. II. Swelling in water and the fiber saturation point. Tappi 50:496–501. doi:10.1002/polc.5070110104

Sundman O (2014) Adsorption of four non-ionic cellulose derivatives on cellulose model surfaces. Cellulose 21:115–124. doi:10.1007/s10570-013-0105-2

Tarkow H, Feist WC, Southerland CF (1966) Interaction of wood with polymeric materials size. For Prod J 16:61–65

Trey SM, Netrval J, Berglund L, Johansson M (2010) Electron-beam-initiated polymerization of poly(ethylene glycol)-based wood impregnants. ACS Appl Mater Interfaces 2:3352–3362. doi:10.1021/am100778q

Ureña-Benavides EE, Ao G, Davis VA, Kitchens CL (2011) Rheology and phase behavior of lyotropic cellulose nanocrystal suspensions. Macromolecules 44:8990–8998. doi:10.1021/ma201649f

Utsuno K, Uludağ H (2010) Thermodynamics of polyethylenimine-DNA binding and DNA condensation. Biophys J 99:201–207. doi:10.1016/j.bpj.2010.04.016

Viet D, Beck-Candanedo S, Gray DG (2006) Dispersion of cellulose nanocrystals in polar organic solvents. Cellulose 14:109–113. doi:10.1007/s10570-006-9093-9

Wågberg L (2000) Polyelectrolyte adsorption onto cellulose fibres—a review. Nord Pulp Pap Res J 15:586–597. doi:10.3183/NPPRJ-2000-15-05-p586-597

Xiao H, Pelton RH, Archie H (1996) Novel rention aids for mechanical pulps. Tappi J 79:129–135

Xu X, Liu F, Jiang L et al (2013) Cellulose nanocrystals vs. Cellulose nanofibrils: a comparative study on their microstructures and effects as polymer reinforcing agents. ACS Appl Mater Interfaces 5:2999–3009. doi:10.1021/am302624t

Yu HY, Zhang DZ, Lu FF, Yao J (2016) New approach for single-step extraction of carboxylated cellulose nanocrystals for their use as adsorbents and flocculants. ACS Sustain Chem Eng 4:2632–2643. doi:10.1021/acssuschemeng.6b00126

Zaman AA (2000) Effect of polyethylene oxide on the viscosity of dispersions of charged silica particles: interplay between rheology, adsorption, and surface charge. Colloid Polym Sci 278:1187–1197. doi:10.1007/s003960000385

Zhang Q, Archer LA (2002) Poly(ethylene oxide)/silica nanocomposites: structure and rheology. Langmuir 18:10435–10442. doi:10.1021/la026338j

Current Opinion in Colloid & Interface Science 29 (2017) 76–82

Contents lists available at ScienceDirect

Current Opinion in Colloid & Interface Science

journal homepage: www.elsevier.com/locate/cocis

The role of hydrogen bonding in non-ionic polymer adsorption to cellulose nanocrystals and silica colloids

Michael S. Reid [a], Marco Villalobos [b], Emily D. Cranston [a],*

[a] Department of Chemical Engineering, McMaster University, Hamilton, Ontario L8S 4L8, Canada
[b] Cabot Corporation, Billerica, MA 01821, USA

ARTICLE INFO

Article history:
Received 17 October 2016
Received in revised form 28 February 2017
Accepted 6 March 2017
Available online 18 March 2017

Keywords:
Cellulose nanocrystals
Non-ionic polymer adsorption
Hydrogen bonding
Silica
Polyethylene glycol

ABSTRACT

A piqued interest in nanocellulose has recently arisen due to the growing need to use sustainable and renewable materials in place of those that are derived from petrochemical resources. Although current commercial uses of nanocellulose remain limited, research over the past two decades demonstrates numerous applications including reinforcing agents in polymer and cement composites, coatings, foams, gels, tissue scaffolds, and rheological modifiers, amongst others. Because of the hydrophilic nature of nanocellulose many of the potential uses will likely be in water-based formulations or employ water-based processing methods. Thus understanding the interactions between nanocellulose and water-soluble polymers is critical. Although polyelectrolyte adsorption to cellulose is well understood, adsorption of non-ionic polymers is less clear, with hydrogen bonding often cited as a governing factor. Recent work suggests that in fact hydrogen bonding does not play a significant role in nanocellulose systems, and that non-ionic polymer adsorption is largely entropically driven. Herein we review current literature that investigates non-ionic polymer adsorption to cellulose nanocrystals (CNCs) and draw upon previous papermaking research to better understand the mechanisms involved. Additionally we analyze recent work that compares the adsorption of polyethylene glycol (PEG) to CNCs and fumed silica that provides further insight into this phenomenon. Our findings, along with current literature, suggest that hydrogen bonding does not significantly impact polymer adsorption in aqueous media despite reports to the contrary.

1. Introduction

The appetite for "green" materials and technologies is more apparent now than ever. Not only limited to public opinion, the push for sustainable practices is a major driving force for innovation in both academia and industry. The American Chemical Society's 12 Principles of Green Chemistry outline areas in which scientists and engineers can make steps towards earth-friendly technologies [1]. Of these principles, the use of renewable feedstocks is perhaps the most readily achievable.

Derived from the most abundant polymer on earth, nanocelluloses, including cellulose nanocrystals (CNCs), cellulose nanofibrils (CNFs) and bacterial cellulose (BC) are renewable and sustainable materials that have received growing interest over the last decade [2]. Originally investigated for their chiral nematic liquid crystalline properties, nanocelluloses are now studied as reinforcing agents, rheological modifiers, emulsion stabilizers, biological and electrical scaffolds and structured templates amongst others leading to a rapid increase in publications over the last two decades (Fig. 1a) [3,4]. Additionally, patents surrounding nanocelluloses have greatly increased (Fig. 1b) with many potential applications in foods, cosmetics, cements, biomedical devices, coatings and rigid polymer nanocomposites [5*]. Due to the hydrophilic nature of nanocelluloses, the most readily attainable applications will be aqueous based and will likely contain a complex mixture of polymers and surfactants [3]. As a result, thorough understanding of the interactions between water-soluble polymers and nanocellulose is critical for the development of these applications.

The field of nanocellulose research has the luxury of standing on nearly a century of papermaking know-how. Many of the findings regarding lignocellulosics and cellulose fiber behavior can be paralleled to CNCs and CNFs. This is largely not the case for materials such as carbon nanotubes, graphenes and metal nanoparticles, which are relatively recent discoveries. As we traverse the literature it is important to be mindful of decades-old research while being aware of potential new mechanisms, behaviors, and sophisticated measurement techniques. Herein we focus specifically on CNCs, as they are (relatively) short rigid colloids, which unlike CNFs and BC show no evidence of entanglement and their interactions in suspension are governed by DLVO theory.

First isolated from cotton cellulose via acid hydrolysis by Nickerson and Habrle [6] and imaged by Rånby and Ribi [7] CNCs have since

---

* Corresponding author.
E-mail address: ecranst@mcmaster.ca (E.D. Cranston).

http://dx.doi.org/10.1016/j.cocis.2017.03.005
1359-0294/© 2017 Elsevier Ltd. All rights reserved.

been produced from numerous cellulose sources including, woods, grasses, BC and tunicate, amongst others [8]. Typically, CNCs are extracted via strong acid hydrolysis, that selectively hydrolyzes amorphous regions of cellulose fibers yielding highly crystalline (>80% cellulose I) rod shaped particles which range from 50 to 3000 nm in length and 3–20 nm in cross section [9•]. Acid hydrolysis, additionally grafts anionic half ester groups (OSO_3^- or OPO_3^- depending on the acid) to the cellulose surface, which serve to electrostatically stabilize particles in aqueous environments. Recently, there has been a growing interest in developing more environmentally conscious CNC extraction methods using organic acids and hydrothermal processes. Chen et al. demonstrated that CNCs and CNFs can be produced via hydrolysis using dicarboxylic acids which can be efficiently recovered and recycled following nanocellulose production [10]. Additionally, the nanocelluloses produced showed improved thermal properties, in comparison to sulfuric acid extracted CNCs, and were colloidally stable resulting from grafted carboxyl groups on the CNC surface. Hydrothermal processes have been investigated with [11] and without [12] the use of acids and both methods exhibit improved thermal properties in comparison to sulfuric acid-extracted CNCs; however, colloidal stability is unclear as the CNCs remained uncharged by some production methods.

Traditionally, CNCs have been produced at the bench scale in academic laboratories but recently industrially produced CNCs have become more common making CNCs more commercially relevant [13, 14]. Currently, in North America sulfuric acid extracted CNCs are produced by CelluForce, InnoTech Alberta (formerly Alberta Innovates - Technology Futures) and the US Department of Agriculture Forest Products Labs (supplied by the University of Maine). In addition to acid hydrolyzed CNCs, Bluegoose Biorefineries, American Process Inc., Renmatix and others are currently producing CNCs and other nanocelluloses via less conventional methods [13].

2. CNCs with water-soluble polymers and hydrogen bonding

Some of the most likely applications of CNCs (and generally all nanocelluloses) will involve complex mixtures of polymers, and/or surfactants in various ionic strength aqueous environments. Indeed, numerous groups have incorporated CNCs into emulsions [15–17], hydrogels [18–20], cements [21,22], and wastewater treatments [23, 24]. For hydrophobic applications, research is aimed towards covalently modifying CNC surfaces to improve compatibility with non-polar polymers [25,26•]. Although significant and impressive progress has been made, surface modification of CNCs at the industrial scale has yet to be fully demonstrated suggesting that aqueous applications are closer to realization.

In aqueous environments, both polyelectrolytes and non-ionic polymers have been observed to adsorb to cellulose surfaces. Polyelectrolyte adsorption to cellulose is generally well understood with initial interaction between the oppositely charged groups of the polymer and the cellulose surface giving way to large entropic gains following the release of bound counter ions [27•]. These interactions lead to strong polymer adsorption which has been used to create flocculants [28] and polyelectrolyte multilayer films [29,30] with potential optical, sensor, biomedical and coatings applications. In contrast, the adsorption of non-ionic polymers to CNCs is less clear with numerous publications questioning the role of hydrogen bonding [31•,32••,33–37]. The adsorption of non-ionic polymers is particularly fascinating when considering polysaccharides and the wide variety of chemical and morphological structures available. Largely, all of these polymers have the capacity to form hydrogen bonding networks with CNCs yet literature shows a diverse set of behaviors.

The first work to investigate the interactions between non-ionic polysaccharides and CNCs was conducted in Derek Gray's group at McGill University, who studied the influence of dextran on the anisotropic phase separation of CNCs [38–40]. In their work, it was observed that dextran did not adsorb to the particle surface and had limited influence on dispersion behavior. However, upon the addition of anionic blue-dextran, CNC phase separation occurred at lower concentrations resulting from increased ionic strength and depletion effects.

More recently, it has been shown that some non-ionic polysaccharides do indeed adsorb to nanocellulose surfaces agreeing with previous observations of cellulose fibers and papermaking [41]. For example Villares et al. observed xyloglucan (XG), adsorption to spin coated CNC thin films via quartz crystal microbalance with dissipation (QCM-D) (Fig. 2a) [42]. Eronen et al. reported adsorption of polysaccharides including guar gum (GG) locust bean gum (LBG) and methylcellulose (MC) to CNF thin films [36]. Hu et al. observed that non-ionic polysaccharides adsorb to CNCs in dispersion and can lower the critical concentration for anisotropic gel formation [43]. The adsorption of hydroxypropyl guar (HPG), hydroxyethyl cellulose (HEC), and LBG, measured by QCM-D (Fig. 2b), dramatically increases the effective volume fraction of CNCs in suspension, shifting the equilibrium towards anisotropic phases. No gel formation was observed for CNC/dextran dispersions indicating no polymer absorption and agreeing with previous studies [38]. The varying adsorption behaviors of chemically similar polysaccharides suggest that there are subtle differences in their interactions with the cellulose surface and that the adsorption is not driven by the common ability to hydrogen bond.

In contrast to the work by Hu et al., Boluk et al. suggest from isothermal titration calorimetry (ITC) and rheological measurements that HEC

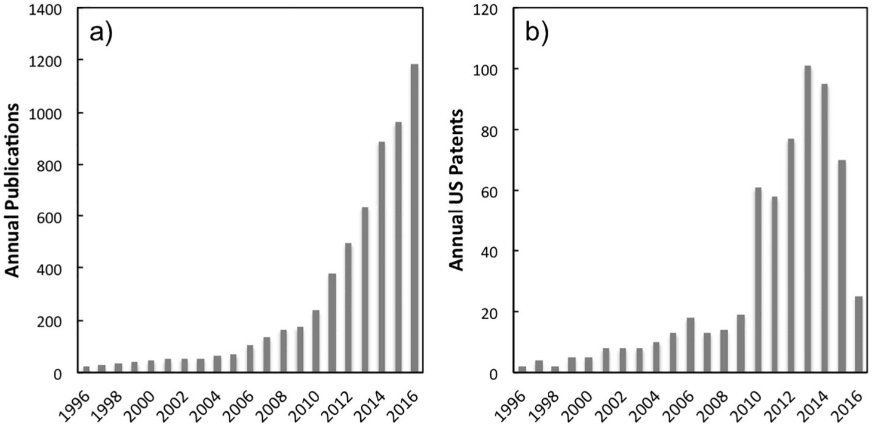

Fig. 1. Annual nanocellulose (a) publications and (b) US patent applications from 1996 to 2016. Publication and US patent claim search conducted using Web of Science and PatSnap databases, respectively, using terms: cellulose nanocrystals, cellulose whiskers, nanocrystalline cellulose, cellulose nanocrystal, nanocellulose, cellulose nanofibrils, cellulose nanofibers, nanofibrillated cellulose, cellulosic nanomaterials, cellulose nanomaterials, cellulose microfibrils, microfibrillated cellulose, nanofibrillated cellulose, bacterial nanocellulose.

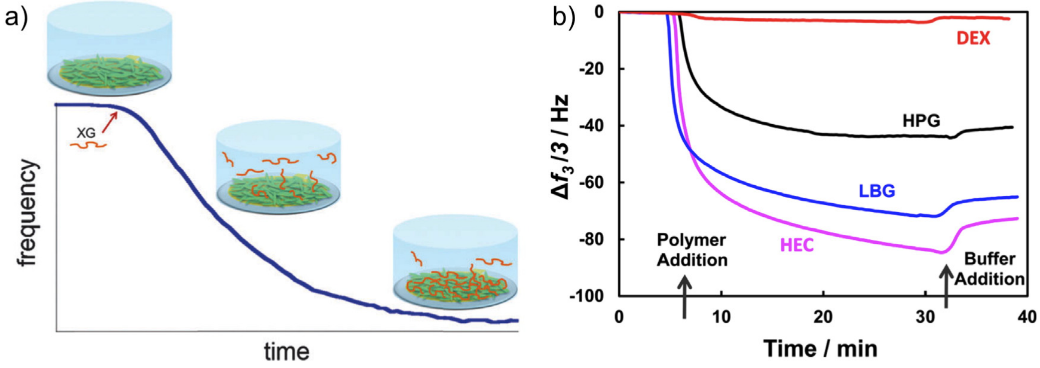

Fig. 2. (a) Illustrative representation of the frequency decrease upon the adsorption of xyloglucan (XG) to CNC thin films as measured by QCM-D. (Reproduced from Ref. [42] with permission from The Royal Society of Chemistry. (b) QCM-D frequency shift of the third overtone indicating adsorption of hydroxyethyl cellulose (HEC), locust bean gum (LBG), hydroxypropyl guar (HPG) to CNC thin films, whereas no adsorption was observed for dextran (DEX). Reprinted with permission from Ref. [43]. Copyright 2014 American Chemical Society.)

and carboxymethyl cellulose (CMC) in fact do not adsorb to cellulose surfaces (or at least no exothermic reaction occurs when CNCs and HEC or CMC are mixed) and any changes to CNC suspensions is a result of aggregation due to depletion effects [44]. This contradicts the conventional opinion in papermaking whereby CMC has long been used to improve paper strength, alter fiber texture and incorporate functional molecules through adsorption [45]. However analyzing experimental details, within the ITC experiments by Boluk et al. the polymer to cellulose ratio was an order of magnitude larger than Hu et al., and likely the polymer saturates the CNC surface masking small enthalpic or entropic changes that occur during the initial stages of adsorption. Evidence of surface saturation has been observed by Lopez et al. who explored adsorption of XG to CNCs via ITC at various concentrations [46]. High XG to cellulose ratios rapidly saturated the surface masking behavior in the early stages of adsorption.

Building upon this work, further experimental and computational studies have examined that XG adsorption to various cellulose surfaces including, CNCs, amorphous cellulose and regenerated cellulose II films [42,47–49]. Overall literature indicates that XG, with its comparatively more hydrophobic characteristics, does not adsorb through hydrogen bonding but is entropically driven by the release of structured water from the hemicellulose and co-crystallization at the cellulose surface [49].

The adsorption of polysaccharides is not only important for potential CNC applications but recent studies by Bouchard et al. show that oligosaccharides precipitate/adsorb to CNC surfaces during production [50•]. The presence of an oligosaccharide layer on the CNC surface affects both rheological and liquid crystal properties because the layer has the ability to swell and release counter ions [51,52]. Oligosaccharide deposition occurs in the water quenching step during the acid hydrolysis production of CNCs because the oligosaccharides are only soluble in concentrated acid and precipitate onto the CNC surface upon dilution. Adsorbed oligosaccharides byproducts have been measured to be as high as 12% of the total CNC mass [50•]. Understanding the mechanisms of interaction, whether it be hydrogen bonding, van der Waals, co-crystallization or hydrophobic effects is critical to the removal or control of these bound oligossacharides.

Although a significant amount of work has sought to understand non-ionic polymer adsorption by investigating polysaccharides, the diverse set of structures (e.g. branching) and hydrophilicities can make it difficult to isolate interactions and driving forces. As such, below we explore the adsorption of non-ionic, water soluble polymers by considering "simple" linear polymers, specifically polyethylene glycol (PEG) (also known as polyethylene oxide, PEO, $M_w > 20{,}000$ g/mol or polyoxyethylene), and compare them to thoroughly studied silica colloids with similar surface chemistry. We additionally explore recent evidence, which suggests that hydrogen bonding is not the dominant mechanism of non-ionic polymer adsorption to CNC surfaces.

3. PEG and CNCs

PEG, a linear water-soluble polymer, has an overwhelming number of commercial, pharmaceutical and industrial uses ranging from cosmetics, inks, lubricants and laxatives to dispersants, solvents and surfactants [53]. The good water solubility of PEG is due to the ether oxygen which accepts protons during hydrogen bonding, leading to a highly hydrated structure that has been measured to bind 1.6–3.3 water molecules per repeat unit, depending on molecular weight [54,55]. The relatively simple structure of PEG makes it an excellent model for investigating hydrogen bonding and polymer adsorption as no co-crystallization (as observed in polysaccharide adsorption [56]) is expected to occur. Moreover, with the wide range of aqueous uses, it is possible that PEG and CNCs will be incorporated into products or applications together making understanding of these interactions critical for development.

Recently, PEG/CNC interactions have been investigated in both rigid and flexible polymer nanocomposites, aqueous dispersions and on CNC model films [57–62]. In the cases where PEG is proposed to adsorb to CNC surfaces, much of the work cites hydrogen bonding as the primary mechanism of interaction. Xu et al. incorporated CNCs into high molecular weight PEG (10^6 g/mol) nanocomposites by both solvent casting [58] and electrospinning [57] and observed improved mechanical properties compared to the homopolymer similar to Changsarn et al. [62]. Fourier transform infrared (FTIR) spectroscopy of the dried nanocomposites showed changes to both CH_2 rocking and C–O–C stretching frequencies, typical of hydrogen bonding, suggesting strong interactions between CNCs and PEG – again noting that these experiments were for solid composites in the absence of water.

In the dispersed state, Cheng et al. demonstrated that incorporating PEG ($M_w = 400$–$10{,}000$ g/mol) can improve the re-dispersibility of CNCs following freeze drying [59]. They suggest that PEG adsorbs to the CNC surface in the aqueous phase via hydrogen bonding forming a structure similar to polymer brushes. Upon drying, the polymer brushes serve to sterically limit CNC/CNC interactions thus improving the re-dispersibility [59]. Similarly, PEG adsorption to CNCs in water was inferred by Bardet et al. who monitored polymer adsorption to thin in situ prepared CNC films via quartz crystal microbalance with dissipation (QCM-D) [60]. Within their study films (a monolayer ca. 7 nm thick) were prepared by flowing a CNC suspension over a cationic polymer-coated gold sensors from which a PEG ($M_w = 200$ g/mol) solution was introduced and allowed to adsorb to the CNC surface. Following adsorption, the films were rinsed with water leaving irreversibly bound polymer to the CNC film [60]. In a more recent study, Oguzlu and Boluk propose that PEO ($M_w = 100{,}000–600{,}000$ g/mol) adsorbs to CNC in dispersion, as evidenced by electrophoretic mobility and polarized optical microscopy measurements [61]. Despite this work supporting PEG adsorption to cellulose, below we examine experimental data and literature examples that contradict these findings and provide further insight into non-ionic polymer adsorption.

The study of PEG/CNC interactions has not been limited to PEG homopolymers; adsorption of PEG triblock copolymers [63,64] and polymers with PEG pendant (or brush) groups have also been investigated [18]. The adsorption of amphiphilic polymers to CNC surfaces is believed to occur not because of PEG adsorption but via hydrophobic effects in which the hydrophobic portion of the polymer adsorbs to the CNC surface to limit water interaction [63]. More specifically, because of the amphiphilic nature of CNCs [31•] the adsorption is expected to occur along the hydrophobic <100> face (or edge) of the CNC particles [65]. Additionally, not only does the PEG portion of the polymer not interact with the CNC, it sterically limits the binding of the hydrophobic component. Evidence of this is can be seen in the work by De France et al. in which increasing the length of the PEG pendant group (and thus hydrogen bonding capacity) does not improve adsorption but in fact reduces the interaction by sterically hindering the adsorption of the hydrophobic polymer backbone [18].

We emphasize caution when attempting to draw general conclusions about adsorption of PEG, specifically hydrogen bonding of PEG, as it is critical to consider the environment surrounding the substrate and its surface chemistry. In the case of using CNCs as the substrate, it is vital to make the distinction between the dry and wet state. For example, only in a state void of competitive water hydrogen bonding, as observed in the composites produced by Xu et al., is hydrogen bonding between PEG and CNCs likely [57,58]. As water is removed during drying, hydrogen bonding between the CNC surface hydroxyl groups and the ether oxygen of the PEG will occur. This is different from the mechanism proposed by Cheng et al. in which hydrogen bonding between PEG and CNCs is proposed to lead to polymer adsorption in aqueous media [59]. Considering previous papermaking research by Pelton et al. [66], Lindström et al. [67,68], and more recently Qasaimeh et al. [69,70] we do not expect PEG to adsorb to CNC surfaces. In these published works, high molecular weight PEG ($>10^5$ g/mol) along with phenolic cofactors are used as retention aids to flocculate fines (small cellulosic fibers, and other additives) in the papermaking process. Critically, it has been observed that PEG or cofactors alone do not absorb to cellulose fibers and are ineffective as retention aids. Only upon the addition of both components does significant flocculation occur. In the cases in which PEG alone has been used as a flocculant, two mechanisms have been proposed; depletion flocculation [66] and PEG adsorption to phenolic lignin residues [68]. Although the mechanism of flocculation is debated [69], and beyond the scope of this work, these reports clearly show that PEG does not adsorb to the surface of cellulose in the presence of water. As a result, we propose that the adsorption/interaction suggested by Cheng et al. only occurs during the freeze drying step, not in aqueous media.

The adsorption of PEG to CNC thin films observed by Bardet et al. is less clear, since no drying steps were involved. However, considering the porous "open" nature of the CNC thin films in water, it is possible that the PEG is interacting with the cationic polyethylenimine (PEI) adlayer, which is underneath the CNC film [60]. Specifically, the pK_a of the primary, secondary and tertiary amines in the PEI (p$K_a = 6.0–8.2$) is similar to silanols can may lead to potential interactions with the ether oxygen of the PEG [71].

Considering the recent publication by Oguzlu and Boluk [61] who propose that PEO adsorbs to CNC surfaces in dispersion, we suggest that their results can be explained by CNC aggregation caused by depletion effects. In their work, they report that reduced particle diffusion constants and electrophoretic mobility are the result of PEO adsorption, which additionally reduces spherulite size in concentrated PEO solutions. However, drawing from previous papermaking studies we suggest that particle aggregation (likely from depletion) increases apparent particle size and reduces the particle mobility. Moreover, transmission electron microscopy shows no statistical change in particle size and early stages of polymer addition measured by nuclear magnetic resonance spectroscopy (NMR) support depletion effects in the presence of PEO. As a result we propose that the inferred increase in particle size is due to depletion effects similar to those previously reported studies [66,69,70] and not the result of polymer adsorption.

4. PEG and silica particles

Silica particles have numerous industrial and pharmaceutical applications including paints, coatings, drug delivery, catalyst supports and reinforcing agents in composite materials [72]. The use and study of silica particles is a tremendously active field with a breadth of research that is beyond the scope of this work. We point readers to the recent review by Hyde et al. [73•] who discuss, the synthesis, application and current industrial standing of silica particles in various forms. Herein we focus specifically on fumed silica properties and behavior that directly relate to CNCs and non-ionic polymer adsorption. Although silica particles have been long used in papermaking [28] and more recently with nanocellulose in composite materials [74] to our knowledge only two studies have directly compared silica particles to CNCs [75,76]. Because of the similar surface chemistry (high density of hydroxyl groups) (Fig. 3) we believe valuable insight can be gained by comparing these systems.

Silica particles can be produced by either liquid or pyrogenic methods with the former holding the majority share of the global market. Liquid processes include precipitated silica, Ströber synthesis and microemulsion synthesis. Particles produced via liquid methods can form a range of structures from discrete spherical particles to complex 3D porous networks [73•]. Pyrogenic or rather fumed silica, first developed in the 1940s, is produced via a flame aerosol process that generates primary silica subparticles (<10 nm), which sinter together to form a 3D fractal aggregate structure, which ranges from 100 to 200 nm in diameter [73•]. Regardless of the production method, silica particles are decorated with surface hydroxyl groups, or silanols, which are critical for post treatment (i.e., silane modification), polymer adsorption and water dispersibility [77•]. Although the density of silanol groups varies across the wide set of silica particles produced, silica serves as an excellent starting point to compare to CNCs.

The adsorption of PEG (or more often PEO) to silica is well understood and is of continuing interest for many composite [78,79] and drug delivery [80–82] applications. First reported by Rubio and Kitchener in 1976, silanols at the particle surface hydrogen bond to the ether oxygen of the PEG leading to polymer adsorption [77•]. Since this pivotal work, Mathur and Moudgil have greatly refined the understanding of the mechanism, which is now thought of as an acid–base reaction yielding strong specific hydrogen bonds at the particle surface [83••]. Specifically, PEG adsorption occurs as the ether oxygen, a Lewis base, and the surface silanol, a Brønsted acid, form strong hydrogen bonds. Comparing adsorption to other inorganic oxides such as TiO_2, MoO_3 and V_2O_5, Mathur and Moudgil highlight that the acidity of the surface hydroxyl is critical for PEG adsorption [83••]. In aqueous media, PEG preferentially hydrogen bonds to surface silanol groups rather than water leading to rapid irreversible adsorption [84–86]. In a series of papers that investigate the structure of adsorbed polymers by small angle X-ray scattering, neutron scattering and NMR, Kim and Zukoski show that PEG forms a 1–2 nm layer of immobilized, "glassy" polymer on the particle surface regardless of molecular weight or temperature [87,88••,89]. Moreover, adsorption has been demonstrated to be extremely rapid, with complete coverage occurring in less than 10 s for a range of PEG molecular weights [90]. Although, silica rigidly binds only a 1–2 nm layer of PEG, the surface is rapidly saturated leaving dangling polymer chains, which can increase the apparent size of the silica particle. For example,

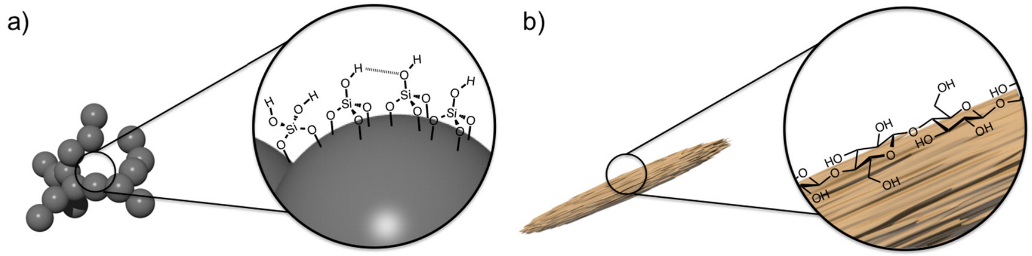

c)

	Adsorbed Mass (mg/m^2)			
	Fumed silica		CNC	
Molar mass (g/mol)	1000 ppm	10 000 ppm	1000 ppm	10 000 ppm
300	0.0 ± 0.1	0.1 ± 0.1	-0.1 ± 0.4	0.2 ± 0.1
1000	0.0 ± 0.1	-0.2 ± 0.3	0.1 ± 0.3	0.2 ± 0.3
6000	1.2 ± 0.6	1.2 ± 0.2	0.2 ± 0.5	0.1 ± 0.2
10 000	1.4 ± 0.3	1.1 ± 0.7	0.1 ± 0.1	-0.2 ± 0.3

Fig. 3. Schematic representation of (a) fumed silica and (b) cellulose nanocrystal particles with high density of surface hydroxyl groups and (c) final adsorbed amounts of PEG on model silica and CNC surfaces, measured by QCM-D after 100 min adsorption and rinsing (data reproduced from Ref. [76]).

Van Heiningen measured a layer thickness > 15 nm for 560,000 g/mol PEG [90]. Critically, above the molecular weight of entanglement of PEG ($M_e = 3000$ g/mol) dangling polymer chains can bridge between particles, creating large network-like structures [88••]. The strong PEG adsorption has been show to improve compatibility in composite applications and greatly impact rheological behavior [91–94].

5. CNCs vs. silica

Because the adsorption of PEG via hydrogen bonding is dependent on the acidity of the surface hydroxyl groups, the differences between cellulose and silica can be understood by a simple comparison of the pK_a values of their respective surface groups. Silanol groups have been measured to have a pK_a of 4.5–8.5 depending on Si coordination [95] whereas glucose is significantly higher with a pK_a of 12.3 [96]. Although the pK_a of CNC hydroxyl groups has not been specifically measured we expect the value to range from 12 to 13, which is common for most sugars. Nonetheless, this is a significant difference, particularly when considering hydrogen bonding that occurs between a Brønsted acid and a Lewis base. Further differences in acidity are observed when considering the vibrational frequency shifts that occur during hydrogen bonding of diethyl ethers to silanols and alcohols [97]. Silanol band shifts are nearly twice as large as alcohols suggesting the acidity of silanols are significantly greater than alcohols. Moreover, because cellulose and water have similar pK_a's we do not expect a significant drive for polymer adsorption in aqueous environments. By these considerations it is not surprising that PEG does not adsorb to macroscopic cellulose fibers. Yet adsorption deduced by Cheng et al. [59], Bardet et al. [60] and Oguzlu and Boluk [61] could perhaps be attributed to the nanoscale dimensions of CNCs, their hydrophobic "edge" interactions, their high crystallinity, or the presence of charged sulfate half ester groups on the particle surface.

5.1. Recent evidence

In recently submitted work, our group explored PEG adsorption to CNCs in direct comparison to fumed silica particles using a variety of techniques to provide further insight into non-ionic polymer adsorption [76]. Adsorption behavior was studied over a range of PEG molecular weights (M_w = 300–10,000 g/mol) and concentrations (100–10,000 ppm). PEG adsorption to particle thin films was investigated using QCM-D and adsorption to particles in dispersion was probed via dynamic light scattering (DLS), isothermal titration calorimetry (ITC) and rheology. For thin films specifically, although the mass increased in the presence of PEG solutions, similar to Bardet et al. [60], the apparent adsorption is attributed to PEG penetrating porous swollen CNC films [98,99], because the subsequent rinsing completely removed all bound PEG from the surface. In contrast, silica films rapidly and irreversibly adsorbed PEG in densities comparable to previously reported studies [100]. Total amounts of PEG adsorbed to CNCs and fumed silica after rinsing (measured using QCM-D) are presented in Fig. 3c. Similar trends were observed via ITC, in which the addition of PEG to fumed silica dispersions was exothermic, suggesting strong hydrogen bonding between fumed silica and PEG. No exothermic or endothermic processes were measured following the addition of PEG to CNC dispersions, indicating that no significant physical or chemical interactions occur between the two components. As such, the results of our work suggest that in aqueous media PEG does not adsorb to CNC surfaces and CNC/PEG hydrogen bonds are not present to any significant degree. Moreover, the nanoscale dimensions and presence of surface anionic groups appear to have little impact on CNC/PEG behavior as our results agree with previous papermaking studies [66,69,70]. Overall this work supports the recent opinion that hydrogen bonding is not a driving mechanism for non-ionic polymer adsorption.

6. Summary

For the successful development of nanocellulose products and applications we require a thorough understanding of particle-polymer and particle-surfactant interactions. In aqueous media, polyelectrolyte and ionic surfactant adsorption to cellulose is well documented however, non-ionic polymer adsorption remains challenging to decipher. Examination of the nanocellulose literature reveals competing theories, however there is an increasing opinion that adsorption is not driven by hydrogen bond formation but by the entropically favored release of structured water from hydrated surfaces. This does not preclude hydrogen bonding from occurring once polymers are adsorbed on a surface but suggests that the enthalpic drive is small or nonexistent during the adsorption process.

We further examined the role of hydrogen bonding by analyzing CNC interactions with PEG, as a model polymer, which is known to have a high hydrogen bonding capacity. Moreover we propose that comparing nanocellulose interactions to the well-understood hydrogen bonding interactions between PEG and silica can serve as an excellent platform in which to investigate non-ionic polymer adsorption. Examination of the surface chemistry shows that the hydroxyl groups on cellulose surfaces are not acidic enough to form hydrogen bonds with the ether oxygen in PEG in the presence of water. Moreover, particle size analysis, nanogravimetric analysis, rheological measurements and isothermal titration calorimetry reveal that PEG does not adsorb to CNCs in any significant amounts. This agrees with conventional “pulp and paper wisdom” and highlights the tremendous wealth of information in the nearly century's worth of work that forms the foundation of nanocellulose understanding. In summary, we emphasize that in order to use nanocelluloses in aqueous applications we must have a firm understanding of particle-polymer interactions. Moreover, it is critical to be conscious of a particle's environment as competing effects can have a significant impact on polymer adsorption and behavior.

Acknowledgements

Funding from the Natural Sciences and Engineering Research Council of Canada, Industrial Postgraduate Scholarship program sponsored by Cabot Corporation is gratefully acknowledged. We additionally acknowledge Cabot Corporation for their donation of CAB-O-SIL® M-5 fumed silica. Professors R. Pelton, A. Guarne, R. Epand and J. Moran-Mirabal are thanked for sharing equipment to characterize CNCs. Additionally, the Biointerfaces Institute and the Brockhouse Institute for Materials Research at McMaster University are acknowledged for support and equipment.

References and recommended reading•,••

[1] American Chemical Society. ACS Green Chemistry Insitute® 2016. https://www.acs.org/content/acs/en/greenchemistry.html. (accessed October 11, 2016).

[2] Mariano M, El Kissi N, Dufresne A. Cellulose nanocrystals and related nanocomposites: review of some properties and challenges. J Polym Sci Part B Polym Phys 2014;52:791–806. http://dx.doi.org/10.1002/polb.23490.

[3] Salas C, Nypelö T, Rodriguez-Abreu C, Carrillo C, Rojas OJ. Nanocellulose properties and applications in colloids and interfaces. Curr Opin Colloid Interface Sci 2014;19:383–96. http://dx.doi.org/10.1016/j.cocis.2014.10.003.

[4] Zhu H, Luo W, Ciesielski PN, Fang Z, Zhu JY, Henriksson G, et al. Wood-derived materials for green electronics, biological devices, and energy applications. Chem Rev 2016;116:9305–74. http://dx.doi.org/10.1021/acs.chemrev.6b00225.

[5•] Charreau H, Foresti ML, Vazquez A. Nanocellulose patents trends: a comprehensive review on patents on cellulose nanocrystals, microfibrillated and bacterial cellulose. Recent Pat Nanotechnol 2013;7:56–80. http://dx.doi.org/10.2174/1872210511307010056.

[6] Nickerson RF, Habrle JA. Cellulose intercrystalline structure. Ind Eng Chem 1947;39:1507–12. http://dx.doi.org/10.1021/ie50455a024.

[7] Ranby B, Ribi E. Uber den Feinbau Zellulose. Experientia 1950;6:12–4.

[8] Klemm D, Kramer F, Moritz S, Lindström T, Ankerfors M, Gray DG, et al. Nanocelluloses: a new family of nature-based materials. Angew Chem Int Ed 2011;50:5438–66. http://dx.doi.org/10.1002/anie.201001273.

[9•] Moon RJ, Martini A, Nairn J, Simonsen J, Youngblood J. Cellulose nanomaterials review: structure, properties and nanocomposites. Chem Soc Rev 2011;40:3941–94. http://dx.doi.org/10.1039/c0cs00108b.

[10] Chen L, Zhu JY, Baez C, Kitin P, Elder T. Highly thermal-stable and functional cellulose nanocrystals and nanofibrils produced using fully recyclable organic acids. Green Chem 2016;18:3835–43. http://dx.doi.org/10.1039/C6GC00687F.

[11] Yu H, Qin Z, Liang B, Liu N, Zhou Z, Chen L. Facile extraction of thermally stable cellulose nanocrystals with a high yield of 93% through hydrochloric acid hydrolysis under hydrothermal conditions. J Mater Chem A Mater Energy Sustain 2013;1:3938–44. http://dx.doi.org/10.1039/c3ta01150j.

[12] Novo LP, Bras J, García A, Belgacem N, Curvelo AADS. A study of the production of cellulose nanocrystals through subcritical water hydrolysis. Ind Crop Prod 2016;93:88–95. http://dx.doi.org/10.1016/j.indcrop.2016.01.012.

[13] Reid MS, Villalobos M, Cranston ED. Benchmarking cellulose nanocrystals: from the laboratory to industrial production. Langmuir 2016. http://dx.doi.org/10.1021/acs.langmuir.6b03765 [acs.langmuir.6b03765].

[14] Future Markets Inc. The global market for Nanocellulose to 2020; 2013.

[15] Kalashnikova I, Bizot H, Cathala B, Capron I. Modulation of cellulose nanocrystals amphiphilic properties to stabilize oil/water interface. Biomacromolecules 2012;13:267–75. http://dx.doi.org/10.1021/bm201599j.

[16] Kalashnikova I, Bizot H, Bertoncini P, Cathala B, Capron I. Cellulosic nanorods of various aspect ratios for oil in water pickering emulsions. Soft Matter 2013;9:952. http://dx.doi.org/10.1039/c2sm26472b.

[17] Cherhal F, Cousin F, Capron I. Influence of charge density and ionic strength on the aggregation process of cellulose nanocrystals in aqueous suspension, as revealed by small-angle neutron scattering. Langmuir 2015;31:5596–602. http://dx.doi.org/10.1021/acs.langmuir.5b00851.

[18] De France KJ, Chan KJW, Cranston ED, Hoare T. Enhanced mechanical properties in cellulose nanocrystal–poly(oligoethylene glycol methacrylate) injectable nanocomposite hydrogels through control of physical and chemical cross-linking. Biomacromolecules 2016;17:649–60. http://dx.doi.org/10.1021/acs.biomac.5b01598.

[19] Yang X, Bakaic E, Hoare T, Cranston ED. Injectable polysaccharide hydrogels reinforced with cellulose nanocrystals: morphology, rheology, degradation, and cytotoxicity. Biomacromolecules 2013;14:4447–55. http://dx.doi.org/10.1021/bm401364z.

[20] Kelly JA, Shukaliak AM, Cheung CCY, Shopsowitz KE, Hamad WY, MacLachlan MJ. Responsive photonic hydrogels based on nanocrystalline cellulose. Angew Chem Int Ed 2013;52:8912–6. http://dx.doi.org/10.1002/anie.201302687.

[21] Cao Y, Zavattieri P, Youngblood J, Moon R, Weiss J. The relationship between cellulose nanocrystal dispersion and strength. Construct Build Mater 2016;119:71–9. http://dx.doi.org/10.1016/j.conbuildmat.2016.03.077.

[22] Cao Y, Tian N, Bahr D, Zavattieri PD, Youngblood J, Moon RJ, et al. The influence of cellulose nanocrystals on the microstructure of cement paste. Cem Concr Compos 2016;74:164–73. http://dx.doi.org/10.1016/j.cemconcomp.2016.09.008.

[23] Kan KHM, Li J, Wijesekera K, Cranston ED. Polymer-grafted cellulose nanocrystals as pH-responsive reversible flocculants. Biomacromolecules 2013;14:3130–9. http://dx.doi.org/10.1021/bm400752k.

[24] Batmaz R, Mohammed N, Zaman M, Minhas G, Berry RM, Tam KC. Cellulose nanocrystals as promising adsorbents for the removal of cationic dyes. Cellulose 2014;21:1655–65. http://dx.doi.org/10.1007/s10570-014-0168-8.

[25] Oksman K, Aitomäki Y, Mathew AP, Siqueira G, Zhou Q, Butylina S, et al. Review of the recent developments in cellulose nanocomposite processing. Compos Part A Appl Sci Manuf 2016;83:2–18. http://dx.doi.org/10.1016/j.compositesa.2015.10.041.

[26•] Habibi Y. Key advances in the chemical modification of nanocelluloses. Chem Soc Rev 2014;43:1519–42. http://dx.doi.org/10.1039/c3cs60204d.

[27•] Wågberg L. Polyelectrolyte adsorption onto cellulose fibres. Nord Pulp Pap Res J 2009;15:147–72. http://dx.doi.org/10.1515/9783110213447.

[28] Hubbe MA, Nanko H, McNeal MR. Retention aid polymer interactions with cellulosic surfaces and suspensions: a review. BioResources 2009;4:850–906.

[29] Martin C, Jean B. Nanocellulose/polymer multilayered thin films: tunable architectures towards tailored physical properties. Nord Pulp Pap Res J 2014;29:19–30.

[30] Cranston ED, Gray DG. Polyelectrolyte multilayer films containing cellulose: a review. In: Roman M, editor. Model Cellul. Surfaces. ACS Symp. Ser.Washington, DC: ACS Publishing; 2010. p. 95–114. http://dx.doi.org/10.1021/bk-2009-1019.ch004.

[31•] Lindman B, Karlström G, Stigsson L. On the mechanism of dissolution of cellulose. J Mol Liq 2010;156:76–81. http://dx.doi.org/10.1016/j.molliq.2010.04.016.

[32••] Medronho B, Romano A, Miguel MG, Stigsson L, Lindman B. Rationalizing cellulose (in)solubility: reviewing basic physicochemical aspects and role of hydrophobic interactions. Cellulose 2012;19:581–7. http://dx.doi.org/10.1007/s10570-011-9644-6.

[33] Glasser WG, Atalla RH, Blackwell J, Malcolm Brown R, Burchard W, French AD, et al. About the structure of cellulose: debating the Lindman hypothesis. Cellulose 2012;19:589–98. http://dx.doi.org/10.1007/s10570-012-9691-7.

[34] Peri S, Muthukumar L, Nazmul Karim M, Khare R. Dynamics of cello-oligosaccharides on a cellulose crystal surface. Cellulose 2012;19:1791–806. http://dx.doi.org/10.1007/s10570-012-9771-8.

[35] Sundman O. Adsorption of four non-ionic cellulose derivatives on cellulose model surfaces. Cellulose 2014;21:115–24. http://dx.doi.org/10.1007/s10570-013-0105-2.

[36] Eronen P, Junka K, Laine J, Österberg M. Interaction between water-soluble polysaccharides and native nanofibrillar cellulose thin films. BioResources 2011;6:4200–17.

[37] Umemura M, Yuguchi Y, Hirotsu T. Hydration at glycosidic linkages of malto- and cello-oligosaccharides in aqueous solution from molecular dynamics simulation: effect of conformational flexibility. J Mol Struct THEOCHEM 2005;730:1–8. http://dx.doi.org/10.1016/j.theochem.2005.05.034.

[38] Edgar CD, Gray DG. Influence of dextran on the phase behavior of suspensions of cellulose nanocrystals. Macromolecules 2002;35:7400–6. http://dx.doi.org/10.1021/ma0204195.

[39] Beck-Candanedo S, Viet D, Gray DG. Induced phase separation in low-ionic-strength cellulose nanocrystal suspensions containing high-molecular-weight blue dextrans. Langmuir 2006;22:8690–5. http://dx.doi.org/10.1021/la061310j.

[40] Beck-Candanedo S, Viet D, Gray DG. Induced phase separation in cellulose nanocrystal suspensions containing ionic dye species. Cellulose 2006;13:629–35. http://dx.doi.org/10.1007/s10570-006-9084-x.

[41] Biermann CJ. Stock preparation and additives for papermaking. Handb. Pulping Papermak. Second. Elsevier / Academic Press; 1996. p. 190–208. http://dx.doi.org/10.1016/B978-012097362-0/50012-1.

[42] Villares A, Moreau C, Dammak A, Capron I, Cathala B. Kinetic aspects of the adsorption of xyloglucan onto cellulose nanocrystals. Soft Matter 2015;11:6472–81. http://dx.doi.org/10.1039/C5SM01413A.

[43] Hu Z, Cranston ED, Ng R, Pelton R. Tuning cellulose nanocrystal gelation with polysaccharides and surfactants. Langmuir 2014;30:2684–92. http://dx.doi.org/10.1021/la404977t.

[44] Boluk Y, Zhao L, Incani V. Dispersions of nanocrystalline cellulose in aqueous polymer solutions: structure formation of colloidal rods. Langmuir 2012;28:6114–23. http://dx.doi.org/10.1021/la2035449.

[45] Kargl R, Mohan T, Bračič M, Kulterer M, Doliška A, Stana-Kleinschek K, et al. Adsorption of carboxymethyl cellulose on polymer surfaces: evidence of a specific interaction with cellulose. Langmuir 2012;28:11440–7. http://dx.doi.org/10.1021/la302110a.

[46] Lopez M, Bizot H, Chambat G, Marais M, Zykwinska A, Ralet M, et al. Enthalpic studies of xyloglucan—cellulose interactions. Biomacromolecules 2010;11:1417–28. http://dx.doi.org/10.1021/bm1002762.

[47] Zhao Z, Crespi VH, Kubicki JD, Cosgrove DJ, Zhong L. Molecular dynamics simulation study of xyloglucan adsorption on cellulose surfaces: effects of surface hydrophobicity and side-chain variation. Cellulose 2014;21:1025–39. http://dx.doi.org/10.1007/s10570-013-0041-1.

[48] Zhang Q, Brumer H, Ågren H, Tu Y. The adsorption of xyloglucan on cellulose: effects of explicit water and side chain variation. Carbohydr Res 2011;346:2595–602. http://dx.doi.org/10.1016/j.carres.2011.09.007.

[49] Benselfelt T, Cranston ED, Ondaral S, Johansson E, Brumer H, Rutland MW, et al. Adsorption of xyloglucan onto cellulose surfaces of different morphologies: an entropy-driven process. Biomacromolecules 2016;17:2801–11. http://dx.doi.org/10.1021/acs.biomac.6b00561.

• Of special interest.

•• Of outstanding interest.

[50] Bouchard J, Méthot M, Fraschini C, Beck S. Effect of oligosaccharide deposition on the surface of cellulose nanocrystals as a function of acid hydrolysis temperature. Cellulose 2016. http://dx.doi.org/10.1007/s10570-016-1036-5.

[51] Beck S, Bouchard J, Berry R. Controlling the reflection wavelength of iridescent solid films of nanocrystalline cellulose. Biomacromolecules 2011;12:167–72. http://dx.doi.org/10.1021/bm1010905.

[52] Shafiei-Sabet S, Hamad WY, Hatzikiriakos SG. Rheology of nanocrystalline cellulose aqueous suspensions. Langmuir 2012;28:17124–33. http://dx.doi.org/10.1021/la303380v.

[53] Knop K, Hoogenboom R, Fischer D, Schubert US. Poly(ethylene glycol) in drug delivery: pros and cons as well as potential alternatives. Angew Chem Int Ed 2010;49:6288–308. http://dx.doi.org/10.1002/anie.200902672.

[54] Graham NB, Zulfiqar M, Chemistry A. Interaction of poly (ethylene oxide) with solvents: 2. Water-poly(ethylene glycol). Polymer (Guildf) 1988;30:528–33.

[55] Huang L, Nishinari K. Interaction between poly(ethylene glycol) and water as studied by differential scanning calorimetry. J Polym Sci Part B Polym Phys 2001;39:496–506. http://dx.doi.org/10.1002/1099-0488(20010301)39:5<496::AID-POLB1023>3.0.CO;2-H.

[56] Laine J, Lindström T, Glad-Nordmark G, Risinger G. Studies on topochemical modification of cellulosic fibres. Part 1. Chemical conditions for the attachment of carboxymethyl cellulose onto fibres. Nord Pulp Pap Res J 2000;15:520–6. http://dx.doi.org/10.3183/NPPRJ-2000-15-05-p520-526.

[57] Xu X, Wang H, Jiang L, Wang X, Payne SA, Zhu JY, et al. Comparison between cellulose nanocrystal and cellulose nanofibril reinforced poly(ethylene oxide) nanofibers and their novel shish-kebab-like crystalline structures. Macromolecules 2014;47:3409–16. http://dx.doi.org/10.1021/ma402627j.

[58] Xu X, Liu F, Jiang L, Zhu JY, Haagenson D, Wiesenborn DP. Cellulose nanocrystals vs. cellulose nanofibrils: a comparative study on their microstructures and effects as polymer reinforcing agents. ACS Appl Mater Interfaces 2013;5:2999–3009. http://dx.doi.org/10.1021/am302624t.

[59] Cheng D, Wen Y, Wang L, An X, Zhu X, Ni Y. Adsorption of polyethylene glycol (PEG) onto cellulose nano-crystals to improve its dispersity. Carbohydr Polym 2015;123:157–63. http://dx.doi.org/10.1016/j.carbpol.2015.01.035.

[60] Bardet R, Belgacem N, Bras J. Flexibility and color monitoring of cellulose nanocrystal iridescent solid films using anionic or neutral polymers. ACS Appl Mater Interfaces 2015;7:4010–8. http://dx.doi.org/10.1021/am506786t.

[61] Oguzlu H, Boluk Y. Interactions between cellulose nanocrystals and anionic and neutral polymers in aqueous solutions. Cellulose 2016:1–16. http://dx.doi.org/10.1007/s10570-016-1096-6.

[62] Changsarn S, Mendez JD, Shanmuganathan K, Foster EJ, Weder C, Supaphol P. Biologically inspired hierarchical design of nanocomposites based on poly(ethylene oxide) and cellulose nanofibers. Macromol Rapid Commun 2011;32:1367–72. http://dx.doi.org/10.1002/marc.201100183.

[63] Holappa S, Kontturi KS, Salminen A, Seppälä J, Laine J. Adsorption of hydrophobically end-capped poly(ethylene glycol) on cellulose. Langmuir 2013;29:13750–9. http://dx.doi.org/10.1021/la402494m.

[64] Li Y, Liu H, Song J, Rojas OJ, Hinestroza JP. Adsorption and association of a symmetric PEO-PPO-PEO triblock copolymer on polypropylene, polyethylene, and cellulose surfaces. ACS Appl Mater Interfaces 2011;3:2349–57. http://dx.doi.org/10.1021/am200264r.

[65] Mazeau K, Rivet A. Wetting the (110) and (100) surfaces of Iβ cellulose studied by molecular dynamics. Biomacromolecules 2008;9:1352–4. http://dx.doi.org/10.1021/bm7013872.

[66] Pelton RH, Allen LH, Nuget HM. Additives for increased retention and pitch control in paper manufacture. US 4,313,790, 1982.

[67] Lindström T, Glad-Nordmark G. Flocculation of latex and cellulose dispersions by means of transient polymer networks. Colloids Surf 1984;8:337–51. http://dx.doi.org/10.1016/0166-6622(84)80128-6.

[68] Lindström T, Glad-Nordmark G. Selective adsorption, flocculation, and fractionation of wood pulps with polyethyleneoxide. J Colloid Interface Sci 1983;94:404–11. http://dx.doi.org/10.1016/0021-9797(83)90280-1.

[69] Abdallah Qasaimeh MR. Causes of transient flocculation of fines with polyethylene oxide and a cofactor: implications for mill performance. Colloids Surf A Physicochem Eng Asp 2011;386:125–30. http://dx.doi.org/10.1016/j.colsurfa.2011.07.008.

[70] Qasaimeh MRA, Qasaimeh A, Hani FB. Factors affecting fines flocculation performance with cofactor-polyethylene oxide. Adv Chem Eng Sci 2014;4:49–55. http://dx.doi.org/10.4236/aces.2014.41007.

[71] Utsuno K, Uludağ H. Thermodynamics of polyethylenimine-DNA binding and DNA condensation. Biophys J 2010;99:201–7. http://dx.doi.org/10.1016/j.bpj.2010.04.016.

[72] Cabot Corporation. Hydrophilic fumed silica. http://www.cabotcorp.com/solutions/products-plus/fumed-metal-oxides/hydrophilic; 2016. [accessed October 11, 2016].

[73] Hyde EDER, Seyfaee A, Neville F, Moreno-Atanasio R. Colloidal silica particle synthesis and future industrial manufacturing pathways: a review. Ind Eng Chem Res 2016;55:8891–913. http://dx.doi.org/10.1021/acs.iecr.6b01839.

[74] Asadi A, Miller M, Sultana S, Moon RJ, Kalaitzidou K. Introducing cellulose nanocrystals in sheet molding compounds (SMC). Compos Part A Appl Sci Manuf 2016;88:206–15. http://dx.doi.org/10.1016/j.compositesa.2016.05.033.

[75] Villalpando-Páez F, Nguyen L, Abitbol T, Komarov A, Prevo BG, Corwin J, et al. Comparison of nanocrystalline cellulose and fumed silica in latex coatings. Green Mater 2014;2:206–21. http://dx.doi.org/10.1680/gmat.14.00017.

[76] Reid MS, Marway HS, Moran-Hidalgo C, Villalobos M, Cranston ED. Will it stick? Polyethylene glycol adsorption to fumed silica versus nanocellulose. Soft Matter 2017 [Submitted SM-ART-02-2017-000283].

[77] Rubio J, Kitchener J. The mechanism of adsorption of poly(ethylene oxide) flocculant on silica. J Colloid Interface Sci 1976;57:132–42. http://dx.doi.org/10.1016/0021-9797(76)90182-X.

[78] Lin D, Liu W, Liu Y, Lee HR, Hsu P, Liu K, et al. High ionic conductivity of composite solid polymer electrolyte via in situ synthesis of monodispersed SiO_2 Nanospheres in poly(ethylene oxide). Nano Lett 2016;16:459–65. http://dx.doi.org/10.1021/acs.nanolett.5b04117.

[79] Qiao XG, Dugas P-Y, Charleux B, Lansalot M, Bourgeat-Lami E. Synthesis of multipod-like silica/polymer latex particles via nitroxide-mediated polymerization-induced self-assembly of amphiphilic block copolymers. Macromolecules 2015;48:545–56. http://dx.doi.org/10.1021/ma5019473.

[80] Ma K, Zhang D, Cong Y, Wiesner U. Elucidating the mechanism of silica nanoparticle PEGylation processes using fluorescence correlation spectroscopies. Chem Mater 2016;28:1537–45. http://dx.doi.org/10.1021/acs.chemmater.6b00030.

[81] Bouchoucha M, C.-Gaudreault R, Fortin M, Kleitz F. Mesoporous silica nanoparticles: selective surface functionalization for optimal relaxometric and drug loading performances. Adv Funct Mater 2014;24:5911–23. http://dx.doi.org/10.1002/adfm.201400524.

[82] Han N, Zhao Q, Wan L, Wang Y, Gao Y, Wang P, et al. Hybrid lipid-capped mesoporous silica for stimuli-Responsive drug release and overcoming multidrug resistance. ACS Appl Mater Interfaces 2015;7:3342–51. http://dx.doi.org/10.1021/am5082793.

[83] Mathur S, Moudgil BM. Adsorption mechanism(s) of poly(ethylene oxide) on oxide surfaces. J Colloid Interface Sci 1997;196:92–8. http://dx.doi.org/10.1006/jcis.1997.5192.

[84] Voronin EF, Gun'ko VM, Guzenko NV, Pakhlov EM, Nosach LV, Leboda R, et al. Interaction of poly(ethylene oxide) with fumed silica. J Colloid Interface Sci 2004;279:326–40. http://dx.doi.org/10.1016/j.jcis.2004.06.073.

[85] Derkaoui N, Said S, Grohens Y, Olier R, Privat M. Polyethylene glycol adsorption on silica: from bulk phase behavior to surface phase diagram. Langmuir 2007;23:6631–7. http://dx.doi.org/10.1021/la070199u.

[86] Klonos P, Pissis P, Gun'ko VM, Kyritsis A, Guzenko NV, Pakhlov EM, et al. Interaction of poly(ethylene glycol) with fumed silica and alumina/silica/titania. Colloids Surf A Physicochem Eng Asp 2010;360:220–31. http://dx.doi.org/10.1016/j.colsurfa.2010.03.002.

[87] Kim SY, Schweizer KS, Zukoski CF. Multiscale structure, interfacial cohesion, adsorbed layers, and thermodynamics in dense polymer-nanoparticle mixtures. Phys Rev Lett 2011;107:225504. http://dx.doi.org/10.1103/PhysRevLett.107.225504.

[88] Kim SY, Meyer HW, Saalwächter K, Zukoski CF. Polymer dynamics in PEG-silica nanocomposites: effects of polymer molecular weight, temperature and solvent dilution. Macromolecules 2012;45:4225–37. http://dx.doi.org/10.1021/ma300439k.

[89] Kim SY, Hall LM, Schweizer KS, Zukoski CF. Long wavelength concentration fluctuations and cage scale ordering of nanoparticles in concentrated polymer solutions. Macromolecules 2010;43:10123–31. http://dx.doi.org/10.1021/ma1021677.

[90] Van Heiningen JA, Hill RJ. Poly(ethylene oxide) adsorption onto and desorption from silica microspheres: new insights from optical tweezers electrophoresis. Macromolecules 2011;44:8245–60. http://dx.doi.org/10.1021/ma2003486.

[91] Hasanzadeh M, Mottaghitalab V, Rezaei M. Rheological and viscoelastic behavior of concentrated colloidal suspensions of silica nanoparticles: a response surface methodology approach. Adv Powder Technol 2015;26:1570–7. http://dx.doi.org/10.1016/j.apt.2015.08.011.

[92] Khandavalli S, Rothstein JP. Extensional rheology of shear-thickening fumed silica nanoparticles dispersed in an aqueous polyethylene oxide solution. J Rheol (N Y N Y) 2014;58:411–31. http://dx.doi.org/10.1122/1.4864620.

[93] Raghavan SR, Walls HJ, Khan SA. Rheology of silica dispersions in organic liquids: new evidence for solvation forces dictated by hydrogen bonding. Langmuir 2000;16:7920–30. http://dx.doi.org/10.1021/la991548q.

[94] Zhang Q, Archer LA. Poly(ethylene oxide)/silica nanocomposites: structure and rheology. Langmuir 2002;18:10435–42. http://dx.doi.org/10.1021/la026338j.

[95] Leung K, Nielsen I, Criscenti L. Elucidating the bimodal acid–base behavior of the water–silica interface from first principles. J Am Chem Soc 2009;131:18358–65. http://dx.doi.org/10.1021/ja906190t.

[96] Bhattacharyya L, Rohrer JS, editors. Applications of ion chromatography for pharmaceutical and biological products. Hoboken, NJ, USA: John Wiley & Sons, Inc.; 2012. http://dx.doi.org/10.1002/9781118147009.

[97] West R, Baney RH. Hydrogen bonding studies. II. The acidity and basicity of silanols compared to alcohols. J Am Chem Soc 1959;81:6145–8. http://dx.doi.org/10.1021/ja01532a011.

[98] Reid MS, Villalobos M, Cranston ED. Cellulose nanocrystal interactions probed by thin film swelling to predict dispersibility. Nanoscale 2016;8:12247–57. http://dx.doi.org/10.1039/C6NR01737A.

[99] Niinivaara E, Faustini M, Tammelin T, Kontturi E. Water vapor uptake of ultrathin films of biologically derived nanocrystals: quantitative assessment with quartz crystal microbalance and spectroscopic ellipsometry. Langmuir 2015;31:12170–6. http://dx.doi.org/10.1021/acs.langmuir.5b01763.

[100] Madathingal RR, Wunder SL. Confinement effects of silica nanoparticles with radii smaller and larger than Rg of adsorbed poly(ethylene oxide). Macromolecules 2011;44:2873–82. http://dx.doi.org/10.1021/ma1021693.

Appendix 6: Chapter 6 Supporting Information

Comparison of polyethylene glycol adsorption to nanocellulose versus fumed silica in water
Reid, M. S.; Marway, H. S.; Moran-Hidalgo, C.; Villalobos, M.; Cranston, E. D.
Cellulose DOI: 10.1007/s10570-017-1482-8

Quartz Crystal Microbalance with Dissipation (QCM-D)

Fumed Silica

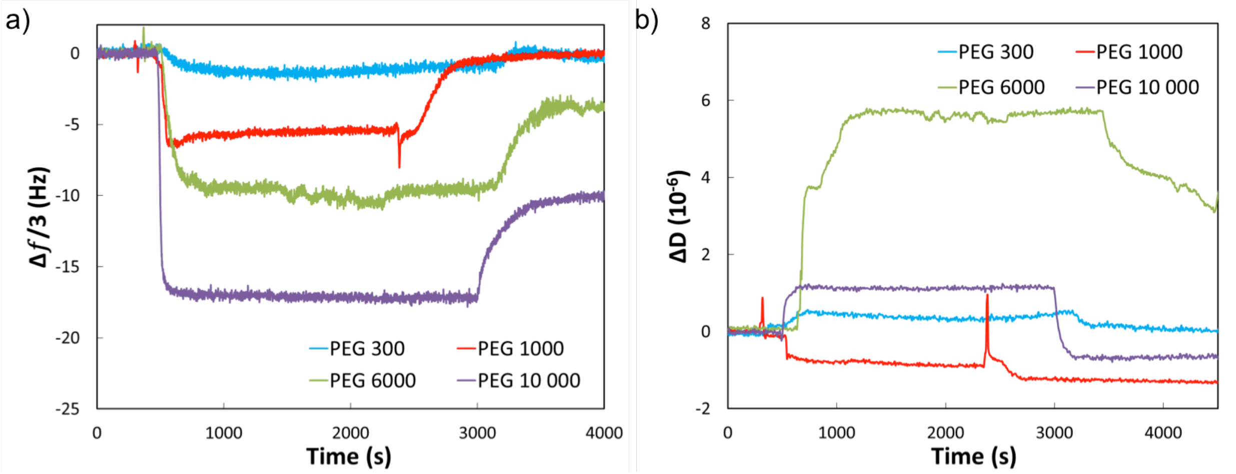

Fig. S1 QCM-D curves showing (a) frequency and (b) dissipation of PEG of various molecular weights at 1000 ppm on a fumed silica thin film

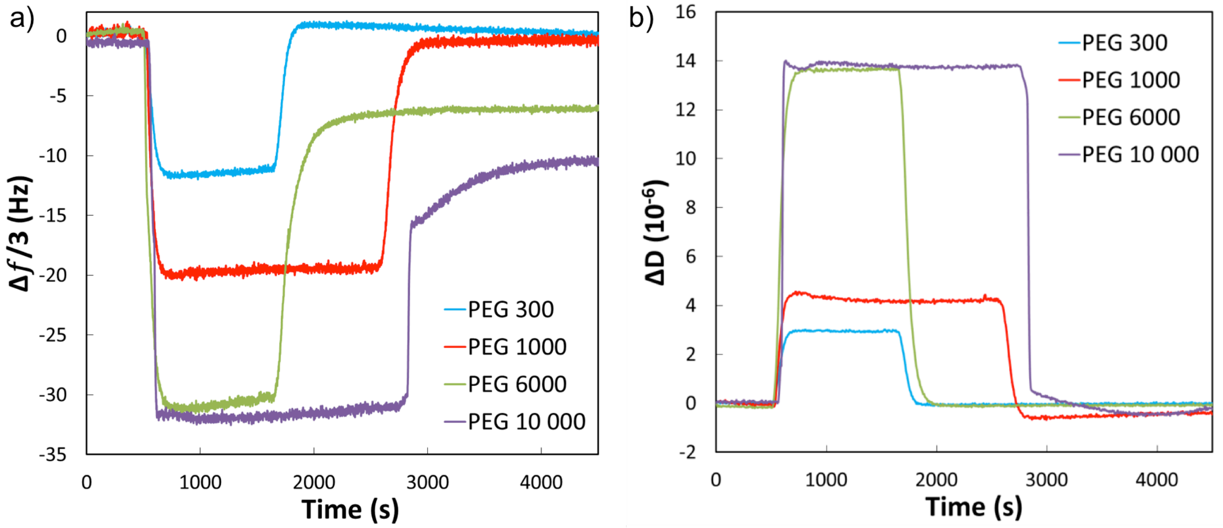

Fig. S2 QCM-D curves showing (a) frequency and (b) dissipation of PEG of various molecular weights at 10 000 ppm on a fumed silica thin film

Cellulose Nanocrystals

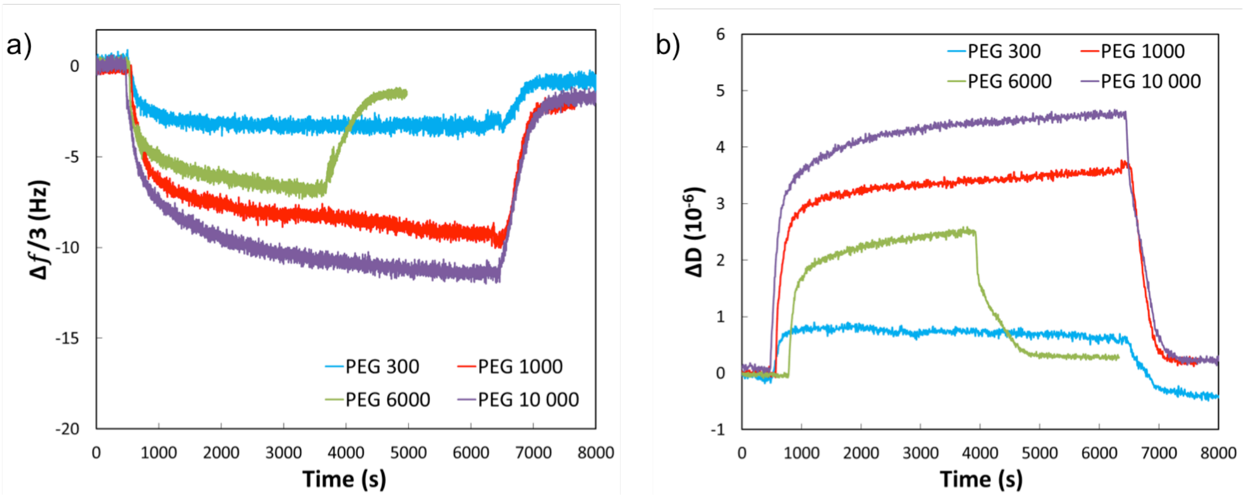

Fig. S3 QCM-D curves showing (a) frequency and (b) dissipation of PEG of various molecular weights at 1000 ppm on a CNC thin film

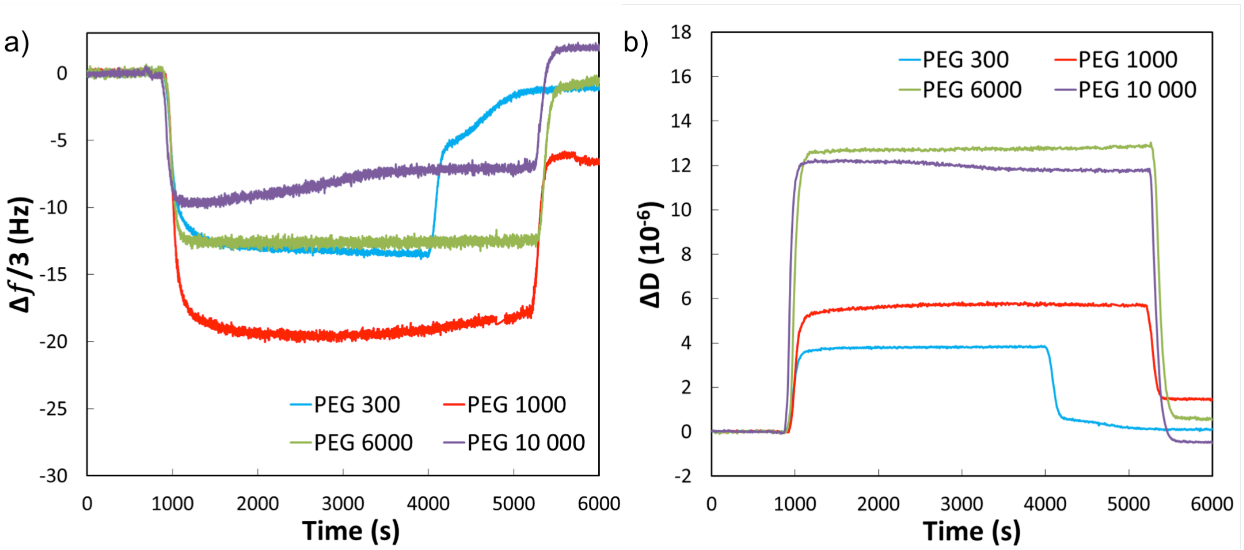

Figure S4: QCM-D curves showing (a) frequency and (b) dissipation of PEG of various molecular weights at 10 000 ppm on a CNC thin film.

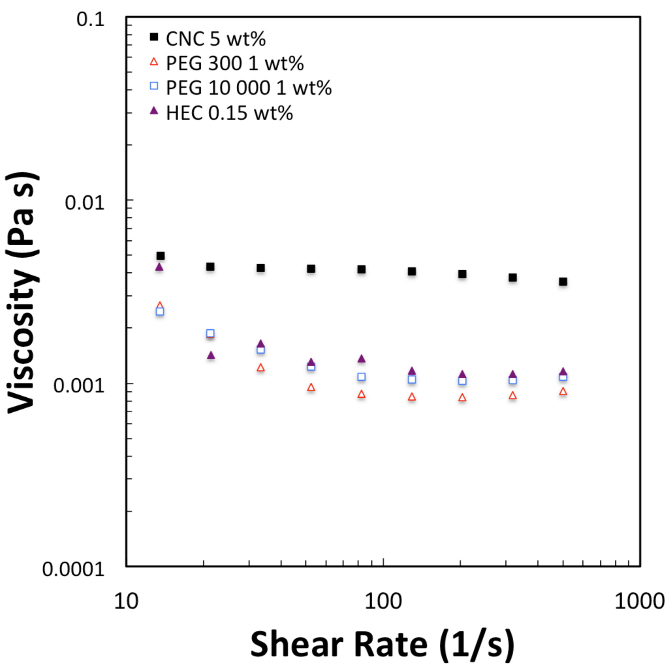

Fig. S5 Steady state shear viscosity as a function of shear rate for 5 wt% CNC dispersions, 0.15 wt% HEC, 1 wt% PEG 300 and 1 wt% PEG 10 000

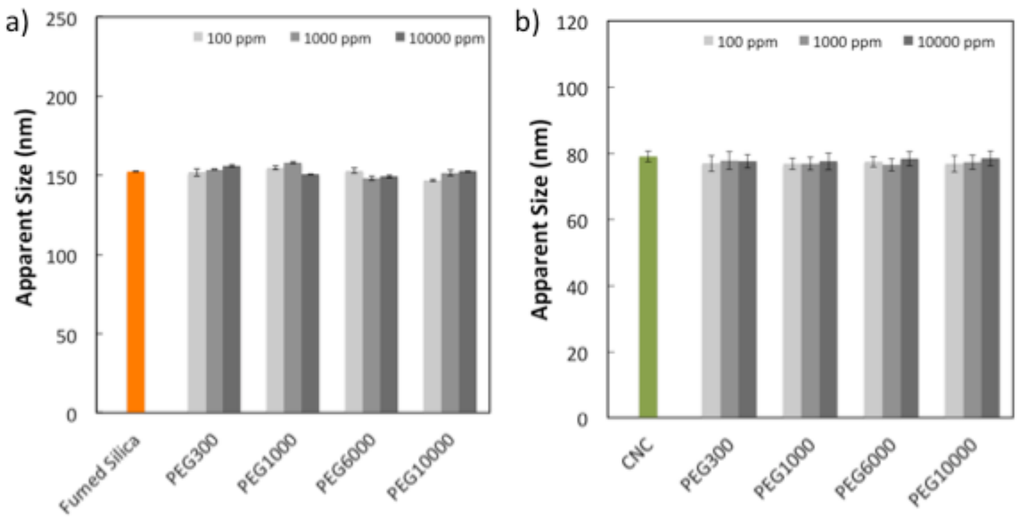

Fig. S6 Apparent particle size as measured by DLS for various PEG solutions containing (a) fumed silica and (b) CNCs

Chapter 7

Comparing Soft Semicrystalline Polymer Nanocomposites Reinforced with Cellulose Nanocrystals and Fumed Silica

As the final step this chapter combines the knowledge of particle-particle and particle-polymer interactions developed in the previous four research chapters to produce well-dispersed polymer composites. Polyethylene oxide polymer nanocomposites reinforced CNCs and fumed silica were prepared and particle dispersibility was linked to composite performance. Note that throughout this chapter polyethylene glycol is referred to as polyethylene oxide which is the conventional name used for polyethylene glycol of molecular weight greater than 20 000 g/mol. Although polyethylene oxide does not adsorb to CNCs in aqueous environments, polymer adsorption *does* occur in dry polymer nanocomposites where there are no competitive water hydrogen bonds. As a result CNC reinforced nanocomposites show good dispersion and improved mechanical properties. Comparison to fumed silica, demonstrates that polymer adsorption in the aqueous phase is not a prerequisite for good composite properties and it is the interruption of particle-particle interactions that has the most significant impact on composite dispersion and performance.

The data within this chapter have been collected by myself with the assistance of Taylor Stimpson who aided in composite preparation and thermomechanical testing. Dr. Bipasha Bose collected and analyzed nanoindentation data. Dr. Elina Niinivaara collected the transmission electron microscopy images. All other data collection and analysis was performed by myself. This chapter is currently being prepared for submission as an invited publication in the journal *Industrial & Engineering Chemistry Research*.

Comparing Soft Semicrystalline Polymer Nanocomposites Reinforced with Cellulose Nanocrystals and Fumed Silica

Michael S. Reid[1], Taylor C. Stimpson [1], Elina Niinivaara[1], Marco Villalobos[2] and Emily D. Cranston[1]*

[1]Department of Chemical Engineering, McMaster University

Hamilton, Ontario, Canada, L8S 4L8

[2]Cabot Corporation,

Billerica, MA, US, 01821

*Corresponding author: reidms@mcmaster.ca

Keywords: cellulose nanocrystals, fumed silica, nanocomposites, poly(ethylene oxide), dispersibility, mechanical testing, differential scanning calorimetry, “shish-kebob” morphology, particle-polymer interactions

Abstract

This work systematically compares solvent cast nanocomposites of poly(ethylene oxide) (PEO) reinforced with cellulose nanocrystals (CNCs) and fumed silica. Nanocomposite mechanical properties and crystallization behaviour were investigated as a function of polymer matrix molecular weight (10 000 – 100 000 g/mol) and filler particle loading (1 – 10 wt.%). Polymer adsorption to both CNC and fumed silica surfaces was found to alter the melting and crystallization temperature of PEO in the reinforced nanocomposites, as measured by differential scanning calorimetry. Moreover, polarized optical microscopy (POM) showed that both CNCs and fumed silica act as nucleation inhibitors by limiting polymer mobility in the molten phase. Atomic force microscopy revealed that PEO adsorption to CNC surfaces occurs is a shish-kebab like morphology that is readily incorporated into the crystalline domains as evidenced by a ca. 10 μm/s increase in spherulite growth rate. Analysis of CNC dispersion via transmission electron microscopy, demonstrated that good particle dispersion was achieved within the nanocomposites, however percolation was *not* observed despite CNCs being added in volumes greater than the percolation threshold. Nanoindentation showed an increase in the reduced modulus at 10 wt.% loading of CNCs and fumed silica however, both particles decreased mechanical properties (in comparison to the homopolymer) at lower loadings (1 – 7.5 wt.%). Tensile testing showed more than a 60 % improvement in the Young's modulus for both CNCs and fumed silica nanocomposites at 10 wt.% loading. The Halpin-Kardos and Guth-Gold micromechanical models were found to effectively describe the Young's modulus for CNC and fumed silica reinforced nanocomposites, respectively. Although focused specifically on hydrophilic polymer nanocomposites, this work provides new insight into the interactions that control nanocomposite dispersibility, crystallization and mechanical reinforcement that may be generalized to other polymer matrices.

Introduction

Despite the public desire for environmentally conscious products, to date there has yet to be any significant implementation of renewable nanoparticles as reinforcing agents. Indeed, the use of starch nanoparticles,[1] chitin whiskers,[2] and cellulose nanocrystals (CNCs)[3] has been largely restricted to academia. However, with the recent intensification of industrially produced material, sustainable nanoparticles are now widely available, greatly expanding the potential for commercial applications.[4] Yet a substantial obstacle remains in that nanoparticles often exhibit poor dispersibility within polymer matrices, resulting in aggregation and minimal improvement of composite properties.[5] As a result, for sustainable nanoparticles to move beyond just an academic curiosity, the forces and interactions that govern nanoparticle dispersibility must be thoroughly understood.

CNCs are renewably-sourced, high-aspect-ratio, rod-shaped particles composed of linear β 1−4 linked D-glucose units, and have been extracted from a number of higher order plants (i.e., woods, grasses, cotton, etc.), bacteria, algae, fungi and tunicates.[6] Depending on the cellulose source and extraction method, CNCs range from 50 to 3000 nm in length with cross sections of 3−20 nm. Furthermore, CNCs have been reported to have an elastic modulus between 56 and 220 GPa, making them ideal candidates for reinforcement applications.[7,8] Indeed, early demonstrations of CNC reinforced polymer latexes showed an increase in the shear modulus that spanned nearly three-orders magnitude.[9,10] Despite these early examples, compatibility within hydrophobic polymer matrices has proven to be a challenge. Several groups have explored surface modification to improve dispersibility[11] however, despite notable improvements, surface modification adds additional steps making scalability more difficult.

Although CNCs have an environmental advantage, for them to make a measurable impact in the global market they must offer comparable or superior performance compared to more conventional nano reinforcing agents such as carbon black, clays, and silica. As a result, because of the hydrophilic nature of CNCs, the most readily achievable applications will be aqueous based/processed, incorporating water-soluble/hydrophilic polymers.

Poly(ethylene oxide) (PEO), also known as poly(ethylene glycol) (PEG) or poly(oxyethylene), is a linear water soluble, non-ionic polymer that is used in countless applications ranging from polyelectrolyte supports[12] to cosmetics and anti-fouling coatings.[13] Because of its availability, PEO-particle interactions have been thoroughly studied for a variety of applications. For example, it is well know that that hydrogen bonding between the ether oxygen of PEO and surface silanols of silica particles leads to strong polymer adsorption in aqueous environments.[14–16] As a result, numerous works have demonstrated excellent control of both rheological and mechanical properties of PEO/silica composites.[17–20]

Similarly PEO/cellulose interactions have been investigated. High molecular weight PEO ($>10^6$ g/mol) has been used along with phenolic cofactors as flocculating agents of cellulose fines in papermaking processes.[21,22] Notably, without cofactors, no polymer adsorption is observed indicating that PEO does not adsorb to cellulose surfaces in water. Our group similarly demonstrated that despite the abundance of hydroxyl groups, PEO does not hydrogen bond to CNC surfaces in aqueous conditions, either as thin films or dispersed particles.[23] Although no adsorption is observed in aqueous conditions, several groups have prepared PEO/CNC composites with improved mechanical properties.[24–28] While PEO's use as a rigid polymer composite is limited, it can serve as an excellent model that can be studied to understand fundamental particle-polymer interactions and their impact on CNC dispersibility and mechanical performance.

Previous work by Samir *et al.* demonstrated that composites of tunicate CNCs and high molecular weight PEO (5×10^6 g/mol) had a percolated network that improved mechanical properties at high temperatures.[24] Moreover, the incorporation of CNCs did not impact ion mobility when composites were used as polymer electrolyte supports.[25,26] More recently, reinforced PEO thin films[27] and electrospun fibers[28,29] have been shown to have improved mechanical properties with the incorporation of CNCs or cellulose nanofibrils (CNF). Modeling the mechanical properties of thin films demonstrated that despite the high loading of CNCs (10 wt.%), a percolated network was not achieved and the Halpin-Kardos model most effectively described composite properties.[27] In contrast, composites containing longer CNFs particles (ca. 1 μm in length) percolated the nanocomposite and the mechanical properties could be fit to the percolation-based Ouali model.[27]

Despite these examples, there has yet to be any significant investigation that directly compares CNCs to more conventional fillers under the same processing conditions. It is well known that preparation methods (solvent casting, melt mixing or in situ polymerization) as well as processing conditions (temperature, shear, etc.) can have a significant impact on composite properties.[30] For example, solvent cast CNC composites, typically show good dispersion as particle-particle interactions can be interrupted and particle spacing can be maintained prior to solidification.[30] In contrast, melt mixed CNC composites often exhibit high degrees of aggregation and poor thermomechanical properties (because CNCs are added in the agglomerated dry state and never properly disperse).[5] Recently, solvent cast composites have been used to create master batches for melt processed composites whereby CNCs are dispersed in solvent and cast to create a high filler density master batch with good particle dispersion.[31] Addition of the master batch to melt extruded composites significantly improves dispersion and thermal stability in comparison to dry particle addition.

Herein we investigate reinforced PEO nanocomposites as a model system to further develop and apply our understanding of particle-particle and particle-polymer interactions and their relation to dispersibility and composite performance. This work explores the effect of polymer molecular weight and filler loading within PEO composites reinforced with CNCs and fumed silica. Analysis of the melting and crystallization behavior showed that both CNCs and fumed silica act as nucleation inhibitors by adsorbing PEO to the particle surface. Composite mechanical properties, obtained by Instron tensile testing and nano indentation, were found to directly relate to particle dispersion. Overall, this work provides new insight into the interactions that govern particle dispersibility and reinforcement in rigid polymer nanocomposites from which a variety of new CNC-based products can be developed.

Experimental

Materials. Poly(ethylene oxide) (PEO) M_w = 10 000 g/mol (PEO10), M_w = 35 000 g/mol (PEO35), and M_w = 100 000 g/mol (PEO100), were purchased from Sigma Aldrich (Oakville, ON, Canada). CAB-O-SIL® M-5 and TS-385 fumed silica were received from Cabot Corporation (Billerica, MA). Cellulose nanocrystals were generously provided by CelluForce (Windsor, QC). All chemicals were used as received. All water used was purified Type I water with a resistivity of 18.2 MΩ·cm (Barnstead Gen Pure Pro system, ThermoScientific, Asheville, NC).

Composite Preparation. All composites were prepared via solvent casting from aqueous suspensions. Typically, 30 g of PEO was dissolved in 200 mL of water for 8 hours under constant magnetic stirring. Similarly, CNCs and fumed silica were dispersed and thoroughly mixed for a minimum of 8 hours. Particle suspensions were then sonicated (Sonifier 450, Branson Ultrasonics, Danbury, CT) at 60% amplitude for 30 s, twice. 100 mL particle suspensions of the appropriate weight percentage were added to PEO solutions and allowed to mix for a minimum of 8 hours. Samples were then dried at 80˚C for 36 hours from which composites were further dried in a vacuum oven at 90˚C for a minimum of 5 hours.

Differential Scanning Calorimetry (DSC). Samples of 3–5 mg were weighed into TZero Hermetic sealed aluminum pans (TA Instruments; New Castle, DE) from which DSC measurements were conducted using a Q200 Differential Scanning Calorimeter (TA Instruments; New Castle, DE). Measurements were performed under a nitrogen gas purge of 50 mL/min following a heat/cool/heat cycle from 10 – 100˚C with a heating and cooling rate of 10˚C/min. Melting and crystallization temperatures were taken as the maximum and minimum peak values of the DSC curve.

Polarized Optical Microscopy (POM). POM images were collected using a Nikon Eclipse LV100POL microscope with a 530 nm phase retardation plate. With the retardation plate, isotropic regions appear as dark violet and ordered phases appear as either blue or yellow, with the difference being a 90˚ in-plane rotation. Samples were prepared by melting PEO nanocomposites on a glass slide with a cover slip at 85˚C for 5 min. Molten samples were immediately place on the microscope stage and allowed to cool/crystallize under nonisothermal conditions. Spherulite growth rates were determined by capturing video following crystal nucleation. Spherulite diameter was measured every 2 s over a 30 s period. The average growth rate is presented with one standard deviation from the mean.

Atomic Force Microscopy (AFM). AFM images were collected using an Asylum MFP-3D instrument (Asylum Research, an Oxford Instrument Company, Santa Barbara, CA) in alternating current (AC) mode under ambient conditions. Surfaces were prepared by hot pressing composites against silicon wafers (See *Instron Tensile Testing* for hot pressing details). Surfaces were imaged using rectangular FMR cantilevers (NanoWorld) with normal spring constants of 1.2−5.5 N/m and resonant frequencies of 60−90 kHz. Images were processed in Igor Pro 6.0 running Asylum Research AFM software (version 13.17) using a second-order flatten routine

Transmission Electron Microscopy (TEM). TEM images were collected using a JEM-1200EX TEM (JEOL Ltd., Japan) at an acceleration voltage of 80 kV. Hot pressed PEO35 nanocomposites were microtomed under ambient conditions. PEO100 nanocomposites were cryomicrotomed at -80˚C using a Leica EM FC7 microtome. 100 nm thick sections were mounted on to Formvar-coated copper TEM grids with no further processing.

Instron Tensile Testing. Tensile testing was performed following the ASTM D3039 standard for polymer matrix composite materials. Rectangular moulded bars were prepared by hot pressing pelletized solvent-cast PEO composites at 85°C. Samples were initially allowed to melt for 10 min followed by 2 min under pressure from which the pressure is released to rid the sample of gas bubbles, followed by a further 5 min under pressure. The rectangular samples had final dimensions of ca. 2 mm × 10 mm × 40 mm. Tensile tests were performed by an Instron 3366 in Tensile Test mode, using a crosshead speed of 1 mm/min with a load cell of 500 kN at a sampling rate of 10 points/s. The sample was mounted with a constant gap length of 11 mm. The average Young's modulus is taken from a minimum of five measurements and one standard deviation from the mean is presented as the error interval.

Nanoindentation. Nanoindentation measurements were performed using a Micro Materials NanoTest indentation testing platform (Micro Materials Ltd., Wrexham, UK) with a diamond Berkovich indenter. Samples were prepared by hot pressing samples against a silicon wafer. A minimum of 8 indents were performed on each sample, 50 µm apart under a maximum load of 10 mN with 10 s loading and unloading times under ambient conditions. The average reduced modulus and hardness were determined using NanoTest software are presented with one standard deviation from the mean.

Results and Discussion

Melting and Crystallization Behaviour. The thermal and crystallization behaviour of PEO nanocomposites, of varying molecular weights (10 000, 35 000, and 100 000 g/mol), reinforced with CNCs and fumed silica (1-10 wt. % loading) was assessed by differential scanning calorimetry (DSC) and polarized optical microscopy (POM). Table 1 displays the melting temperatures (T_m) and the crystallization temperatures (T_c) of PEO nanocomposites after solvent casting as measured by DSC. (See Supporting Information Figure S1 for representative DSC curves.) For all PEO molecular weights analyzed, incorporation of both CNCs and fumed silica increased the melting temperature of the nanocomposite. Previous works have reported both an increase[28] and a decrease[26,27] of PEO melting temperature in the presence of CNCs. Interestingly both the rise and reduction of T_m has been attributed to strong interactions between PEO and CNCs. In the case of reduced melting temperatures, strong particle-polymer interactions in the molten state inhibit chain mobility and suppress crystal formation, resulting in a lower T_m of the composite.[26,27] In contrast, an increase in melting temperature has been attributed to strong polymer adsorption at the particle surface that limits polymer mobility during heating, in addition to the growth of larger spherulites, which require higher temperatures/more energy to reach the molten state.[28]

Comparing the CNC nanocomposites to those prepared with fumed silica we observe similar changes in the melting temperature (Table 1). As a result, this suggests that the increase in melting temperature is the due to strong polymer adsorption to both particle types in the dry nanocomposite. Further evidence of polymer adsorption to CNC surfaces is observed by FTIR (Supporting Information Figure S2) where OH stretching peaks at 3287 cm^{-1} and 3332 cm^{-1} are shifted to 3306 cm^{-1} and 3345 cm^{-1}, respectively, indicating that PEO hydrogen bonds to CNC surfaces when competitive water hydrogen bonds are not available, as previously reported by Xu *et al*.[28]

Considering the T_c and specific heat of crystallization (ΔH_c) of both CNC and fumed silica filled nanocomposites, it is less clear how the incorporation of particles impacts crystallization. For example, silica reduces the crystallization temperature of PEO10, suggesting that particles act as nucleation inhibitors (i.e., reducing the number of spherulites).[24] Whereas for PEG35, fumed silica initially increases the crystallization temperature, acting as a nucleating agent,[32] followed by a reduction of T_c at 10 wt.% loading. Similarly CNC/PEO nanocomposites exhibit varying crystallization temperatures with molecular weight and particle loading (Table 1). While XRD indicates that no new/alternate crystal phases occur within the filled nanocomposites (See Supporting Information Figure S3) the inclusion of reinforcing agents clearly impacts the crystallization of PEO.

The change in crystallization can be further seen by considering the undercooling ($\Delta T_{uc} = T_m - T_c$) of both CNC and fumed silica reinforced nanocomposites (Figure 1).[33] For CNC/PEO10 and CNC/PEO35 nanocomposites, the undercooling increases until a plateau at between 3.5 and 7.5 wt.% loading, from which ΔT_{uc} decreases for PEO10, suggesting that particle-polymer interaction/adsorption has been reduced. The reduction at higher loading is potentially due to CNC aggregation resulting in less interfacial area and fewer particle-polymer interactions. For CNC/PEO100 nanocomposites, the ΔT_{uc} remains relatively constant, indicating that CNCs do not have a significant impact on the crystallization of PEO100. In contrast, the undercooling of fumed silica/PEO nanocomposites increased with particle loading for all molecular weights examined. This is consistent with the well-known strong polymer adsorption observed in both aqueous environments and polymer melts and suggests that adsorption occurs regardless of the PEO molecular weight[15] or the state of aggregation within in the nanocomposite.

Table 1. Melting and crystallization temperatures (˚C) and specific heat of crystallization (ΔH_c) of CNC and fumed silica reinforced PEO composites as measured by DSC.

		CNC			Fumed Silica	
Filler Content (wt. %)	T_m	T_c	ΔH_c (J/g)	T_m	T_c	ΔH_c (J/g)
PEO10						
0	61.7	39.0	184	61.7	39.0	184
1	64.1	35.0	192	62.6	36.5	180
3.5	68.8	35.0	184	62.8	35.6	185
7.5	68.8	31.3	186	62.6	36.8	168
10	61.2	35.1	178	66.4	33.2	132
PEO35						
0	64.2	39.2	172	64.2	39.2	163
1	68.0	39.1	165	65.3	40.9	175
3.5	68.0	32.8	152	66.9	41.1	175
7.5	64.8	34.0	173	68.0	37.6	175
10	67.3	34.1	154	70.1	32.9	175
PEO100						
0	62.5	42.4	159	62.5	42.4	159
1	61.7	39.7	195	64.3	44.2	151
3.5	62.0	38.7	165	65.2	43.5	157
7.5	64.3	41.1	159	66.9	42.9	154
10	66.4	41.0	167	67.6	40.4	159

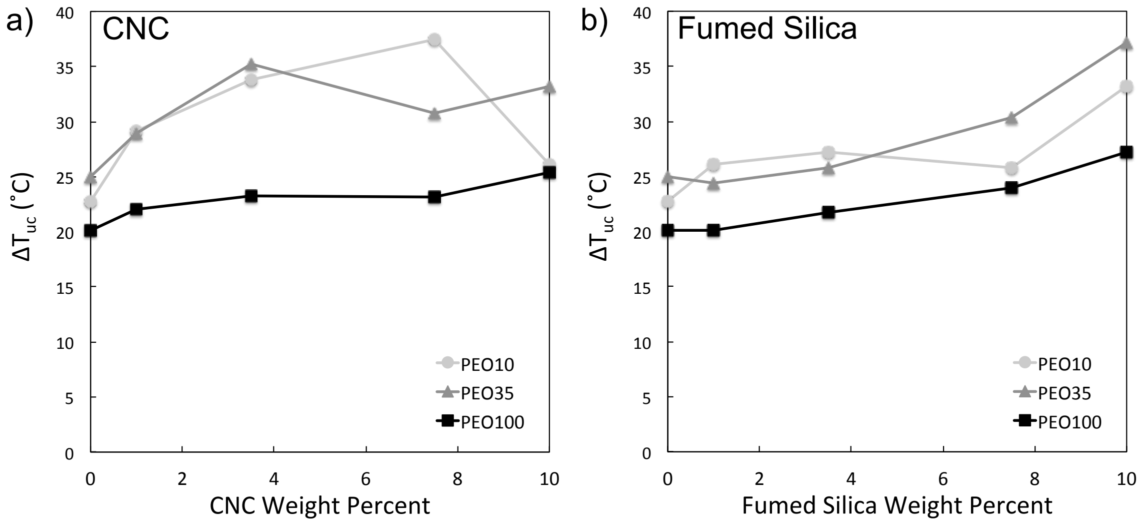

Figure 1. The undercooling ($\Delta T_{uc} = T_m - T_c$) of PEO composites reinforced with a) CNCs and b) fumed silica.

The crystallization and order within the PEO nanocomposites was further examined by POM. Figure 2 shows POM images of PEO10 homopolymer and filled nanocomposites after heating at 85˚C for 5 min, where isotropic phases are observed as the dark violet regions. Note PEO35 and PEO100 nanocomposites remained highly viscous above the melting temperature of PEO in agreement with previous work by Samir *et al.*[24] As a result PEO35 and PEO100 nanocomposites could not be prepared thin enough for optical microscopy analysis. Figure 2 shows that in the molten state, PEO10 homopolymer is uniformly isotropic, indicating that no crystalline domains remain after heating. Similarly, no significant anisotropy was observed for fumed silica nanocomposites (only 10 wt.% loading shown) as expected, as particles are approximately spherical and thus are not birefringent. In contrast, CNC filled nanocomposites showed a high degree of anisotropy as evidenced by the blue, red and yellow regions within Figure 2. As particle loading increases, so does the level of order within the composites where, 7.5 wt.% and 10 wt.% loadings are completely anisotropic. While it is unclear whether, PEO is "trapped" within the anisotropic regions, the fact that ordered CNC structures remain within molten polymer indicates that once CNCs are incorporated particle mobility is limited. This suggests that particle dispersion cannot be significantly altered once the nanocomposite has been cast and highlights the need to interrupt particle-particle interactions prior to composite solidification.

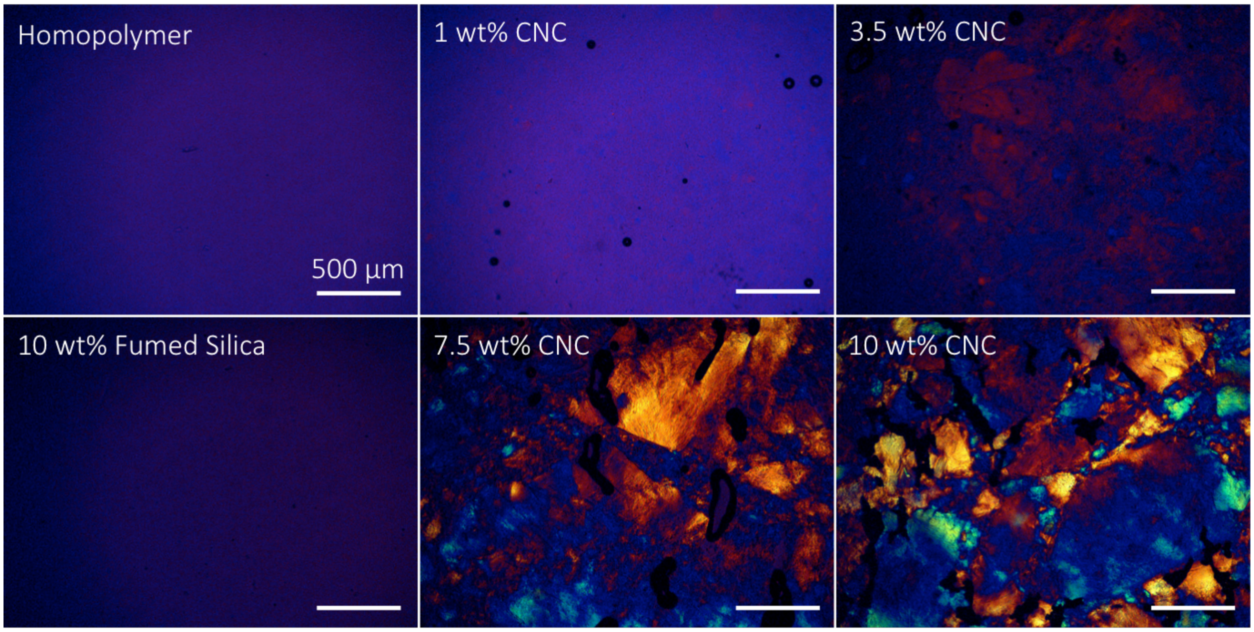

Figure 2. Polarized optical microscopy images of PEO10 homopolymer (10 000 g/mol) and nanocomposites filled with fumed silica and CNCs as indicated after heating at 85˚C for 5 min (no cooling). Isotropic regions are represented by dark violet. Dark/black regions are bubbles within the molten polymer. Scale bar is 500 µm.

Figure 3 shows spherulite morphology following the cooling of molten PEO10 homopolymer and nanocomposites at 7.5 wt.% loading, where it can be seen that the inclusion of both CNCs and fumed silica reduce spherulite nucleation density. Similar behaviour was observed for all other particle loadings, which supports trends observed in Table 1, where increased melting temperature and decreased crystallization temperatures demonstrate that both CNCs and fumed silica act as nucleation inhibitors. Nucleation inhibition has been previously reported by Samir *et al.* within tunicate CNC-reinforced PEO nanocomposites, however at much higher particle loadings of 30 wt.%.[24] The high loadings required in previous works suggest that particles have aggregated within the nanocomposite (reducing interfacial area), as sufficient polymer adsorption has *not* occurred to alter crystallization at lower loadings. The aggregation is potentially due to the ability to fully disperse tunicate CNCs prior to solvent casting, as the extremely high aspect ratio of tunicate CNCs (ca. 100) causes gel formation at concentrations of less that 1 wt.%.[34] In contrast, the CNCs used in this work are much shorter in length (ca. 200 nm)[4] allowing for good dispersion prior to casting. As a result, at loadings of 1 wt.% there is sufficient interfacial area and polymer adsorption, to limit polymer mobility and the propensity to crystallize. Notably, this is opposite to previous reports in which CNCs were found to nucleate crystallization of hydrophobic polypropylene[35] and poly($_\text{L}$-lactide),[36] where polymer adsorption is not expected to occur. This further demonstrates that when favourable interactions and polymer adsorption occurs within the nanocomposite (as in the case of PEO and CNCs), polymer mobility is reduced along with the density of spherulites.

To examine the crystal growth following composite processing (i.e. cooling after hot pressing) the nonisothermal spherulite growth rates for homopolymer and filled nanocomposites were examined. Nonisothermal growth rates have been shown to follow the same trends as isothermal conditions but exhibit significantly faster growth rates.[37] Table 2 presents the spherulite growth rates of PEO10 homopolymer and filled nanocomposites where it can be seen that upon the inclusion of CNCs, the spherulite growth rate increases independent of particle loading. In comparison, fumed silica does not change spherulite growth until 10 wt.% loading from which the growth rate is reduced below that of the homopolymer.[38] The difference in spherulite growth rates observed for CNCs and fumed silica suggests that different adsorption behaviour occurs at each particle surface. These differences are potentially due to differing surface chemistry and particle morphology.[39] For CNCs, the increased growth rate indicates that polymer adsorption facilitates polymer crystallization, potentially due to crystalline nature and high aspect ratio of the particle. In contrast, strong PEO adsorption to silica surfaces (which is not expected to be crystalline) limits polymer mobility, leading to slower growth rates at high particle loadings. This further indicates that while PEO adsorption to CNCs may not occur in the aqueous phase prior to casting, it does occur in the dry nanocomposite, potentially improving the reinforcing effect of CNCs.

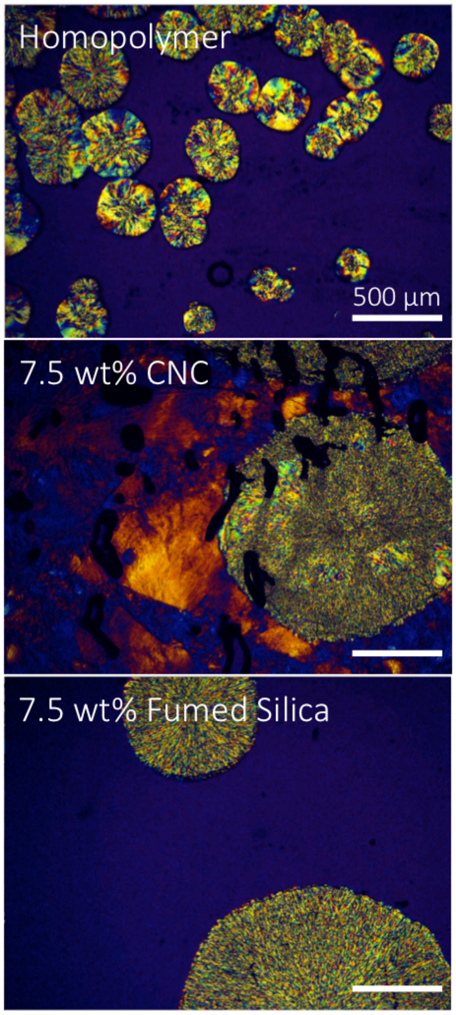

Figure 3. Polarized optical microscopy images of spherulites during nonisothermal crystallization of PEO10 homopolymer and CNC and silica filled nanocomposites after being removed from heat for ca. 2 minutes. Scale bar is 500 µm.

Table 2. Spherulite growth rate of PEO10 homopolymer and filled nanocomposites measured from polarized optical microscopy.

	Filler Content (wt. %)	Spherulite Growth Rate (µm/s)
PEO10	0	37 ± 10
CNC	1	47 ± 6
	3.5	41 ± 5
	7.5	47 ± 4
	10	46 ± 4
Fumed Silica	1	37 ± 8
	3.5	36 ± 3
	7.5	38 ± 6
	10	27 ± 4

Particle Dispersion and Polymer Adsorption. Particle dispersion in the PEO nanocomposites was assessed by atomic force microscopy (AFM) and transmission electron microscopy (TEM). For AFM analysis, PEO nanocomposites were hot pressed against silicon wafers to produce surfaces smooth enough for surface probe measurements. Figure 4 shows AFM amplitude images of PEO35 nanocomposites filled with a 10 wt.% loading of fumed silica and CNCs at three different scales (Supporting Information Figure S4 for representative AFM height and phase images). Notably, within fumed silica composites, structures larger than 500 nm are observed, however currently it is unclear whether these are artifacts from the hot pressing process or highly aggregated particles. Nonetheless, from Figure 4, aggregated and individualized fumed silica particles are clearly evident at the composite surface. Moreover, regions void of particles can be seen, signifying that the dispersion (at least at the composite surface) is not uniform. This potentially is due to initial state of dispersion during solvent casting. PEO is well known to adsorb to silica surfaces in the aqueous phase, and has been shown to cause flocculation at molecular weights as low as 6000 g/mol.[40] Additionally, unlike CNCs, fumed silica does not possess surface charge groups that maintain colloidal stability. As a result, during the casting process particle aggregation can occur, which translates to non-uniform dispersion within the dry nanocomposite. This highlights the need to interrupt particle-particle interactions and maintain particle spacing throughout composite processing.

Comparatively, CNC particles at the composite surface are less evident. As a result, it is difficult to determine particle dispersion from topographical images. However, at higher magnifications individual CNCs can be seen indicating that CNCs are well incorporated into the polymer matrix (Figure 4). This is further evidenced by the morphology of PEO at the CNC surface. For all CNCs imaged, PEO exhibits a shish-kebab-like morphology with individual lamella structures of ca. 10 nm decorating the CNC surface across the particle axis (Figure 4f). While shish-kebab morphology has been previously reported for electrospun PEO composites containing nanocellulose bundles,[28] to our knowledge this is the first evidence of shish-kebab morphology occurring on individual CNC particles. This indicates that PEO adsorbs and crystallizes at the CNC surface in dry nanocomposites and inhibits spherulite nucleation as seen from POM measurements (Figure 3). In other words, as the composite cools, PEO adsorbs to the CNC surface limiting the potential for spherulite nucleation. However, as spherulites grow, PEO/CNC shish-kebabs are readily incorporated into the crystalline domains of PEO thus increasing the growth rate of the spherulite. In contrast, PEO adsorbed to fumed silica surfaces does not exhibit any apparent crystallinity. As a result, while PEO adsorption limits spherulite nucleation, the PEO/fumed silica hybrid is not incorporated into crystalline domains as efficiently, causing slower spherulite growth (Table 2).

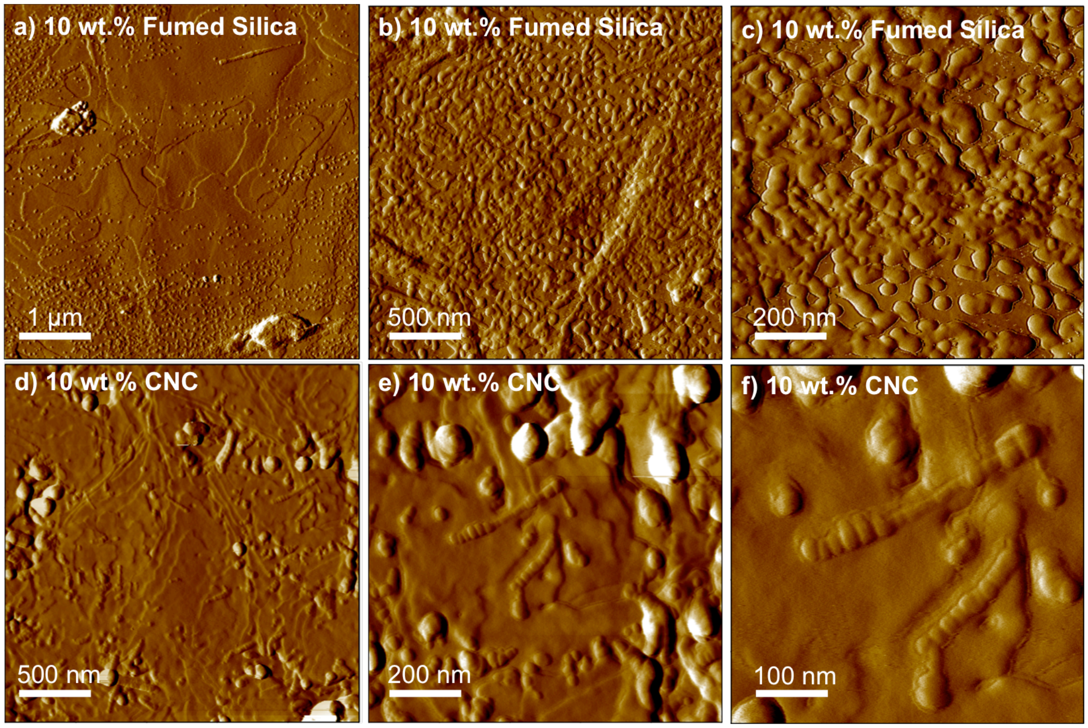

Figure 4. AFM amplitude images of PEO35 nanocomposites filled with (a, b, c) fumed silica and (d, e, f) CNCs at 10% loading.

To examine particle dispersion within PEO nanocomposites, hot pressed samples were microtomed and imaged via TEM. Figure 5 shows TEM images of PEO35 and PEO100 nanocomposites at 10 wt.% loading of CNCs and fumed silica. CNC/PEO35 nanocomposites show uniform particle dispersion throughout the composite, and do not appear to be percolated despite being added in volumes above the percolation threshold. For CNCs, in this work the percolation threshold was calculated to be 3.1 vol.% or 4.6 wt.%.[27] Similar discrepancies in achieving percolation have been previously reported.[27] This highlights, that even a small degree of aggregation can significantly increase the volume required to reach percolation. High-resolution TEM images of CNC nanocomposites (Supporting Information Figure S5) do not show any shish-kebab-like morphology suggesting that polymer electron density at the particle surface is equivalent to the bulk matrix.

TEM images of fumed silica/PEO35 nanocomposites (Figure 5c) show that particles are distributed throughout the polymer matrix, yet regions of aggregation can be seen, in good agreement with AFM images of the nanocomposite surface (Figure 4a). The fact that fumed silica composites show poorer dispersion in PEO35 despite having stronger particle-polymer interactions supports the notion that particle dispersion is largely governed by particle-particle interactions and it is these forces which need to be overcome to achieve uniform particle dispersion in a polymer matrix. Increasing the molecular weight, CNC/PEO100 nanocomposites at 10 wt.% loading (Figure 5b) show significantly more aggregation within the composite. In contrast, fumed silica/PEO100 nanocomposites (Figure 5d) exhibit dense uniform dispersion throughout the polymer matrix. The TEM images demonstrate that polymer molecular weight can greatly influence particle dispersion. While we expect, particle-polymer interactions within PEO35 and PEO100 composites to be similar, we note that PEO100 polymer solutions were significantly more viscous during processing, indicating that shear can impact particle-particle interactions and overall particle dispersion.

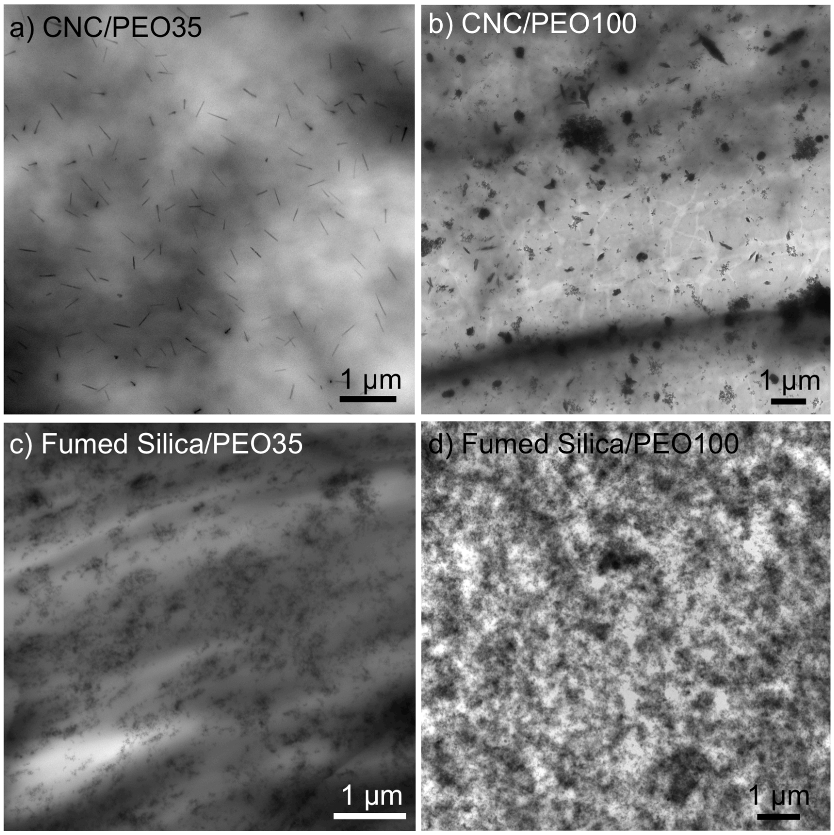

Figure 5. TEM images of microtomed of (a) CNC/PEO35, (b) CNC/PEO100 and (c) fumed silica/PEO35 and (d) fumed silica/PEO100 nanocomposites containing 10 wt.% particle loading.

Mechanical Properties. The mechanical properties of hot pressed PEO nanocomposites were examined by Instron tensile testing and nanoindentation. Notably PEO10 nanocomposites were found to be extremely brittle and could not be reproducibly measured, and thus mechanical data is only presented for PEO35 and PEO100 nanocomposites (Table 3). A CNC loading of 10 wt.% improved the Young's modulus of PEO35 and PEO100 by 86% and 63%, respectively. Similarly, fumed silica increased the Young's modulus of PEO100 by 78%, however no significant change was observed for PEO35 nanocomposites, potentially due to particle aggregation.

Due to the relatively poor mechanical properties of PEO, its use in rigid, high strength composite applications is limited, particularly for polymers with molecular weights less than 100 000 g/mol.

Where tensile measurements have been performed, the moduli of PEO homopolymers of comparable molecular weights (200 000 – 600 000 g/mol) have been reported as 160 – 250 MPa.[49–51] Clay[50,51] and graphene oxide[49] reinforced nanocomposites at 10 wt.% loading, show an increased moduli of 300 – 500 MPa, in good agreement with the results in Table 3 for both CNCs and fumed silica. Comparatively Xu *et al.* investigated very high molecular weight PEO (10^6 g/mol) CNC-reinforced nanocomposites where PEO homopolymer was measured to have a Young's modulus of 760 MPa.[27] A maximum modulus of 937 MPa was observed for nanocomposites reinforced 7 wt.% CNC loading, which in absolute terms is similar to the improvement observed in this work.

Examining the mechanical properties via nanoindentation shows that inclusion of CNCs and fumed silica *decreases* the reduced modulus at low loadings, in comparison to the homopolymer. Similar observations have been reported for clay-reinforced PEO composites[46] and fumed silica-reinforced epoxy composites.[47] While it is unclear why this occurs, it is potentially due to voids within the nanocomposites that can be seen in as black regions in Figure 3. Inclusion of nanoparticles increases the viscosity of the matrix resulting in trapped bubbles/voids. As a result the thin polymer walls between the voids can buckle under compression resulting in a lower reduced modulus and hardness compared to the homopolymer. This is potentially similar to the mechanical behaviour observed in polymeric foams.[48] Nonetheless, as filler loading increases, so does the reinforcing effect and the trends from nanoindentation (apart from homopolymer) follow closely to those observed in tensile measurements. Moreover, at 10 wt.% particle loading, the reduced modulus exceeds that of the homopolymer despite the presence of voids within the composite.

Table 3. Mechanical properties of PEO nanocomposites filled with CNCs and fumed silica, showing the Young's modulus measured by tensile measurements, and the reduced modulus and hardness measured my nanoindentation.

		Young's Modulus (MPa)		**Reduced Modulus (GPa)**		**Hardness (MPa)**	
	Filler Content (wt. %)	*CNC*	*Fumed Silica*	*CNC*	*Fumed Silica*	*CNC*	*Fumed Silica*
PEO35							
	0	220 ± 30	220 ± 20	2.2 ± 0.2	2.2 ± 0.2	90 ± 10	90 ± 10
	1	250 ± 40	200 ± 10	1.3 ± 0.1	1.1 ± 0.3	65 ± 4	50 ± 20
	3.5	320 ± 20	240 ± 10	1.7 ± 0.1	1.6 ± 0.3	69 ± 2	50 ± 20
	7.5	360 ± 50	280 ± 30	2.0 ± 0.1	1.8 ± 0.4	76 ± 3	78 ± 7
	10	410 ± 30	240 ± 40	2.6 ± 0.1	2.0 ± 0.4	82 ± 4	80 ± 20
PEO100							
	0	248 ± 9	248 ± 9	1.5 ± 0.1	1.5 ± 0.1	71 ± 7	71 ± 7
	1	320 ± 6	250 ± 20	1.2 ± 0.1	1.7 ± 0.2	55 ± 4	69 ± 6
	3.5	379 ± 9	329 ± 9	1.6 ± 0.1	1.9 ± 0.2	66 ± 6	76 ± 8
	7.5	400 ± 20	370 ± 10	1.7 ± 0.1	2.0 ± 0.2	70 ± 3	80 ± 4
	10	400 ± 30	440 ± 10	1.7 ± 0.1	2.3 ± 0.2	71 ± 3	88 ± 6

Comparing the Young's modulus, measured by tensile testing, to the reduced modulus, measured by nanoindentation, suggests that PEO nanocomposites have superior mechanical properties under compression. Similar deviations between the moduli have been previously reported for both CNC[41,42] and fumed silica[43] filled nanocomposites and discrepancies between nanoindentation and macroscopic mechanical tests are well known.[44] One reason for the observed differences, is that, nanoindentation only probes "surface" mechanical properties, which can differ from bulk or "core" properties, particularly for semi-crystalline polymers where spherulite size and morphology can change depending on probe depth (i.e. surface vs. core).[45]

Considering more conventional hydrophobic polymer matrices, significant variation in mechanical properties have been reported, making it difficult to establish specific trends.[30] While much of the differences can be attributed to varying composite processing methods (i.e., solvent casting, melt mixing or *in situ* polymerization), conflicting results for the same systems (and processing conditions) exist. For example, inclusion of CNCs into solvent cast poly(ε-caprolactone) nanocomposites have been reported to reduce[52] and increase[53] the Young's modulus of the material. Particle dispersion was not specifically addressed in either study, making it is difficult to assess the cause of the discrepancy, however it is presumed that particle aggregation is responsible for poor mechanical properties.[52] Although absolute trends cannot be extracted from the literature, in general, improved mechanical properties are only obtained when CNCs are well-dispersed.

Numerous models have been used to describe the mechanical properties of CNC composites, but generally they can be classified as either mean field or percolation based approaches.[8] In early reports by Favier *et al.* the percolation based Ouali model was used to describe nanocomposite behaviour, whereby above a critical volume fraction significant mechanical improvements are observed.[9,10] However, more recent re-evaluation of this work suggests that mean field models more accurately describe behaviour, particularly for filler volumes below the percolation threshold.[8] Commonly CNC filled nanocomposites are fit using the mean field, semi-empirical Halpin-Kardos model for short fibers, which approximates 3-dimensional composites as a series of laminated sheets containing oriented fibers.[54] The Young's modulus parallel ($E_{||}$) and transverse ($E_{\perp}$) to the fiber direction are given by:

$$E_{||} = E_m \frac{1 + \eta_{||}\zeta\varphi_f}{1 - \eta_{||}\varphi_f} \qquad [1]$$

$$E_{\perp} = E_m \frac{1 + 2\eta_{\perp}\zeta\varphi_f}{1 - \eta_{\perp}\varphi_f} \qquad [2]$$

where,

$$\eta_{||} = \frac{\frac{E_f}{E_m} - 1}{\frac{E_f}{E_m} + \zeta} \qquad [3]$$

$$\eta_{\perp} = \frac{\frac{E_f}{E_m} - 1}{\frac{E_f}{E_m} + 2} \qquad [4]$$

where φ_f is the filler volume fraction, E_m is the Young's modulus of the matrix, determined from PEO homopolymer measurements. E_f is the modulus of the CNCs taken to be 150 GPa.[7] ζ is a shape factor dependent on fiber geometry, determined by the length (L) and width (w) of individual CNCs where $\zeta = 2L/w$.[27] Particle geometry is taken from previous AFM measurements to be L = 183 nm and w = 8 nm.[4] Assuming CNCs are randomly oriented through the matrix, the composite modulus (E_c) is then calculated by:

$$E_{\mathrm{C}} = 0.184E_{||} + 0.816E_{\perp} \qquad [5]$$

Figure 6 presents the Young's modulus of PEO35 and PEO100 nanocomposites as a function of filler volume fraction where experimental results of CNC-reinforced PEO35 composites agree well with the moduli predicted by the Halpin-Kardos model. The CNCs within the PEO35 nanocomposite are well dispersed, randomly oriented and do not form a percolated network as seen by TEM (Figure 5a). In contrast, while the Young's modulus of CNC-reinforced PEO100 nanocomposites increases with particle loading, the experimental results are not effectively described by the Halpin-Kardos model. Above 3.5 wt.% the Young's modulus plateaus, and at 10 wt.% loading experimental results are well below the values predicted by the Halpin-Kardos model, which is attributed to the aggregation observed in within the nanocomposite (Figure 5b).

Whereas the Halpin-Kardo model is appropriate for fiber reinforced composite materials the Young's modulus of sphere-like fumed silica reinforced PEO nanocomposites can be described using a modified version of the commonly used Guth-Gold model, which originates from Einstein's decription of colloidal particles.[55–58]

$$E_{\mathrm{C}} = E_m(1 + 2.5\varphi_e + 6{\varphi_e}^2) \qquad [6]$$

where effective filler volume fraction, φ_e, is given by:

$$\varphi_e = k\varphi_f \qquad [7]$$

Where k is a scaling factor (>1 for polymer melts) that adjusts the filler volume fraction, and the traditional Guth-Gold model, to account for adsorbed/bound polymer, which increases the effective volume fraction of the filler[57,59] Using a least squares regression it was determined that k = 1 and k = 2.9 for PEO35 and PEO100 nanocomposites respectively. Because PEO strongly adsorbs to silica, increasing the effective volume fraction, it is expected for all molecular weights $k > 1$. However, the fact that for PEO35 k = 1 (i.e. no change to volume fraction) indicates that although PEO adsorbs to the surface, aggregation within the composite, reduces the interfacial area, and thus exhibits minimal improvement to the mechanical properties. In contrast PEO100, composites are well described by the modified Guth-Gold model, which shows that particles are well dispersed as seen in Figure 5d. Polymer adsorption effectively increases the fumed silica volume fraction (k = 2.9) leading to substantial improvements to the Young's modulus. Moreover, at higher loadings, reinforcement does not appear to plateau suggesting that that fumed silica can be added in higher loadings and remain well-dispersed throughout the nanocomposites.

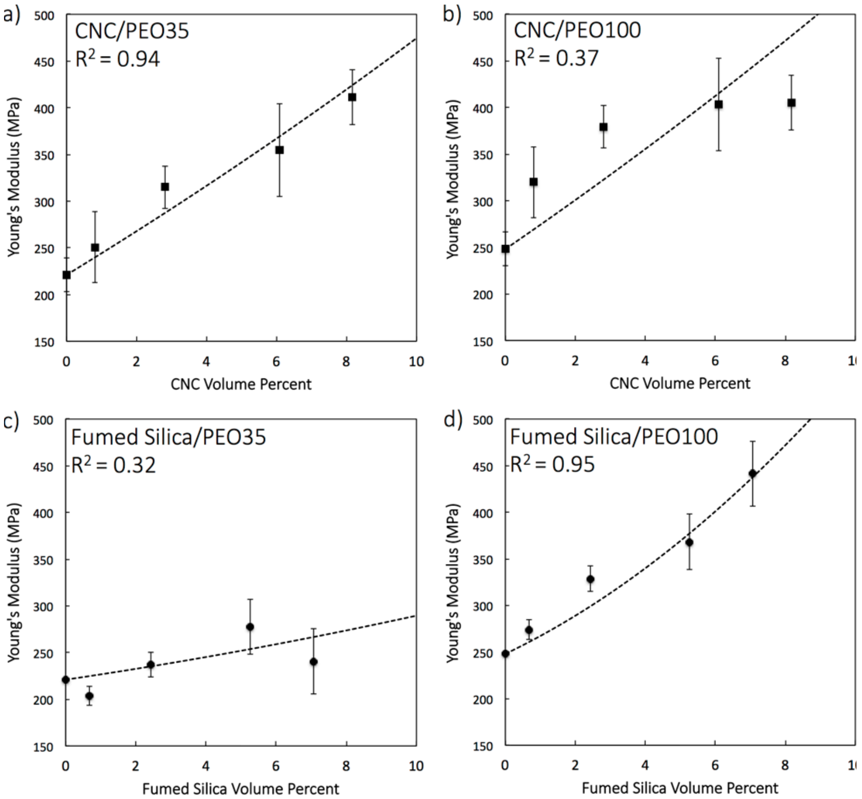

Figure 6. The Young's modulus (from Instron measurements) of PEO35 and PEO100 nanocomposites plotted as a function of (a, b) CNC and (c, d) fumed silica volume fraction. CNC and fumed silica composites were fit to the Halpin-Kardos and modified Guth-Gold models, respectively. PEO35 and PEO100 fumed silica reinforced composites were fit using $\boldsymbol{k}$ = 1 and $\boldsymbol{k}$ = 2.9, respectively.

Notably, no adjustments to the CNC volume fraction was required to describe the mechanical properties by the Halpin-Kardos model. This demonstrates that although PEO adsorbs to the surface of CNCs in the dry composite, as seen by AFM measurements (Figure 4f), the bound polymer has properties similar to the bulk matrix. This is supported by TEM images (Supporting Information Figure S5) and the increased spherulite growth rate, which indicates that PEO/CNC hybrids are readily incorporated into the bulk. This further highlights the difference between PEO/CNC and PEO/silica interactions and suggests that if equivalent dispersion is achieved (i.e. interrupting all particle-particle interactions) particle-polymer interactions are a determinant factor of mechanical properties.

Conclusions

This work systematically examined the properties of PEO nanocomposites reinforced with CNCs and fumed silica. In general PEO was found to adsorb to both particle surfaces, reducing polymer mobility and decreasing the overall density of spherulites in comparison to homopolymer. This is opposite to the behaviour reported within hydrophobic polymer matrices, indicating that polymer adsorption inhibits spherulite nucleation. Further analysis by AFM revealed that PEO adsorption to CNCs differs significantly to that of fumed silica. At CNC surfaces, PEO exhibited a shish-kebab-like morphology, which was more effectively incorporated into the crystalline domains of the matrix, leading to increased spherulite growth rates. The Young's modulus of both PEO35 and PEO100 polymer matrices was increased upon the inclusion of both CNCs and fumed silica. Analysis of the Young's modulus demonstrated that when good particle dispersion was achieved, CNC and fumed silica nanocomposites could be effectively described by the Halpin-Kardos and the Guth-Gold models, respectively. The reduced modulus, measured by nanoindentation, decreased upon the inclusion of CNCs and fumed silica, potentially due to the presence of bubbles and voids which collapse under compression. However, as filler loading increased, so did the reduced modulus, mirroring the trends observed in tensile measurements, and ultimately surpassing that of the homopolymer at particle loadings of 10 wt.%. While this work examines an ideal system of hydrophilic reinforcing agents in water-soluble polymer matrices, we believe the understanding of particle-particle and particle-polymer interactions may be generalized to more commercially relevant polymer composites.

References

(1) Le Corre, D.; Bras, J.; Dufresne, A. Starch Nanoparticles: A Review. *Biomacromolecules* **2010**, *11* (5), 1139–1153.

(2) Zeng, J. B.; He, Y. S.; Li, S. L.; Wang, Y. Z. Chitin Whiskers: An Overview. *Biomacromolecules* **2012**, *13* (1), 1–11.

(3) Klemm, D.; Kramer, F.; Moritz, S.; Lindström, T.; Ankerfors, M.; Gray, D. G.; Dorris, A. Nanocelluloses: A New Family of Nature-Based Materials. *Angew. Chemie - Int. Ed.* **2011**, *50*, 5438–5466.

(4) Reid, M. S.; Villalobos, M.; Cranston, E. D. Benchmarking Cellulose Nanocrystals: From the Laboratory to Industrial Production. *Langmuir* **2017**, *33* (7), 1583–1598.

(5) Lin, N.; Dufresne, A. Physical And/or Chemical Compatibilization of Extruded Cellulose Nanocrystal Reinforced Polystyrene Nanocomposites. *Macromolecules* **2013**, *46* (14), 5570–5583.

(6) Habibi, Y.; Lucia, L. A.; Rojas, O. J. Cellulose Nanocrystals: Chemistry, Self-Assembly, and Applications. *Chem. Rev.* **2010**, *110* (6), 3479–3500.

(7) Mariano, M.; El Kissi, N.; Dufresne, A. Cellulose Nanocrystals and Related Nanocomposites: Review of Some Properties and Challenges. *J. Polym. Sci. Part B Polym. Phys.* **2014**, *52*, 791–806.

(8) Moon, R. J.; Martini, A.; Nairn, J.; Simonsen, J.; Youngblood, J. Cellulose Nanomaterials Review: Structure, Properties and Nanocomposites. *Chem. Soc. Rev.* **2011**, *40* (7), 3941–3994.

(9) Favier, V.; Cavaille, J. Y.; Canova, G. R.; Shrivastava, S. C. Mechanical Percolation in Cellulose Whisker Nanocomposites. *Polym. Eng. Sci.* **1997**, *37* (10), 1732–1739.

(10) Favier, V.; Chanzy, H.; Cavaille, J. Y. Polymer Nanocomposites Reinforced by Cellulose Whiskers. *Macromolecules* **1995**, *28* (18), 6365–6367.

(11) Lin, N.; Huang, J.; Dufresne, A. Preparation, Properties and Applications of Polysaccharide Nanocrystals in Advanced Functional Nanomaterials: A Review. *Nanoscale* **2012**, *4* (11), 3274.

(12) Long, L.; Wang, S.; Xiao, M.; Meng, Y. Polymer Electrolytes for Lithium Polymer Batteries. *J. Mater. Chem. A* **2016**, *4* (26), 10038–10069.

(13) Knop, K.; Hoogenboom, R.; Fischer, D.; Schubert, U. S. Poly(ethylene Glycol) in Drug Delivery: Pros and Cons as Well as Potential Alternatives. *Angew. Chemie Int. Ed.* **2010**, *49* (36), 6288–6308.

(14) Mathur, S.; Moudgil, B. M. Adsorption Mechanism(s) of Poly(Ethylene Oxide) on Oxide Surfaces. *J. Colloid Interface Sci.* **1997**, *196* (1), 92–98.

(15) Kim, S. Y.; Meyer, H. W.; Saalwächter, K.; Zukoski, C. F. Polymer Dynamics in PEG-Silica Nanocomposites: Effects of Polymer Molecular Weight, Temperature and Solvent Dilution. *Macromolecules* **2012**, *45* (10), 4225–4237.

(16) Voronin, E. F.; Gun'ko, V. M.; Guzenko, N. V.; Pakhlov, E. M.; Nosach, L. V.; Leboda,

R.; Skubiszewska-Zięba, J.; Malysheva, M. L.; Borysenko, M. V.; Chuiko, a. a. Interaction of Poly(ethylene Oxide) with Fumed Silica. *J. Colloid Interface Sci.* **2004**, *279*, 326–340.

(17) Lin, D.; Liu, W.; Liu, Y.; Lee, H. R.; Hsu, P.; Liu, K.; Cui, Y. High Ionic Conductivity of Composite Solid Polymer Electrolyte via In Situ Synthesis of Monodispersed SiO 2 Nanospheres in Poly(ethylene Oxide). *Nano Lett.* **2016**, *16* (1), 459–465.

(18) Hasanzadeh, M.; Mottaghitalab, V.; Rezaei, M. Rheological and Viscoelastic Behavior of Concentrated Colloidal Suspensions of Silica Nanoparticles: A Response Surface Methodology Approach. *Adv. Powder Technol.* **2015**, *26* (6), 1570–1577.

(19) Khandavalli, S.; Rothstein, J. P. Extensional Rheology of Shear-Thickening Fumed Silica Nanoparticles Dispersed in an Aqueous Polyethylene Oxide Solution. *J. Rheol. (N. Y. N. Y).* **2014**, *58* (2), 411–431.

(20) Zhang, Q.; Archer, L. A. Poly(ethylene Oxide)/silica Nanocomposites: Structure and Rheology. *Langmuir* **2002**, *18* (26), 10435–10442.

(21) Lindström, T.; Glad-Nordmark, G. Selective Adsorption, Flocculation, and Fractionation of Wood Pulps with Polyethyleneoxide. *J. Colloid Interface Sci.* **1983**, *94* (2), 404–411.

(22) Ishimaru, Y.; Lindström, T. Adsorption of Water-Soluble, Nonionic Polymers onto Cellulosic Fibers. *J. Appl. Polym. Sci.* **1984**, *29* (5), 1675–1691.

(23) Reid, M. S.; Villalobos, M.; Cranston, E. D. The Role of Hydrogen Bonding in Non-Ionic Polymer Adsorption to Cellulose Nanocrystals and Silica Colloids. *Curr. Opin. Colloid Interface Sci.* **2017**, *29*, 76–82.

(24) Azizi Samir, M. A. S.; Alloin, F.; Sanchez, J. Y.; Dufresne, A. Cellulose Nanocrystals Reinforced Poly(oxyethylene). *Polymer (Guildf).* **2004**, *45* (12), 4149–4157.

(25) Azizi Samir, M. A. S.; Chazeau, L.; Alloin, F.; Cavaillé, J.-Y.; Dufresne, A.; Sanchez, J.-Y. POE-Based Nanocomposite Polymer Electrolytes Reinforced with Cellulose Whiskers. *Electrochim. Acta* **2005**, *50* (19), 3897–3903.

(26) Ahmed, M.; Azizi, S.; Alloin, F.; Gorecki, W.; Sanchez, J.; Dufresne, A. Nanocomposite Polymer Electrolytes Based on Poly (Oxyethylene) and Cellulose Nanocrystals. *J.Phys. Chem. B* **2004**, *108*, 10845–10852.

(27) Xu, X.; Liu, F.; Jiang, L.; Zhu, J. Y.; Haagenson, D.; Wiesenborn, D. P. Cellulose Nanocrystals vs. Cellulose Nanofibrils: A Comparative Study on Their Microstructures and Effects as Polymer Reinforcing Agents. *ACS Appl. Mater. Interfaces* **2013**, *5* (8), 2999–3009.

(28) Xu, X.; Wang, H.; Jiang, L.; Wang, X.; Payne, S. a.; Zhu, J. Y.; Li, R. Comparison between Cellulose Nanocrystal and Cellulose Nanofibril Reinforced Poly(ethylene Oxide) Nanofibers and Their Novel Shish-Kebab-like Crystalline Structures. *Macromolecules* **2014**, *47* (10), 3409–3416.

(29) Changsarn, S.; Mendez, J. D.; Shanmuganathan, K.; Foster, E. J.; Weder, C.; Supaphol, P. Biologically Inspired Hierarchical Design of Nanocomposites Based on Poly(ethylene Oxide) and Cellulose Nanofibers. *Macromol. Rapid Commun.* **2011**, *32* (17), 1367–1372.

(30) Oksman, K.; Aitomäki, Y.; Mathew, A. P.; Siqueira, G.; Zhou, Q.; Butylina, S.; Tanpichai, S.; Zhou, X.; Hooshmand, S. Review of the Recent Developments in Cellulose Nanocomposite Processing. *Compos. Part A Appl. Sci. Manuf.* **2016**, *83*, 2–18.

(31) Mariano, M.; Pilate, F.; de Oliveira, F. B.; Khelifa, F.; Dubois, P.; Raquez, J.-M.; Dufresne, A. Preparation of Cellulose Nanocrystal-Reinforced Poly(lactic Acid) Nanocomposites through Noncovalent Modification with PLLA-Based Surfactants. *ACS Omega* **2017**, *2* (6), 2678–2688.

(32) Pielichowska, K.; Pielichowski, K. Crystallization Behaviour of PEO with Carbon-Based Nanonucleants for Thermal Energy Storage. *Thermochim. Acta* **2010**, *510* (1–2), 173–184.

(33) Chatterjee, T.; Yurekli, K.; Hadjiev, V. G.; Krishnamoorti, R. Single-Walled Carbon Nanotube Dispersions in Poly(ethylene Oxide). *Adv. Funct. Mater.* **2005**, *15* (11), 1832–1838.

(34) van den Berg, O.; Capadona, J. R.; Weder, C. Preparation of Homogeneous Dispersions of Tunicate Cellulose Whiskers in Organic Solvents. *Biomacromolecules* **2007**, *8* (4), 1353–1357.

(35) Gray, D. G. Transcrystallization of Polypropylene at Cellulose Nanocrystal Surfaces. *Cellulose* **2008**, *15* (2), 297–301.

(36) Pei, A.; Zhou, Q.; Berglund, L. A. Functionalized Cellulose Nanocrystals as Biobased Nucleation Agents in Poly(l-Lactide) (PLLA) - Crystallization and Mechanical Property Effects. *Compos. Sci. Technol.* **2010**, *70* (5), 815–821.

(37) Shangguan, Y.; Song, Y.; Zheng, Q. Kinetic Analysis on Spherulite Growth Rate of Polypropylene Catalloys. *Polymer (Guildf).* **2007**, *48* (15), 4567–4577.

(38) Waddon, A. J.; Petrovic, Z. S. Spherulite Crystallization in Poly(ethylene oxide)–Silica Nanocomposites. Retardation of Growth Rates through Reduced Molecular Mobility. *Polym. J.* **2002**, *34* (12), 1–6.

(39) Palza, H.; Vera, J.; Wilhelm, M.; Zapata, P. Spherulite Growth Rate in Polypropylene/silica Nanoparticle Composites: Effect of Particle Morphology and Compatibilizer. *Macromol. Mater. Eng.* **2011**, *296* (8), 744–751.

(40) Eisenlauer, J.; Killmann, E.; Korn, M. Stability of Colloidal Silica (Aerosil) Hydrosols. II. Influence of the pH Value and the Adsorption of Polyethylene Glycols. *J. Colloid Interface Sci.* **1980**, *74* (1), 120–135.

(41) Zimmermann, T.; Pöhler, E.; Schwaller, P. Mechanical and Morphological Properties of Cellulose Fibril Reinforced Nanocomposites. *Adv. Eng. Mater.* **2005**, *7* (12), 1156–1161.

(42) Pakzad, A.; Simonsen, J.; Yassar, R. S. Elastic Properties of Thin Poly(vinyl Alcohol)–cellulose Nanocrystal Membranes. *Nanotechnology* **2012**, *23* (8), 85706.

(43) Xu, G. C.; Li, a Y.; De Zhang, L.; Yu, X. Y.; Xie, T.; Wu, G. S. Nanomechanic Properties of Polymer-Based Nanocomposites with Nanosilica by Nanoindentation. *J. Reinf. Plast. Compos.* **2004**, *23* (13), 1365–1372.

(44) Díez-Pascual, A. M.; Gómez-Fatou, M. A.; Ania, F.; Flores, A. Nanoindentation in Polymer Nanocomposites. *Prog. Mater. Sci.* **2015**, *67*, 1–94.

(45) Guo, C.; Zhou, L.; Lv, J. Effects of Expandable Graphite and Modified Ammonium Polyphosphate on the Flame-Retardant and Mechanical Properties of Wood Flour-Polypropylene Composites. *Polym. Polym. Compos.* **2013**, *21* (7), 449–456.

(46) Beake, B. D.; Chen, S.; Hull, J. B.; Gao, F. Nanoindentation Behavior of Clay/poly(ethylene Oxide) Nanocomposites. *J. Nanosci. Nanotechnol.* **2002**, *2* (1), 73–79.

(47) Tzetzis, D.; Mansour, G.; Tsiafis, I.; Pavlidou, E. Nanoindentation Measurements of Fumed Silica Epoxy Reinforced Nanocomposites. *J. Reinf. Plast. Compos.* **2013**, *32* (3), 160–173.

(48) Deshpande, V. S.; Fleck, N. A. Multi-Axial Yield Behaviour of Polymer Foams. *Acta Mater.* **2001**, *49* (10), 1859–1866.

(49) Chang, Y. W.; Lee, K. S.; Lee, Y. W.; Bang, J. H. Poly(ethylene Oxide)/graphene Oxide Nanocomposites: Structure, Properties and Shape Memory Behavior. *Polym. Bull.* **2015**, *72* (8), 1937–1948.

(50) Burgaz, E. Poly(ethylene-Oxide)/clay/silica Nanocomposites: Morphology and Thermomechanical Properties. *Polymer (Guildf).* **2011**, *52* (22), 5118–5126.

(51) Ratna, D.; Divekar, S.; Samui, A. B.; Chakraborty, B. C.; Banthia, A. K. Poly(ethylene Oxide)/clay Nanocomposite: Thermomechanical Properties and Morphology. *Polymer (Guildf).* **2006**, *47* (11), 4068–4074.

(52) Siqueira, G.; Bras, J.; Dufresne, A. Cellulose Whiskers versus Microfibrils: Influence of the Nature of the Nanoparticle and Its Surface Functionalization on the Thermal and Mechanical Properties of Nanocomposites. *Biomacromolecules* **2009**, *10* (2), 425–432.

(53) Habibi, Y.; Goffin, A.-L.; Schiltz, N.; Duquesne, E.; Dubois, P.; Dufresne, A. Bionanocomposites Based on Poly(ε-Caprolactone)-Grafted Cellulose Nanocrystals by Ring-Opening Polymerization. *J. Mater. Chem.* **2008**, *18* (41), 5002.

(54) Halpin, J. C.; Kardos, J. L. Moduli of Crystalline Polymers Employing Composite Theory. *J. Appl. Phys.* **1972**, *43* (5), 2235–2241.

(55) Guth, E. Theory of Filler Reinforcement. *J. Appl. Phys.* **1945**, *16* (1), 20–25.

(56) Song, Y.; Zheng, Q. A Guide for Hydrodynamic Reinforcement Effect in Nanoparticle-Filled Polymers. *Crit. Rev. Solid State Mater. Sci.* **2016**, *8436* (March), 1–29.

(57) Kim, S. Y.; Zukoski, C. F. Super- and Sub-Einstein Intrinsic Viscosities of Spherical Nanoparticles in Concentrated Low Molecular Weight Polymer Solutions. *Soft Matter* **2012**, *8*, 1801.

(58) Einstein, A. On the Motion of Small Particles Suspended in a Stationary Liquid, as Required by the Molecular Kinetic Theory of Heat. *Ann. Phys.* **1906**, *322*, 549–560.

(59) Camenzind, A.; Caseri, W. R.; Pratsinis, S. E. Flame-Made Nanoparticles for Nanocomposites. *Nano Today* **2010**, *5* (1), 48–65.

Appendix 7: Chapter 7 Supporting Information

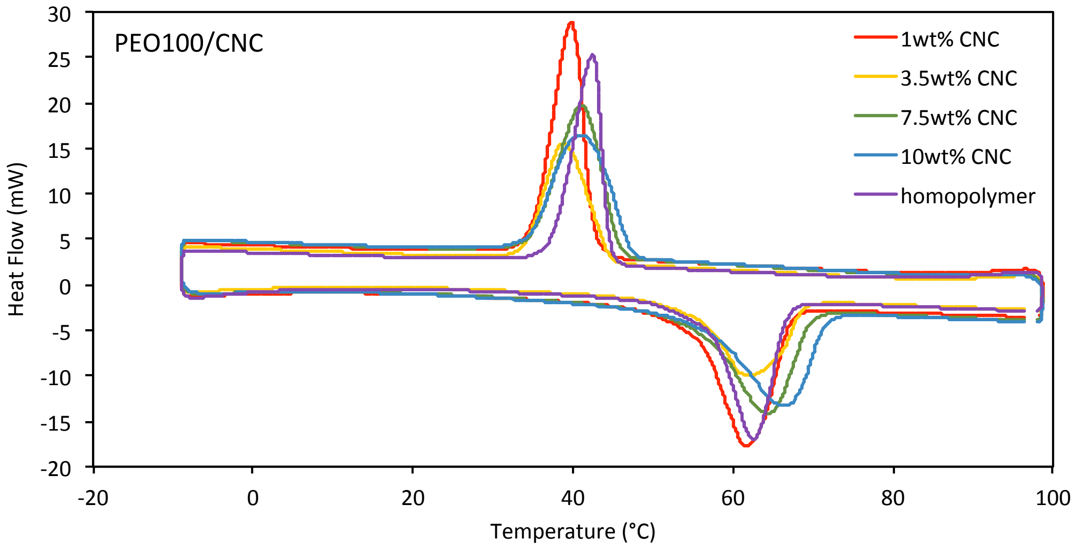

Figure S1. Representative DSC curves for PEO100/CNC nanocomposites.

Attenuated total reflectance Fourier transform infrared spectroscopy (ATR-FTIR) was performed on thinly sliced PEO nanocomposites using a Bruker Vertex 70 FTIR. A total of 64 scans were compiled with 4 cm^{-1} step.

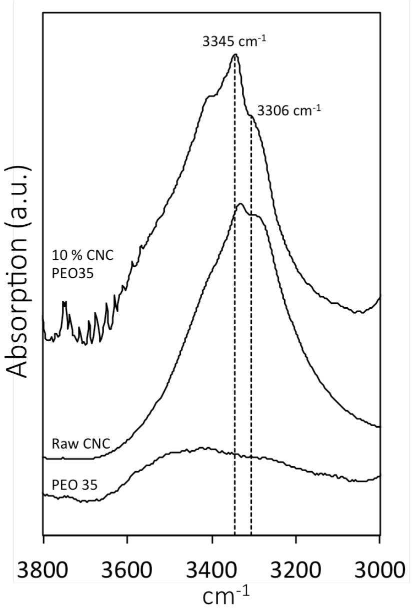

Figure S2. ATR-FTIR spectrums of PEO35, CNCs and PEO35 nanocomposite containing 10wt.% CNC. In the composite the OH stretching peaks at 3287 cm^{-1} and 3332 cm^{-1} are shifted to 3306 cm^{-1} and 3345 cm^{-1} respectively, indicating that PEO hydrogen bonds to CNC surfaces when competitive water hydrogen bonds are not available

XRD measurements, were performed on PEO35 homopolymer and nanocomposites containing 10 wt.% CNCs and fumed silica, using a Bruker D8 Davinci diffractometer (Bruker, USA) with a cobalt sealed tube source (λavg = 1.79026 Å), 35 kV, 45 mA with a parallel focus Goebel Mirror, Vantec 500 area detector, and 0.5 mm microslit and 0.5 mm short collimator over a 2θ range of 8−45°. Two-dimensional area detector frames were integrated to produce diffraction patterns, which then underwent Rietveld refinement. Diffraction patterns were compared to the single crystal information file (CIF) to analyze for changes in crystal structure.

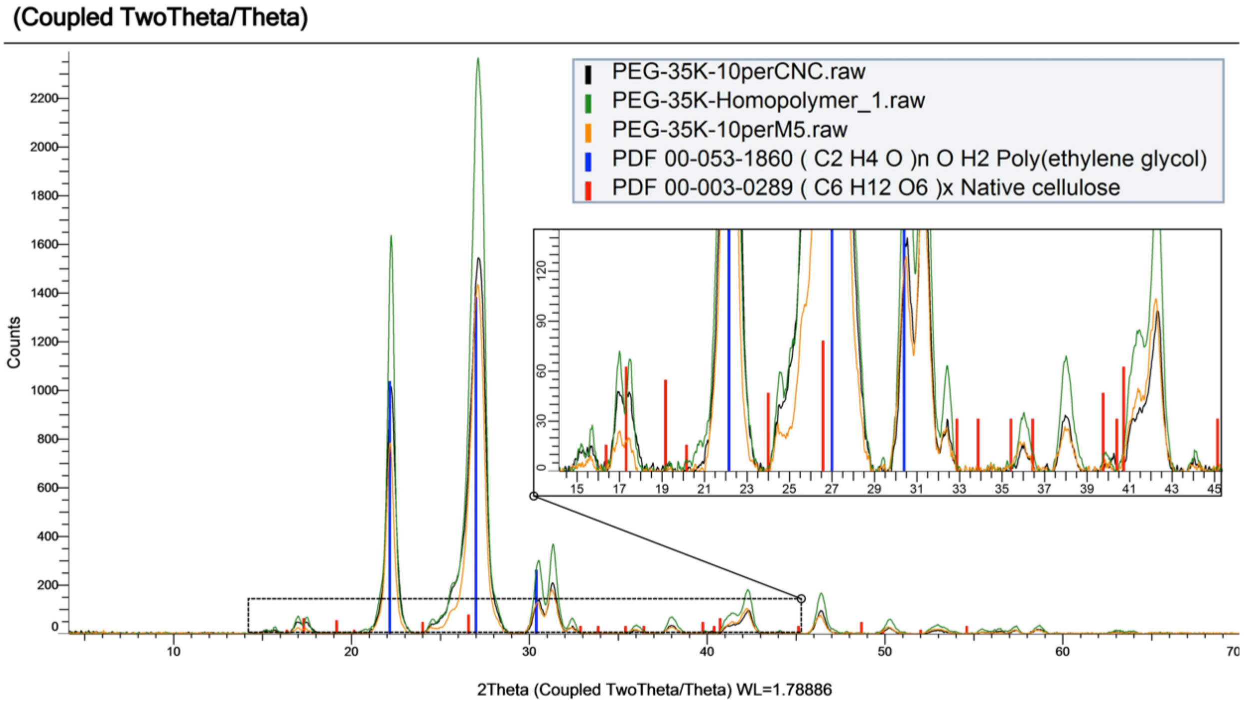

Figure S3. XRD pattern of PEO35 homopolymer and PEO35 nanocomposites containing 10 wt.% CNCs and fumed silica where no significant changes to the XRD pattern are evident upon the inclusion of reinforcing agents.

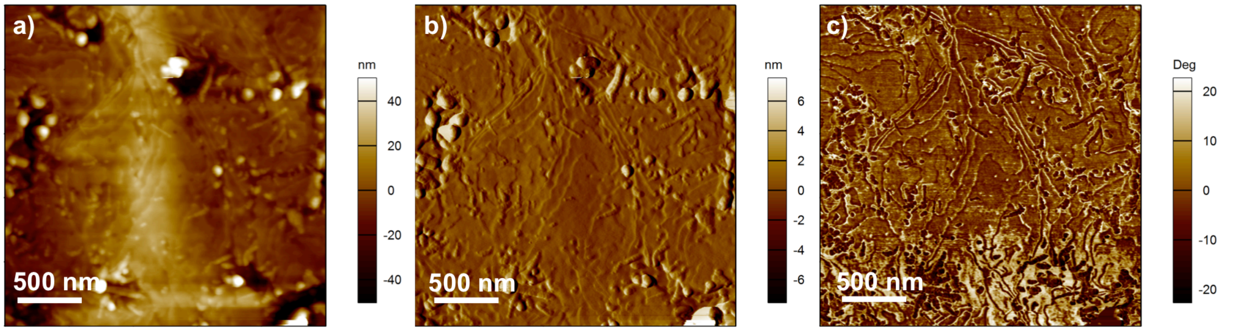

Figure S4. AFM images of PEO35 nanocomposites reinforced with 10wt.% CNCs, displaying **a)** height, **b)** amplitude, and **c)** phase images.

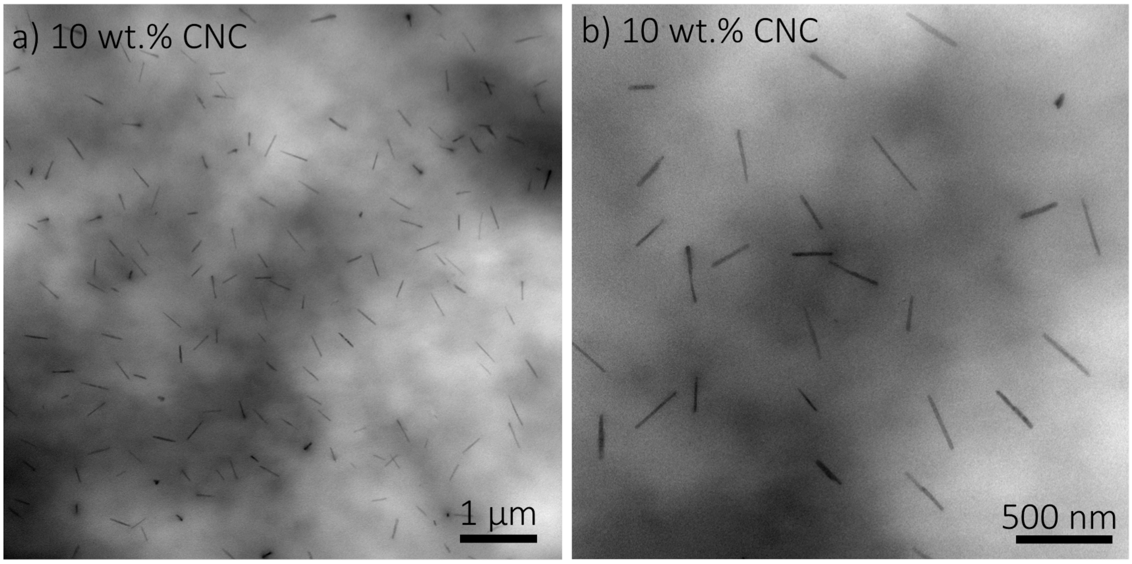

Figure S5. TEM images of PEO35 nanocomposite containing CNC at 10 wt.% loading at (a) low and (b) high magnification.

Chapter 8

Concluding Remarks

Throughout this work, CNCs were investigated with the aim of developing a deeper understanding of the forces and interactions that control particle dispersibility and behaviour. Specifically, particle-particle and particle-polymer interactions were probed in a variety of aqueous and non-aqueous environments, using surface sensitive techniques including surface plasmon resonance, quartz crystal microbalance and atomic force microscopy, amongst others. Overall this work was achieved by addressing and fulfilling the goals outlined in *Chapter 1,* specifically:

1. **Thoroughly characterize and benchmark CNCs.** The work within *Chapter 3* extensively characterized CNCs produced by current North American industrial producers and compared them to CNCs traditionally extracted in the laboratory. While, minor differences between particles were found, generally the morphology, crystallinity, colloidal/thermal stability, and self-assembly of CNCs produced at the industrial scale compared well with CNCs produced at the bench scale. Not only does this provide a foundation from which particle-particle and particle-polymer interactions can be understood, it demonstrates that knowledge gained by studying laboratory extracted CNCs is readily translatable to commercial CNC products and applications. This contribution to the literature is timely for the quickly growing field of nanocellulose and the understanding gained from this work will help others to carry-out reproducible and comparable research (and product development).
2. **Develop new methods to probe and measure particle-particle interactions.** *Chapter 4* presented a surface plasmon resonance based technique from which interactions within CNC only thin film were explored as analogues for CNC aggregates. Monitoring film swelling from the dry to the wet state in both aqueous and non-aqueous media demonstrated that interrupting particle-particle hydrogen bonding was critical for dispersion however; van der Waals forces are the primary interactions keeping films (and aggregates) intact. It is therefore essential to overcome these forces to achieve good dispersion within CNC composites. Within *Chapter 5* this surface plasmon resonance technique was extended to monitor the kinetics of CNC film swelling in various ionic strength media. The rate of film swelling was found to scale with osmotic pressure

between the film and the surrounding media. The total film thickness and particle spacing, however was independent of both ionic strength and surface charge density which demonstrated that electrostatic double layer forces do not significantly impact particle-particle interactions within the aggregated state. This is somewhat counterintuitive as it is normally believed that electrostatics are the governing force between particles/fibrils, and adding surface charge to nanocellulose should facilitate dispersion. While it is true that surface charge helps prevent particle/fibril aggregation in suspension, it is not sufficient to separate particles/fibrils, which are already in contact. As such, mechanical energy is always needed to separate particles/fibrils to distances where electrostatic repulsion will allow for colloidal stability.

3. **Explore particle-polymer interactions.** The interactions between water-soluble polyethylene glycol and CNCs were examined in direct comparison to fumed silica in *Chapter 6*. Polymer adsorption to both dispersed particles and model films was studied and similar results were obtained, yet nuances of the techniques and sample formats were observed: this type of evaluation is often overlooked in the literature. Whereas hydrogen bonding between surface silanols and the ether oxygen of polyethylene glycol leads to strong polymer adsorption, no adsorption was observed for CNCs in aqueous environments, despite the abundance of hydroxyl groups. This contribution to the literature is important as it disproves the often erroneously presumed and reported notion that polyethylene glycol adsorbs to cellulose surfaces in aqueous media. However, dispersibility was found to improve when CNCs were dried in the presence of polyethylene glycol indicating that in the dry state, where competitive water hydrogen bonds are not present, polyethylene glycol does adsorb to CNC surfaces. This is significant as it demonstrates that polymer adsorption is media dependent, and that the particle environment can be tuned to facilitate or inhibit polymer adsorption.

4. **Demonstrate good dispersion of CNCs in a polymer nanocomposite.** In *Chapter 7* well dispersed CNC and fumed silica reinforced polyethylene oxide nanocomposites were prepared by solvent-casting and showed improved mechanical properties in comparison to the homopolymer. While CNC reinforced polyethylene oxide nanocomposites have been previously reported, this work uniquely examined the impact of polymer adsorption and particle dispersion on the crystallization and mechanical performance of the nanocomposite, and directly links to the understanding gained in the previous research chapters. Polymer adsorption to CNC surfaces was observed to occur in a shish-kebab-like morphology that limited spherulite nucleation, yet increased spherulite growth rate. This finding is significant for the community because it expands our understanding of polymer crystallization within CNC nanocomposites. Unlike crystallization in hydrophobic polymer matrices where poor interactions promote nucleation, favourable particle-polymer interactions (and polymer adsorption) reduce polymer mobility and decrease spherulite density. Although, it is well known that

> dispersion is essential for mechanical improvement, this work demonstrates that interrupting particle-particle interactions prior to polymer incorporation is a critical step in achieving well-dispersed, high performance nanocomposites.

As an emerging green nanomaterial, the knowledge gained herein will aid in the development of CNC based composites/materials for both aqueous and non-aqueous applications. For example, the finding that CNC particle-particle interactions in the aggregated state are governed by van der Waals forces indicates that dispersibility is largely independent of surface charge (noting that long term colloidal stability *does* depend on surface charge). This is particularly useful when considering industrially produced CNCs, typically sold as either spray-dried or freeze-dried powders, from which surface chemistry can vary depending on the cellulose source. In addition, the adsorption of polyethylene glycol/polyethylene oxide to CNCs in the dry composites demonstrates that polymer adsorption is media dependent and further is not a prerequisite for reinforcement. As a result, if good particle dispersion can be achieved and maintained, CNCs have the potential to act as reinforcing agents and predictable modifiers regardless of the polymer matrix.

8.1 Ongoing Research

Although good dispersion and improved mechanical properties were achieved within reinforced hydrophilic nanocomposites, an important step forward is to develop a more thorough understanding of CNC behaviour within hydrophobic matrices. This includes investigating the effect of particle surface chemistry and polymer mobility (i.e., glass transition temperature) on particle dispersion and composite mechanical properties. As such, current work is focused on preparing and examining poly(methyl methacrylate-co-butyl methacrylate) nanocomposites reinforced with native and surface modified CNCs and fumed silica.

To investigate polymer mobility atom transfer radical polymerization was used to prepare poly(methyl methacrylate-co-butyl methacrylate) with varying monomer ratios, yielding low and high glass transition temperatures (and a gradient of hydrophobicity), from which solvent cast nanocomposites are to be produced. Surface modification of CNCs has been chosen to mimic the surface chemistry of treated fumed silica (CAB-O-SIL TS-382), whereby octyltrimethoxysilane is grafted to the CNC surface via a one-step modification procedure. Preliminary results indicate that CNC morphology is unchanged following modification and the contact angle increases from < 20˚ for native CNCs to ca. 130˚ for surface modified CNCs. Continuation of this project, involves further characterization of surface modified CNCs, preparation of nanocomposites, and testing nanocomposite thermo/mechanical properties.

8.2 Outlook and Future Work

From the perspective of this work, while favourable particle-polymer interactions are important for good interfacial adhesion, it is the interruption of particle-particle interactions that is most critical for dispersibility. Once, particles are introduced into the matrix, strong particle-polymer interactions alone are not sufficient to achieve good dispersion. As a result, when designing CNC surface modifications, it is perhaps more effective to modify the surface such to limit van der Waals interactions between particles instead of attempting to improve compatibility with the matrix. This will potentially allow for low shear mixing to break particle aggregates more effectively, yielding better dispersed composites. Furthermore, the use of solvent cast master batches, where good dispersion can be achieved and maintained, as recently reported,[1] is a method which can potentially yield well dispersed nanocomposites via melt mixing.

Because interrupting particle-particle interactions is paramount to achieving good dispersion, aqueous based/processed composites remain as the ideal application for CNCs. One such system is the interfacial polymerization of polyamide, where for example, hexane-1,6-diamine (aqueous phase) with decanedioyl dichloride (oil phase) polymerize at the oil/water interface to form nylon 6,10. Dispersing CNCs within the aqueous phase prior to polymerization has the potential to create well-dispersed reinforced nanocomposites that can take the form of fibers, latexes or bulk materials for further melt processing. Success in this approach will require CNCs to be at the interface during polymerization. As CNCs are not surface active particles, modification, potentially via adsorption of water soluble polymers/polysaccharides,[2] may be needed to achieve good dispersion and effective reinforcement.

References

(1) Mariano, M.; Pilate, F.; de Oliveira, F. B.; Khelifa, F.; Dubois, P.; Raquez, J.-M.; Dufresne, A. Preparation of Cellulose Nanocrystal-Reinforced Poly(lactic Acid) Nanocomposites through Noncovalent Modification with PLLA-Based Surfactants. *ACS Omega* **2017**, *2* (6), 2678–2688.

(2) Hu, Z.; Patten, T.; Pelton, R.; Cranston, E. D. Synergistic Stabilization of Emulsions and Emulsion Gels with Water-Soluble Polymers and Cellulose Nanocrystals. *ACS Sustain. Chem. Eng.* **2015**, *3* (5), 1023–1031.